025921-21-T

Applications of the Conjugate Gradient FFT Method in Scattering and Radiation Including Simulations with Impedance Boundary Conditions

Authors: Kasra Barkeshli and John L. Volakis

May 1991

National Aeronautics and
Space Administration
Ames Research Center
Moffett Field, CA 94035
Grant NAG-2-541

(NASA-CR-188214) APPLICATIONS OF THE CONJUGATE GRADIENT FFT METHOD IN SCATTERING AND RADIATION INCLUDING SIMULATIONS WITH IMPEDANCE BOUNDARY CONDITIONS Technical Report, Feb. - Sep. 1991 (Michigan Univ.) N91-24485
Unclas
G3/32 0014418

THE UNIVERSITY OF MICHIGAN
Radiation Laboratory
Department of Electrical Engineering
and Computer Science
Ann Arbor, Michigan 48109-2122
USA

UM Report #025921-21-T

TECHNICAL REPORT
FOR
NASA Grant NAG-2-541
NASA Technical Monitor: Alex Woo

Grant Title:	A NEW TECHNIQUE FOR SIMULATING COMPOSITE MATERIAL
Institution:	The Radiation Laboratory Department of Electrical Engineering and Computer Science The University of Michigan Ann Arbor, MI 48109-2122
Period Covered:	February 1991 - September 1991
Report Title:	Applications of the Conjugate Gradient FFT Method in Scattering and Radiation Including Simulations with Impedance Boundary Conditions
Report Authors:	Kasra Barkeshli and John L. Volakis
Principal Investigator:	John L. Volakis Telephone: (313)764-0500

025921-21-T

Applications of the Conjugate Gradient FFT Method in Scattering and Radiation Including Simulations with Impedance Boundary Conditions

Authors: Kasra Barkeshli and John L. Volakis

May 1991

National Aeronautics and
Space Administration
Ames Research Center
Moffett Field, CA 94035
Grant NAG-2-541

APPLICATIONS OF THE CONJUGATE GRADIENT FFT METHOD IN SCATTERING AND RADIATION INCLUDING SIMULATIONS WITH IMPEDANCE BOUNDARY CONDITIONS

Kasra Barkeshli and John L. Volakis

Radiation Laboratory
Department of Electrical Engineering and Computer Science
The University of Michigan
Ann Arbor, MI 48109-2122
(May 1991)

APPLICATIONS OF THE CONJUGATE GRADIENT FFT METHOD IN SCATTERING AND RADIATION INCLUDING SIMULATIONS WITH IMPEDANCE BOUNDARY CONDITIONS

Abstract

The theoretical and computational aspects related to the application of the Conjugate Gradient FFT (CGFFT) method in computational electromagnetics are examined. The advantages of applying the CGFFT method to a class of large scale scattering and radiation problems are outlined. The main advantages of the method stem from its iterative nature which eliminates a need to form the system matrix (thus reducing the computer memory allocation requirements) and guarantees convergence to the true solution in a finite number of steps. Moreover, since the CGFFT algorithm is highly vectorizable, it can be efficiently implemented on supercomputers and multiprocessor machines.

Results are presented for various radiators and scatterers including thin cylindrical dipole antennas, thin conductive and resistive strips and plates, as well as dielectric cylinders.

Solutions of integral equations derived on the basis of generalized impedance boundary conditions (GIBC) are also examined. These boundary conditions can be used to replace the profile of a material coating by an impedance sheet or insert, thus, eliminating the need to introduce unknown polarization currents within the volume of the layer. Moreover, by applying these surface boundary conditions, the difficulties associated with the calculation of the Green's function are avoided. Impedance boundary conditions of up to the third order are employed and shown to be compatible with the basic CGFFT formulation, allowing an efficient simulation of large coated structures and filled cavity-backed apertures by further reducing the memory demand. For the purpose of validation of these simulations, a general full-wave analysis of two- and three-dimensional rectangular grooves and cavities is presented which will also serve as reference for future work.

TABLE OF CONTENTS

CHAPTER

LIST OF FIGURES

Figure

LIST OF TABLES

Table

LIST OF APPENDICES

Appendix

CHAPTER I

INTRODUCTION

Despite its long life in classical electrodynamics, the study of "Radiation" and "Scattering" has enjoyed renewed interest in recent years, particularly in connection with improved antenna designs required by the technological progress in radio communication, advances in radar signature analysis and control, and more recently, the growing computing power offered by high speed computers. These have contributed to the emergence of *Computational Electromagnetics* (CEM), the numerical study of electromagnetic wave phenomena.

When the operating frequency is such that the object's linear dimensions are comparable to the wavelength, the available high frequency methods are no longer applicable and more accurate formulations must be adopted. Moreover, these asymptotic techniques are predominantly suitable for conducting bodies of canonical geometries and shapes. Therefore, they cannot be employed for simulating material bodies which constitute modern composite vehicles and structures. Furthermore, because of an increase in the complexity of the formulations and corresponding limitations on justifiable approximations, the need for consistent and stable numerical schemes arises to ensure convergence of the solutions under consideration. These restrictions, coupled with the limitations on available computer resources (memory and speed), represent a challenge in the modeling of large scale problems. It is this class of problems that this study attempts to address.

1.1 Motivation

In radiation and scattering, we are interested in defining the electromagnetic fields in the presence of a source distribution. The key to the solution of any such problem is a knowledge of the induced current density on the surface or in the volume of the antenna or scatterer. Once this is found, the radiated or scattered fields can be computed via the standard radiation integrals.

The induced volumetric current density **J** on the body of the scatterer or radiator satisfies an integral equation which may be expressed in functional form as

$$\mathcal{E}^i = \mathcal{A}[\mathbf{J}] \tag{1.1}$$

where $\mathcal{E}^i$ is a vector representing the impressed field and $\mathcal{A}$ is an integrodifferential operator (functional) relating the impressed fields to the induced current. Traditionally, equation (1.1) is solved directly by discretizing the unknown current density and forming a linear system of equations. Typically, such a discretization results in a square matrix demanding a memory storage of order $\mathcal{O}(N^2)$, where N is the number of unknown coefficients in the current density expansion. The system of equations is usually solved by standard matrix inversion methods such as Gaussian elimination or LU decomposition. However, the limitations on available computing resources (including memory and processing time) associated with the numerical formulation of large systems, limit the range of applicability of such direct methods to relatively low frequencies. In addition, for large scale simulations, the memory demand of these methods results in prohibitive storage requirements and, thus, traditional matrix inversion approaches are not attractive and alternative methods are needed.

To address this need, iterative approaches have been used by researchers. In iterative methods, an initial solution for the current distribution is assumed, and this is improved through successive iterations. The process continues until a preassigned accuracy (tolerance) is reached. The main advantage of iterative methods is that the calculations can proceed without a need to generate the system matrix, because iterative methods often require only the multiplication of matrices with vectors. This reduces the memory requirement to a lower order $\mathcal{O}(N)$ and therefore renders iterative schemes suitable for large scale simulations. Furthermore, while a matrix inversion approach may fail to yield an accurate solution due to a large condition number of the matrix operators, an iterative method in such cases merely requires more iterations before reaching convergence.

In this study, we will explore the application of an iterative scheme, namely the Conjugate Gradient Method (CGM), in the solution of systems of equations arising in scattering and radiation problems. From its introduction nearly forty years ago [1, 2], the CGM has been of considerable interest to mathematicians and engineers, primarily because, in theory, it ***ensures convergence*** for arbitrary initial estimates–a feature not shared by many of the iterative algorithms used in the past.

The guaranteed convergence of the conjugate gradient method, as well as its efficient storage requirements as an iterative scheme, are prerequisites for its application to general configurations of interest. Another advantage of the CGM, however, stems from an interesting property shared by the integrodifferential operators encountered in most radiation and scattering problems. For these problems, $\mathcal{A}$ is a convolution operator involving the induced current density and the pertinent Green's function. Thus, by employing the convolution theorem, the evaluation of the functional reduces to simple algebraic operations on the Fourier transforms of the convolved quantities. This simplification often results in a notable improvement in the speed of the calculations ($N \log N$ in contrast to N^2). In practice, the Fourier transforms are calculated efficiently via the fast Fourier transform (FFT) [3]. A CGM algorithm which incorporates the FFT to carry out the convolution operations is often referred to as CGFFT method of solution [4].

Other iterative methods utilizing the FFT algorithm have also been applied to a number of scattering problems [5]-[7]. However, these solution techniques usually suffer from two major defficiencies common to most iterative approaches: 1) convergence is not strictly guaranteed, and 2) convergence is often slow. The conjugate gradient method virtually eliminates the first problem because it guarantees monotonic convergence throughout the process. As for the second problem, the number of iterations required for the conjugate gradient method to yield a reasonable accuracy is often a fraction of the total number of unknowns. This depends primarily on the distribution of the dominant eigenvalues of the operator projected onto the system matrix. It has been argued convincingly [8] that the standard conjugate gradient method requires roughly twice as much computation time per solution as the Gaussian elimination, which is an $\mathcal{O}(N^3)$ operation. However, the CGFFT is considerably faster since it requires only $4N(1+\log_2 N)$ operations per iteration–an overall $\mathcal{O}(N^2)$ operation.

The speed of the CGFFT method can be improved further by incorporating the subsectional expansion (basis) functions into the algorithm. In direct methods, it is well known that the use of appropriate expansion functions to represent the unknown current distribution plays an important role in the accuracy and convergence of the solutions. In fact, a large body of literature exists on various types of basis functions and their implementation and performance in connection with direct approaches [9]-[11]. This is not the case with regard to the CGFFT method and, therefore, it is of interest to study the incorporation of these functions in the context of the CGFFT. It was found in the course of this research that such a treatment results in a drastic improvement (up to 100 percent) in the convergence rate of the method depending on the type of basis that is employed for the current expansion.

Another area of interest addressed in this study is the incorporation of the generalized impedance boundary conditions [12, 13] in the CGFFT method. Generalized Impedance Boundary Conditions (GIBC) are higher order boundary conditions which involve derivatives of the fields beyond the first. They have been found to be more effective than the traditional first order (standard) conditions in modeling thick dielectric coatings and layers [14]. The GIBCs have been successfully utilized in a number of analytical and asymptotic applications such as the Weiner-Hopf technique and function theoretic approaches [14]. However, their utility in numerical methods has not been studied beyond the first order [15]. Applying these conditions on the surface of a dielectrically coated scatterer circumvents the need for sampling within the target's volume and hence considerably reduces the number of unknowns required in the discretization of the problem. However, solution of these problems by direct methods is challenging due to the difficulty in handling higher order derivatives involved in the formulation. On the other hand, when the CGFFT method is employed, the derivatives may be carried out in the transform domain without much difficulty. These features make the formulation of such structures by generalized boundary conditions highly desirable and, therefore, a part of this study is devoted to the implementation and numerical study of GIBCs in connection with the CGFFT method.

Before closing this section, we remark that an inherent limitation of the iterative solution methods is their requirement that the solution process be repeated for each excitation. In direct approaches, on the other hand, once the system matrix is inverted, the solution for any excitation is virtually at hand. For this reason, iterative solution methods may be computationally intensive in those scattering problems where the target's responses to a number of different excitations are of interest. This may be the case, for a example, when generating the backscatter pattern for an object, where the iterative solution must be repeated for each excitation. A partial remedy in this case is to use the results of the previous excitation as the starting point (initial guess) for the solution of the next excitation. For a certain class of large problems, however, the memory consideration may outweigh the possible disadvantages in speed associated with the multiple excitations. Therefore, in choosing an iterative method for these problems, the intensity of the computations and accuracy requirements as well as the merits of low memory allocations offered by such methods must be carefully examined. In this regard, some vector and parallel processing features offered by modern computing facilities are important in reducing the CPU time in reaching convergence. At any rate, for problems involving a single excitation such as antenna radiation problems, the CGFFT is generally much faster than the general purpose matrix inversion techniques.

1.2 Scope

This dissertation is divided into three parts. Part One (Chapters II through IV) presents the CGFFT method as applied to radiation and scattering. In particular, Chapter II discusses the basic formulation and the incorporation of the subsectional expansion functions into the CGFFT method. Chapters III and IV present applications of the method to one and two dimensional problems classified according to the dimensionality of the employed Fourier transforms, respectively. These include

- Radiation from thin wire dipoles,
- Scattering by flat and cylindrical strips,
- Radiation of cylindrical reflector antennas,
- Radiation of dipoles in the presence of flat plates, and
- Scattering by dielectric cylinders.

For each application, the pertinent integral equations are derived and placed in a form suitable for a solution via the CGFFT method. Chapter V presents the generalized impedance boundary conditions and their incorporation into the CGFFT formulation for the simulation of two- and three-dimensional impedance sheets.

Part Two presents a general study of a class of cavity structures and their analysis using CGFFT in conjunction with the GIBCs. In particular, Chapter VI is a study of two-dimensional grooves of infinite extent, while Chapter VII presents a corresponding study of three-dimensional cavities recessed in perfectly conducting ground planes.

Part Three discusses a vector-concurrent implementation of the CGFFT algorithm on supercomputers and multiprocessor machines. Chapter VIII presents results from a numerical implementation of an optimized CGFFT algorithm, which further illustrate the potentials of the CGFFT in solving large electromagnetic scattering and radiation problems.

In most cases, the accuracy of the solutions is confirmed by a comparison of the obtained results with available measured data or data obtained from alternative solution techniques. Some of the presented results are out of the reach of direct solution techniques and can, thus, serve for validating future methodologies for large scale electromagnetic simulations.

1.3 Basic Concepts

When an object is exposed to electromagnetic fields, the scattered field $\mathbf{U}^s$ is defined as the difference between the total field $\mathbf{U}^T$ in the presence of the object and the incident field $\mathbf{U}^i$ that would exist if the object were absent. That is

$$\mathbf{U}^s = \mathbf{U}^T - \mathbf{U}^i \tag{1.2}$$

The fundamental laws governing the behavior of electromagnetic fields in space and time are Maxwell's equations commonly expressed in differential form as

$$\begin{aligned} \nabla \times \mathbf{E} &= -\frac{\partial \mathbf{B}}{\partial t} && (1.3) \\ \nabla \times \mathbf{H} &= \frac{\partial \mathbf{D}}{\partial t} + \mathbf{J} && (1.4) \\ \nabla \cdot \mathbf{D} &= \rho && (1.5) \\ \nabla \cdot \mathbf{B} &= 0 && (1.6) \end{aligned}$$

where

$\mathbf{E}$ = *Electric field intensity*, volts/m

$\mathbf{H}$ = *Magnetic field intensity*, amperes/m

$\mathbf{D}$ = *Electric flux density (displacement)*, coulombs/m^2

$\mathbf{B}$ = *Magnetic flux density (induction)*, webers/m^2

$\mathbf{J}$ = *Electric current density*, amperes/m^2

ρ = *Electric charge density*, coulombs/m^3

and we shall use MKSC units throughout this study as indicated. The two curl equations (1.3) and (1.4) are Faraday's induction law and the generalized Ampere's circuit law, respectively, while the two divergence relations (1.5) and (1.6) are Gauss' law for the electric and magnetic fields, respectively. The media interacting with the electromagnetic fields are characterized by the so called constitutive relations and can be classified according to their molecular structures and properties of their associated bound charge particles. For a sufficiently simple medium these relations are

$$\mathbf{D} = \epsilon \mathbf{E} \tag{1.7}$$

$$\mathbf{B} = \mu \mathbf{H} \tag{1.8}$$

$$\mathbf{J} = \sigma \mathbf{E} \tag{1.9}$$

where ϵ, μ and σ denote the permittivity, permeability, and conductivity of the medium, respectively.

In the presence of stationary material interfaces(the surface of a scatterer, say), an electromagnetic field satisfies the implicit(natural) boundary conditions

$$\hat{n} \times (\mathbf{E}_1 - \mathbf{E}_2) = 0 \tag{1.10}$$

$$\hat{n} \times (\mathbf{H}_1 - \mathbf{H}_2) = \mathbf{K} \tag{1.11}$$

$$\hat{n} \cdot (\mathbf{D}_1 - \mathbf{D}_2) = \rho_s \tag{1.12}$$

$$\hat{n} \cdot (\mathbf{B}_1 - \mathbf{B}_2) = 0 \tag{1.13}$$

where $\mathbf{K}$ and ρ_s denote surface current and charge densities at the interface separating the two regions to which subscripts 1 and 2 correspond and $\hat{n}$ is the unit normal to the interface(usually taken to be outward with respect to the scatterer). The above boundary conditions are easily established on the assumption that the tangential components of $\mathbf{D}$ and $\mathbf{B}$ remain finite at the interface surface. It should be noted, however, that the last two conditions are not independent of the first two for time-varying fields and are, therefore, redundant [16]. Moreover, if one medium is perfectly conducting ($\sigma \rightarrow \infty$), no electric field exists in that medium as asserted by (1.9). Therefore, it follows from (1.10) that the tangential component of **E** is zero at the surface of a perfect conductor.

In addition to (1.10)-(1.13), boundary conditions must be imposed at infinity to obtain unique solutions to the radiation problems. Physically, these radiation conditions require that solutions which represent outgoing waves traveling in a lossy medium vanish at infinity.

Throughout this work we will consider harmonic time varying fields and adopt the time convention $e^{j\omega t}$. Thus, the Maxwell equations (1.3) and (1.4) become

$$\nabla \times \mathbf{E} = -j\omega \mathbf{B} \tag{1.14}$$

$$\nabla \times \mathbf{H} = j\omega \mathbf{D} + \mathbf{J} \tag{1.15}$$

with the explicit time dependence suppressed. The constitutive parameters under the time harmonic assumption are, in general, complex quantities. In particular, for a conducting medium, Ampere's law (1.15) reads

$$\nabla \times \mathbf{H} = \mathbf{J}_e + \mathbf{J}_c + j\omega \mathbf{D} \tag{1.16}$$

where $\mathbf{J}_e$ represents the externally impressed current source and $\mathbf{J}_c$ is the conduction current generated in the medium due to ohmic loss. Employing the constitutive relations (1.7) and (1.9), equation (1.16) can be rewritten

$$\nabla \times \mathbf{H} = \mathbf{J}_e + j\omega(\epsilon - j\sigma/\omega)\mathbf{E} \tag{1.17}$$

where, the quantity

$$\epsilon_c = \epsilon - j\sigma/\omega \tag{1.18}$$

may be identified as the complex permittivity of the medium.

The solution of a scattering problem consists of finding the solution of Maxwell equations which satisfy the boundary conditions at the surface of the scatterer and which displays the proper behavior at infinity. Typically, this is carried out by deriving a suitable integral equation in terms of the unknown current density excited on the scatterer. Two popular integral equations for the time-harmonic electromagnetic fields are the *electric field integral equation* (EFIE) and the *magnetic field integral equation* (MFIE). The EFIE enforces the boundary condition on the tangential electric field and can be used for both closed and open surfaces. The MFIE, on the other hand, enforces the boundary condition on the tangential components of the magnetic field and remains valid only for closed surfaces [17]. Since we are interested in both types of scatterers, the EFIE is developed and applied in this study.

An equation for **E** may be obtained from Maxwell's equations by eliminating **H** in (1.14) and (1.15) and using (1.7)-(1.9). Thus, assuming a homogeneous surrounding medium, we have for the scattered electric field

$$\nabla \times \nabla \times \mathbf{E}^s - k^2 \mathbf{E}^s = -j\omega\mu\mathbf{J} \tag{1.19}$$

where $k = \omega\sqrt{\mu\epsilon}$ is the wave number in the medium. This is known as the vector wave equation and the solution may be expressed as [18, 19]

$$\mathbf{E}^s = -jkZ \iiint_V \bar{\mathbf{\Gamma}}(\mathbf{r};\mathbf{r}') \cdot \mathbf{J}(\mathbf{r}')\,\mathrm{dv}' \tag{1.20}$$

where $Z = \sqrt{\mu/\epsilon}$ is the intrinsic impedance of the medium, $\bar{\mathbf{\Gamma}}$ denotes the electric dyadic Green's function in unbounded space given by

$$\bar{\mathbf{\Gamma}}(\mathbf{r};\mathbf{r}') = \left(\bar{\mathbf{I}} + \frac{1}{k^2}\nabla\nabla\right) G(\mathbf{r};\mathbf{r}') \tag{1.21}$$

and G is the scalar Green's function

$$G(\mathbf{r};\mathbf{r}') = \frac{e^{-jk|\mathbf{r}-\mathbf{r}'|}}{4\pi|\mathbf{r}-\mathbf{r}'|} \tag{1.22}$$

In the above, $\mathbf{r}$ and $\mathbf{r}'$ denote the field and source points, respectively and an explicit expression of $\bar{\mathbf{\Gamma}}$ in Cartesian coordinates is

$$\bar{\mathbf{\Gamma}} = \begin{pmatrix} (1+\frac{1}{k^2}\frac{\partial^2}{\partial x^2}) & \frac{1}{k^2}\frac{\partial^2}{\partial x\partial y} & \frac{1}{k^2}\frac{\partial^2}{\partial x\partial z} \\ \frac{1}{k^2}\frac{\partial^2}{\partial y\partial x} & (1+\frac{1}{k^2}\frac{\partial^2}{\partial y^2}) & \frac{1}{k^2}\frac{\partial^2}{\partial y\partial z} \\ \frac{1}{k^2}\frac{\partial^2}{\partial z\partial x} & \frac{1}{k^2}\frac{\partial^2}{\partial z\partial y} & (1+\frac{1}{k^2}\frac{\partial^2}{\partial z^2}) \end{pmatrix} G(\mathbf{r};\mathbf{r}') \tag{1.23}$$

The magnetic field is then obtained from Faraday's law (1.14).

Equation (1.20) in conjunction with the appropriate boundary conditions on the tangential component of the total electric field gives the EFIE integral equation to be solved for the unknown current $\mathbf{J}$. The specific form of this integral equation depends on the particular problem under study. Once the current distribution is evaluated from the integral equation, the scattered field throughout space may be calculated from the scattering integral (1.20).

In radar applications, the target is completely characterized for the radar system by a quantity known as the radar cross section (RCS) or echo area denoted by σ(not to be confused with the conductivity σ). It is a measure of the reflective strength of the target and is mathematically defined as

$$\sigma = \lim_{R\to\infty} 4\pi R^2 \frac{P_s}{P_i} \tag{1.24}$$

where P_s is the power flux density of the scattered wave in a specified direction at a distance R from the scatterer, and P_i is the power flux density of the incident plane wave. The radar cross section is in general a function of frequency, polarization, and angle of incidence. When the incident and pertinent scattering directions are coincident but opposite in sense, (1.24) provides the monostatic or backscattering cross section.

For two-dimensional targets which are infinite in extent along a given direction, the scattering parameter is referred to as the radar cross section per unit length or echo width and is defined as

$$\sigma^{2d} = \lim_{\rho\to\infty} 2\pi\rho^2 \frac{P_s}{P_i} \cdot \tag{1.25}$$

When the scatterer is long but finite in one dimension, the physical optics approximation may be used to relate the three-dimensional radar cross section of the target to the associated two-dimensional echo width calculated on the assumption of infinite length. Hence, for plane wave illumination normal to the long dimension of the scatterer, we have

$$\sigma^{3d} = 2(\frac{\ell}{\lambda})^2\sigma^{2d} \tag{1.26}$$

where ℓ denotes the length of the target in the long dimension.

Part I

THE CONJUGATE GRADIENT FFT METHOD

CHAPTER II

THE CGFFT FORMULATION

2.1 Introduction

The integrodifferential equations considered in radiation and scattering have the general form

$$\mathbf{E}^i(\mathbf{r}) = \eta(\mathbf{r})\,\mathbf{J}(\mathbf{r}) + \iiint_V \bar{\mathbf{\Gamma}}(|\mathbf{r}-\mathbf{r}'|)\cdot\mathbf{J}(\mathbf{r}')\,\mathrm{d}\mathbf{v}' \tag{2.1}$$

where $\mathbf{E}^i$ denotes the excitation field, $\mathbf{J}$ is the unknown current density vector, $\bar{\mathbf{\Gamma}}$ is the associated dyadic Green's function, $\mathbf{r}$ and $\mathbf{r}'$ specify the observation and integration points and η is the scalar function which depends on the electrical properties of the scatterer or radiator.

In general, the above integral equation may be solved using direct methods such as the Method of Moments [20]. However, as the size of the problem increases, iterative techniques become more attractive for the solution of such equations. This is mainly because iterative methods avoid the process of matrix inversion which is subject to numerical instability for ill-conditioned matrices. Also, these schemes often involve only the multiplication of matrices with vectors and thus do not require an explicit storage of the system matrix.

2.2 Description of the Conjugate Gradient Method

The conjugate gradient method is a nonlinear semi-direct purely-iterative scheme. That is, assuming no truncation and roundoff errors, the exact solution is obtained in a finite number of steps depending on the number of independent eigenvalues of the operator matrix. This is achieved by applying the method to the normal equations obtained by premultiplying the system matrix by its adjoint. Moreover, the solution is improved at a monotonic rate throughout the process and convergence is guaranteed for a given number of unknowns and as the order of approximation is increased [21]. Convergence is accomplished via a systematic orthogonalization of the solution vector with respect to the residual vector defined as the difference between the left and right hand sides of the system at the end of each iteration. That is, for a system representing N unknowns, the solution vector is constructed from a set of N linearly independent (mutually conjugate) vectors orthogonal to the residual vectors. Since these also form a linearly independent set, the exact solution is obtained at the N-th iteration, but in general the solution can be constructed, rather accurately, with only a few of the orthogonal vectors that span the solution space. As a result, the desired tolerance is achieved in less than N iterations.

The method starts out with an initial guess $\mathbf{J}_0$ and a corresponding residual error $\mathbf{R}_0$. In each iteration, the residual vector is minimized not only along each local search direction but also over the entire span of search directions. To this end, the solution is expanded in terms of search vectors which would be generated by the modified Gram-Schmidt orthogonalization scheme when applied to the sequence of residual vectors as the basis functions[1]. The set of search vectors $\{\mathbf{P}_n\}$, so constructed are

---

[1] The choice of the N-dimensional coordinate unit vectors as the basis functions would yield Gaussian elimination.

mutually A-orthogonal or conjugate (as opposed to orthogonal)

$$< \mathbf{P}_i, \mathcal{A}[\mathbf{P}_j] >= 0 \quad , \quad i \neq j \tag{2.2}$$

The significance of this set of directions is as follows: for a quadratic function, successive line minimizations along a conjugate set of directions will achieve the minimum without the need to repeat minimization in any direction. Consequently, the minimum is achieved at the end of a finite number of steps. For nonquadratic functions, this guarantees quadratic convergence as the process goes on.

A version of the conjugate gradient algorithm to be used herein is [4]

$$\mathbf{R}_0 = \mathcal{A}[\mathbf{J}_0] - \mathbf{E}^i$$

$$\mathbf{P}_0 = -b_{-1}\mathcal{A}^a[\mathbf{R}_0]$$

Main Iteration Loop

$$t_n = \frac{1}{||\mathcal{A}[\mathbf{P}_n]||^2}$$

$$\mathbf{J}_{n+1} = \mathbf{J}_n + t_n\mathbf{P}_n$$

$$\mathbf{R}_{n+1} = \mathbf{R}_n + t_n\mathcal{A}[\mathbf{P}_n] \tag{2.3}$$

$$b_n = \frac{1}{||\mathcal{A}^a[\mathbf{R}_n]||^2}$$

$$\mathbf{P}_{n+1} = \mathbf{P}_n - b_n\mathcal{A}^a[\mathbf{R}_{n+1}]$$

$$\frac{||\mathbf{R}||}{||\mathbf{E}^i||} \overset{?}{\leq} \delta$$

Repeat If Necessary

The norm and the adjoint operator are defined in terms of the inner product as

$$||\mathbf{U}||^2 =< \mathbf{U}, \mathbf{U} > \tag{2.4}$$

and

$$< \mathcal{A}[\mathbf{U}], \mathbf{V} > = < \mathbf{U}, \mathcal{A}^a[\mathbf{V}] > \tag{2.5}$$

It may be shown that [21]

$$\mathcal{A}^a[\mathbf{J}] = \eta^\star(\mathbf{r})\,\mathbf{J}(\mathbf{r}) + \iiint_V \bar{\mathbf{\Gamma}}^\star(|\mathbf{r}-\mathbf{r}'|)\cdot\mathbf{J}(\mathbf{r}')\,\mathbf{dv}' \tag{2.6}$$

where $\star$ denotes the complex conjugate.

2.3 Conjugate Gradient FFT Formalism

The scattering integral in (2.1) is of convolution type and can, therefore, be evaluated in the spectral domain by invoking the convolution theorem. To describe this process, we must introduce the forward and inverse Fourier transformations. For one-dimensional functions, the Fourier transform pair is

$$\tilde{g}(k_x) = \int_{-\infty}^{\infty} g(x)e^{-jk_x x}dx \tag{2.7}$$

$$g(x) = \frac{1}{2\pi}\int_{-\infty}^{\infty} \tilde{g}(k_x)e^{jk_x x}\,dk_x \tag{2.8}$$

where k_x is the spectral variable and we use the following symbolism to indicate the relationship among the transform pair

$$g(x) \overset{\mathcal{F}}{\Longleftrightarrow} \tilde{g}(f_x) \tag{2.9}$$

Based on the above definitions, the convolution theorem is stated as [22]:

$$\int_{-\infty}^{\infty} g(x')h(x-x')dx' = g(x) * h(x) \overset{\mathcal{F}}{\Longleftrightarrow} \tilde{g}(k_x)\cdot\tilde{h}(k_x) \tag{2.10}$$

Similarly, the two dimensional Fourier transform pair is defined as

$$\tilde{g}(k_x, k_y) = \int_{-\infty}^{\infty}\int_{-\infty}^{\infty} g(x,y)e^{-j(k_x x + k_y y)}dxdy \tag{2.11}$$

$$g(x,y) = \frac{1}{(2\pi)^2}\int_{-\infty}^{\infty}\int_{-\infty}^{\infty} \tilde{g}(k_x,k_y)e^{j(k_x x + k_y y)}dk_x dk_y \tag{2.12}$$

with the convolution theorem expressed as

$$\int_{-\infty}^{\infty}\int_{-\infty}^{\infty} g(x',y')h(x-x',y-y')dx' = g(x,y) * h(x,y) \overset{\mathcal{F}}{\Longleftrightarrow} \tilde{g}(k_x,k_y)\cdot\tilde{h}(k_x,k_y) \tag{2.13}$$

As usual, the transform of differentiated functions is given by

$$\frac{\partial g}{\partial x} \overset{\mathcal{F}}{\Longleftrightarrow} jk_x\tilde{g}(k_x) \tag{2.14}$$

Using the Fourier transform notation, equation (2.1) can now be formally written as

$$\mathbf{E}^i = \eta\mathbf{J} + \mathcal{F}^{-1}\{\tilde{\bar{\bar{\mathbf{\Gamma}}}}\cdot\tilde{\mathbf{J}}\} \tag{2.15}$$

where $\mathcal{F}^{-1}$ denotes the inverse Fourier transform operator. Clearly, (2.15) avoids the generation of the square matrix corresponding to the operator $\mathcal{A}$ implying a storage requirement of $\mathcal{O}(N)$ as compared to $\mathcal{O}(N^2)$ required with direct implementations. The solution of (2.15) via the CGM will be referred to as the CGFFT solution method.

The Fourier transforms implied in (2.15) are, of course, continuous whereas in practice they will be replaced with discrete Fourier transforms (DFTs). It is, therefore, necessary that an accurate relationship of the transforms in the discrete and continuous domains be established. Otherwise, a solution in one domain may not be representative of that in the other. Alternatively, excessive sampling may be required to represent the continuous system.

Consider the finite-duration function g whose M consecutive sampled values covering the entire domain of its definition are given by

$$g_n = g(x_n) \qquad x_n = n\Delta x \qquad n = 0,\cdots,N-1 \tag{2.16}$$

The one-dimensional forward and inverse discrete Fourier transforms (DFT) of this sampled train are defined as [22]

$$\hat{g}_p = \sum_{n=0}^{N-1} g_n e^{-j2\pi np/N} \tag{2.17}$$

and

$$g_n = \frac{1}{N} \sum_{p=0}^{N-1} \hat{g}_p e^{j2\pi np/N} \tag{2.18}$$

where the consecutive spectral samples $\hat{g}_p$ are separated by the spatial frequency interval $\Delta f_x = 1/(N\Delta x)$. Similarly, the two-dimensional DFT pair is defined as

$$\hat{g}_{pq} = \sum_{m=0}^{M-1} \sum_{n=0}^{N-1} g_{mn} e^{-j2\pi(mp/M+nq/N)} \tag{2.19}$$

and

$$g_{mn} = \frac{1}{MN} \sum_{p=0}^{M-1} \sum_{q=0}^{N-1} \hat{g}_{pq} e^{j2\pi(mp/M+nq/N)} \tag{2.20}$$

For consistency, the transform of the differential operator (2.14) may be replaced by first approximating the operator by its discrete counterpart. For example, using a 3-point central difference scheme, we have

$$\frac{\partial g}{\partial x}(x_i) \simeq \left[\frac{\Delta g}{\Delta x}\right]_3 = \frac{g(x_i + \frac{\Delta x}{2}) - g(x_i - \frac{\Delta x}{2})}{\Delta x} \tag{2.21}$$

whose Fourier transform is given by

$$\frac{\partial g}{\partial x} \overset{\mathcal{F}}{\Longleftrightarrow} \tilde{g}(k_x) \frac{e^{jk_x\frac{\Delta x}{2}} - e^{-jk_x\frac{\Delta x}{2}}}{\Delta x} \tag{2.22}$$

or more compactly as

$$\frac{\partial g}{\partial x} \overset{\mathcal{F}}{\Longleftrightarrow} jD_x(k_x)\tilde{g}(k_x) \tag{2.23}$$

where

$$D_x = k_x \mathrm{sinc}(k_x \frac{\Delta x}{2}) \tag{2.24}$$

and $\mathrm{sinc}(x) \equiv \frac{\sin(x)}{x}$ is known as the sampling function. It is seen that the transforms of the continuous and discrete derivatives (equations (2.14) and (2.23)) become equal as the spatial sampling interval becomes vanishingly small since

$$\lim_{x \to 0} \mathrm{sinc}(x) = 1$$

More accurate expressions may be derived by using higher order difference formulae. For example, employing the 5-point central difference scheme, we have

$$\frac{\partial g}{\partial x}(x_i) \simeq \left[\frac{\Delta g}{\Delta x}\right]_5 = \frac{8g(x_i + \frac{\Delta x}{2}) - g(x_i + \frac{3\Delta x}{2}) + g(x_i - \frac{3\Delta x}{2}) - 8g(x_i - \frac{\Delta x}{2})}{12\Delta x} \tag{2.25}$$

and the corresponding transform pair is given by

$$\frac{\partial g}{\partial x} \overset{\mathcal{F}}{\Longleftrightarrow} jk_x[\frac{2}{3}\mathrm{sinc}(k_x\frac{\Delta x}{2}) - \frac{1}{4}\mathrm{sinc}(3k_x\frac{\Delta x}{2})]\tilde{g}(k_x)\cdot \tag{2.26}$$

2.4 Incorporation of Subsectional Expansion Functions

In the Method of Moments, it is well known that the use of appropriate expansion (basis) functions to represent the unknown current distribution, plays an important role in the accuracy and convergence of the solutions.

The employment of the subsectional basis functions to iterative methods involving the FFT was initially proposed in connection with the Spectral Iterative Technique (SIT) [23] and was shown to produce improvements in the rate of convergence. However, no quantitative conclusions were drawn because of convergence difficulties associated with the SIT. Here, a systematic study of the incorporation of basis functions into the CGFFT method will be considered.

An assumption in the derivation of the DFT pair (2.17)-(2.18) is the validity of the integral approximation

$$\tilde{g}(k_x) = \int_{-\infty}^{\infty} g(x)e^{-jk_x x}dx \approx \sum_n g_n e^{-jk_x x_n}\Delta x \tag{2.27}$$

implying that the integrand is constant over each sampling interval in (2.27). In other words,

$$g(x)e^{-jk_xx} = g_{rn} + jg_{in} = \text{const.} \qquad x_n \leq x \leq x_{n+1} \tag{2.28}$$

where $g_{rn} = \Re e\{g_n\}$ and $g_{in} = \Im m\{g_n\}$. A consequence of (2.28) is that $g(x)$ is not constant over the interval and is, in fact, a function of both spatial and spectral variables. Thus, from a solution of (2.28)

$$\begin{aligned} g_r(x) &= \Re e\{g(x)\} = g_{rn}\cos(k_xx) - g_{in}\sin(k_xx) & (2.29)\\ g_i(x) &= \Im m\{g(x)\} = g_{rn}\sin(k_xx) + g_{in}\cos(k_xx) & (2.30) \end{aligned}$$

It has been observed [24] that the above dependence of the implied discrete representation of a given continuous function can play a major role in degrading the convergence rate of the CGFFT solution. It is, therefore, essential that some corrective procedure be taken and an obvious approach is to employ a higher order integration formula to replace (2.27). This was discussed in [24] but as can be expected, it results in a slower DFT algorithm. An alternative [23, 25] is to expand $g(x)$ in a sequence of subsectional expansion functions $\{f_n\}$ as

$$g(x) = \sum_{n=0}^{N-1} g_n f_n(x) = \sum_{n=0}^{N-1} g_n f(x - x_n) \tag{2.31}$$

where the second equality implies the invariance of the basis functions with respect to translation in the x-coordinate. Introducing the Dirac delta function

$$\delta(x) = \begin{cases} 1, & x = 0 \\ 0, & \text{else} \end{cases} \tag{2.32}$$

equation (2.31) may be rewritten as a convolution in the form

$$g(x) = f(x) * \sum_{n=0}^{N-1} g_n \delta(x - x_n) \tag{2.33}$$

The Fourier transform of $g(x)$ is thus given by

$$\tilde{g} = \tilde{f} \cdot \hat{g} \tag{2.34}$$

where $\tilde{f}$ is the Fourier transforms of the chosen basis function and $\hat{g}$ is the discrete Fourier transform of g as given by (2.18). Equation (2.34) establishes the relationship between the continuous and discrete Fourier transforms when subsectional expansion functions are employed.

Customary forms of the basis function $f(x)$ include the piecewise constant (PWC) and the overlapping piecewise sinusoidal (PWS) expansion functions given by

$$P(x) = \begin{cases} 1 & |x| < \frac{\Delta x}{2} \\ 0 & \text{else} \end{cases} \tag{2.35}$$

$$Q(x) = \begin{cases} \dfrac{\sin[k_o(\Delta x - |x|)]}{\sin(k_o \Delta x)} & |x| \leq \Delta x \\ 0 & \text{else} \end{cases} \tag{2.36}$$

respectively where k_o denotes the free space wave number. For these choices, we have the Fourier transforms

$$\tilde{P}(k_x) = \Delta x \text{sinc}(k_x \frac{\Delta x}{2}) \tag{2.37}$$

$$\tilde{Q}(k_x) = \frac{k_o[\cos(k_x \Delta x) - \cos(k_o \Delta x)]}{\sin(k_o \Delta x)\,(k_o^2 - k_x^2)} \tag{2.38}$$

and we observe that for a sufficiently small sampling interval

$$\lim_{\Delta x \to 0} \tilde{P}(k_x) = \Delta x \tag{2.39}$$

$$\begin{aligned} \lim_{\Delta x \to 0} \tilde{Q}(f_x) &= \frac{k_o \sin(k_o \Delta x) - k_x \sin(k_x \Delta x)}{\cos(k_o \Delta x)(k_o^2 - k_x^2)} \\ &= \Delta x \end{aligned} \tag{2.40}$$

where use has been made of l'Hôpital's rule and the approximations

$$\sin x \sim x \qquad \cos x \sim 1 \qquad , |x| \ll 1$$

Therefore, for vanishingly small sub-intervals, the relation

$$\tilde{g}(f_x) \simeq \Delta x \cdot \hat{g} \tag{2.41}$$

holds when the above expansion functions are employed. Apart from the multiplying constant, (2.41) is the transform of $g(x)$ when $f(x) = \delta(x)$–delta basis. Since the same result can also be derived via direct application of the rectangular rule of integration (2.27) in the computation of the Fourier integral, (2.41) has been exclusively associated with the conventional application of the FFT algorithm despite the fact that it holds true for subsectional expansion functions as well. As will be shown later, the convergence of the CGFFT method is improved considerably if the more accurate expression (2.34) is used in the formulation instead of (2.41).

In the case of a two dimensional current representations, an appropriate expansion is

$$g(x,y) = f(x,y) * \sum_{n=0}^{N-1} \sum_{m=0}^{M-1} g_{nm}\delta(x-x_n)\delta(y-y_m) \tag{2.42}$$

where $f(x,y)$ denotes the surface basis function and (2.34) still holds with the transforms interpreted as two-dimensional ones.

Often, it is necessary that the basis function be chosen to have a different functional dependence in the x and y directions. For example, when representing the currents on a thin plate a more suitable basis function is of the form

$$f(x,y) = P(x)Q(y) \qquad \text{or} \qquad f(x,y) = Q(x)P(y) \tag{2.43}$$

having the corresponding Fourier transforms

$$\tilde{f} = \tilde{P}(k_x)\tilde{Q}(k_y) \qquad \text{and} \qquad \tilde{f} = \tilde{Q}(k_x)\tilde{P}(k_y) \tag{2.44}$$

and P, Q, $\tilde{P}$, and $\tilde{Q}$ are given in (2.35)-(2.36) and (2.37)-(2.38). Again, as Δx and Δy both go to zero, equations (2.44) reduce to

$$\tilde{g}(k_x, k_y) \simeq \Delta S \hat{g} \tag{2.45}$$

where $\Delta S = \Delta x \Delta y$ is the incremental surface element.

The above analysis enables one to incorporate the subsectional expansion functions into the CGFFT formulation. Using (2.34), equation (2.15) can now be written as

$$\mathbf{E}^i = \bar{\eta} \cdot \mathbf{J} + \mathcal{F}^{-1}\left\{\tilde{\bar{\mathbf{\Gamma}}} \cdot \hat{\mathbf{J}} \tilde{f}\right\} \tag{2.46}$$

Obviously, the transform $\tilde{f}$ of the basis function needs to be computed only once and thus the computations per iteration implied by (2.15) and (2.46) are essentially the same.

2.5 Numerical Considerations

Equations (2.15) and (2.46) are valid only on the body of the scatterer. That is the domain of the Fourier transform is not infinite and for this reason, they cannot be solved directly for $\tilde{\mathbf{J}}$ in the spectral domain. To solve for $\mathbf{J}$, (2.15) and (2.46) must be enforced on the scatterer in the spatial domain along with the sampling requirements and linearity of the corresponding discrete convolution [22]. In a discrete implementation of (2.46), the sampling intervals should be chosen so that the Nyquist criterion is satisfied in the spatial domain. Also the length of the FFT (referred to as FFT pad) must be large enough to accommodate the spectral contents of the convolved quantities. That is, the truncation of the spectrum should cause minimal errors in the iteration process.

In general, the period M of the array to be transformed is chosen according to the relation

$$N' = 2^{\nu} : \qquad N' > N_{\mathrm{Nyquist}} \qquad N' \geq 2N - 1 \tag{2.47}$$

where N is the number of unknown coefficients in the discretization of the current density and ν is an integer. In practice, ν is chosen to be the smallest integer satisfying the relation

$$\nu \geq \log_2(2N - 1) + \varrho \tag{2.48}$$

where ϱ is also an integer (usually unity) setting the order of the FFT pad. The array elements beyond the physical extent of the scatterer are set to zero before (forward) and after (inverse) transformation.

In scattering computations, a usual practice in the implementation of (2.46) is to employ a sampling interval of at least 1/10 of a wavelength and an FFT length at least twice (order $\varrho = 1$) that of the linear dimension of the scatterer in order to accommodate the spectral spreading due to the convolution. The sampling requirement is more serious for antenna problems where one is interested in an accurate evaluation of the surface fields for input impedance calculations. The FFT size should be chosen to minimize aliasing errors caused by the truncation of the Fourier transform of the Green's function. However, as seen from (2.15) and (2.46), when minimizing aliasing, the entire quantity in the curly brackets must be considered. This involves the product of the transforms of the current with the Green's function. When the current density is not expected to be associated with spatial singularities, its transform will be essentially bandlimited and an FFT length of order $\varrho = 1$ should be adequate to represent the spectral content of the convolution without noticeable aliasing error. However, when the current density is associated with spatial singularities as in the case of E-polarized excitation for a thin conducting strip, aliasing is expected to cause substantial error unless corrective means are introduced. In general, to eliminate aliasing errors when employing the discrete Fourier transform, we must form periodic functions in the spatial and spectral domains [26] and this is the basis of the corrective procedure discussed later in the thesis.

2.6 Summary

A general overview of the conjugate gradient algorithm for solving electromagnetic scattering and radiation problems was presented. By introducing the Fourier transform pair and employing the convolution theorem, the electric field integral equation was placed in a form suitable for a solution via the conjugate gradient method.

The incorporation of subsectional expansion functions into the CGFFT method was also discussed. A simple relationship between the continuous and discrete Fourier transforms of the unknown function was established in terms of the transform of the employed expansion function. The relationship holds for both one- and two-dimensional cases and may be considered as a generalization of a commonly used expression in the conventional application of FFT. The practical advantages of using the subsectional basis functions will be examined in the next two chapters.

Finally, since the Fourier transforms involved in the calculations are computed by the fast Fourier transform, some numerical aspects of the method were also addressed.

CHAPTER III

RADIATION AND SCATTERING FROM WIRES AND STRIPS

3.1 Introduction

In this chapter the CGFFT method will be applied to the analysis of wire dipoles as well as flat and circular cylindrical strips.

The radiation by a center-fed cylindrical wire dipole has been extensively studied with analytical approaches [27, 28] as well as traditional numerical techniques such as the method of moments [29, 30]. It is, thus, instructive to consider an application of the CGFFT solution method to this problem first. Two classic integral equations for the total current distribution over conducting wires are referred to as Pocklington's integrodifferential equation and Hallen's integral equation. The latter is usually restricted to the use of a delta-gap voltage source model at the feed of a wire antenna while the former is more general and is adaptable to other excitations.

The scattering behavior of thin strips has also been studied in some detail in the last three decades. These include the scattering from conductive [31] and resistive strips [32, 33] as well as the analysis and synthesis of tapered strips [34, 35]. These studies have focused on flat strips. On the other hand, a numerical solution method for thin dielectric slabs of uniform thickness and arbitrary shape was given as early as 1965 [36, 37] by discretizing the slab and forming a linear system of equations to be solved via the Method of Moments.

In the present study, the CGFFT will be applied for computing the scattering by the flat and circular strip problem. It is shown that for circular strips the convolutional form of the integral is preserved in terms of the angular parameter ϕ.

3.2 Radiation of a Thin Wire Dipole

Consider a z-directed cylindrical dipole of length ℓ and radius $a \ll \ell$ radiating in free space. The electric field due to the excited current distribution K_z over the antenna is given by the scattering integral (1.20). If the wire is thin, the current at the end faces is negligible and the radiated field in the cylindrical coordinates is then given by

$$E_z^s(\rho, z) = -jk_o Z_o \left(1 + \frac{1}{k_o}\frac{\partial^2}{\partial z^2}\right) \int_{-\frac{\ell}{2}}^{\frac{\ell}{2}} \int_0^{2\pi} K_z(\phi', z') \frac{e^{-jk_o R}}{4\pi R} a\, d\phi' dz' \tag{3.1}$$

where R is the distance between the observation point (ρ, ϕ, z) and the source point (a, ϕ', z')

$$R = \sqrt{\rho^2 + a^2 - 2\rho a \cos(\phi - \phi') + (z - z')^2} \tag{3.2}$$

and Z_o and k_o are the intrinsic impedance and wave number of the free space, respectively. For a $\phi -$ symmetric method of feeding [38], the surface current density K_z is azimuthally uniform and the total current is given by $I_z = 2\pi a K_z$. Moreover, since the radiated field is independent of ϕ, we may set $\phi = 0$ for convenience. By enforcing the boundary condition

$$E_z^i(a, z) + E_z^s(a, z) = 0, \tag{3.3}$$

stating that the tangential field vanishes on the wire surface, we obtain the Pocklington's integral equation [39]

$$E_z^i(z) = jk_oZ_o\left(1 + \frac{1}{k_o}\frac{\partial^2}{\partial z^2}\right)\int_{-\frac{\ell}{2}}^{\frac{\ell}{2}} I_z(z')G_w(z-z')dz' \tag{3.4}$$

In the above, $G_w(z, z')$ is the Green's function (also referred to as the *exact kernel*) given by

$$G_w(z-z') = \frac{1}{2\pi}\int_0^{2\pi}\frac{e^{-jk_oR}}{4\pi R}d\phi \tag{3.5}$$

where

$$R = \sqrt{(z-z')^2 + 4a^2\sin^2\frac{\phi}{2}} \tag{3.6}$$

The above integral equation may be simplified further for an electrically thin dipole($k_oa \ll 1$). In this case, a total filamentary line-source may be assumed to flow along the center of the antenna along the z-axis. The angular integration over ϕ is avoided and G_w is replaced by the *reduced kernel*

$$G_w(z-z') = \frac{e^{-jk_or}}{4\pi r} \tag{3.7}$$

where r is the distance from a field point (a, ϕ, z) on the cylindrical surface to a source point $(0, 0, z')$ on the z-axis

$$r = \sqrt{(z-z')^2 + a^2} \tag{3.8}$$

Comparing (3.4) with (1.1) we may identify the right hand side of (3.4) as $\mathcal{A}[I]$ whose adjoint is given by

$$A^a[I] = -jk_oZ_o\left(1 + \frac{1}{k_o}\frac{\partial^2}{\partial z^2}\right)\int_{-\frac{\ell}{2}}^{\frac{\ell}{2}} I(z')G_w^*(z-z')dz' \tag{3.9}$$

A form of (3.4) compatible with (2.15) is

$$E_z^i(z) = \frac{jZ_o}{k_o}\mathcal{F}^{-1}\left\{(k_o^2 - k_z^2)\tilde{G}_w(k_z)\tilde{f}(k_z)\hat{I}\right\} \tag{3.10}$$

where

$$\tilde{G}_w(k_z) = \begin{cases} \frac{1}{2\pi} I_o(a\sqrt{k_z^2 - k_o^2})\, K_o(a\sqrt{k_z^2 - k_o^2}) & \text{exact kernel} \\ \\ \frac{1}{2\pi} K_o(a\sqrt{k_z^2 - k_o^2}) & \text{reduced kernel} \end{cases} \tag{3.11}$$

is the Fourier transform of the Green's function in which I_o and K_o are the zeroth order modified Bessel functions of the first and second kind, respectively. Upon the specification of the excitation field $\mathbf{E}^i$, expression (3.10) is now suitable for a solution via the CGFFT method.

3.2.1 Dipole Excitation Models

Two excitation models commonly used in the analysis of the wire antennas, namely the voltage gap model and the magnetic frill model are considered here.

Voltage Gap Model

In this model we assume that the antenna is excited by a finite constant voltage V_i across its feed terminal gap giving rise to an impressed electric field which is entirely confined to the gap. Thus, the impressed field is expressed by

$$\mathbf{E}^i = \hat{z} V_i / \Delta \qquad |z| \leq \frac{\Delta}{2} \tag{3.12}$$

where Δ is the gap width.

Magnetic Frill Model

The delta gap model (3.12) does not account for the fringing fields present outside the gap region and, therefore, may not be accurate for near field and impedance calculations. Clearly, this situation becomes worse as the gap becomes wider. To

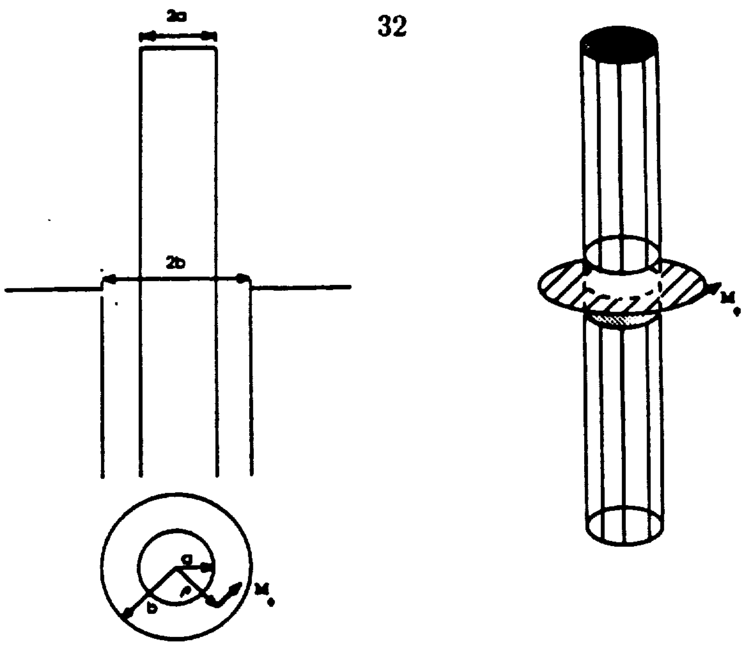

Figure 3.1: The magnetic frill model for antenna excitation.

include the effects of finite gap widths, the magnetic frill model was introduced [40]. This model is of practical importance specially in modeling of coaxial lines feeding monopoles on a ground plane (Figure 3.1). The feed terminal is replaced by an equivalent azimuthally directed magnetic current density that exists over an annular ring. The inner radius of the ring is chosen to be the same as the radius of the wire a, while the outer radius b is that of the coaxial cable feeding the monopole and whose characteristic impedance is

$$Z_c = Z_o \frac{\ln(b/a)}{2\pi} \tag{3.13}$$

Assuming that the coaxial structure supports a purely TEM mode, its aperture field may be approximated by

$$\mathbf{E}^i = \hat{\rho} \frac{V_i}{2\rho \ln(b/a)} \tag{3.14}$$

and upon closing the aperture with a perfect conductor and invoking the equivalence principle in conjunction with image theory, we find that this field excitation can be replaced by the equivalent magnetic current

$$\begin{aligned} \mathbf{M} &= 2\mathbf{E}^i \times \hat{n} \\ &= -\hat{\phi}\frac{1}{\rho \ln(b/a)} \end{aligned} \tag{3.15}$$

The electric field generated by this source on the axis of the antenna is readily found to be [40]

$$E_z^i(0,z) = \frac{1}{2\ln(b/a)}(\frac{e^{-jkR_1}}{R_1} - \frac{e^{-jkR_2}}{R_2}) \tag{3.16}$$

where

$$R_1 = \sqrt{z^2 + a^2} \qquad R_2 = \sqrt{z^2 + b^2}$$

3.2.2 Input Impedance

Once the current distribution on the cylindrical body is known, the input impedance can be computed from

$$Z_{in} = -\frac{1}{|I(0)|^2}\int_{-l}^{l} E_z^s(a,z')I^*(z')dz' \tag{3.17}$$

where E_z^s is the tangential surface field on the antenna given by

$$E_z^s(a,z) = -E_z^i \tag{3.18}$$

Thus, the input impedance is given by

$$Z_{in} = \frac{1}{|I(0)|^2}\int_{-l}^{l} E_z^i(a,z')I^*(z')dz' \tag{3.19}$$

and for a voltage gap model, the above equation reduces to the well known Ohm's law

$$Z_{in} = \frac{V_0}{|I(0)|} \tag{3.20}$$

Figures 3.2 – 3.4 show results based on the above formulation along with comparisons with data obtained by the method of moments (MoM). In particular, Figure 3.2 and 3.3 show the convergence of the solutions as a function of sampling density using a magnetic frill model for the excitation fields and it is seen that the CGFFT and MoM solutions exhibit the same convergence characteristics. Also Figure 3.4 depicts the convergence of the input impedance (3.19) as a function of sample density and it is again observed that the CGFFT and MoM [41] solutions converge to the same result.

The effect of incorporating various expansion functions is considered next. The current distribution on a 9λ dipole based on a voltage gap excitation model is given in Figure 3.5 as predicted via a CGFFT or an MoM solution. Although all expansion functions considered give similar results, the employment of the piecewise sinusoidal basis functions (PWS) drastically improves the convergence of the CGFFT as seen from Figure 3.6. Typically, an estimated 100% improvement in the convergence rate of the CGFFT method was observed when employing the PWS expansion functions.

Finally, Figure 3.7 shows the improvement in CPU time that can be attained on employing a CGFFT solution method versus a standard MoM solution. Clearly, the CPU time required for a CGFFT solution is a linear function of the system unknowns, whereas in the case of a MoM solution the dependence is quadratic. Also, shown in Figure 3.7 is the improved convergence attributed to the use of higher order basis functions.

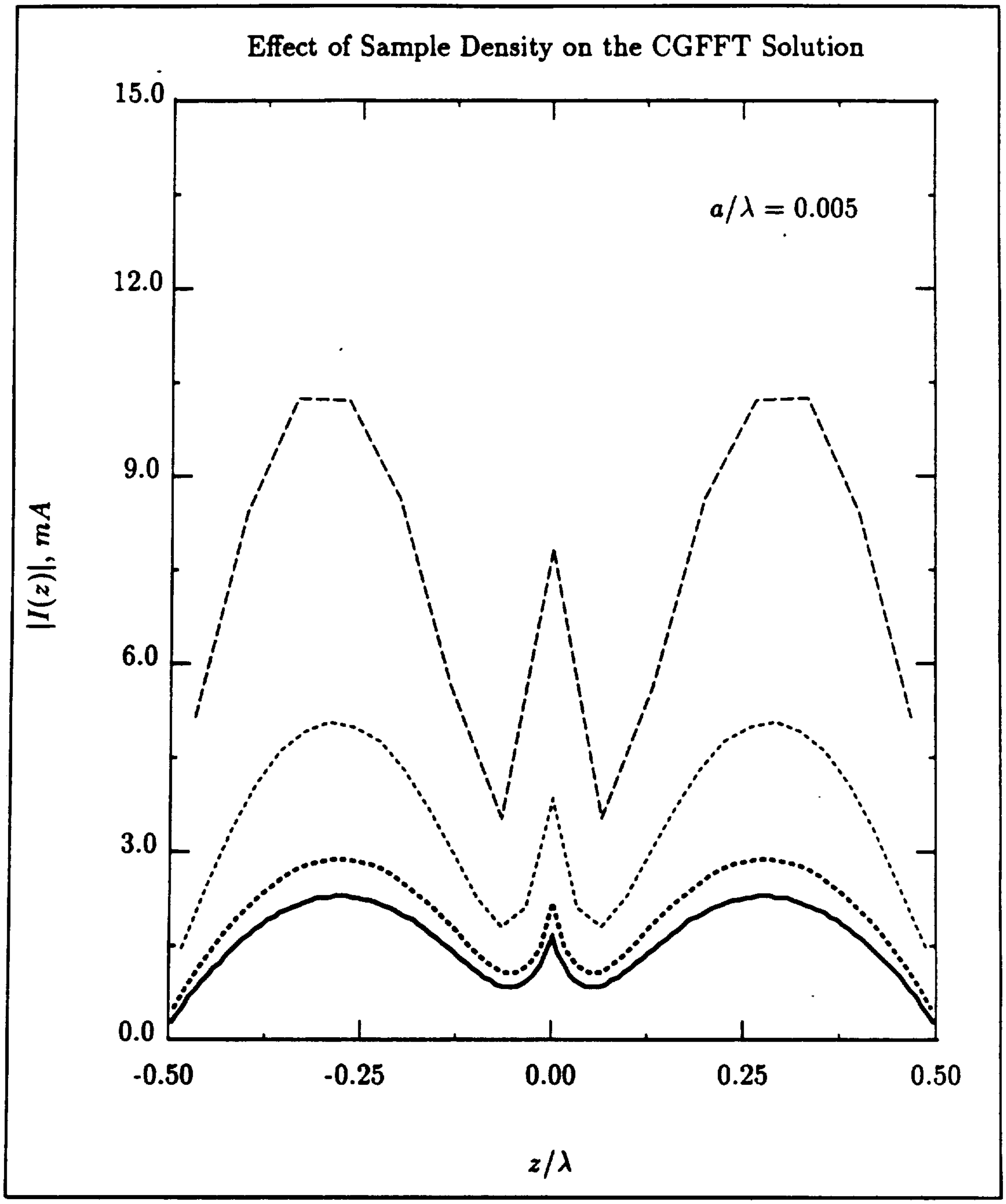

Figure 3.2: Numerical convergence of the linear current distribution for a 1λ dipole with increasing sampling density evaluated by the CGFFT. Top to bottom: No. of samples = 15, 31, 63, 127; FFT pad order ϱ= 2, 2, 2, 1; Magnetic frill excitation model.

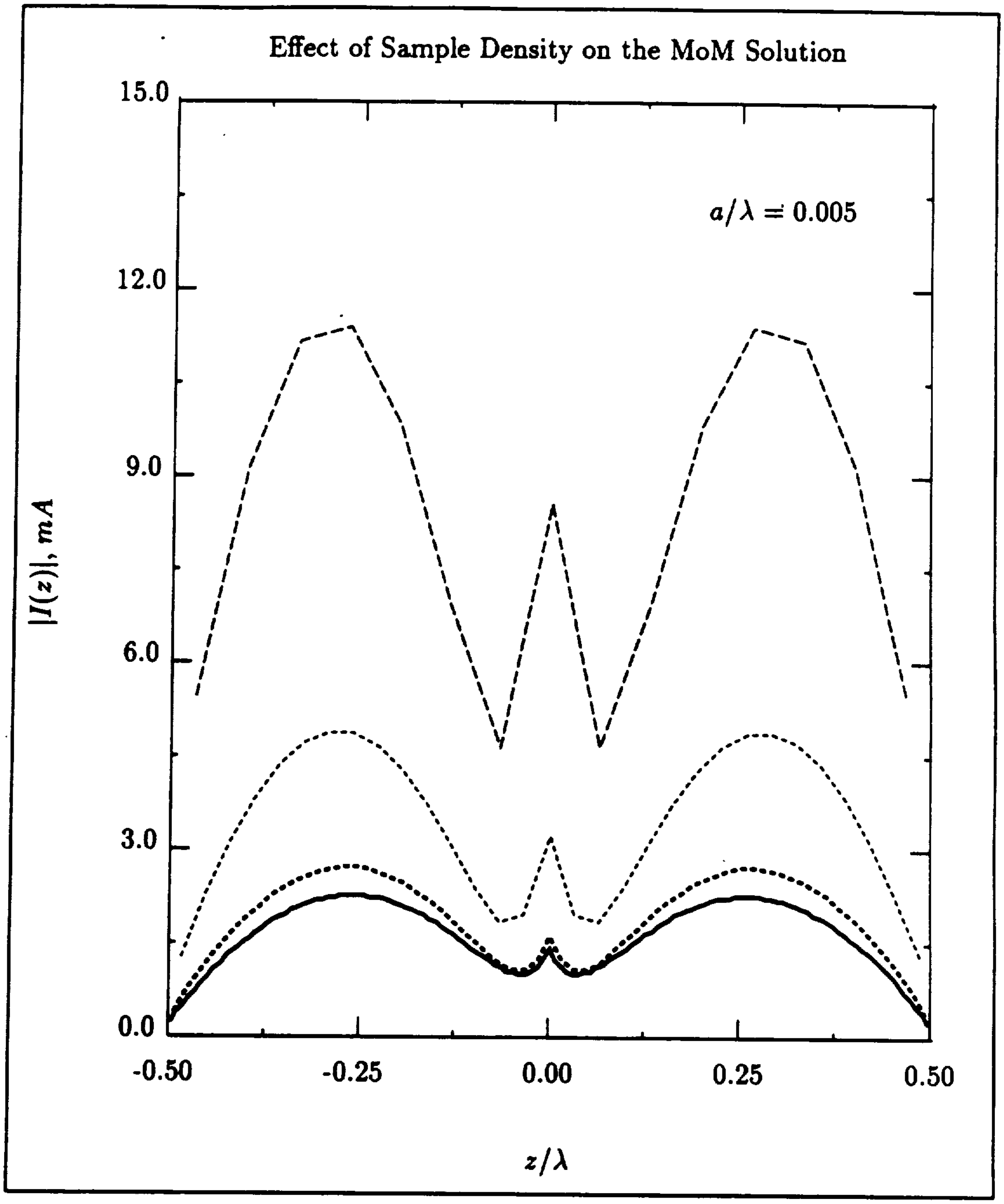

Figure 3.3: Numerical convergence of the linear current distribution for a 1λ dipole with increasing sampling density evaluated by the MoM. Top to bottom: No. of samples = 15, 31, 63, 127; Magnetic frill excitation model.

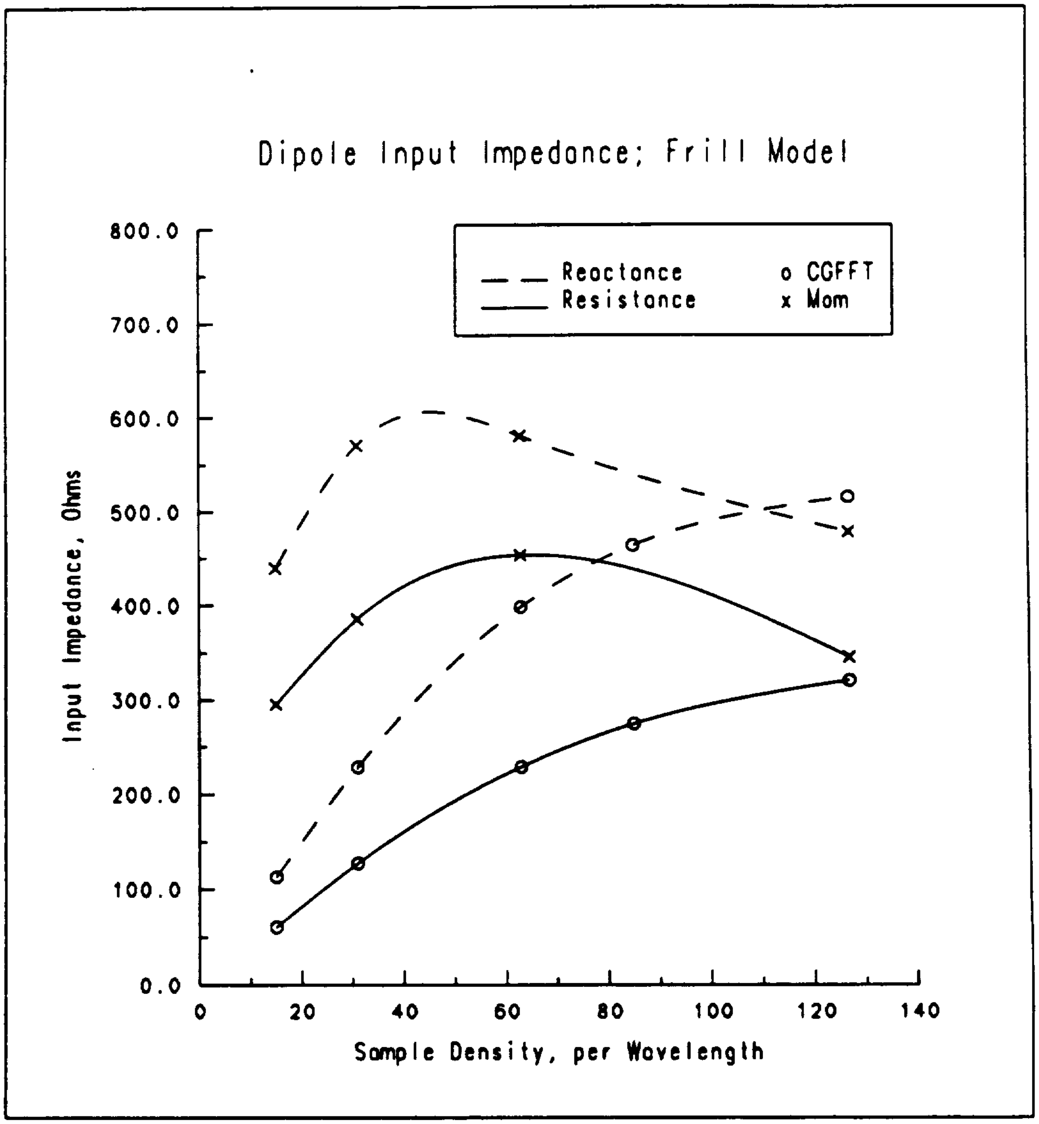

Figure 3.4: Real and imaginary parts of the input impedance for a 1λ dipole ($a/\lambda = 0.005$) as a function of sampling density.

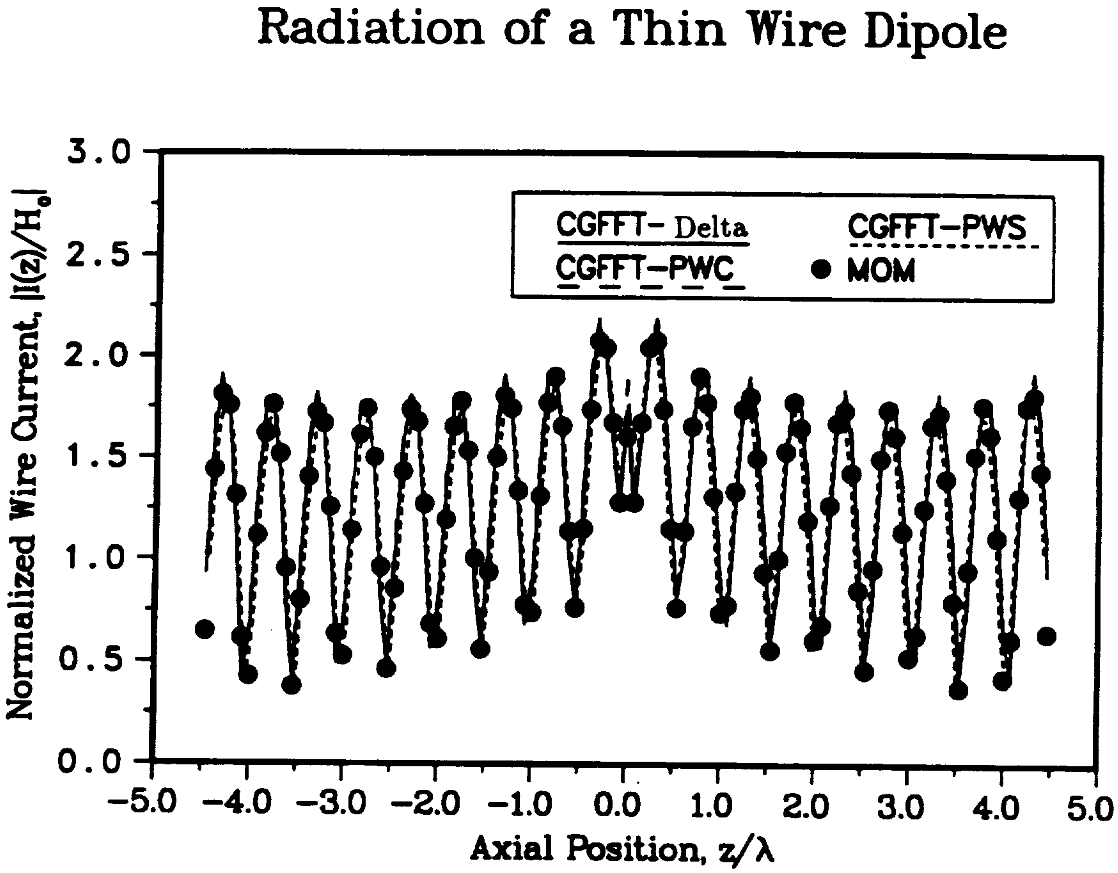

Figure 3.5: Current magnitude for a 9λ dipole ($a = 0.005\lambda$) computed by the MoM and the CGFFT using different basis functions and a voltage gap model for the source (13 unknown/λ).

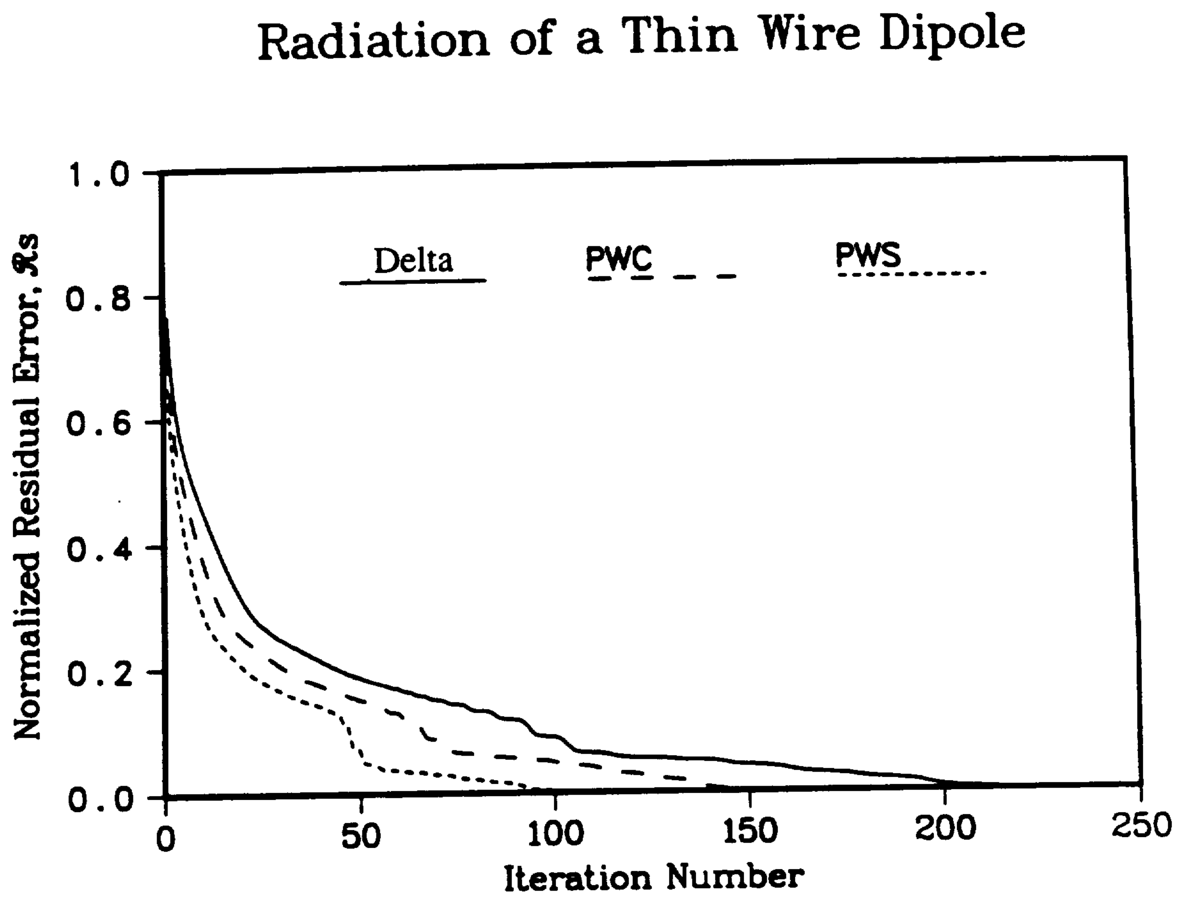

Figure 3.6: CGFFT convergence patterns for the 9λ dipole (13 unknowns/λ).

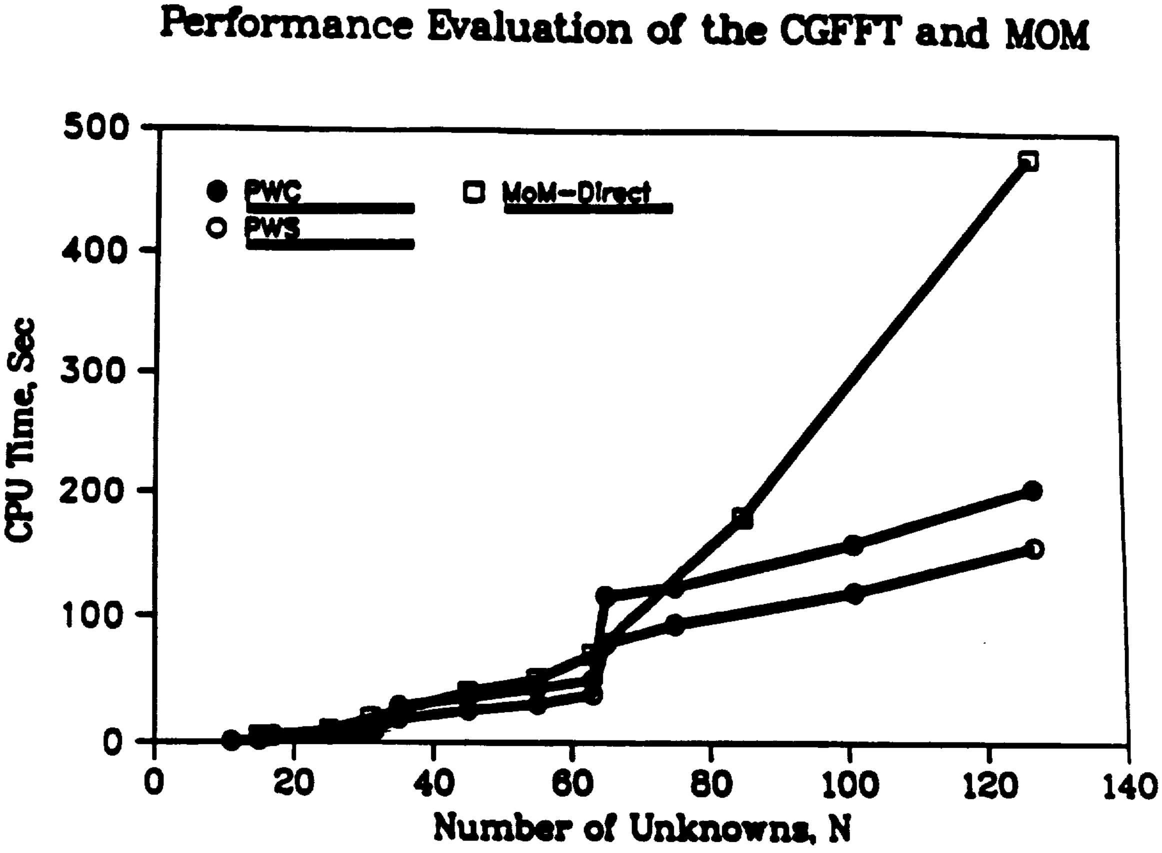

Figure 3.7: A comparison of the CPU times required by the MoM and the CGFFT for the solution of the resonant dipole problem (CGFFT tolerance: 0.003).

3.3 Scattering from Flat Resistive Strips

A thin conducting sheet or non-magnetic dielectric layer can be represented by a resistive sheet. In the case of a source-free dielectric layer having thickness τ, we have from (1.17)

$$\nabla \times \mathbf{H} = j\omega\epsilon_c \mathbf{E} \tag{3.21}$$

It is customary to characterize the layer by an equivalent electric current density as

$$\begin{aligned} \nabla \times \mathbf{H} &= j\omega(\epsilon_c - \epsilon_o)\mathbf{E} + j\omega\epsilon_o\mathbf{E} \\ &= \mathbf{J}_{eq} + j\omega\epsilon_o\mathbf{E} \end{aligned} \tag{3.22}$$

where the equivalent current

$$\mathbf{J}_{eq} \equiv j\omega\epsilon_o(\epsilon_r - 1)\mathbf{E} \tag{3.23}$$

is now assumed to radiate in free space. In the above, ϵ_r is the relative complex permittivity of the layer ϵ_c/ϵ_0. When the layer is electrically thin ($k\tau \ll 1$), the normal component of the electric field inside the layer is negligible. The dielectric layer can therefore be replaced by a *resistive* sheet of surface current density

$$\mathbf{K} = \lim_{\tau \to 0} \tau \, [\mathbf{J}_{eq}]_{\tan} \tag{3.24}$$

where

$$[\mathbf{J}_{eq}]_{\tan} = \mathbf{J}_{eq} - (\hat{n} \cdot \mathbf{J}_{eq})\, \hat{n} \tag{3.25}$$

is the transverse volumetric current flowing across the layer. ($\hat{n}$ is the upward unit normal to the layer). In view of (3.23) we may write

$$\mathbf{E} - (\hat{n} \cdot \mathbf{E})\, \hat{n} = Z_s \mathbf{K} \tag{3.26}$$

where Z_s is the resistivity (in Ω per unit squared) of the sheet

$$Z_s = \frac{Z_o}{jk_o\tau(\epsilon_r - 1)} \tag{3.27}$$

Therefore, a resistive sheet is an electric current sheet whose strength is proportional to the local tangential electric field. For a thin conducting sheet of conductivity σ, (3.27) reduces to

$$Z_s = \frac{1}{\sigma\tau} \tag{3.28}$$

Mathematically, the resistive sheet satisfies the boundary conditions [42]

$$\begin{aligned} -\frac{1}{2}\hat{n} \times \hat{n} \times (\mathbf{E}^+ + \mathbf{E}^-) &= Z_s\mathbf{K} \\ \hat{n} \times (\mathbf{E}^+ - \mathbf{E}^-) &= 0 \end{aligned} \tag{3.29}$$

where $\mathbf{E}^{\pm}$ denotes the total field above and below the sheet. Using (3.29), integral equations may be derived for computing the current induced on the strips for a given excitation and in the following we consider their derivation and solution for each of the principal polarizations separately.

3.3.1 Integral Equations

E-Polarization

Consider the E-Polarized wave

$$\mathbf{E}^i = \hat{z}e^{jk_o(x\cos\phi_o + y\sin\phi_o)} \tag{3.30}$$

$$\mathbf{H}^i = -(\hat{x}\sin\phi_o - \hat{y}\sin\phi_o)Y_oe^{jk_o(x\cos\phi_o + y\sin\phi_o)} \tag{3.31}$$

incident on the resistive strip of resistivity Z_s and width w coincident with the x-axis as shown in Figure 3.8. This excitation generates on the strip a z-directed current

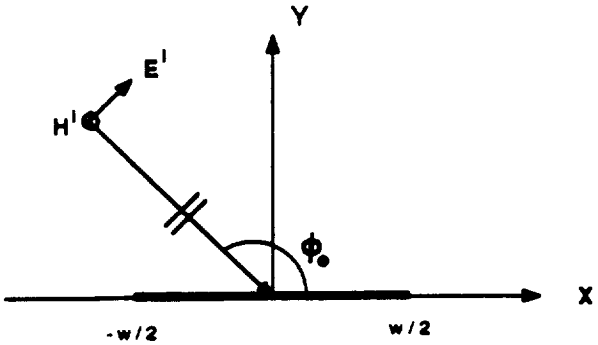

Figure 3.8: Geometry of a strip illuminated by a plane wave.

K_z, giving rise to the scattered field

$$E_z^s = -jk_oZ_o \int_{-w/2}^{w/2} K_z(x')G_s(k_o|x-x'|)dx' \tag{3.32}$$

where G_s is the two dimensional Green's function given by

$$G_s(x-x') = \frac{1}{4j} H_o^{(2)}(k_o|x-x'|) \tag{3.33}$$

and $H_o^{(2)}$ is the zeroth order Hankel function of the second kind. Imposing the condition (3.26) on the total tangential electric field over the strip, an integral equation for K_z is obtained as

$$Y_o e^{jk_ox\cos\phi_o} = \eta_s K_z(x) + \frac{k_o}{4}\int_{-w/2}^{w/2} K_z(x')H_o^{(2)}\left(k_o|x-x'|\right)\, dx' \tag{3.34}$$

where $\eta_s = Z_s/Z_o$ is the normalized surface impedance of the strip.

H-Polarization

Consider now the H-polarized plane wave

$$\mathbf{H}^i = \hat{z}\, e^{jk_o(x\cos\phi_o + y\sin\phi_o)} \tag{3.35}$$

$$\mathbf{E}^i = Z_o(\hat{x}\sin\phi_o - \hat{y}\cos\phi_o)\, e^{jk_o(x\cos\phi_o + y\sin\phi_o)} \tag{3.36}$$

incident on the resistive strip. This excitation generates an x-directed current density responsible for the scattered field given by

$$E_x^s = -jk_oZ_o\left(1+\frac{1}{k_o^2}\frac{\partial^2}{\partial x^2}\right)\int_{-w/2}^{w/2}K_x(x')G_s(k_o|x-x'|)dx' \tag{3.37}$$

Again, by imposing the resistive boundary condition, the integral equation satisfied by the current density K_x is obtained as

$$\sin\phi_o e^{jk_ox\cos\phi_o} = \eta_s K_x(x) + \frac{k_o}{4}\left(1+\frac{1}{k_o^2}\frac{\partial^2}{\partial x^2}\right)\int_{-w/2}^{w/2}K_x(x')H_o^{(2)}(k_o|x-x'|)dx' \tag{3.38}$$

The far zone scattered fields at the cylindrical point (ρ,ϕ) can be computed from the scattering integral using the large argument approximation of the Hankel function

$$H_o^{(2)}(k_o\rho) \sim \sqrt{\frac{2j}{\pi k_o\rho}}e^{-jk_o\rho}, \qquad k_o\rho\rightarrow\infty \tag{3.39}$$

Upon using the approximations

$$|\rho-\rho'| \simeq \rho - x'\cos\phi \approx \rho \tag{3.40}$$

for the phase and amplitude considerations, respectively, we have

$$E_z^s = -\frac{e^{-jk_o\rho}}{\sqrt{\rho}}e^{j\frac{\pi}{4}}\frac{k_oZ_o}{4}\sqrt{\frac{2}{\pi k_o}}\int_{-w/2}^{w/2}K_z(x')e^{jk_ox'\cos\phi}dx' \tag{3.41}$$

and

$$E_\phi^s = \frac{e^{-jk\rho}}{\sqrt{\rho}}e^{j\frac{\pi}{4}}\frac{k_oZ_o}{4}\sqrt{\frac{2}{\pi k_o}}\sin\phi\int_{-w/2}^{w/2}K_x(x')e^{jk_ox'\cos\phi}dx' \tag{3.42}$$

for E and H polarizations. The two-dimensional scattering echo width is defined as

$$\sigma = \lim_{\rho\rightarrow\infty}2\pi\rho\frac{|\mathbf{E}^s|^2}{|\mathbf{E}^i|^2} \tag{3.43}$$

and therefore

$$\sigma_e = \frac{k_o}{4}\left|Z_o \int_{-w/2}^{w/2} K_z(x')e^{jk_o x' \cos\phi}dx'\right|^2 \tag{3.44}$$

$$\sigma_h = \frac{k_o}{4}\left|\sin\phi \int_{-w/2}^{w/2} K_x(x')e^{jk_o x' \cos\phi}dx'\right|^2 \tag{3.45}$$

Typically, a solution of (3.34) and (3.38) can be accomplished numerically. However, approximate analytical solutions exist for the perfectly conducting case if the strip is electrically very narrow or very wide. These solutions are based on the quasi-static and physical optics approximations of the pertinent integral equations, respectively. They may be used to find closed form expressions for the echo width of the strip.

For a perfectly conducting strip $Z_s = 0$ and the integral equations for the surface current densities are given by

$$e^{jk_o x \cos\phi_o} = \frac{k_o Z_o}{4} \int_{-w/2}^{w/2} K_z(x')H_o^{(2)}(k_o|x - x'|)dx' \tag{3.46}$$

and

$$\sin\phi_o e^{jk_o x \cos\phi_o} = \frac{k_o}{4}\left(1 + \frac{1}{k_o^2}\frac{\partial^2}{\partial x^2}\right) \int_{-w/2}^{w/2} K_x(x')H_o^{(2)}(k_o|x - x'|)dx' \tag{3.47}$$

3.3.2 Very Narrow Strips

A general analysis of narrow strips and slots can be carried out analytically by employing certain quasi-static approximations to the integral equations developed in the previous section [43]. Since a similar analysis will be carried out in the study of narrow filled grooves in Chapter 6, we will present it here for completeness.

When $k_o w \ll 1$ in the integral equations (3.46) and (3.47), we may introduce the small argument expansion for the Hankel function [44],

$$H_o^{(2)}(z) \simeq 1 - j\frac{2}{\pi}\ln\left(\frac{\gamma z}{2}\right) + \mathcal{O}(z^2, z^2\ln z) \tag{3.48}$$

where $\ln\gamma = 1.78108\ldots$ is Euler's constant. Retaining only terms to $\mathcal{O}(k_o w)$ in the Hankel function as well as the incident fields, we have

$$\int_{-w/2}^{w/2} K_z(x')\ln|x - x'|dx' = \frac{2\pi j}{k_o Z_o} - \left[\ln\left(\frac{k_o\gamma}{2}\right) + j\frac{\pi}{2}\right]\int_{-w/2}^{w/2} K_z(x')dx' \tag{3.49}$$

for E-polarization and

$$\frac{\partial^2}{\partial x^2}\int_{-w/2}^{w/2} K_x(x')\ln|x - x'|dx' = 2\pi j k_o \sin\phi_o \tag{3.50}$$

for H-polarization. Further, by introducing the change of variables

$$\xi = \frac{2x}{w}\ , \quad \xi' = \frac{2x'}{w} \tag{3.51}$$

equations (3.49) and (3.50) respectively become

$$\int_{-1}^{1} K_z(\xi')\ln|\xi - \xi'|d\xi' = \frac{4j\pi}{k_o w Z_o} - \left[\ln\left(\frac{k_o w\gamma}{4}\right) + \frac{j\pi}{2}\right]\int_{-1}^{1} K_z(\xi')d\xi' \tag{3.52}$$

$$\frac{d^2}{d\xi^2}\int_{-1}^{1} K_x(\xi')\ln|\xi - \xi'|d\xi' = j\pi k_o w \sin\phi_o \tag{3.53}$$

To solve (3.52) and (3.53) we recall the following identities from the finite Hilbert transform theory [43, 45]:

$$\int_{-1}^{1} \frac{\ln|x - x'|}{\sqrt{1 - x'^2}}dx' = -\pi\ln 2 \qquad x \in [-1, 1] \tag{3.54}$$

and

$$\frac{d^2}{dx^2}\int_{-1}^{1} \sqrt{1 - x'^2}\ln|x - x'|dx' = \pi \qquad x \in [-1, 1] \tag{3.55}$$

and since the right hand sides of (3.52) of (3.53) are independent of ξ we deduce that

$$K_z(\xi) \;=\; \frac{\chi_e}{Z_o\sqrt{1 - \xi^2}} = \frac{\chi_e}{Z_o\sqrt{1 - \left(\dfrac{x}{w/2}\right)^2}} \tag{3.56}$$

and

$$K_x(\xi) \;=\; \chi_h\sqrt{1-\xi^2} = \chi_h\sqrt{1-\left(\frac{x}{w/2}\right)^2} \tag{3.57}$$

where χ_e and χ_h are constants to be determined. By substituting (3.56)-(3.57) into (3.52)-(3.53) we readily obtain

$$\chi_e = \frac{4j}{k_o w\left[\ln\left(\frac{k_o w\gamma}{8}\right)+j\frac{\pi}{2}\right]} \tag{3.58}$$

and

$$\chi_h = jk_o w\sin\phi_o \tag{3.59}$$

As expected (3.56) and (3.57) display the familiar edge behaviors at the terminations of the strip [46].

The scattering echo widths are computed from (3.44) and (3.45). However, in this case, we may use the approximation (3.40) for both amplitude and phase due to the small width of the strip. Thus,

$$\sigma_e \;=\; \frac{k_o}{4}\left|Z_o\int_{-w/2}^{w/2} K_z(x')dx'\right|^2 \tag{3.60}$$

$$\sigma_h \;=\; \frac{k_o}{4}\left|\sin\phi\int_{-w/2}^{w/2} K_x(x')dx'\right|^2 \tag{3.61}$$

and upon substituting for the currents, we obtain the simple expressions

$$\sigma_e = k_o\left|\frac{\pi w}{4}\chi_e\right|^2 = \frac{\pi\lambda}{2\left|\ln\left(\frac{k_o w\gamma}{8}\right)+j\frac{\pi}{2}\right|^2} \tag{3.62}$$

and

$$\sigma_h = k_o\left|\frac{\pi w}{8}\chi_h\sin\phi\right|^2 = \frac{\pi\lambda}{8}\left(\frac{k_o w}{2}\sin\phi\right)^4 \tag{3.63}$$

valid in the backscatter direction.

3.3.3 Very Wide Strips

For electrically wide strips, the local electric current may be assumed to be that corresponding to an infinitely wide strip. This is known as the physical optics approximation and is expressed as

$$\mathbf{K} = 2\hat{n} \times \mathbf{H} \tag{3.64}$$

or more explicitly,

$$K_z(x) \;=\; 2Y_o \sin\phi_o e^{jk_o x \cos\phi_o} \tag{3.65}$$

for E-polarization and

$$K_x(x) \;=\; 2e^{jk_o x \cos\phi_o} \tag{3.66}$$

for H-polarization.

The physical optics approximations may also be derived directly from the governing integral equating (3.46) and (3.47) when the strip is assumed to be infinite in extent. Hence, we have

$$e^{jk_o x \cos\phi_o} = jk_o Z_o \lim_{k_o w \to \infty} \int_{-w/2}^{w/2} K_z(x') G_s(x;x') dx' \tag{3.67}$$

for E-polarization and

$$\sin\phi_o e^{jk_o x \cos\phi_o} = \frac{j}{k_o} \lim_{k_o w \to \infty} \int_{-w/2}^{w/2} K_x(x') \left[\left(k_o^2 + \frac{\partial^2}{\partial x^2}\right)\right] G_s(x;x') dx' \tag{3.68}$$

for H-polarization. The integrals on the right hand sides of (3.67) and (3.68) are equivalent to

$$\int_{-\infty}^{\infty} K_z(x') G_s(x;x') dx' \tag{3.69}$$

$$\int_{-\infty}^{\infty} K_x(x') \left[\left(k_o^2 + \frac{\partial^2}{\partial x^2}\right)\right] G_s(x;x') dx' \tag{3.70}$$

and are identified as convolutions in the infinite domain. Thus, upon invoking the convolution theorem and using the transform pair

$$e^{jk_o x\cos\phi_o} \overset{\mathcal{F}}{\Longleftrightarrow} 2\pi\delta(k_x - k_0\cos\phi_o) \tag{3.71}$$

we have, by taking the Fourier transforms of both sides of (3.67) and (3.68)

$$2\pi\delta(k_x - k_0\cos\phi_o) = jk_oZ_o\widetilde{K}_z(k_x)\tilde{G}_s(k_x) \tag{3.72}$$

$$2\pi\sin\phi_o\delta(k_x - k_0\cos\phi_o) = \frac{j}{k_o}\widetilde{K}_x(k_x)(k_o^2 - k_x^2)\tilde{G}_s(k_x) \tag{3.73}$$

Formally, the above equations can be solved algebraically for the transforms of the currents $\widetilde{K}_z$ and $\widetilde{K}_x$ to yield

$$\widetilde{K}_z(k_x) = \frac{2\pi\delta(k_x - k_0\cos\phi_o)}{jk_oZ_o\tilde{G}_s(k_x)} \tag{3.74}$$

and

$$\widetilde{K}_x(k_x) = \frac{2\pi k_o\sin\phi_o\delta(k_x - k_0\cos\phi_o)}{j(k_o^2 - k_x^2)\tilde{G}_s(k_x)} \tag{3.75}$$

Taking the inverse transforms of both sides now gives

$$\begin{aligned} K_z(x) &= \frac{1}{jk_oZ_o}\int_{-\infty}^{\infty}\frac{\delta(k_x - k_0\cos\phi_o)}{\tilde{G}_s(k_x)}e^{jk_x x}dk_x \\ &= \frac{e^{jk_o x\cos\phi_o}}{jk_oZ_o\tilde{G}_s(k_o\cos\phi_o)} \end{aligned} \tag{3.76}$$

$$\begin{aligned} K_x(x) &= \frac{k_o\sin\phi_o}{j}\int_{-\infty}^{\infty}\frac{\delta(k_x - k_0\cos\phi_o)}{(k_o^2 - k_x^2)\tilde{G}_s(k_x)}e^{jk_x x}dk_x \\ &= \frac{k_o\sin\phi_o e^{jk_o x\cos\phi_o}}{j(k_o^2 - k_x^2)\tilde{G}_s(k_o\cos\phi_o)} \end{aligned} \tag{3.77}$$

where use was made of the properties of the δ function. The Fourier transform of the Green's function $\tilde{G}_s$ is given by (Appendix B)

$$\tilde{G}_s(k_x) = \frac{1}{2j\sqrt{k_o^2 - k_x^2}} \tag{3.78}$$

and when this is substituted in (3.76) and (3.77), we recover (3.65) and (3.66).

To find the physical optics echo widths, we substitute (3.76) and (3.77) into (3.44) and (3.45). In the backscatter direction $\phi_o = \phi$, we readily find

$$\sigma = k_o w^2 \sin\phi \operatorname{sinc}^2(k_o w \cos\phi) \tag{3.79}$$

for both polarizations.

3.3.4 CGFFT Solution

We will now consider the solution of (3.34) and (3.38) for arbitrary size strip via the CGFFT method. To do this, we must rewrite these equations in a form compatible with (2.46). The Fourier transform of G_s is given by (3.78)

$$\tilde{G}_s(k_x) = \frac{1}{2j\sqrt{k_o^2 - k_x^2}}$$

and therefore (3.34) and (3.38) may be rewritten as

$$Y_o e^{jk_o x\cos\phi_o} = \eta_s K_z(x) + jk_o \mathcal{F}^{-1}\left\{\tilde{G}_s(k_x)\widehat{K}_z(k_x)\tilde{f}(k_x)\right\} \tag{3.80}$$

and

$$\sin\phi_o e^{jk_o x\sin\phi_o} = \eta_s K_x(x) + \frac{j}{k_o}\mathcal{F}^{-1}\left\{(k_o^2 - k_x^2)\tilde{G}_s(k_x)\widehat{K}_x\tilde{f}(k_x)\right\} \tag{3.81}$$

respectively. These may now be solved via the CGFFT algorithm.

Echo width patterns based on a CG solution of (3.80) and (3.81) are compared with MoM data in Figures 3.9 and 3.10, respectively. The strip is 4λ wide and has a non-uniform resistivity as shown. In practice, tapered resistive cards are often employed for radar cross section reduction and Figure 3.11 demonstrates an example of such a reduction in connection with a strip having a resistivity that is tapered parabolically as given in Figures 3.9 and 3.10. The choice of basis functions is again

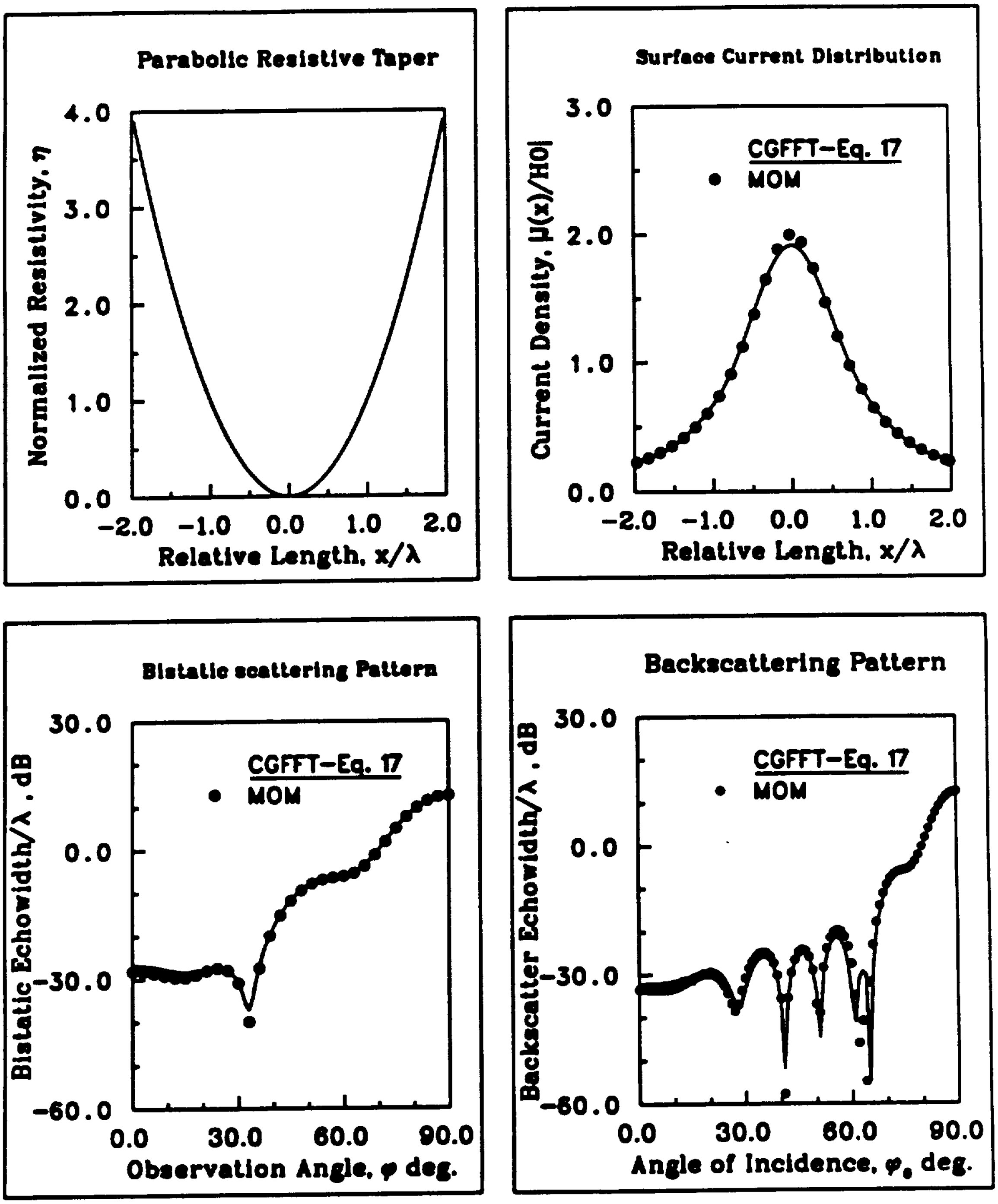

Figure 3.9: E-polarization scattering results for a 4λ parabolically tapered strip.

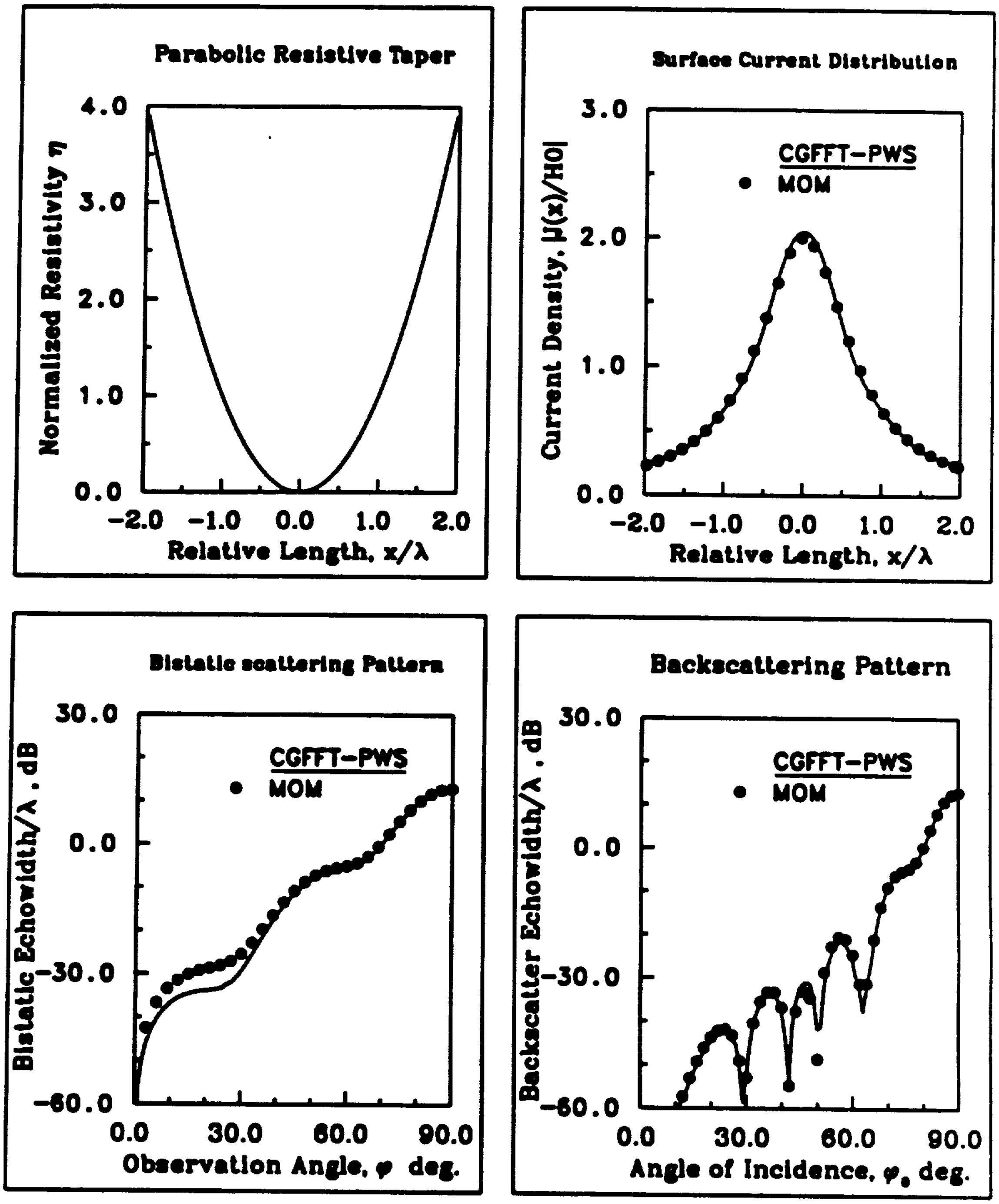

Figure 3.10: H-polarization scattering results for a 4λ parabolically tapered strip.

a factor in the convergence of the CG solution and similarly with the wire example, the sinusoidal basis functions were found to provide a substantial improvement in the convergence rate (almost 100 percent). This is shown in Figure 3.12 for the H-polarization.

It should be noted that the expected behavior of the current density plays a major role in the choice of the FFT pad used in the calculations. This is related to the spectral content of the current as well as the singularity of the pertinent Green's function. The field distributions over open conducting bodies and their singular behavior have been studied by several authors in order to establish such behavior in explicit numerical terms (see for example [47]).

Consider the H-polarization case (TE_Z) first. In this case, the current density is not singular and–like the current density on the wire dipole studied in the previous section–it vanishes at the edges, rendering its transform essentially band-limited. Therefore, an FFT length of order 1 ($\varrho = 1$) should be adequate to satisfy the spectral spreading due to convolution without noticeable aliasing error.

On the other hand, for the E-polarization incidence (TM_Z) the current density is singular at the edges and aliasing is expected to occur in the transform domain. This may cause substantial error unless high sampling rates are employed in the spatial and spectral domains to avoid aliasing. For example, the CGFFT solution for the perfectly conducting strip presented in Figure 3.9 for the E-polarization case required an FFT pad of order $\varrho = 3$. This is, of course, undesirable because it will increase the memory demand and execution time per iteration.

As mentioned in the previous section, employing the analytical transform of the Green's function is valid if the integral equation is defined on the entire real axis (infinite domain). This was the case for the wide strip in the limit as the width

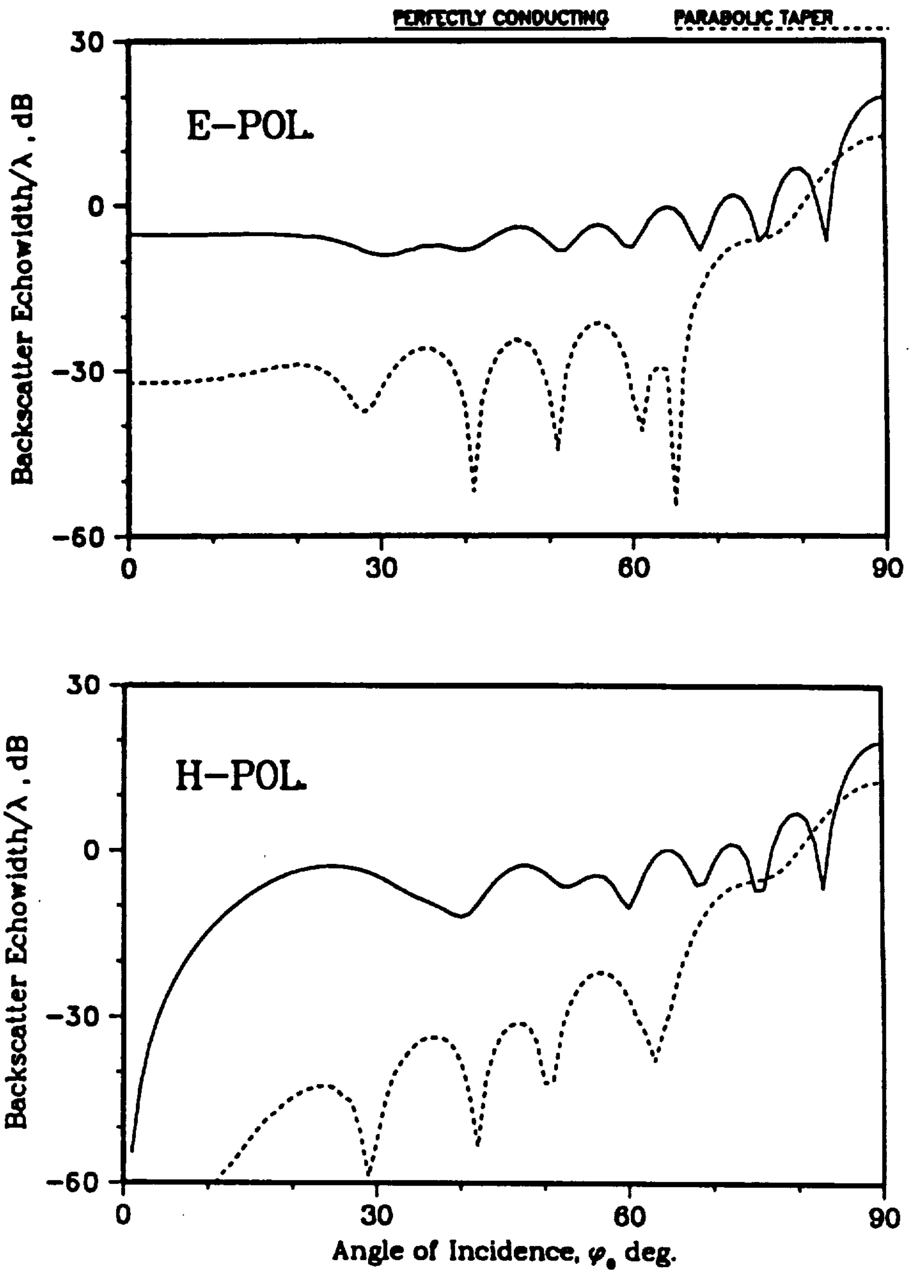

Figure 3.11: Comparison of the backscatter echo widths of a 4λ perfectly conducting and parabolically tapered strips.

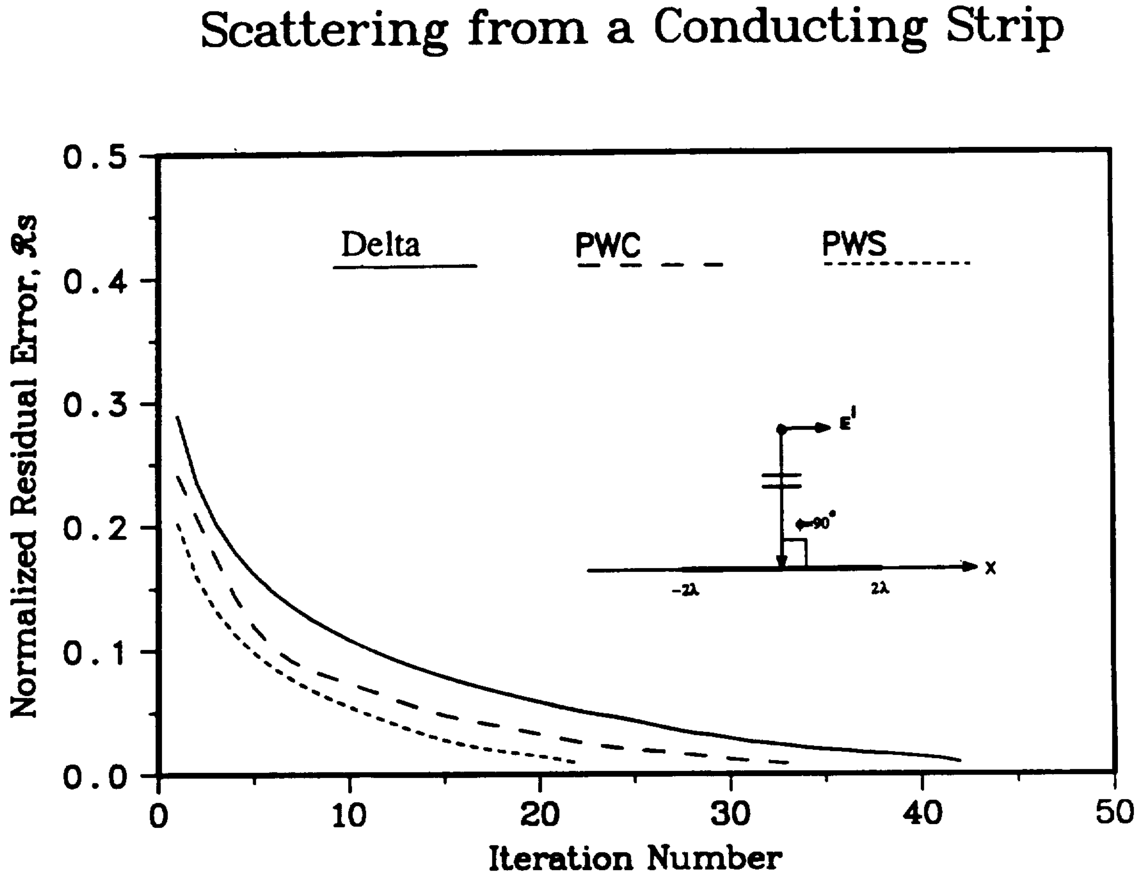

Figure 3.12: Convergence patterns for the 4λ strip illuminated by an H-polarized plane wave using 20 unknowns/λ.

was taken to infinity. For finite strips, however, this approach gives an approximate solution which improves by extending the size of the FFT pad to include higher spectral components. For a given strip, the degree of improvement achieved depends on the sampling density and the polarization of incident field.

To overcome this difficulty, an alternative is to discretize the integral in (3.34) before proceeding with its computation via the discrete Fourier transform. That is, assuming a pulse basis expansion for the current density,

$$K_z(x) = \sum_{n=0}^{N-1} K_z(x_n) P(x - x_n), \qquad x_n = n\Delta + \frac{\Delta}{2} \tag{3.82}$$

we substitute (3.82) into the integral equation (3.34) and enforce it at discrete points(point-matching) $x_m = m\Delta + \frac{\Delta}{2}$, $m = 0, \ldots, N-1$. This yields a linear system of equations for the solution of the current density. In particular, we have

$$\int_{-w/2}^{w/2} K_z(x') H_o^{(2)}(k_o|x_m - x'|)\, dx' = \int_{-w/2}^{w/2} \left[\sum_{n=0}^{N-1} K_z(x_n)\right] H_o^{(2)}(k_o|x_m - x'|)\, dx' \tag{3.83}$$

and by interchanging the order of summation and integration,

$$\sum_{n=0}^{N-1} K_z(x_n) \int_{x_n - \frac{\Delta x}{2}}^{x_n + \frac{\Delta x}{2}} H_o^{(2)}(k_o|x_m - x'|)\, dx' = \sum_{n=0}^{N-1} K_z(x_n) \Upsilon(x_m - x_n) \tag{3.84}$$

In the above, $\Upsilon(x_m - x_n) = \Upsilon_{mn}$ are the mutual admittance elements given by

$$\Upsilon_{mn} \simeq \begin{cases} \frac{k_o}{4}\Delta\left[1 - \frac{j2}{\pi}\left(\ln(\frac{k_o\gamma\Delta}{4}) - 1\right)\right], & n = m \\ \\ \frac{k_o}{4}\Delta H_o^{(2)}(k_o|x_m - x_n|), & n \neq m \end{cases} \tag{3.85}$$

in which $\ln\gamma$ is the Euler's constant. Since Υ is not singular anywhere, the evaluation of the convolution integral may now be carried out without aliasing errors via the discrete Fourier transform as

$$\int_{-w/2}^{w/2} K_z(x') H_0^{(2)}(k_o|x_m - x'|) dx' = \text{DFT}^{-1}\left\{\widehat{K}_z \widehat{\Upsilon}\right\} \tag{3.86}$$

where DFT $^{-1}$ denotes the inverse discrete Fourier transform and $\hat{\Upsilon}$ is the discrete transform of the sample train $\Upsilon_{on}, n = -(N-1), \cdots, N-1$.

Expression (3.86) renders the evaluation of the convolution relatively insensitive to the length of the FFT provided the convolution requirement is satisfied. As illustrated in Figure 3.13 for the case of normal incidence on a perfectly conducting strip one wavelength wide, the predicted current distribution agrees with the MoM result when (3.86) is employed in the CGFFT algorithm with an FFT size just twice the length of the strip (FFT pad of order $\varrho = 1$). In contrast, when employing the sampled continuous analytical transform for the evaluation of the convolution integral, the resulting current distribution remains in disagreement with the MoM solution unless at least an FFT pad of order $\varrho = 3$ (four times the size of the strip) is used. The corresponding comparison of the bistatic scattering patterns is shown in Figure 3.14 and the same observations again apply.

Hereon, the solution of (3.86) via the conjugate gradient method will be referred to as the CGDFT method and the corresponding method of solution based on (3.80) or (3.81) will be referred to as the CGFT method.

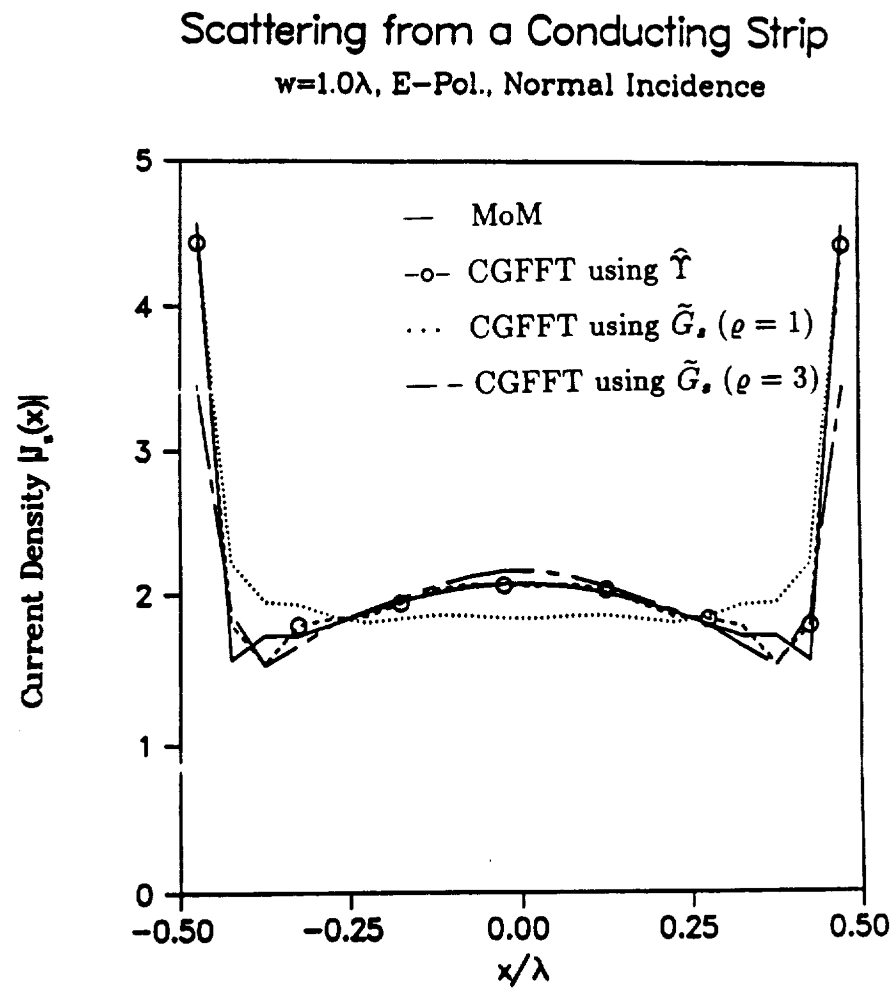

Figure 3.13: Comparison of the current distribution on a 1λ wide perfectly conducting strip illuminated by a plane wave (E-pol, $\phi_o = 0$) as computed by various methods.

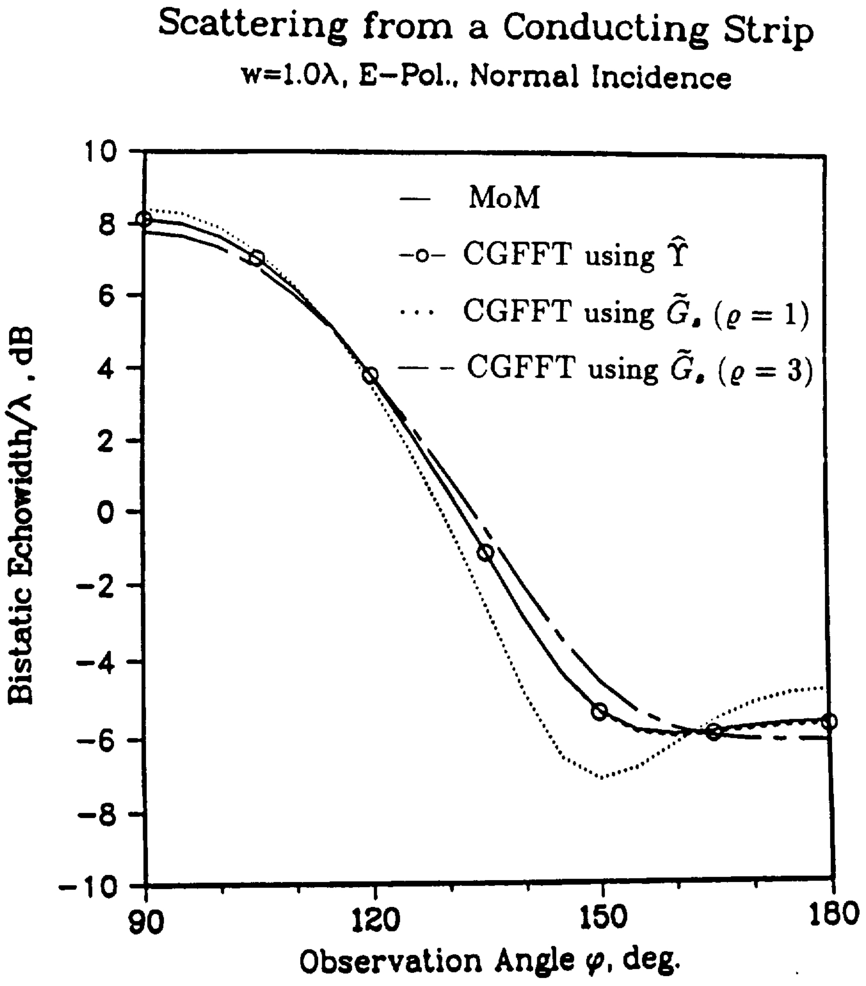

Figure 3.14: Comparison of the bistatic echo width of a 1λ wide perfectly conducting strip illuminated by a plane wave (E-pol, $\phi_o = 0$) as computed by various methods.

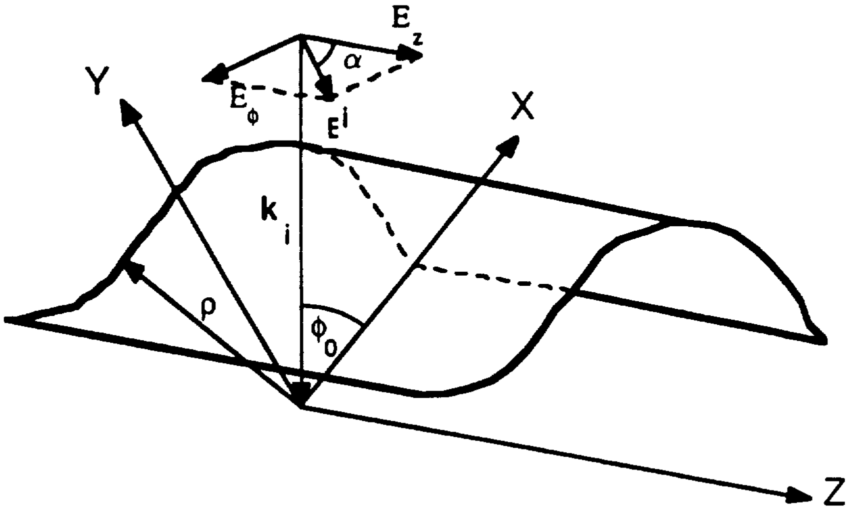

Figure 3.15: Geometry of an infinitely long curved strip illuminated by a plane wave.

3.4 Scattering from Cylindrical Strips

Consider a thin cylindrical shell of resistivity η illuminated by a plane wave $\mathbf{E}^i$ of wave number k_o and polarization angle ψ (Figure 3.15). The incident field is given by

$$\mathbf{E}^i(\boldsymbol{\rho}) = (\hat{\phi}\sin\psi + \hat{z}\cos\psi)Z_o e^{-jk_o(\hat{k}_i \cdot \boldsymbol{\rho})} \tag{3.87}$$

where $\psi = 0$ corresponds to E-polarization ($\mathrm{TM_Z}$) while $\psi = -\pi/2$ corresponds to H-polarization ($\mathrm{TE_Z}$).

The scattered electric field due to the excited surface current $\mathbf{K}$ on the shell is expressed by the line integral

$$\mathbf{E}^s(\boldsymbol{\rho}) = -jk_o Z_o \int_c \mathbf{K}(\boldsymbol{\rho}') \cdot \bar{\Gamma}(\boldsymbol{\rho};\boldsymbol{\rho}')dl' \tag{3.88}$$

where $\bar{\Gamma}$ denotes the electric dyadic Green's function in unbounded space given by

$$\bar{\Gamma}(\boldsymbol{\rho};\boldsymbol{\rho}') = \left(\bar{\mathbf{I}} + \frac{1}{k_o^2}\nabla\nabla\right) G_s(\boldsymbol{\rho};\boldsymbol{\rho}') \tag{3.89}$$

In the above, G_s is the two-dimensional free space Green's function given by

$$G_s(\rho;\rho') = \frac{1}{4j}H_o^{(2)}(k_o|\rho-\rho'|) \tag{3.90}$$

The explicit form of $\bar{\Gamma}$ in cylindrical coordinates is

$$\bar{\Gamma} = \begin{pmatrix} (1+\frac{1}{k_o^2}\frac{\partial^2}{\partial\rho^2}) & \frac{1}{k_o^2}\frac{1}{\rho}\frac{\partial^2}{\partial\rho\partial\phi} & 0 \\ \frac{1}{k_o^2}\frac{1}{\rho}\frac{\partial^2}{\partial\phi\partial\rho} & (1+\frac{1}{(k_o\rho)^2}\frac{\partial^2}{\partial\phi^2}) & 0 \\ 0 & 0 & 1 \end{pmatrix} G_s(\rho;\rho') \tag{3.91}$$

The total tangential electric field on the strip satisfies the resistive boundary condition (3.26)

$$\mathbf{E}^T - (\hat{n}\cdot\mathbf{E}^T)\,\hat{n} = \left[\mathbf{E}^i + \mathbf{E}^s\right]_{\tan} = Z_s\mathbf{K}$$

which upon substitution of (3.88) yields the desired integral equation

$$-\hat{n}\times\hat{n}\times\mathbf{E}^i(\rho) = Z_s(\rho)\mathbf{K}(\rho) + jk_oZ_o\int_c \mathbf{K}(\rho')\cdot\bar{\Gamma}(\rho;\rho')dl' \tag{3.92}$$

to be solved for the unknown current distribution. In view of (3.90) this represents a convolutional integral equation in $\mathbf{K}$.

Let us now consider a solution of (3.92) for the special case of a circular strip of radius a. Referring to Figure 3.16 and defining the phase reference at the origin, we may write

$$\begin{aligned} dl &= a d\phi \\ |\rho-\rho'| &= a\left[(\cos\phi-\cos\phi')^2 + (\sin\phi-\sin\phi')^2\right]^{\frac{1}{2}} \\ &= 2a\sin(|\frac{\phi-\phi'}{2}|), \end{aligned} \tag{3.93}$$

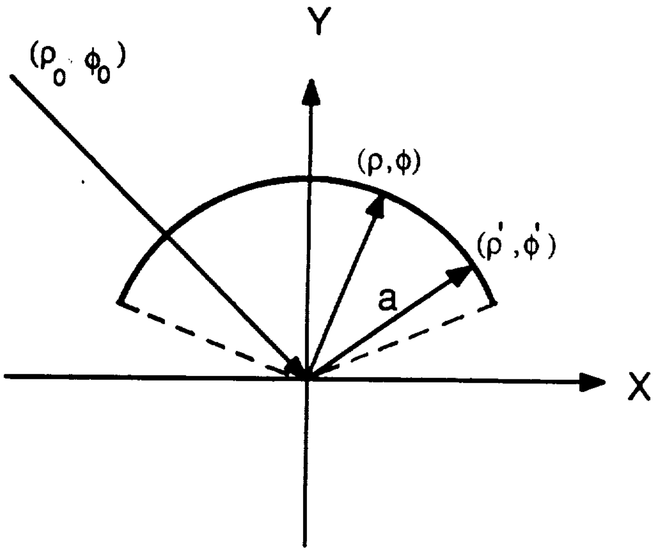

Figure 3.16: Geometry of a circularly curved strip.

and

$$\hat{k}_i \cdot \rho = \rho_0 - a\cos(\phi - \phi_0) \tag{3.94}$$

Also, since there is no variation in ρ and the strip is infinitesimally thin, (3.91) reduces to

$$\bar{\Gamma}(\phi;\phi') = \frac{1}{4j}\left\{\left[1+\frac{1}{(k_o a)^2}\frac{\partial^2}{\partial\phi^2}\right]\hat{\phi}\hat{\phi}+\hat{z}\hat{z}\right\} H_o^{(2)}\left[2k_o a\sin(\frac{|\phi-\phi'|}{2})\right] \tag{3.95}$$

The integral in (3.92) can thus be expressed as a convolution in ϕ yielding

$$(\hat{\phi}\sin\psi+\hat{z}\cos\psi)e^{-jk_o\cos(\phi-\phi_o)} = \eta_s(\phi)\mathbf{K}(\phi)+jk_o\int_c \mathbf{K}(\phi')\cdot\bar{\Gamma}(\phi;\phi')ad\phi' \tag{3.96}$$

where η_s is the normalized surface resistance of the strip and use has been made of (3.94). For $\mathrm{TE_Z}$ incidence this becomes

$$E_\phi^i(\phi) = \eta_s(\phi)K_\phi(\phi)+\frac{k_o a}{4}\left[1+\frac{1}{(k_o a)^2}\frac{\partial^2}{\partial\phi^2}\right]\int_c K_\phi(\phi')H_o^{(2)}\left[2k_o a\sin(\frac{|\phi-\phi'|}{2})\right]d\phi' \tag{3.97}$$

while for $\mathrm{TM_Z}$ incidence we have

$$E_z^i(\phi) = \eta_s(\phi)K_z(\phi)+\frac{k_o a}{4}\int_c K_z(\phi')H_0^{(2)}\left[2k_o a\sin(\frac{|\phi-\phi'|}{2})\right]d\phi', \tag{3.98}$$

Clearly, both (3.97) and (3.98) are amenable to a CGFFT solution.

It is noted that if the radius of the strip is large compared to its width, we may modify the approximations (3.93) and (3.94) as

$$\begin{aligned}
\lim_{a\to\infty} |\rho - \rho'| &= a|\phi - \phi'| \simeq |x - x'| \\
\lim_{a\to\infty} a\cos(\phi - \phi_0) &\simeq a\sin\phi_0 + a(\pi/2 - \phi)\cos\phi_0 \\
&= a\sin\phi_0 + x\cos\phi_0 \qquad (3.99)
\end{aligned}$$

and the formulation reduces to that of scattering from a flat strip (see (3.38) and (3.34))

$$\begin{aligned}
(-\hat{x}\sin\psi\sin\phi + \hat{z}\cos\psi)e^{jk_o(a\sin\phi_0 + x\cos\phi_0)} &= \\
\eta_s(x)\mathbf{K}(x) + jk_o\int_{-w/2}^{w/2} \mathbf{K}(x')\cdot\bar{\mathbf{\Gamma}}(x;x')dx' & \qquad (3.100)
\end{aligned}$$

where $\mathbf{K}(x) = \hat{x}K_x(x) + \hat{z}K_z(x)$ and $\bar{\mathbf{\Gamma}}$ is now given by

$$\bar{\mathbf{\Gamma}}(x;x') = \frac{1}{4j}\left[(1 + \frac{1}{k_o^2}\frac{\partial^2}{\partial x^2})\hat{x}\hat{x} + \hat{z}\hat{z}\right] H_0^{(2)}(k_o|x - x'|) \qquad (3.101)$$

To solve (3.96) the current density is expanded in terms of a subsectional surface basis function $\bar{\mathbf{\Psi}}$ as

$$\mathbf{K}(\phi) = \sum_{n=0}^{N-1} \mathbf{K}_n \cdot \bar{\mathbf{\Psi}}_{\mathbf{n}}(\phi) \qquad (3.102)$$

where

$$\bar{\mathbf{\Psi}}_{\mathbf{n}}(\phi) = \bar{\mathbf{\Psi}}(\phi - \phi_n) \qquad (3.103)$$

and upon using the piecewise constant basis function,

$$\bar{\mathbf{\Psi}}(\phi) = (\hat{\phi}\hat{\phi} + \hat{z}\hat{z})P(\phi) \qquad (3.104)$$

with

$$P(\phi) = \begin{cases} 1 & -\Delta\phi/2 < \phi < \Delta\phi/2 \\ 0 & else \end{cases} \qquad (3.105)$$

Substituting for the current expansion in the integral on the right hand side of (3.96) and interchanging the order of summation and integration, gives

$$a \sum_{n} \mathbf{K}_n \cdot \int_{c'} \bar{\bar{\Psi}}_n(\phi') \cdot \bar{\bar{\Gamma}}(\phi;\phi') d\phi' \tag{3.106}$$

Introducing (3.106) into (3.96) and applying Galerkin's method (Appendix A) yields the system of equations

$$\mathbf{V}_m = \Delta\phi \eta_{sm} \mathbf{K}_m + \frac{k_o a}{4} \sum_{n} \bar{\bar{\Xi}}_{mn} \cdot \mathbf{K}_n \tag{3.107}$$

where

$$\mathbf{V}_m = (\hat{\phi} \sin\psi + \hat{z}\cos\psi) \int_{\phi_m-\Delta\phi/2}^{\phi_m+\Delta\phi/2} e^{jk_o \cos(\phi-\phi_o)} d\phi \tag{3.108}$$

The dyadic function

$$\bar{\bar{\Xi}} = \xi^{\phi\phi}\hat{\phi}\hat{\phi} + \xi^{zz}\hat{z}\hat{z} \tag{3.109}$$

is a discrete kernel whose elements are given by

$$\xi^{\phi\phi}_{mn} = \int_{\phi_m-\Delta/2}^{\phi_m+\Delta/2} \int_{\phi_n-\Delta/2}^{\phi_n+\Delta/2} \left[1 + \frac{1}{(k_o a)^2}\frac{\partial^2}{\partial\phi^2}\right] H_o^{(2)}\left[2k_o a \sin(\frac{|\phi-\phi'|}{2})\right] d\phi' d\phi \tag{3.110}$$

$$\xi^{zz}_{mn} = \int_{\phi_m-\Delta/2}^{\phi_m+\Delta/2} \int_{\phi_n-\Delta/2}^{\phi_n+\Delta/2} H_o^{(2)}\left[2k_o a \sin(\frac{|\phi-\phi'|}{2})\right] d\phi' d\phi \tag{3.111}$$

It is noted that both $\xi^{\phi\phi}$ and ξ^{zz} have integrable singularities corresponding to the self-cell interaction which can be approximated analytically. In particular,

$$\xi^{zz}_{nn} \simeq \frac{2}{(k_o a)^2}) \left[\sqrt{\pi} k_o a \Delta\phi H_1^{(2)}\left(\frac{k_o a \Delta\phi}{\sqrt{\pi}}\right) - 2j\right] \tag{3.112}$$

and a similar expression may be obtained for $\xi^{\phi\phi}_{nn}$. The remaining terms ($n \neq m$) may be evaluated numerically.

Applying the discrete convolution theorem in (3.107) now gives

$$\mathbf{V}_m = \Delta\phi \eta_{sm} \mathbf{K}_m + \frac{k_o a}{4} \,\mathrm{DFT}^{-1}\{\hat{\bar{\bar{\Xi}}} \cdot \hat{\mathbf{K}}\} \tag{3.113}$$

which is in a form suitable for solution via the conjugate gradient method.

Once the surface current density is evaluated, the scattered field can be computed using (3.88) as

$$\mathbf{E}^s(\phi) = -jZ_o k_o a \int_c \mathbf{K}(\phi') \cdot \bar{\mathbf{\Gamma}}(|\phi - \phi'|)d\phi'$$

Specializing this to the far-field, we find the scattering echo widths for the two principal polarizations to be

$$\sigma_e(\phi) = \frac{k_o}{4}\left| a \int_c K_z(\phi')e^{jk_oa\cos(\phi-\phi_0)}d\phi' \right|^2 \tag{3.114}$$

for TM$_Z$ polarization and

$$\sigma_h(\phi) = \frac{k_o}{4}\left| a \sin\phi_0 \int_c K_\phi(\phi')e^{jk_oa\cos(\phi-\phi_0)}d\phi' \right|^2 \tag{3.115}$$

for TE$_Z$ polarization.

Sample calculations are now presented for circularly curved strips using the above formulation. Figure 3.18 shows the bistatic scattering patterns for a 2λ flat strip as it is uniformly bent to form a closed circular cylinder keeping its width (perimeter) constant. The strip is positioned symmetrically around the y axis and illuminated by a TM$_Z$ plane wave incident at 90 degrees. It is noted that as the curvature κ increases from zero (flat strip), the main (specular) lobe drops and eventually disappears in the limit when the complete cylinder is achieved. The numerical result for the closed cylinder is in agreement with the classical eigen-function solution [17]

$$\sigma_e(\phi) = \frac{2}{\pi}\left| \sum_{n=0}^{\infty} \frac{2}{1+\delta_{no}} \frac{J_n(k_oa)}{H_n^{(2)}(k_oa)} \cos(n\phi) \right|^2 \tag{3.116}$$

where J_n is the Bessel function of order n and δ_{pq} is the Kronecker delta function

$$\delta_{pq} = \begin{cases} 1 & p = q \\ 0 & p \neq q \end{cases} \tag{3.117}$$

This is illustrated in Figure 3.19 for the same strip.

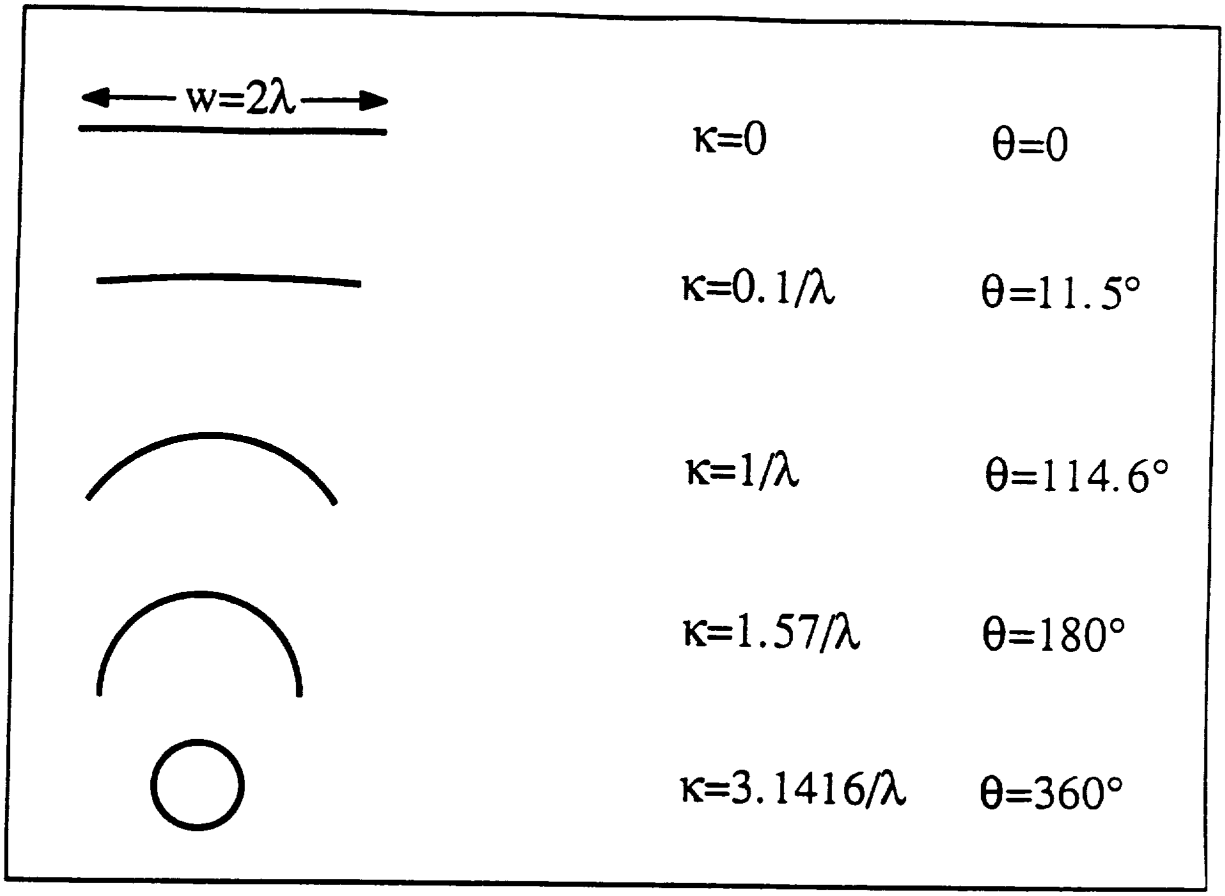

Figure 3.17: A 2λ wide conducting strip as it is uniformly bent to form a hollow cylindrical tube. κ is the curvature of the strip and θ is the polar angle subtended by the strip.

3.5 Radiation by Cylindrical Reflector Antennas

Consider the circular cylindrical reflector shown in Figure 3.20 illuminated by the line source

$$E_z = -I_e \frac{k_o Z_o}{4} H_0^{(2)}(k_o \rho) \tag{3.118}$$

The total electric field $\mathbf{E}^{\mathrm{T}}$ is evaluated in the far zone($k_o\rho >> 1$) as

$$E_z^T = -\frac{k_o Z_o}{4}\sqrt{\frac{2j}{\pi k_o}}\left[I_e + a\int_c K_z(\phi') e^{jk_o a\cos(\phi - \phi')} d\phi' \right] \frac{e^{jk_o\rho}}{\sqrt{\rho}} \tag{3.119}$$

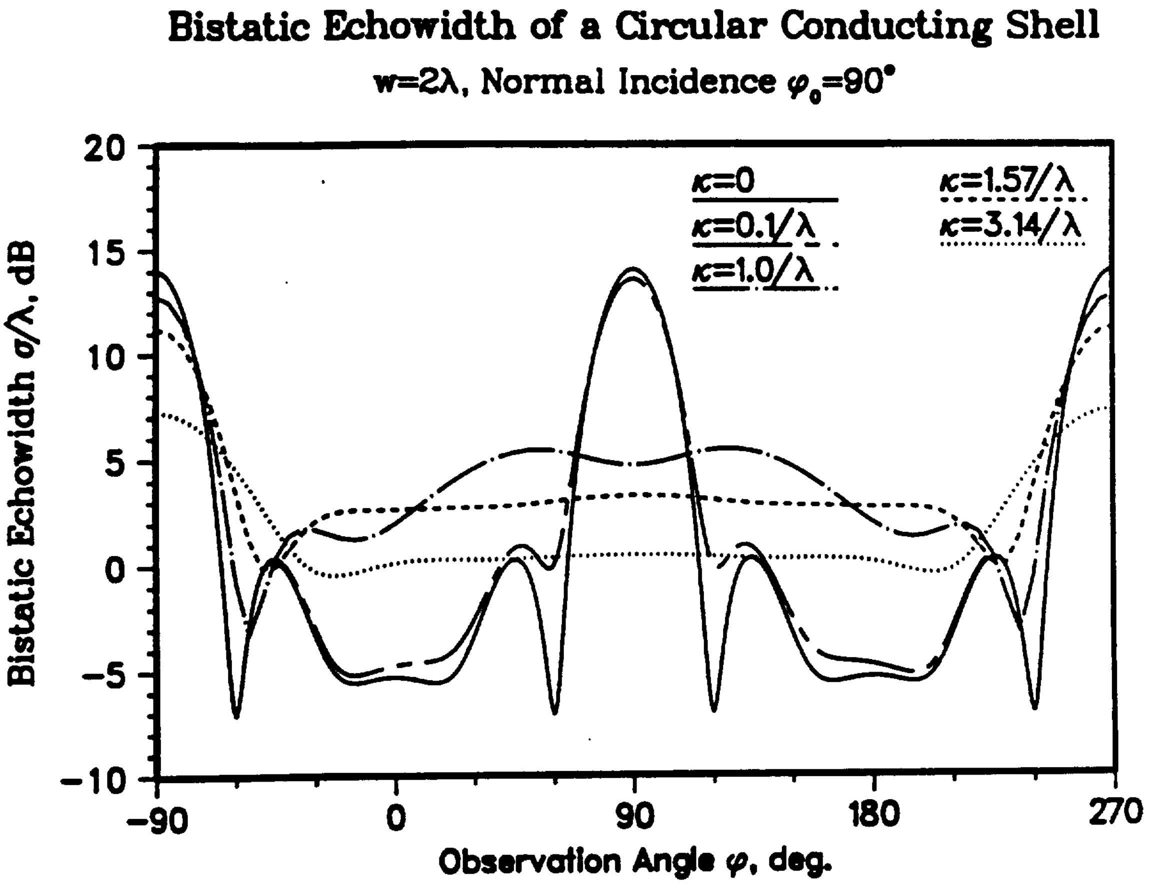

Figure 3.18: The bistatic echo width of the strip in Figure 3.17 illuminated at normal incidence.

with the normalized radiation pattern of the reflector antenna given by

$$F_n(\phi) = \left| 1 + \frac{a}{I_e} \int_c K_z(\phi') e^{j k_o a \cos(\phi - \phi')} d\phi' \right|^2 \tag{3.120}$$

Figure 3.21 shows the radiation pattern of an infinite electric line source in the presence of a $2\pi\lambda$ cylindrical resistive strip ($a = 4\lambda/3$). The line source is positioned at the center of the strip and radiates through a right angle slit. As expected, the nonzero resistivity reduces the directivity of the reflector.

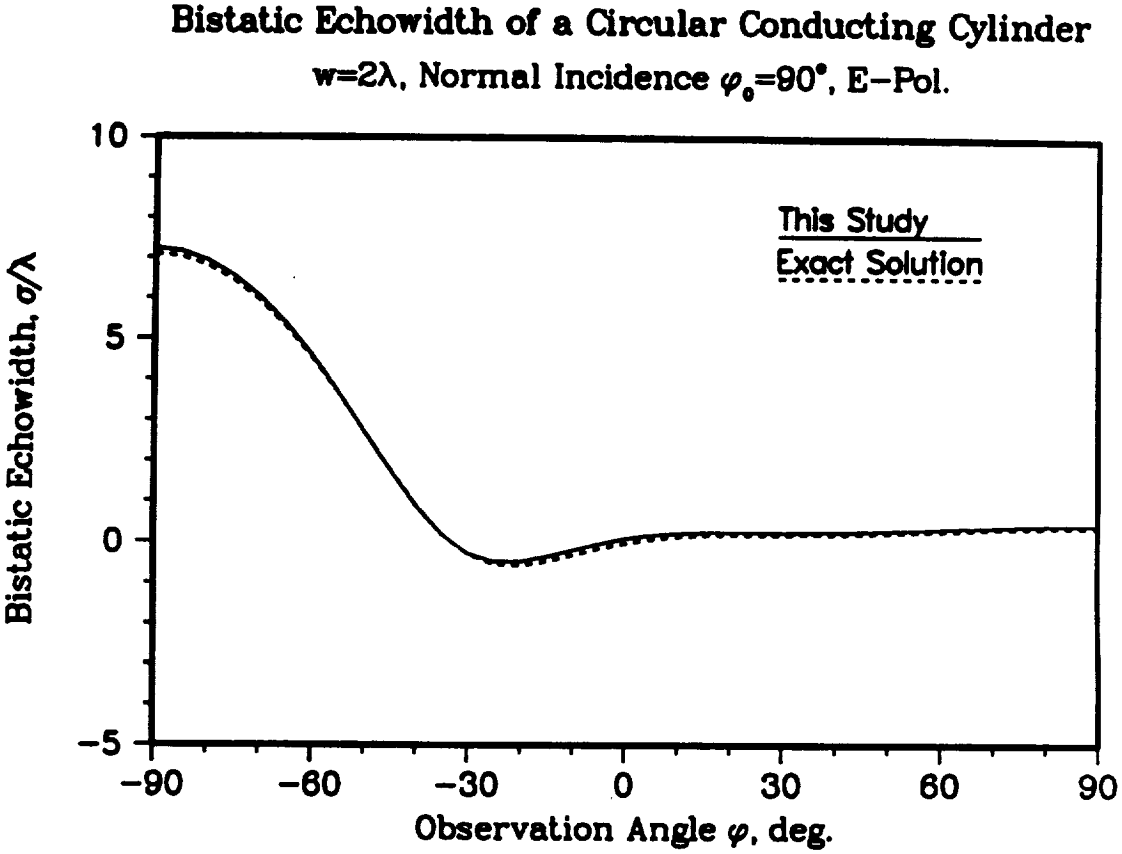

Figure 3.19: A comparison of the computed bistatic echo width of a circular conducting cylinder with the 20-term eigen-function solution.

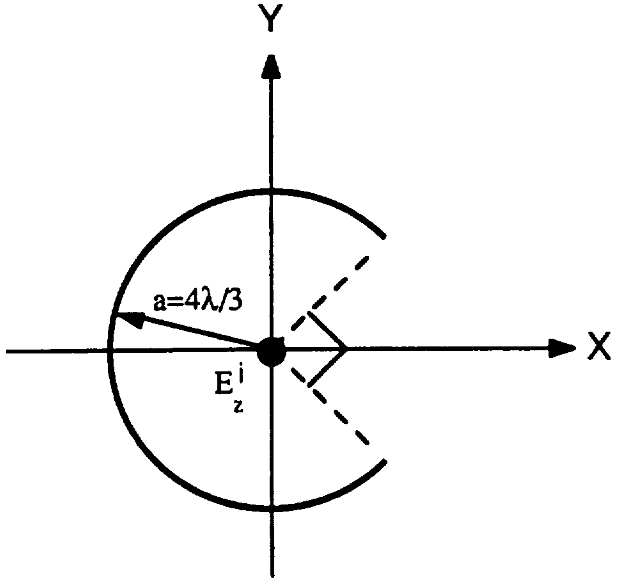

Figure 3.20: Geometry of a cylindrical reflector antenna with a 90 degree circular slit excited by an infinite electric line source.

3.6 Summary

Scattering and radiation from thin wires and strips were formulated using a standard integral equation approach. The convolutional integral equation was uniformly discretized allowing the implementation of the fast Fourier transform for carrying out the calculations. For the antenna problem, a larger sampling density was required to yield an accurate evaluation of the input impedance.

Two formulations for a conjugate gradient solution of the scattering by resistive strips were presented. The first formulation, namely, the CGFT method employed the sampled continuous transform of the Green's function for the evaluation of the convolution integrals. The other formulation, called CGDFT, employed finite duration discrete Fourier transforms for the evaluation of the same integrals. This was found to provide a more accurate as well as a more efficient simulation since it eliminated all aliasing errors. Notably, the system solved by the CGDFT method is the same as that generated by the standard moment method procedure.

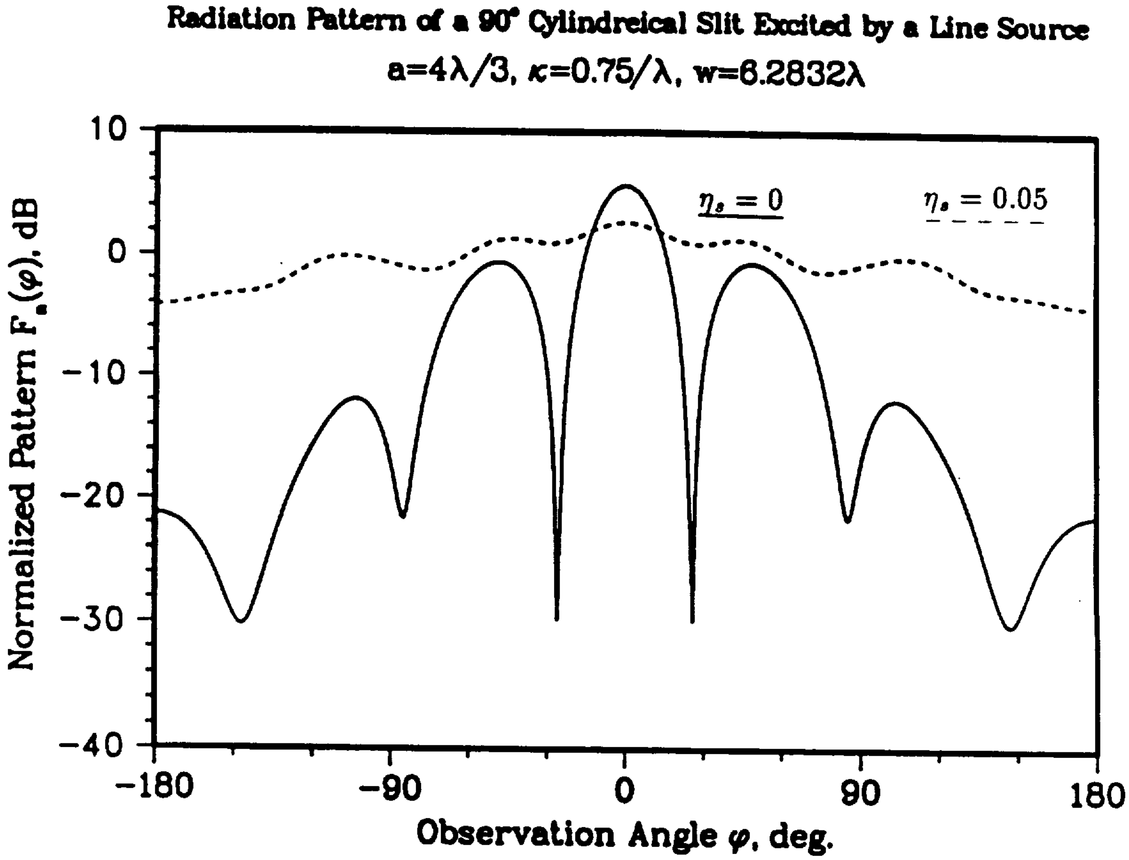

Figure 3.21: The normalized radiation pattern of the reflector antenna.

It should be noted that (3.38) and (3.81) are also applicable for computing the scattering by an impedance insert of width w. This simply requires the replacement of Z_s by the impedance of the insert and changing the polarization of incident field. The resulting echo width is then twice that given for the resistive strip to account for the presence of the ground plane. It should also be noted that the formulation discussed in connection with the thin strips is equally applicable to circular slabs of finite thickness by introducing equivalent volumetric currents instead of surface electric currents.

CHAPTER IV

RADIATION AND SCATTERING FROM PLATES AND CYLINDERS

4.1 Introduction

Planar and cylindrical structures constitute simple but nevertheless important components in man-made structures. Simulation of electromagnetic scattering from these targets is of academic interest as well as practical value in computational electromagnetics. Understanding the electromagnetic scattering behavior of these structures is also important in modeling more complex targets as well as in radar detection and cross section reduction. Although plates and cylinders have been the subject of intense study in a wide range of frequencies, their numerical analysis have been limited to the low frequency region, primarily due to computational limitations of the traditional direct methods. In particular, experience with various numerical and asymptotic methods of solution as well as comparison with measured data reveals that there is a serious difficulty in accurately predicting the scattering behavior of plates at grazing incidences where the edge currents and corner diffraction effects are significant.

In this chapter, we first develop the necessary integral equations which are then transformed to a suitable form for a solution via the CGFFT method. Two approaches will be employed in the application of the method. The first implementation, previously referred to as the CGFT method in connection with the strip analysis, employs the sampled continuous Fourier transform of the free space Green's function for the evaluation of the pertinent convolution integrals. This approach assumes an infinite spatial domain in the definition of the Green's function. Thus, as far as the Green's function is concerned, the finiteness of the target's physical extent is not accounted for and unless a large FFT 'pad' with extended zero elements is used, the method suffers from aliasing errors. A pad at least 3 times the size of the target in each dimension is often needed to obtain acceptable results at oblique and close to grazing incidences [48]. To alleviate this difficulty, another approach, previously referred to as the CGDFT method in connection with the strip problem, will be employed where the pertinent integral equation is first cast into a discrete form before the application of the convolution theorem to evaluate the integrals. As observed in the case of the strip, this eliminates all aliasing errors, except perhaps those attributed to a possible under-sampling of the current density.

Below, we discuss both of the above formulations for the solution of integral equations arising in the computation of the scattering by resistive plates and dielectric cylinders of arbitrary shapes and cross sections. The accuracy and efficiency of these formulations are then examined by a comparison with measured data and data generated by alternative techniques.

4.2 Scattering from Thin Plates

Consider a thin inhomogeneous plate of resistivity Z_s illuminated by an incident field $\mathbf{E}_i$ and we are interested in evaluating the scattered field from the plate.

The scattered field due to the excited surface current density, $\mathbf{K}$ on the plate is given by the surface integral

$$\mathbf{E}^s(\mathbf{r}) = -jk_oZ_o\int_{s'}\mathbf{K}(\mathbf{r}')\cdot\bar{\mathbf{\Gamma}}(\mathbf{r};\mathbf{r}')ds' \tag{4.1}$$

where $\bar{\mathbf{\Gamma}}$ denotes the electric dyadic Green's function in unbounded space given by

$$\bar{\mathbf{\Gamma}}(\mathbf{r};\mathbf{r}') = \left(\bar{\mathbf{I}} + \frac{1}{k^2}\nabla\nabla\right)G_p(\mathbf{r};\mathbf{r}') \tag{4.2}$$

with

$$G_p(\mathbf{r};\mathbf{r}') = \frac{e^{-jk_o|\mathbf{r}-\mathbf{r}'|}}{4\pi|\mathbf{r}-\mathbf{r}'|} \tag{4.3}$$

The explicit form of $\bar{\mathbf{\Gamma}}$ is now given by

$$\bar{\mathbf{\Gamma}} = \begin{pmatrix} (1+\frac{1}{k_o^2}\frac{\partial^2}{\partial x^2}) & \frac{1}{k_o^2}\frac{\partial^2}{\partial x\partial y} \\ \frac{1}{k_o^2}\frac{\partial^2}{\partial y\partial x} & (1+\frac{1}{k_o^2}\frac{\partial^2}{\partial y^2}) \end{pmatrix} G_p(\mathbf{r};\mathbf{r}') \tag{4.4}$$

The total tangential electric field on the plate satisfies the resistive boundary condition (3.26) and the desired integral equation for the unknown current density is

$$\left[\mathbf{E}^i(\mathbf{r})\right]_{\tan} = Z_s(\mathbf{r})\mathbf{K}(\mathbf{r}) + jk_oZ_o\int_{s'}\mathbf{K}(\mathbf{r}')\cdot\bar{\mathbf{\Gamma}}(\mathbf{r};\mathbf{r}')ds' \tag{4.5}$$

in which $\mathbf{r}$ and $\mathbf{r}'$ denote the field and source points on the surface of the plate. Expanding the current density in terms of a subsectional surface basis function $\bar{\mathbf{\Psi}}$, we write

$$\mathbf{K}(x,y) = \sum_{m=0}^{M-1}\sum_{n=0}^{N-1}\mathbf{K}_{mn}\cdot\bar{\mathbf{\Psi}}_{\mathbf{mn}}(x,y) \tag{4.6}$$

where

$$\bar{\mathbf{\Psi}}_{\mathbf{mn}}(x,y) = \bar{\mathbf{\Psi}}(x-x_m, y-y_n) \tag{4.7}$$

and

$$\bar{\mathbf{\Psi}}(x,y) = \hat{x}\hat{x}\psi_x(x,y) + \hat{y}\hat{y}\psi_y(x,y) \tag{4.8}$$

in which ψ_x and ψ_y are the expansion functions in the x and y directions, respectively.

4.2.1 Formulation Using Continuous Transforms

Through application of the convolution theorem, the continuous transform of $\mathbf{J}(x,y)$ as given in (4.6) can be written as

$$\tilde{\mathbf{J}} = \hat{\mathbf{J}} \cdot \widetilde{\bar{\bar{\mathbf{\Psi}}}} \tag{4.9}$$

where $\hat{\mathbf{J}} = \hat{x}\hat{J}_x(x,y) + \hat{y}\hat{J}_y(x,y)$ denotes the two dimensional discrete Fourier transform of the train $\mathbf{J}_{mn}$ defined in (2.19). Also, $\tilde{\mathbf{J}}(k_x,k_y) = \hat{x}\widetilde{J_x}(k_x,k_y) + \hat{y}\widetilde{J_y}(k_x,k_y)$ is the continuous Fourier transform of $\mathbf{J}$ defined in (2.11) and $\widetilde{\bar{\bar{\mathbf{\Psi}}}}$ denotes the continuous transform of the basis function.

By invoking the relation (2.14), the continuous transform of the free space dyadic Green's function can also be written as

$$\tilde{\bar{\bar{\mathbf{\Gamma}}}} = \begin{pmatrix} 1 - \dfrac{k_x^2}{k_o^2} & -\dfrac{k_x k_y}{k_o^2} \\ \\ -\dfrac{k_x k_y}{k_o^2} & 1 - \dfrac{k_y^2}{k_o^2} \end{pmatrix} \tilde{G}_p(k_x,k_y) \tag{4.10}$$

where $\tilde{G}_p$ is the transform of the Green's function given by (Appendix B)

$$\tilde{G}_p(k_x,k_y) = \frac{1}{2j\sqrt{k_o^2 - k_x^2 - k_y^2}} \tag{4.11}$$

Equations (4.10) and (4.11) constitute analytical expressions for the Fourier transform of the free space dyadic Green's function. Substituting these into (4.5) and testing the resulting equation at discrete points (point-matching), yields the system

$$\mathbf{E}_{ij} = \mathbf{Z}_{sij}\mathbf{J}_{ij} + jk_oZ_o\mathcal{F}^{-1}\{(\tilde{\bar{\bar{\mathbf{\Gamma}}}} \cdot \widetilde{\bar{\bar{\mathbf{\Psi}}}}) \cdot \hat{\mathbf{J}}\} \tag{4.12}$$

where the subscript ij denotes the value of the quantity at the test point (x_i,y_j) on the plate. It should be noted, though,that in performing the Fourier transformation implied by (4.12), an FFT pad at least twice the size of the plate in each dimension must be employed. In general, however, a much larger pad is required when the analytical transform of the Green's function is used. Also care must be applied when implementing (4.12) to avoid sampling at the singularity of the transform of the Green's function as given in (4.11).

4.2.2 Formulation Using Discrete Transforms

In this formulation, the integral equation (4.5) is first discretized leading to expressions that can be identified as finite domain discrete convolutions. These can then be evaluated via application of the discrete convolution theorem which is inherently cyclic, thus, avoiding aliasing errors. To cast the integral equation (4.5) in discrete form we first employ (4.6) to rewrite the right hand side integral as

$$\int_{S'} \left[\sum_{m=0}^{M-1} \sum_{n=0}^{N-1} \mathbf{J}_{mn} \cdot \bar{\bar{\Psi}}_{mn}(x,y) \right] \cdot \bar{\bar{\Gamma}}(x,y;x',y')ds' \tag{4.13}$$

which, upon interchanging the order of summation and integration, may be written as

$$\sum_{m=0}^{M-1} \sum_{n=0}^{N-1} \mathbf{J}_{mn} \cdot \int_{s'} \bar{\bar{\Psi}}_{mn}(x',y') \cdot \bar{\bar{\Gamma}}(x,y;x',y')ds' \tag{4.14}$$

Introducing (4.14) into (4.5) and satisfying the resulting equation at a discrete set of points (point matching) yields the system of equations

$$\mathbf{E^i}_{ij} = \mathbf{Z}_{sij}\mathbf{K}_{ij} + jk_oZ_o \sum_{mn} \bar{\bar{\Xi}}_{ij} \cdot \mathbf{K}_{mn} \tag{4.15}$$

The dyadic function

$$\bar{\bar{\Xi}} = \begin{pmatrix} \xi^{xx} & \xi^{xy} \\ \xi^{yx} & \xi^{yy} \end{pmatrix} \tag{4.16}$$

is a discrete kernel whose elements are given by

$$\xi^{xx}_{ij} = (1 + \frac{1}{k_o^2}\frac{\partial^2}{\partial y^2}) \int_{\sigma_{mn}} G_p(x,y;x',y')\psi_x(x'-x_m,y'-y_n)ds'$$

$$
\begin{aligned}
\xi_{ij}^{xy} &= \frac{1}{k_o^2}\frac{\partial^2}{\partial x \partial y}\int_{\sigma_{mn}} G_p(x,y;x',y')\psi_y(x'-x_m,y'-y_n)ds' \\
& \qquad\qquad\qquad\qquad\qquad\qquad\qquad\qquad\qquad\qquad\qquad\qquad (4.17) \\
\xi_{ij}^{yx} &= \frac{1}{k_o^2}\frac{\partial^2}{\partial x \partial y}\int_{\sigma_{mn}} G_p(x,y;x',y')\psi_x(x'-x_m,y'-y_n)ds' \\
\xi_{ij}^{yy} &= (1+\frac{1}{k_o^2}\frac{\partial^2}{\partial x^2})\int_{\sigma_{mn}} G_p(x,y;x',y')\psi_y(x'-x_m,y'-y_n)ds'
\end{aligned}
$$

where σ_{mn} is the incremental surface element corresponding to the mnth cell on the plate and all expressions are evaluated at $(x,y)=(x_i,y_j)$ upon differentiation. Obviously, the convolutional nature of the operation is preserved once the above functions are evaluated at the appropriate field points. Applying the discrete convolution theorem in (4.15) now gives

$$
\mathbf{E}_{ij} = Z_{sij}\mathbf{K}_{ij} + jkZ_o\,\mathrm{DFT}^{-1}\{\hat{\hat{\boldsymbol{\Xi}}}\cdot\widehat{\mathbf{K}}\} \qquad (4.18)
$$

where $\hat{\hat{\boldsymbol{\Xi}}}$ denotes the discrete Fourier transform of $\hat{\boldsymbol{\Xi}}$.

To calculate the elements of $\hat{\hat{\boldsymbol{\Xi}}}$, the partial derivatives may be carried out by finite difference formulae. In particular, using a 3-point central difference scheme (2.23), we find that

$$
\hat{\hat{\boldsymbol{\Xi}}} = \frac{1}{k_o^2}\begin{pmatrix} k_o^2 - D_x^2 & -D_xD_y \\ -D_yD_x & k_o^2 - D_y^2 \end{pmatrix}\hat{\xi} \qquad (4.19)
$$

where $\hat{\xi}$ is the discrete Fourier transform of the sequence(assuming piecewise constant basis functions)

$$
\xi_{mn} = \int_{\sigma_{mn}} \frac{e^{-jk_o\sqrt{x^2+y^2}}}{4\pi\sqrt{x^2+y^2}}ds \qquad (4.20)
$$

and

$$
\begin{aligned}
D_x &= k_x \mathrm{sinc}(k_x\frac{\Delta x}{2}) \qquad (4.21) \\
D_y &= k_y \mathrm{sinc}(k_y\frac{\Delta y}{2}) \qquad (4.22)
\end{aligned}
$$

as given in (2.24). It is noted that ξ has an integrable singularity when $x_m = y_n = 0$ corresponding to the self-cell interaction. This term can be evaluated analytically using one of the following approximations:

Approximate integration: From [49]

$$\begin{aligned} \xi_{00} \simeq\; & \frac{1}{\pi}\left\{ \Delta x \ln \left| \tan\left(\frac{\pi}{4} + \frac{1}{2}\tan^{-1}\frac{\Delta y}{\Delta x}\right)\right| \right. \\ & \left. + \Delta y \ln \left| \tan\left(\frac{\pi}{4} + \frac{1}{2}\tan^{-1}\frac{\Delta x}{\Delta y}\right)\right| - jk_o \frac{\Delta x \Delta y}{2} \right\} \end{aligned} \qquad (4.23)$$

Taylor series expansion: Expanding the integrand of (4.20) as [50]

$$\frac{e^{-jk_oR}}{R} \simeq \frac{1}{R}\left(1 - jk_oR + \frac{(jk_oR)^2}{2} - \frac{(jk_oR)^3}{6}\right) \qquad (4.24)$$

ξ_{00} can then be expressed as

$$\xi_{00} \simeq \frac{1}{4\pi}\left(I_1 - jk_oI_2 - \frac{k_o^2}{2}I_3 + j\frac{k_o^3}{6}I_4\right)\Big|_{x=-\frac{\Delta x}{2}}^{\frac{\Delta x}{2}}\Big|_{y=-\frac{\Delta y}{2}}^{\frac{\Delta y}{2}} \qquad (4.25)$$

where

$$\begin{aligned} I_1 &= \iint \frac{1}{R} ds = x\ln(y+R) + y\ln(x+R) \\ I_2 &= \iint ds = \Delta x \Delta y \\ I_3 &= \iint R ds = \frac{xyR}{3} + \frac{x^3}{6}\ln(y+R) + \frac{y^3}{6}\ln(x+R) \\ I_4 &= \iint R^2 ds = \frac{xyR^2}{3} \end{aligned}$$

Circular disk approximation:

$$\begin{aligned} \xi_{00} &\simeq \int_0^{2\pi}\int_0^{r_0} \frac{e^{-jk_or}}{4\pi r} r\,dr\,d\phi \\ &= \frac{r_0}{2} e^{-jk_or_0/2} \mathrm{sinc}\left(\frac{k_or_0}{2}\right) \end{aligned} \qquad (4.26)$$

where

$$r_0 = \sqrt{\Delta x \Delta y / \pi} \qquad (4.27)$$

Figure 4.1 shows a comparison of these expressions for ξ_{oo} for square cells ($\Delta x = \Delta y = \Delta$) of different sizes. As seen, they all give values that are essentially indistinguishable for $\Delta < 0.1\lambda$. The remaining terms ξ_{mn} are evaluated numerically via Gaussian quadrature integration. Using the above formulations, computations were performed for a variety of plate sizes and shapes under two different excitations, namely, plane wave excitation and Hertzian dipole excitation.

4.2.3 Plane Wave Scattering

Plates have been of considerable interest in plane wave scattering because they often represent building blocks in the simulation of more complex configurations of practical interest. An understanding of their scattering characteristics can, therefore, provide insightful information for design applications. In this case, simple high frequency formulae are usually more suitable, but unfortunately, available expressions have not been found to yield accurate results. On the other hand, numerical simulations demand an excessive storage requirement making the CGFFT solution method attractive for such simulations.

Consider the plate in Figure 4.2 illuminated by a plane wave

$$\mathbf{E}^{\mathbf{i}} = \mathbf{E}_o e^{-jk_o(\hat{k}_i \cdot \mathbf{r})} \tag{4.28}$$

$$\mathbf{H}^{\mathbf{i}} = \frac{1}{Z_o}\hat{k}_i \times \mathbf{E}^{\mathbf{i}} \tag{4.29}$$

where Z_o and k_o are the free space intrinsic impedance and wave number, respectively. In the above, $\hat{k}_i$ is the unit propagation vector

$$\hat{k}_i = -[\sin\theta_o(\hat{x}\cos\phi_o + \hat{y}\sin\phi_o) + \hat{z}\cos\theta_o] \tag{4.30}$$

and

$$\mathbf{E}_o = \hat{x}E_{ox} + \hat{y}E_{oy} + \hat{z}E_{oz}$$

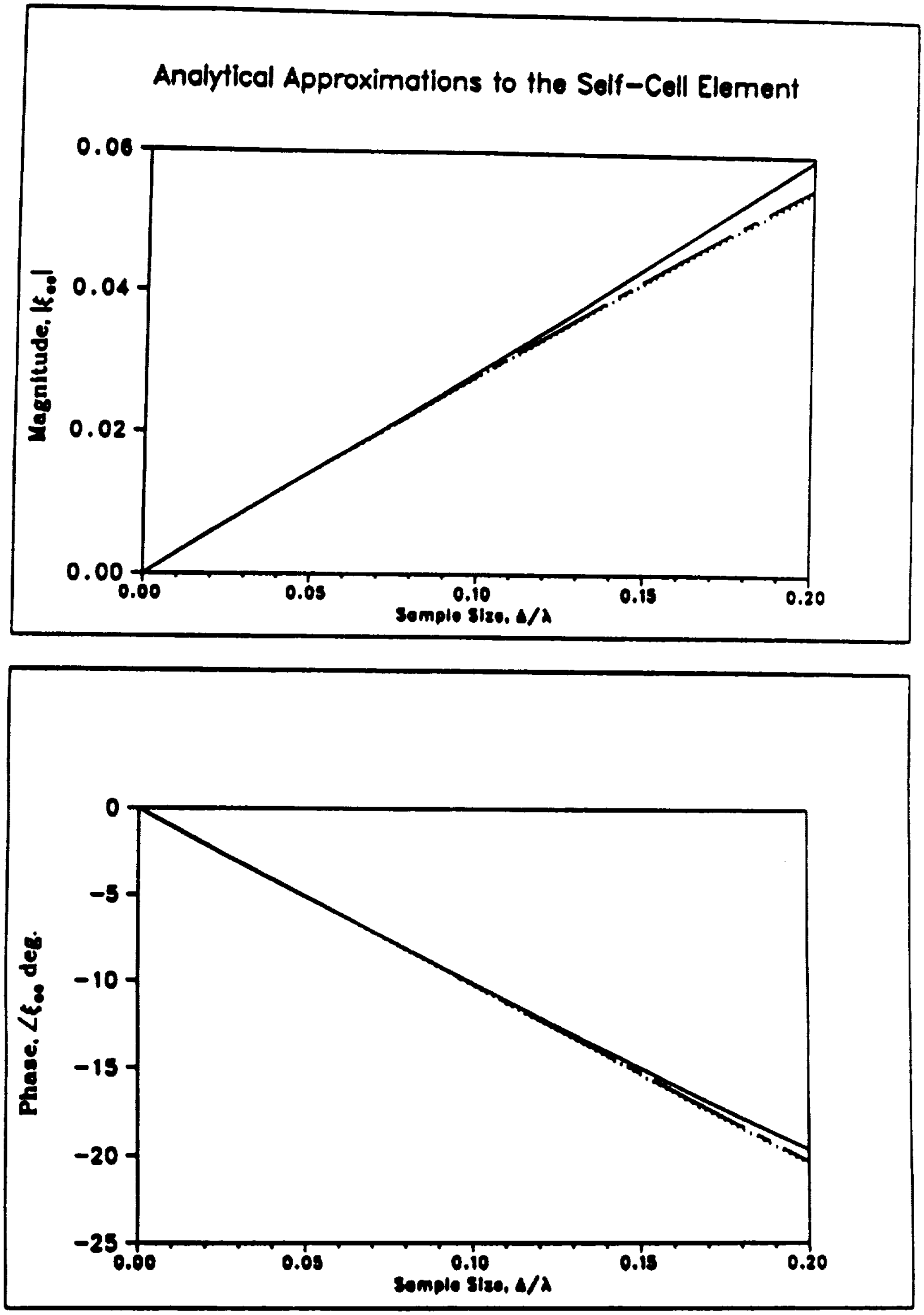

Figure 4.1: Evaluation of the self-cell element using approximate integration (—), four-term Taylor series expansion (···), and circular disk approximation (- - -).

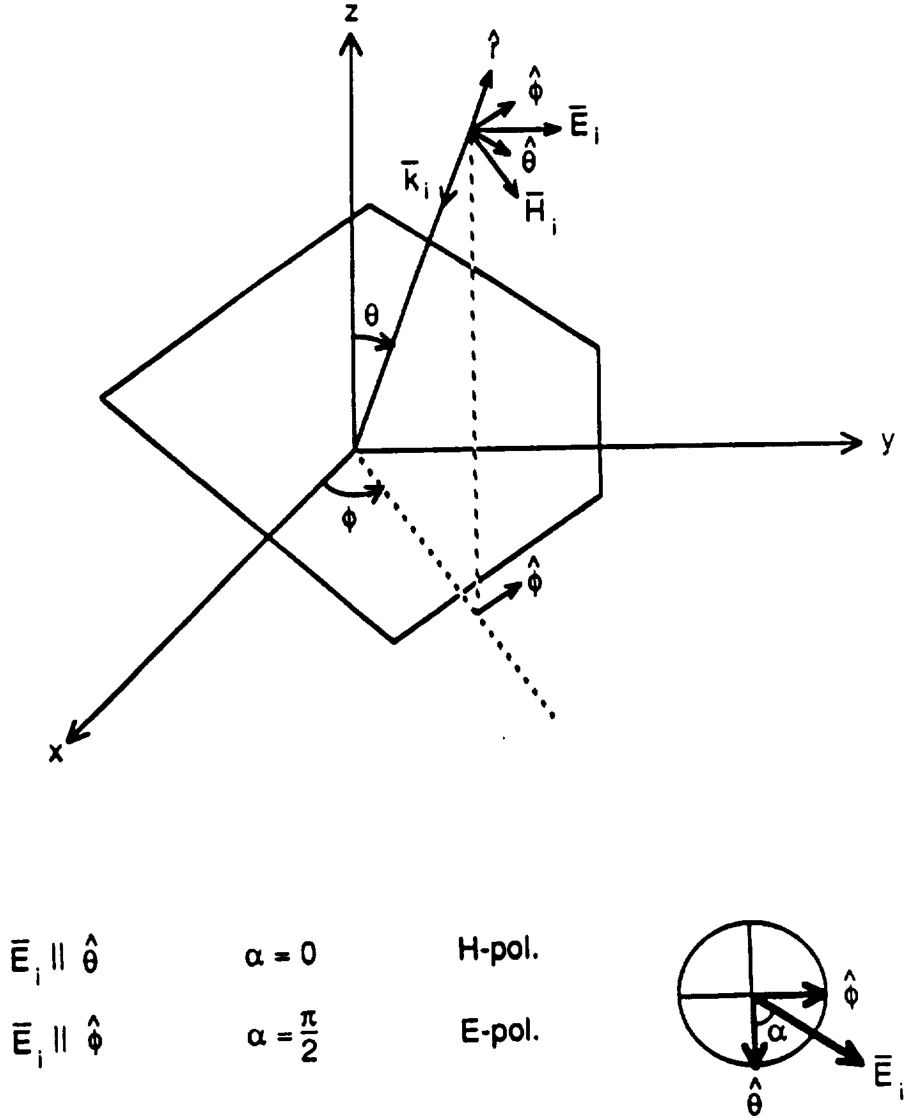

Figure 4.2: Geometry of a polygonal plate illuminated by a plane wave.

C-2

with

$$\begin{aligned} E_{0x} &= E_0(\cos\alpha\cos\theta_o\cos\phi_o - \sin\alpha\sin\phi_o) \\ E_{0y} &= E_0(\cos\alpha\cos\theta_o\sin\phi_o + \sin\alpha\cos\phi_o) \\ E_{0z} &= -E_0\cos\alpha\sin\theta_o \end{aligned} \tag{4.31}$$

where α represents the polarization angle of the incident field. It is the angle between $\mathbf{E}^i$ and $\hat{\theta}$. In particular, when $\alpha = 0$ then $H_z^i = 0$, corresponding to H-polarization, and $\alpha = \pi/2$ then $E_z^i = 0$, corresponding to E-polarization incidence. Upon evaluation of the current $\mathbf{K}$, the scattered field is given by

$$\mathbf{E}^s(\theta,\phi) = -jk_oZ_o\frac{e^{-jk_or}}{4\pi r}\mathbf{N}_t(\theta,\phi) \tag{4.32}$$

where (r,θ,ϕ) are the spherical coordinates of the observation point. Also,

$$\mathbf{N}_t(\theta,\phi) = \hat{\theta}N_{t\theta}(\theta,\phi) + \hat{\phi}N_{t\phi}(\theta,\phi) \tag{4.33}$$

$$N_{t\theta}(\theta,\phi) = \cos\theta\left[\cos\phi S_x(\theta,\phi) + \sin\phi S_y(\theta,\phi)\right] - \sin\theta S_z(\theta,\phi) \tag{4.34}$$

$$N_{t\phi}(\theta,\phi) = -\sin\phi S_x(\theta,\phi) + \cos\phi S_y(\theta,\phi) \tag{4.35}$$

and

$$\mathbf{S}(\theta,\phi) = \int\int_s \mathbf{K}(x',y')e^{jk_o\cos\theta[x'\cos\theta + y'\sin\theta]}dx'dy' \tag{4.36}$$

The field $\mathbf{E}^s$ can also be described as that attributed to the radiation of the plate currents and is responsible for the radar cross section of the plate defined as

$$\sigma = \lim_{r\to\infty} 4\pi r^2\frac{|\mathbf{E}^s\cdot\hat{p}_r|^2}{|\mathbf{E}^i|^2} \tag{4.37}$$

in which $\hat{p}_r$ is a unit vector denoting the polarization of the receiver.

First, it is of interest to examine the current distributions on the rectangular plate as it has a rather unique and predictable behavior, particularly for principal plane incidences. Figure 4.3 depicts three-dimensional views of the co- and cross-polarization currents on a $2\lambda \times 2\lambda$ conducting plate. An important observation with regard to these plots is the high current density values near the edges and the dominance of the co-polarized current component relative to the cross-polarized component. The singular behavior of the K_x currents at the edges is generic to perfectly conducting structures with sharp edges. These singularities are responsible for the diffracted fields and are the primary source of difficulty in numerical simulations. As θ increases, the strength of the cross-polarization currents also increases effecting the behavior of the co-polarized currents, especially those toward the back edge of the plate. When $\theta = 90°$, K_y have their greatest strength. They are concentrated near the side edges and are responsible for the travelling edge waves which, although not radiating at backscatter, are crucial in determining the back edge co-polarized current behavior. The lobing structure of the edge currents is particularly interesting and unique to all rectangular plates regardless of their size. Generally, for an $n\lambda \times n\lambda$ plate, the magnitude of the co-polarized currents are associated with n maxima near the front and back edges, whereas the cross polarized currents have $2n$ maxima near the side edges.

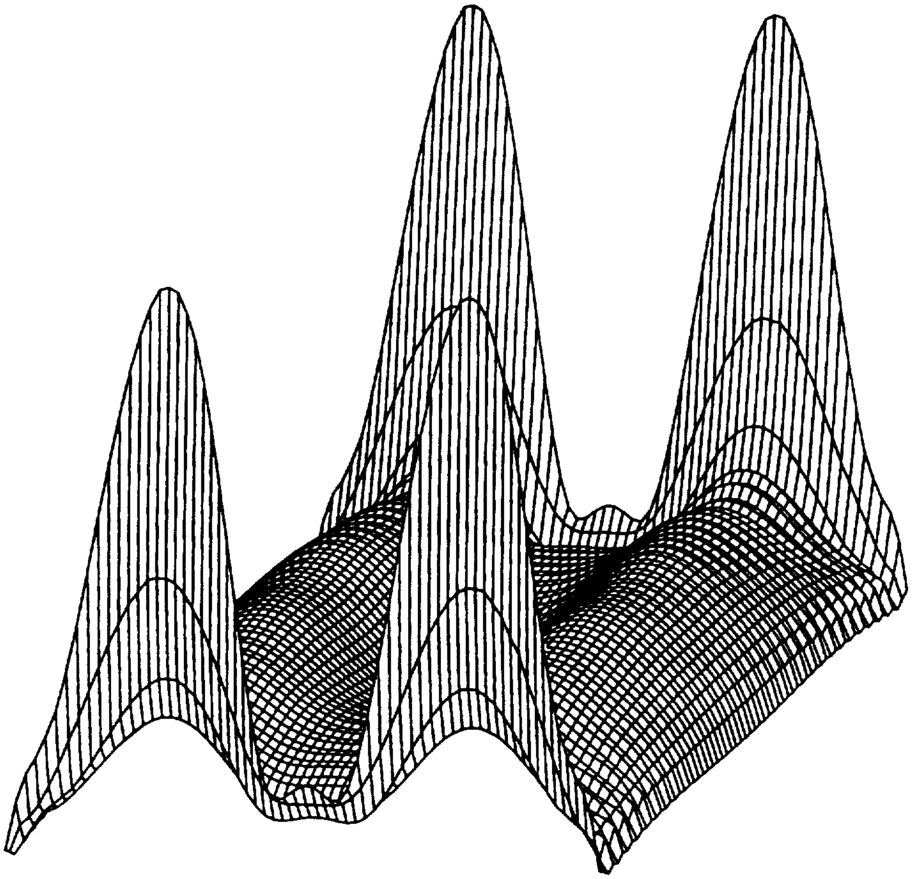

(a)

Figure 4.3: E-polarization plane wave scattering from a $2\lambda \times 2\lambda$ conducting plate at normal incidence ($\theta_i = 0°$, $\phi_i = 90°$, $\alpha = 90°$); No. of samples: 66×66; FFT pad size: 512×512. (a) Co-polarized component of the current density. (b) Cross-polarized component of the current density.

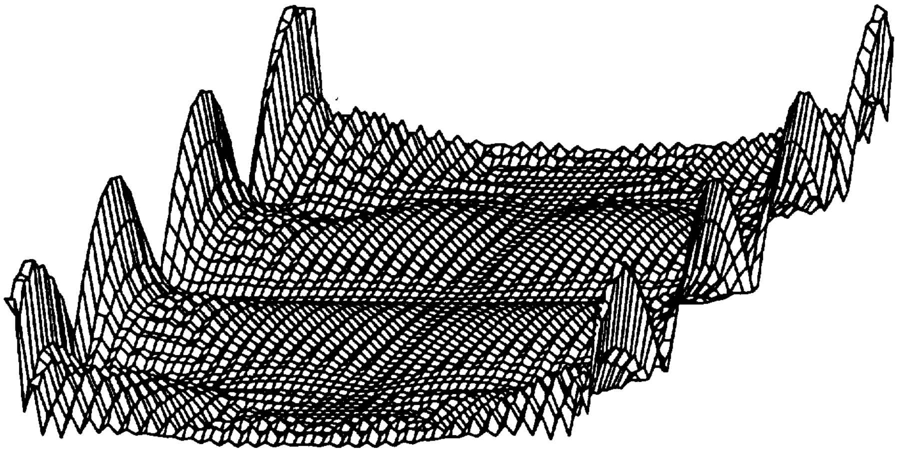

(b)

Since the RCS of a structure is an easily measured quantity, it provides a means for validating the solutions. Using the computed plate current densities, the radar cross section (RCS) of the plate can be found in accordance with (4.37). Figure 4.4 illustrates the convergence of the far zone scattered field (using pulse basis) by a square perfectly conducting $2\lambda \times 2\lambda$ plate as the size of the FFT pad is progressively increased. In all cases the algorithm was terminated when the residual reached a normalized value of about 0.01. Also shown in Figure 4.4 is the improved result using the CGDFT method. It is observed that an FFT pad of order 1 (minimum size) is sufficient when using the CGDFT to yield results that are in agreement with the measured data. In contrast, at least a pad of order 3 (along each dimension) is required to obtain acceptable results when using the CGFT method and although the general behavior of the backscattering cross section approaches that of the measured, the convergence to the measured value is not clear near grazing incidence even with higher order pads. The principal plane backscatter RCS patterns as computed via the CGDFT for the $2\lambda \times 2\lambda$ square plate are compared with the measured data in Figure 4.5. The results are seen to be in very good agreement in this case.

Often of interest is the computation of the plate's edge-on scattering. As is well known, for edge-on incidences the plate currents are rapidly varying and this makes their computation a more challenging task. The accuracy of the proposed formulations can therefore be best evaluated by examining the edge-on scattered field. Some measured data for the edge-on radar cross section have been reported in the literature. For example, Figure 4.6 shows the edge-on behavior of a plate of constant width ($b = 2\lambda$) and varying length ($2\lambda < a < 2.5\lambda$) with the electric field aligned with the shorter side reported in [51]. As can be seen, they compare quite favorably with corresponding values computed via the CGDFT formulation.

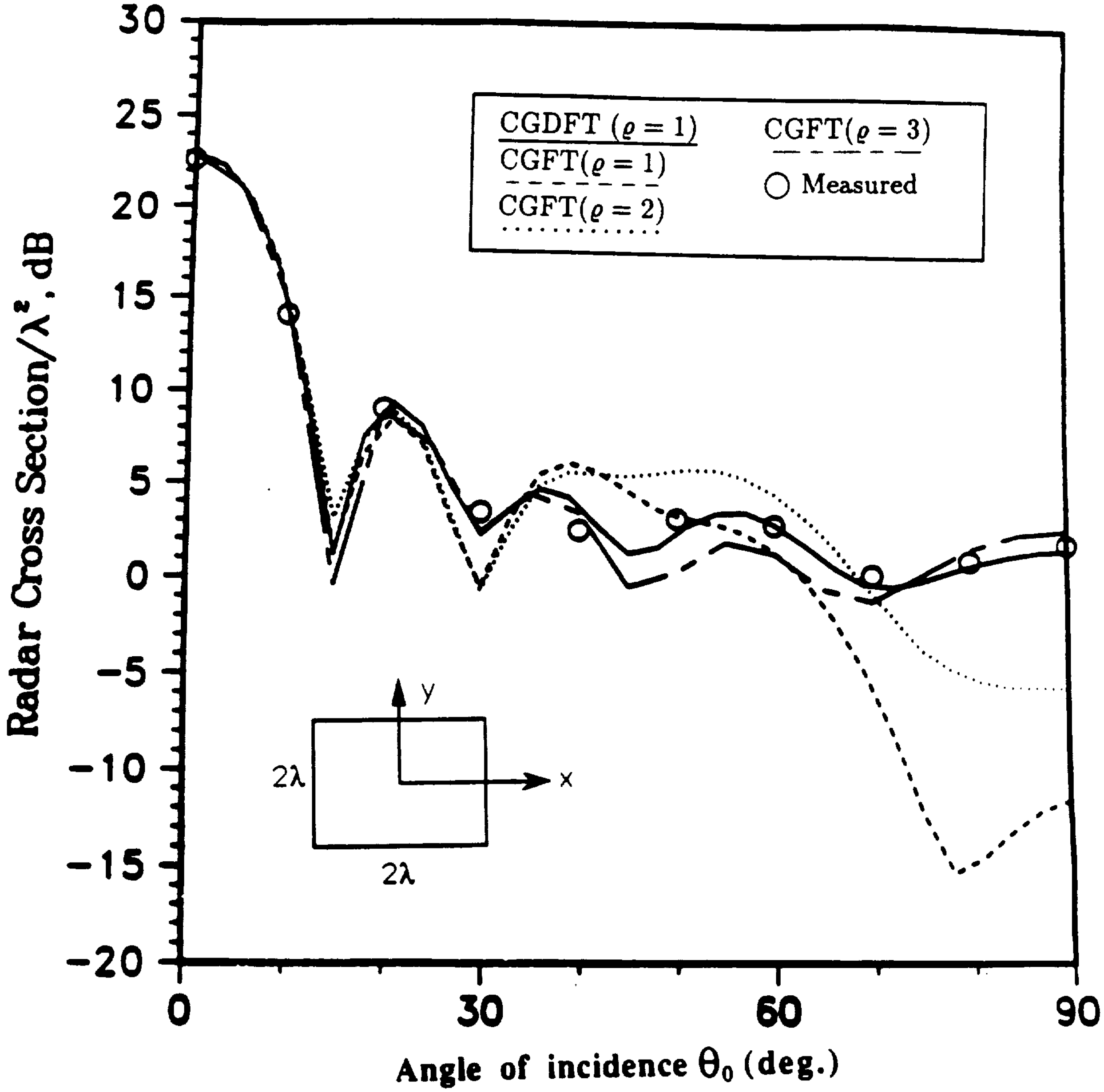

Figure 4.4: Comparison of backscatter RCS patterns for a square $2\lambda \times 2\lambda$ conducting plate as computed via the CGFT and CGDFT methods using FFT pads of various orders (E-Pol., normal incidence).

It should be noted that the CGFT method employing the continuous transform of the Green's function was found inadequate for an accurate prediction of the edge-on scattering behavior [48].

The radar scattering from a polygonal plate is shown in Figure 4.7 along with the corresponding measured data [52]. The scattering characteristics of geometrically complex targets may also be simulated by approximating the target by a polygon of n sides. This is illustrated in Figure 4.8 where the plate has been modeled as a polygon of 8 corners.

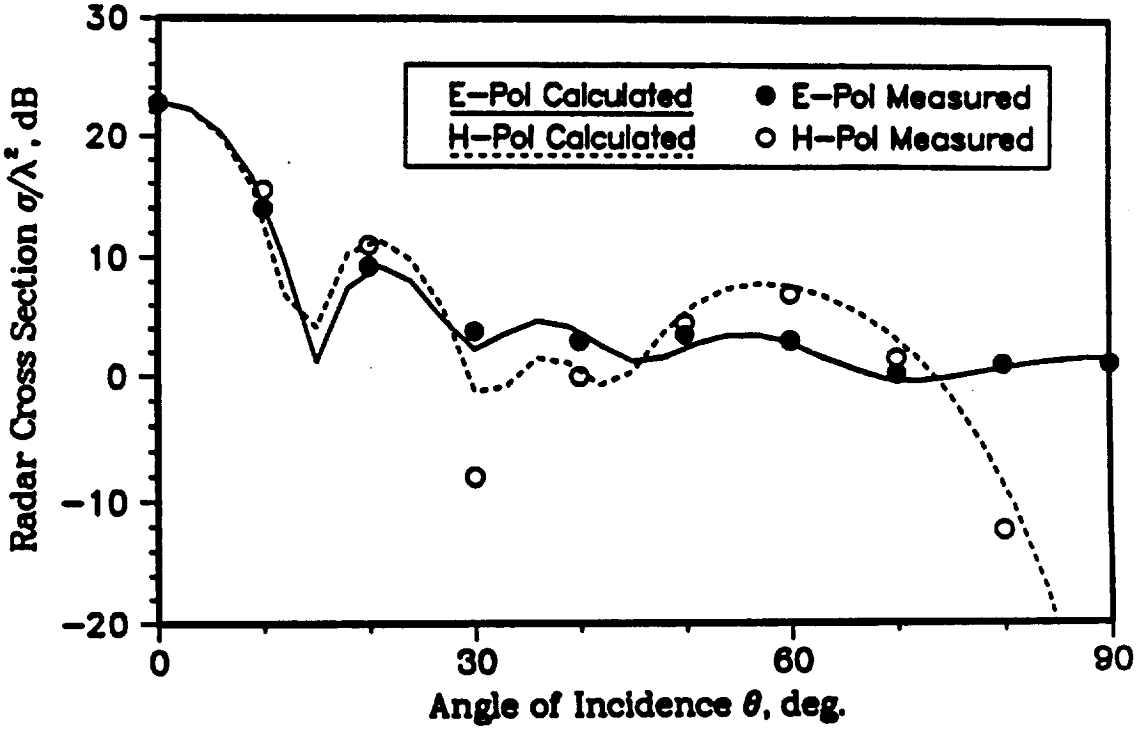

Figure 4.5: Backscattering pattern of a $2\lambda \times 2\lambda$ conducting plate.

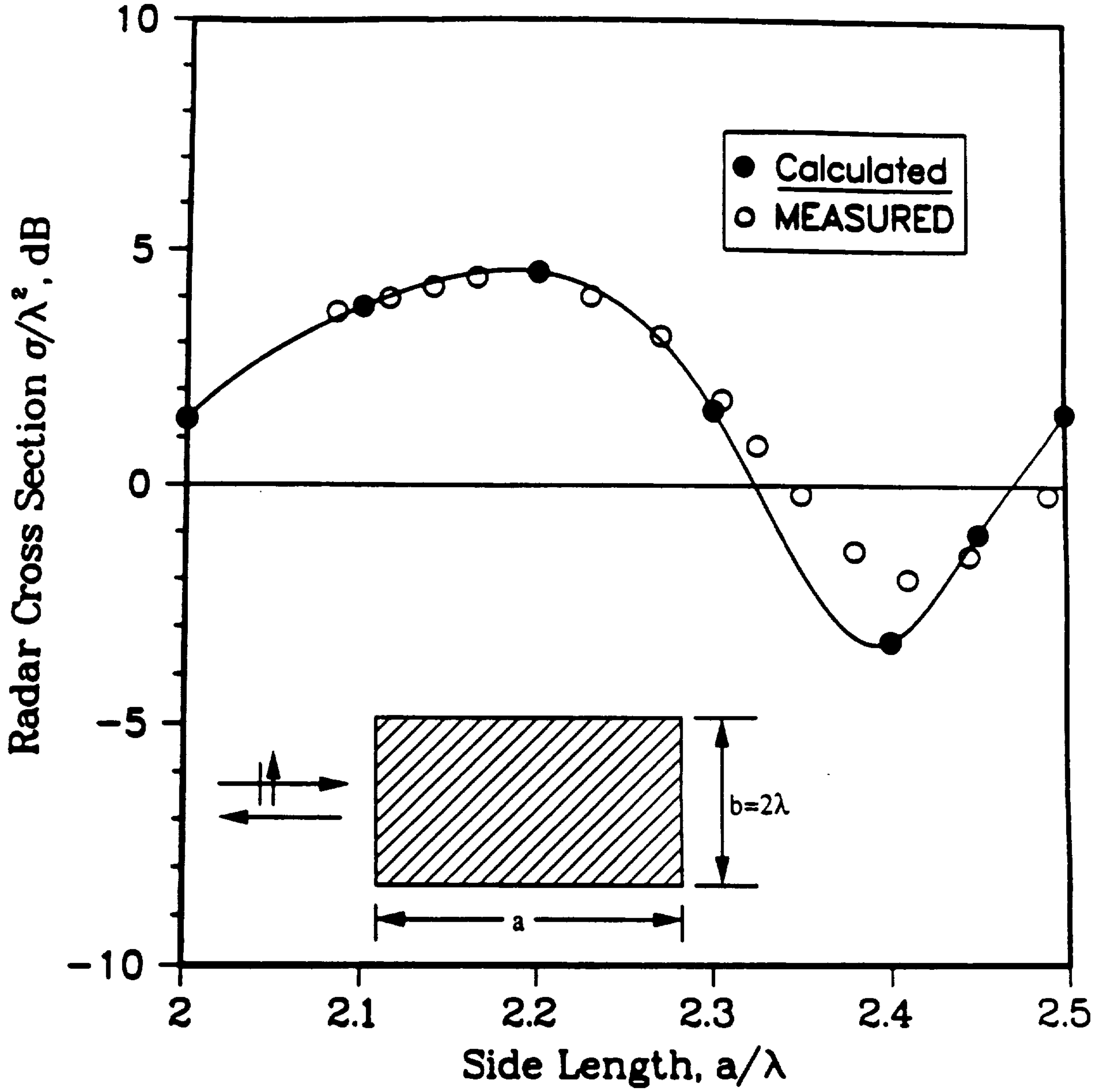

Figure 4.6: E-polarization edge-on RCS for a rectangular metalic plate.

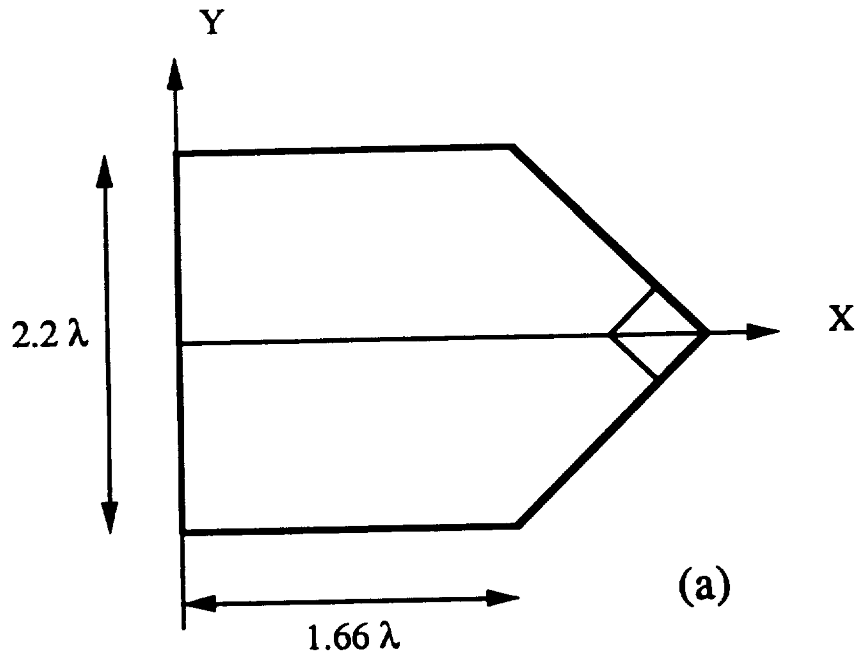

Figure 4.7: E-polarization scattering from an irregular-edged conducting plate. (a) Geometry. (b) Elevation-plane backscattering CGDFT result (—) compared with measured data [52] (o o o).

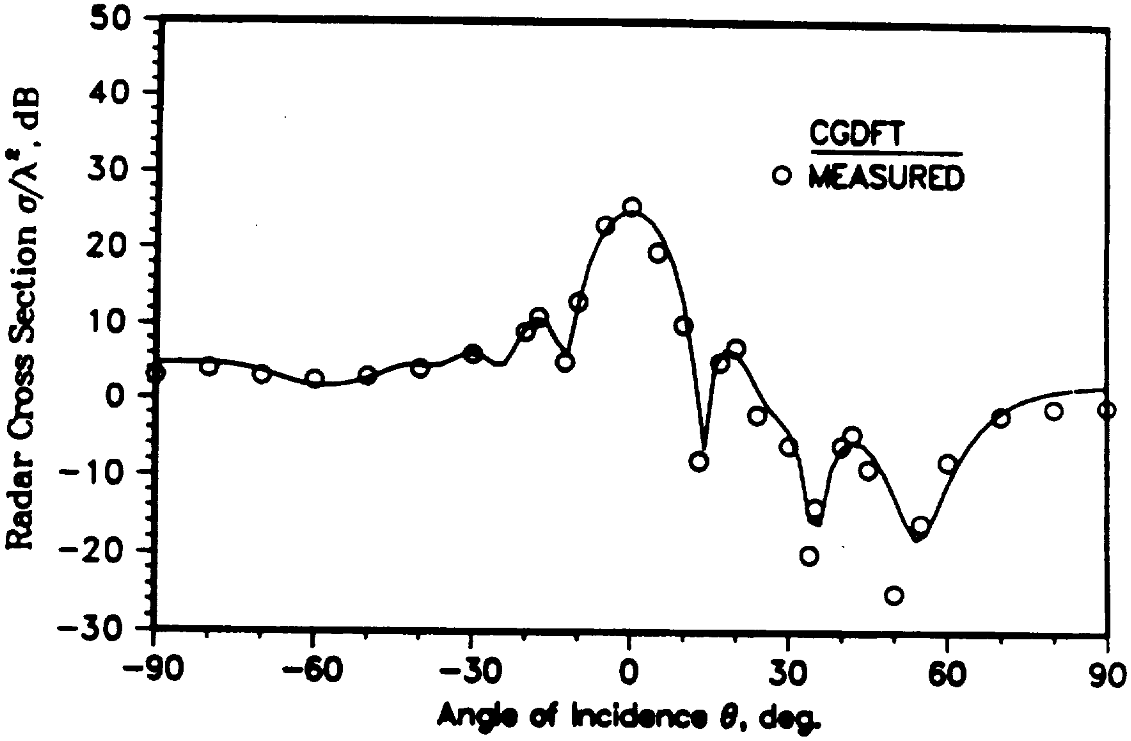
50
40
30
20
10
0
−10
−20
−30
Radar Cross Section σ/λ², dB
CGDFT
○ MEASURED
−90
−60
−30
0
30
60
90
Angle of Incidence θ, deg.

(b)

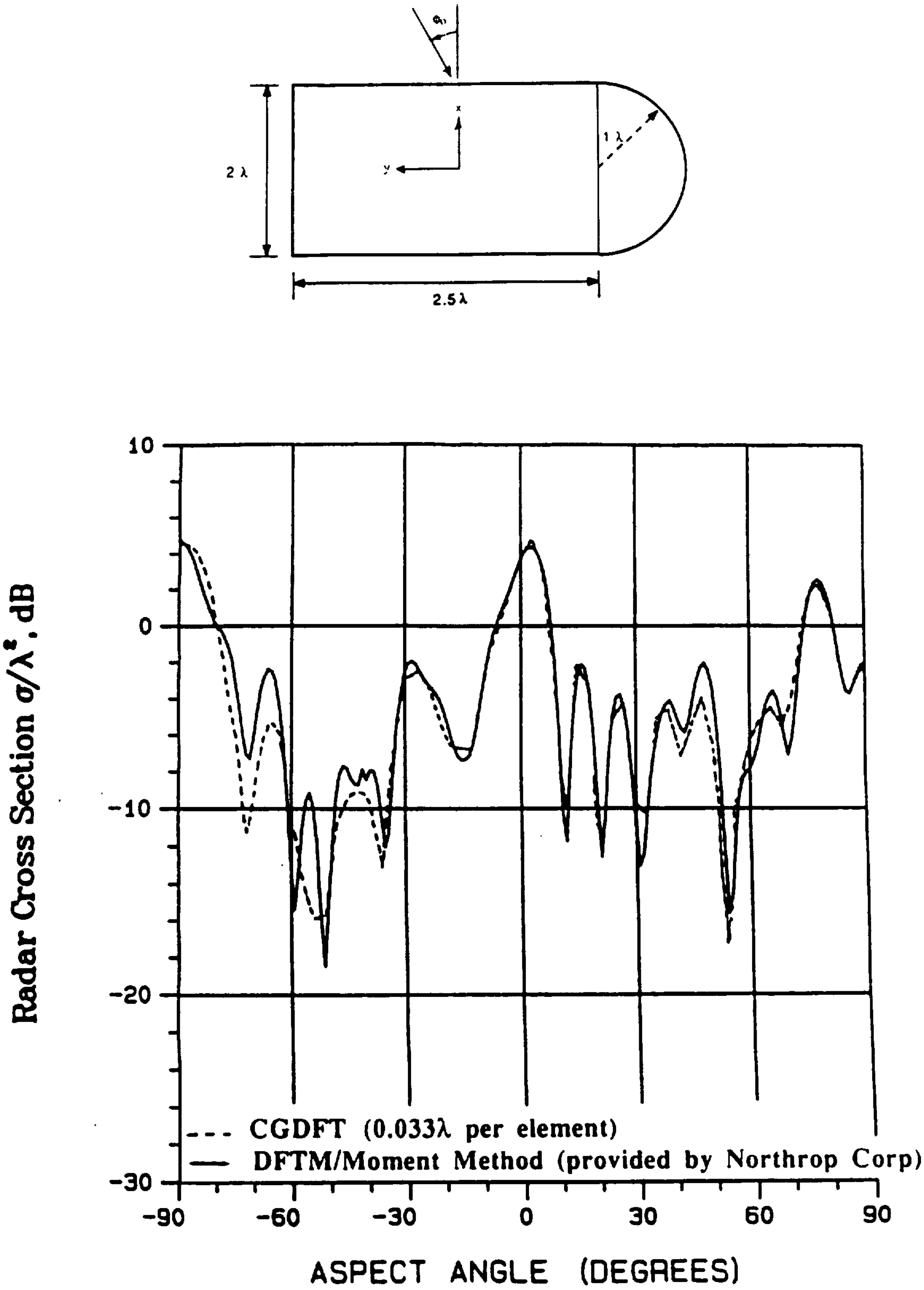

Figure 4.8: E-polarization scattering from an irregular-curved conducting plate. (a) Geometry. (b) Near-grazing conical ($\theta = 80°$) backscattering CGDFT result (- - -) compared with the MoM data (—).

Resistive plates are considered next. In practice conducting surfaces are replaced with resistive cards for cross section reduction purposes. By defining the surface resistivity Z_s as a function of position, different resistivity tapers may be treated. As an example, the resistivity can be expressed by a nonlinear function

$$Z_s(x,y) = Z_c + (Z_e - Z_c)\left[\left(\frac{|x-x_o|}{x_l/2}\right)^{\tau_x} + \left(\frac{|y-y_o|}{y_l/2}\right)^{\tau_y}\right] \tag{4.38}$$

where Z_c and Z_e may be considered as the resistivities at the center and the edges of a rectangular plate, respectively and τ_x and τ_y denote the tapers in the corresponding directions. Figure 4.9 shows the effect of uniform and non-uniform (parabolic) resistive tapers on the monostatic cross section of a $2\lambda \times 2\lambda$ plate. The bistatic behavior of a polygon of 5 sides in the azimuth plane of $\theta = 60°$ is shown in Figure 4.10. Also shown is the result for the same plate with a parabolically tapered resistivity given by

$$Z_s(x,y) = \frac{Z_o}{2}\left[\frac{(x/\lambda)-2}{2}\right]^2 + \frac{Z_o}{4}\left[\frac{(y/\lambda)-2}{2}\right]^2 \tag{4.39}$$

where Z_o is the intrinsic impedance of free space.

The convergence characteristics of the CGDFT solution for a square $2\lambda \times 2\lambda$ conducting plate illuminated under normal incidence is shown in Figure 4.11. At each iteration, both the normalized residual error, R_s and the incremental error in the backscattering cross section, $\Delta\sigma$ are given. These are respectively defined as

$$R_s = \frac{||\mathcal{A}[\mathbf{J}_m] - \mathbf{E}^i||}{||\mathbf{E}^i||} \tag{4.40}$$

and

$$\Delta\sigma = \sigma_m - \sigma_{m-1} \text{ , dB} \tag{4.41}$$

where m denotes the iteration number. It is observed that for far field calculations, accurate results can be obtained in much less number of iterations than that required to reach the true solution for the current density. In this case for example, an incremental error of 0.1 dB (a relative error of 2%) in the backscattering RCS was reached within only 6 iterations. At this point, the normalized residual error was about 18%.

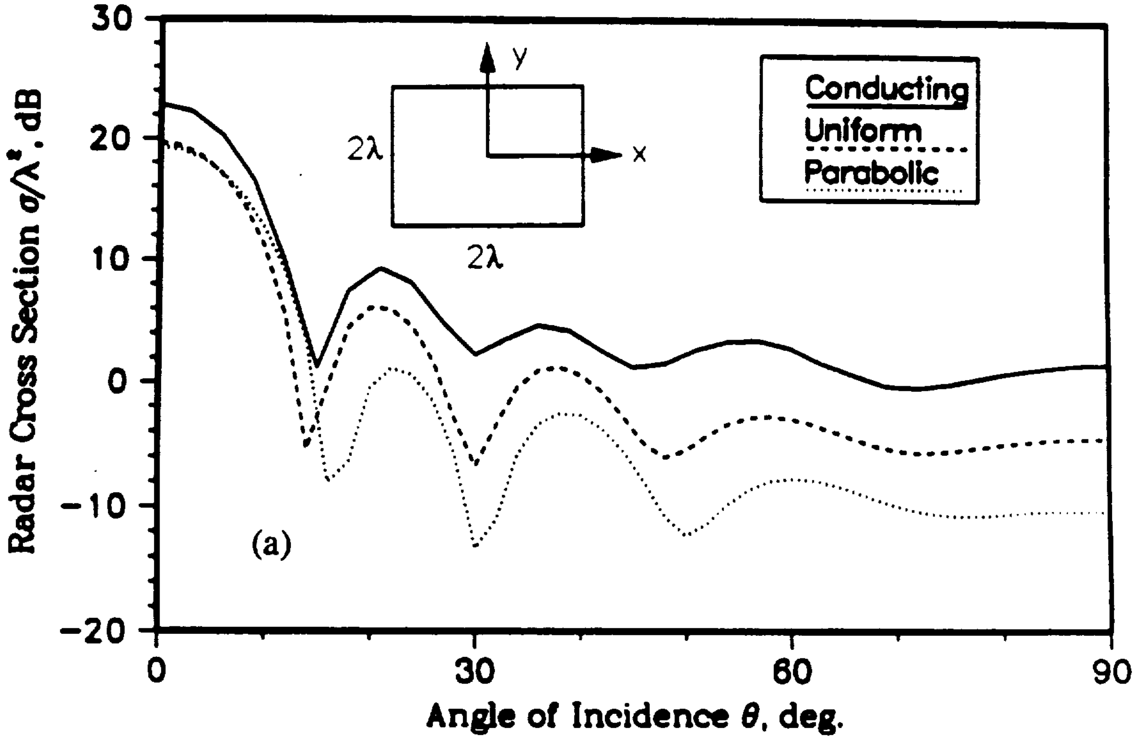

Figure 4.9: E-polarization scattering from a square $2\lambda \times 2\lambda$ plate with and without resistive taper. (a) Backscatter RCS patterns for conducting plate (—), uniformly tapered plate $Z_s = Z_o/4$ (- - -), and parabolically tapered plate (· · ·). (b) Three-dimensional view of the parabolic resistive taper for the plate ($Z_{s_{min}} = 0$).

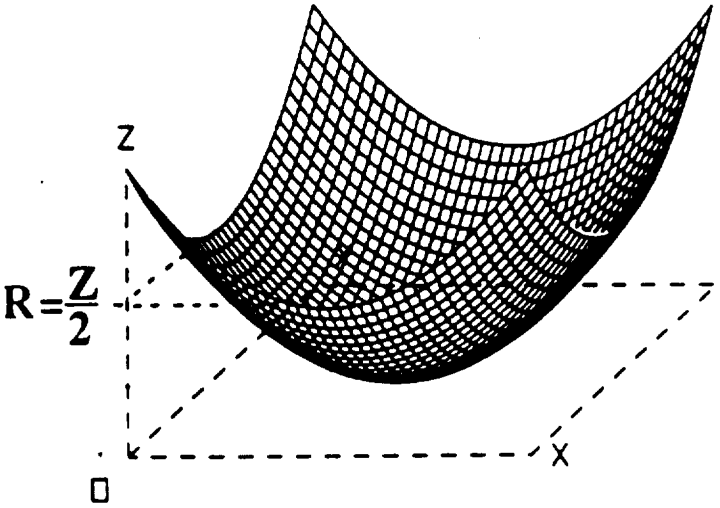

(b)

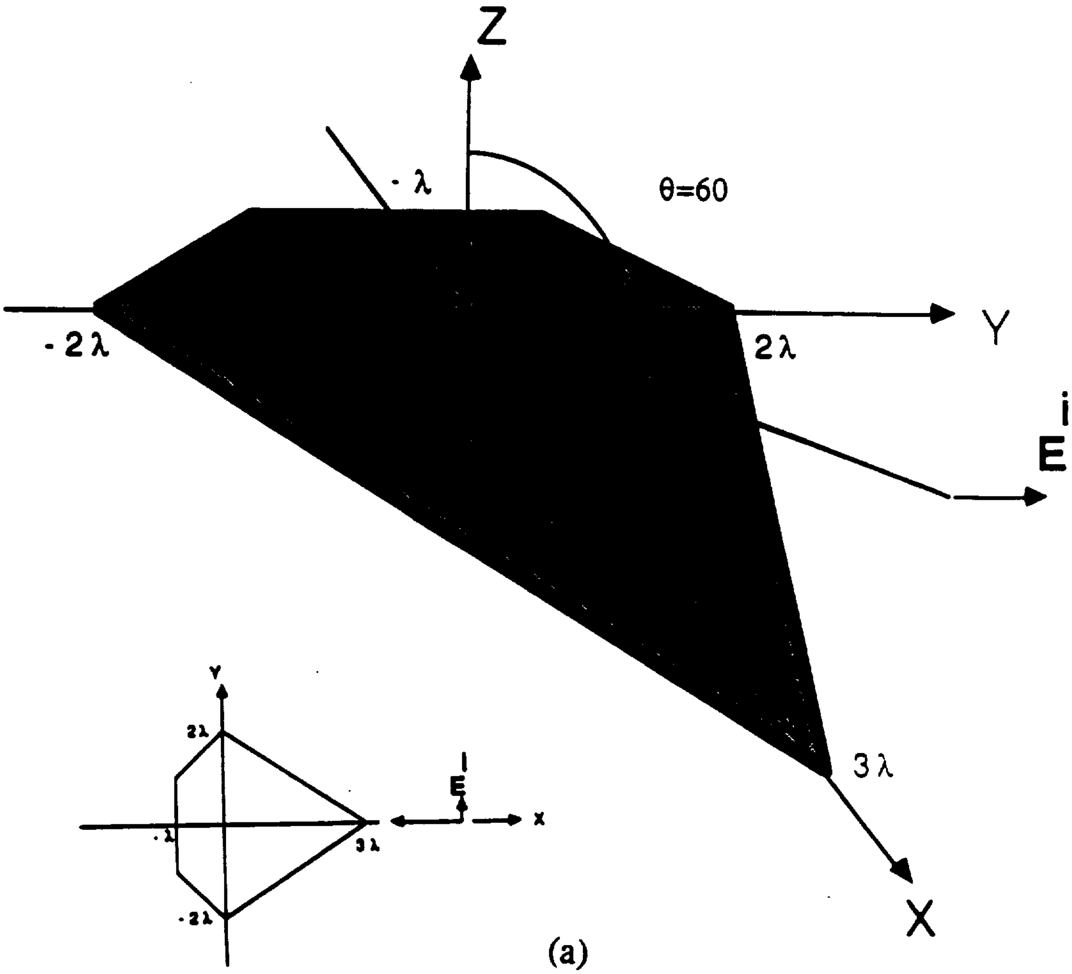

Figure 4.10: E-polarization scattering from an irregular conducting plate with and without resistive taper. Incidence angles: $\theta_o = 60°, \phi_o = 0°$; Sampling density = $225/\lambda^2$. (a) Geometry. (b) Bistatic scattering patterns with (- - -) and without (—) resistive taper. (c) Three-dimensional view of the parabolic resistive taper for the plate.

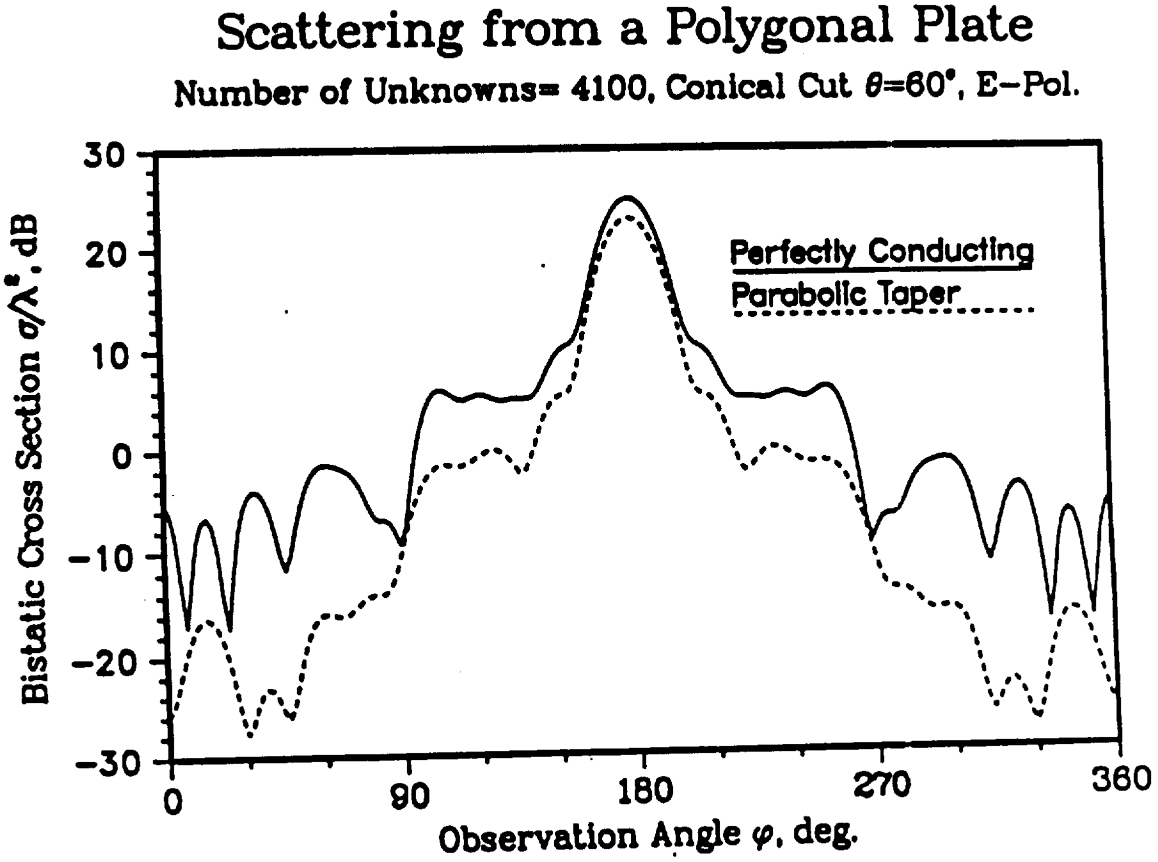
Scattering from a Polygonal Plate
Number of Unknowns= 4100, Conical Cut θ=60°, E-Pol.
Bistatic Cross Section σ/λ², dB
30
20
10
0
−10
−20
−30
0
90
180
270
360
Observation Angle φ, deg.
Perfectly Conducting
Parabolic Taper

(b)

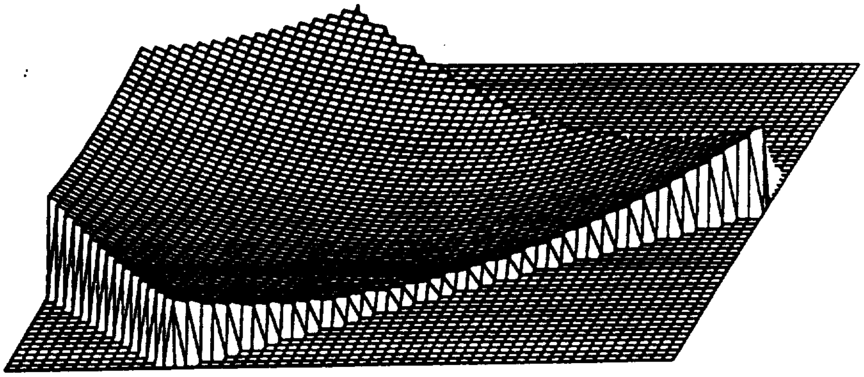

(c)

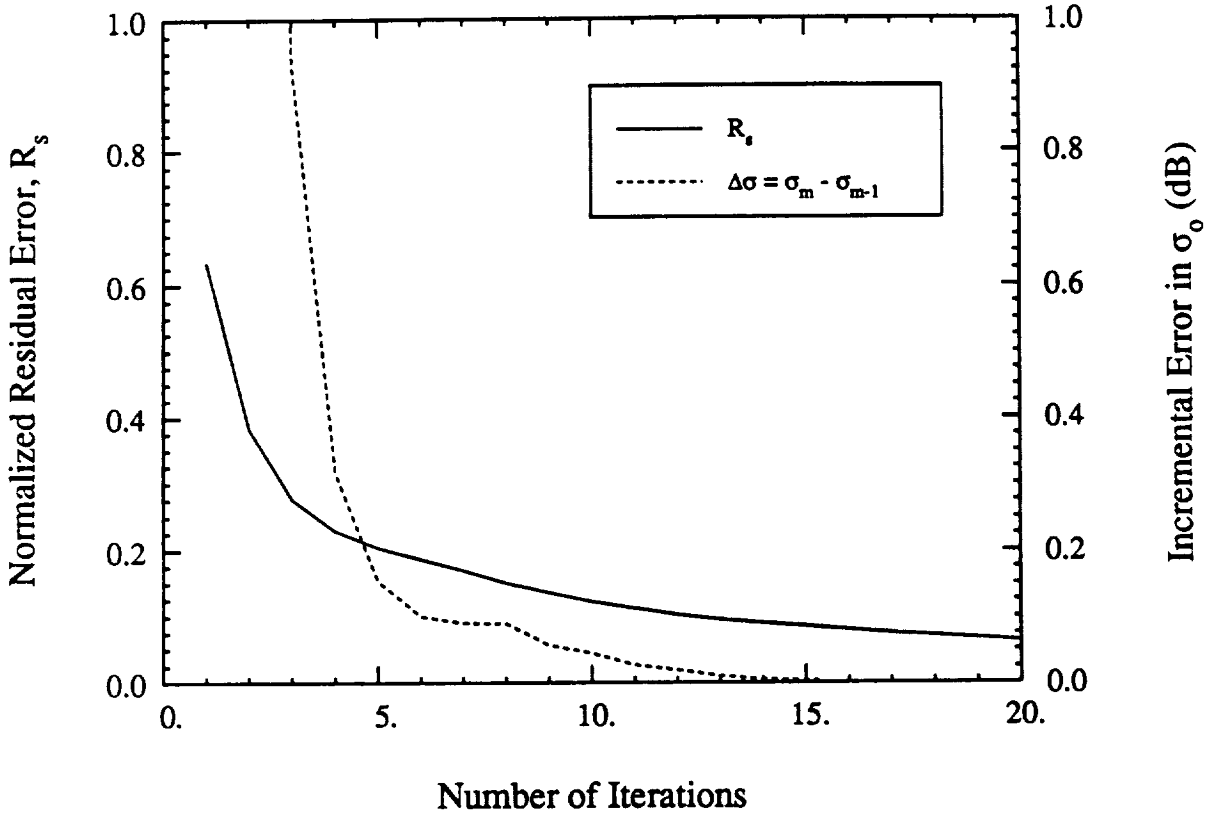

Figure 4.11: Convergence rate of the CGDFT solution for a square 2λ × 2λ conducting plate at normal incidence.

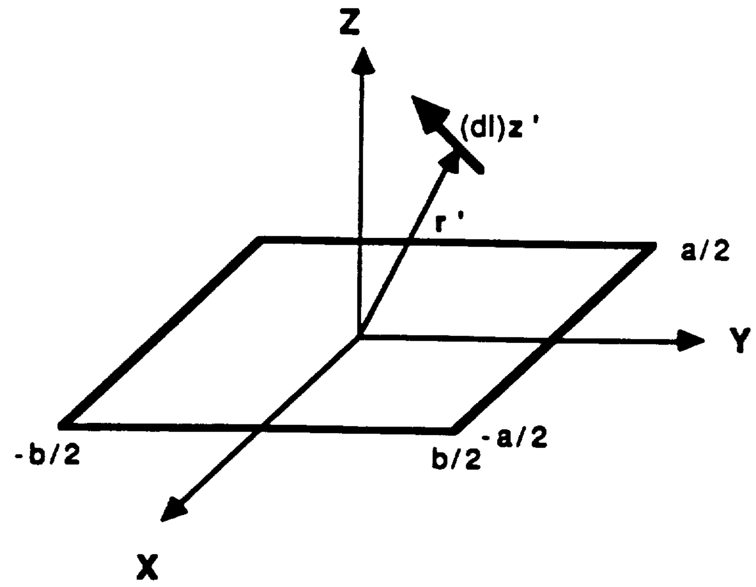

Figure 4.12: Geometry of an arbitrarily oriented Hertzian dipole in the vicinity of a plate.

4.2.4 Radiation of a Dipole in the Presence of a Plate

In this section, we consider the problem of radiation by a Hertzian dipole in the presence of a resistive plate, illustrated in Figure 4.12. The dipole is centered at (x_1, y_1, z_1), is of length $\ell \ll \lambda$ and carries a constant excitation current equal to unity. Its presence excites currents on the resistive plate which contribute to the overall radiation pattern. To compute the plate currents we must solve either (4.12) or (4.18) with the incident field given as

$$E_x^i = (E_{r'}\hat{r}' + E_{\theta'}\hat{\theta}') \cdot \hat{x} \tag{4.42}$$

$$E_y^i = (E_{r'}\hat{r}' + E_{\theta'}\hat{\theta}') \cdot \hat{y} \tag{4.43}$$

where the primes indicate spherical system parameters measured with respect to the coordinate system at the dipole as shown in Figure 4.12. We have

$$E_{r'} = 2 Z_o k_o \ell \left(1 + \frac{1}{j k_o r'}\right) \frac{e^{-jk_o r'}}{4\pi k_o r'^2} (\hat{z}' \cdot \hat{r}') \tag{4.44}$$

$$E_{\theta'} = j Z_o k_o \ell \left[1 + \frac{1}{j k_o r'} - \frac{1}{(k_o r')^2}\right] \frac{e^{-jk_o r'}}{4\pi r'} \sqrt{1 - (\hat{z}' \cdot \hat{r}')^2} \tag{4.45}$$

in which $\hat{z}'$ denotes the dipole orientation and can be represented as

$$\hat{z}' = \cos\phi_r \sin\theta_r \hat{x} + \sin\phi_r \sin\phi_r \hat{y} + \cos\theta_r \hat{z} \tag{4.46}$$

where (θ_r, ϕ_r) are the spherical angles of the dipole axis with respect to the plate's coordinate system. Also, $\mathbf{r}' = r'\hat{r}'$ is the vector drawn from the dipole's location to the observation point on the plate and

$$\hat{\theta}' = \frac{\hat{z}' \times \hat{r}'}{|\hat{z}' \times \hat{r}'|} \times \hat{r}' \tag{4.47}$$

Numerical results based on a solution of (4.12) are given in Figures 4.13 through 4.18. An FFT pad of order $\varrho = 2$ and piecewise sinusoidal basis functions were used to generate these results. In particular, Figure 4.13 illustrates the current components on a perfectly conducting and a resistive $1\lambda \times 1\lambda$ rectangular plate due to illumination by a vertical electric dipole positioned at a distance $\lambda/4$ above the center of the plate. Figure 4.14 shows the spectrum (the magnitude of the Fourier transform) of the x-component of the current density. The principal plane radiation patterns of the dipole are shown in Figure 4.15. As seen, the pattern computed with the CGFT is in good agreement with that based on the MoM. The corresponding results for a horizontally oriented dipole above the same plate are given in Figures 4.16 through 4.17.

Finally, the improvement obtained in the convergence rate of the CGFT technique when using piecewise sinusoidal (PWS) surface expansion functions is illustrated in Figure 4.18. As before, an estimated 100 percent improvement in the convergence rate was observed when the PWS basis functions were employed.

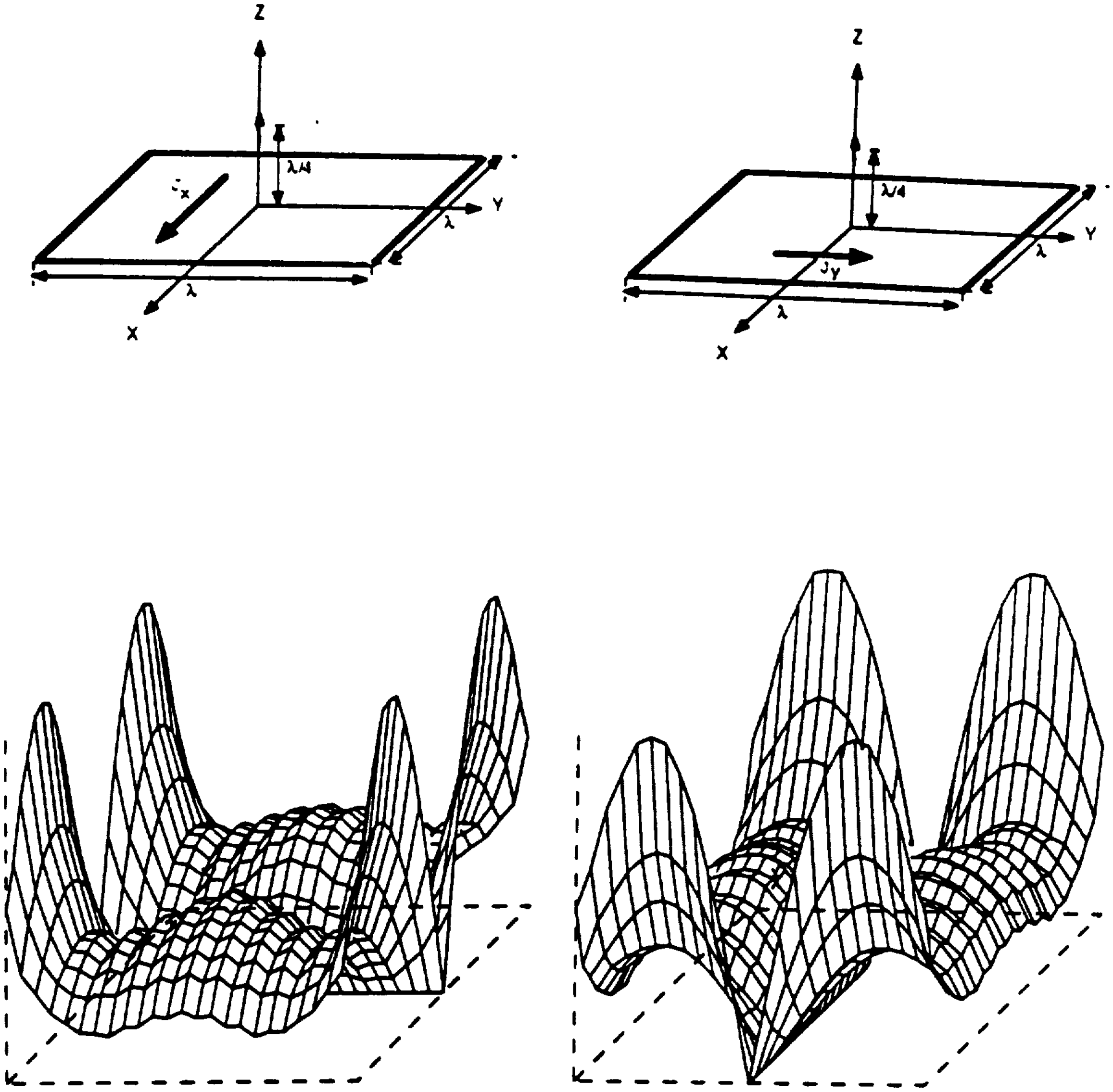

Figure 4.13: The excited surface current density on a $1\lambda \times 1\lambda$ conducting plate irradiated by a vertical Hertzian dipole positioned a distance $\lambda/4$ above the center of the plate; 25×25 unknowns and FFT pad of order $= 2$. (a) X-component. (b) Y-component.

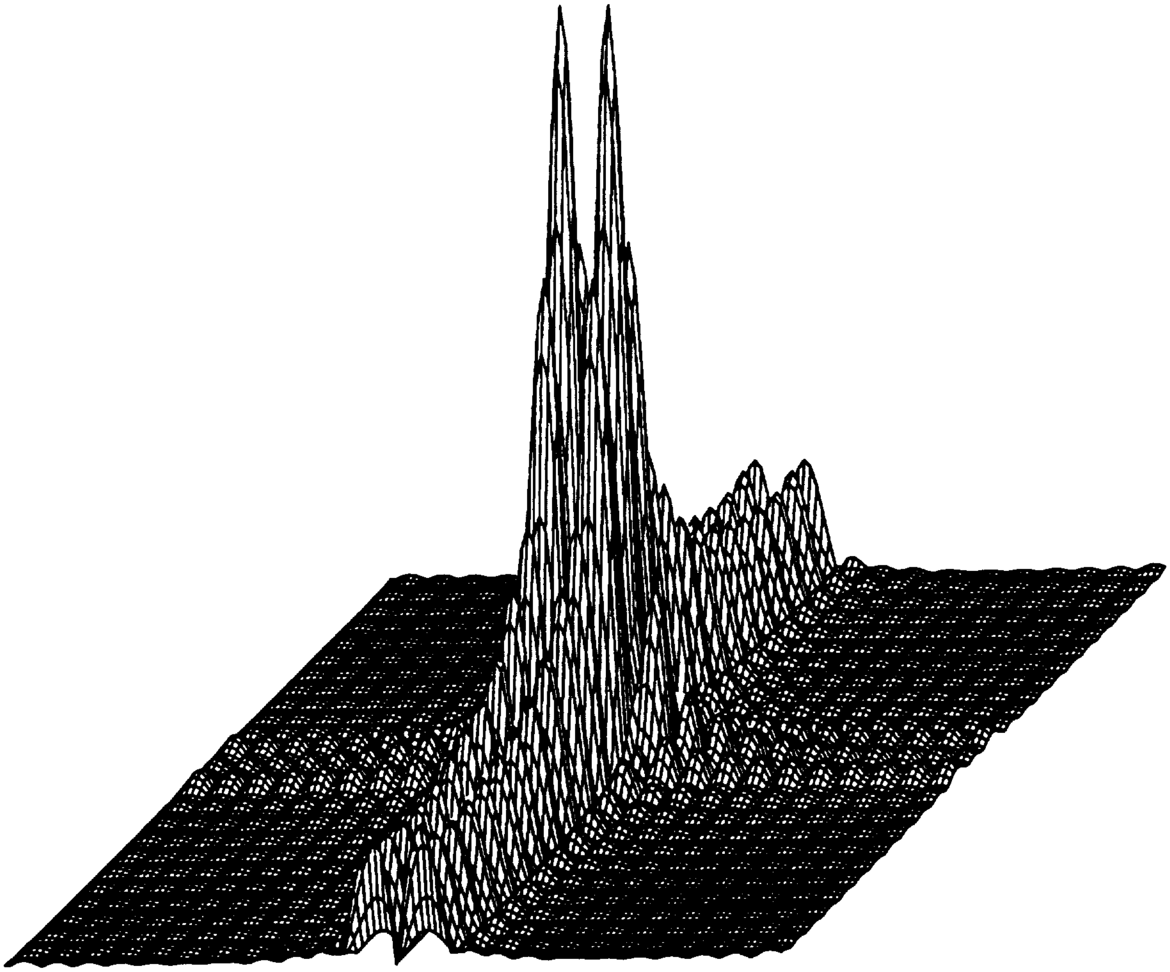

Figure 4.14: The spectrum of the surface current density (x-component) on a $1\lambda \times 1\lambda$ plate irradiated by a vertical Hertzian dipole positioned a distance $\lambda/4$ above the center of the plate (25×25 unknowns and FFT pad of order $\varrho = 2$).

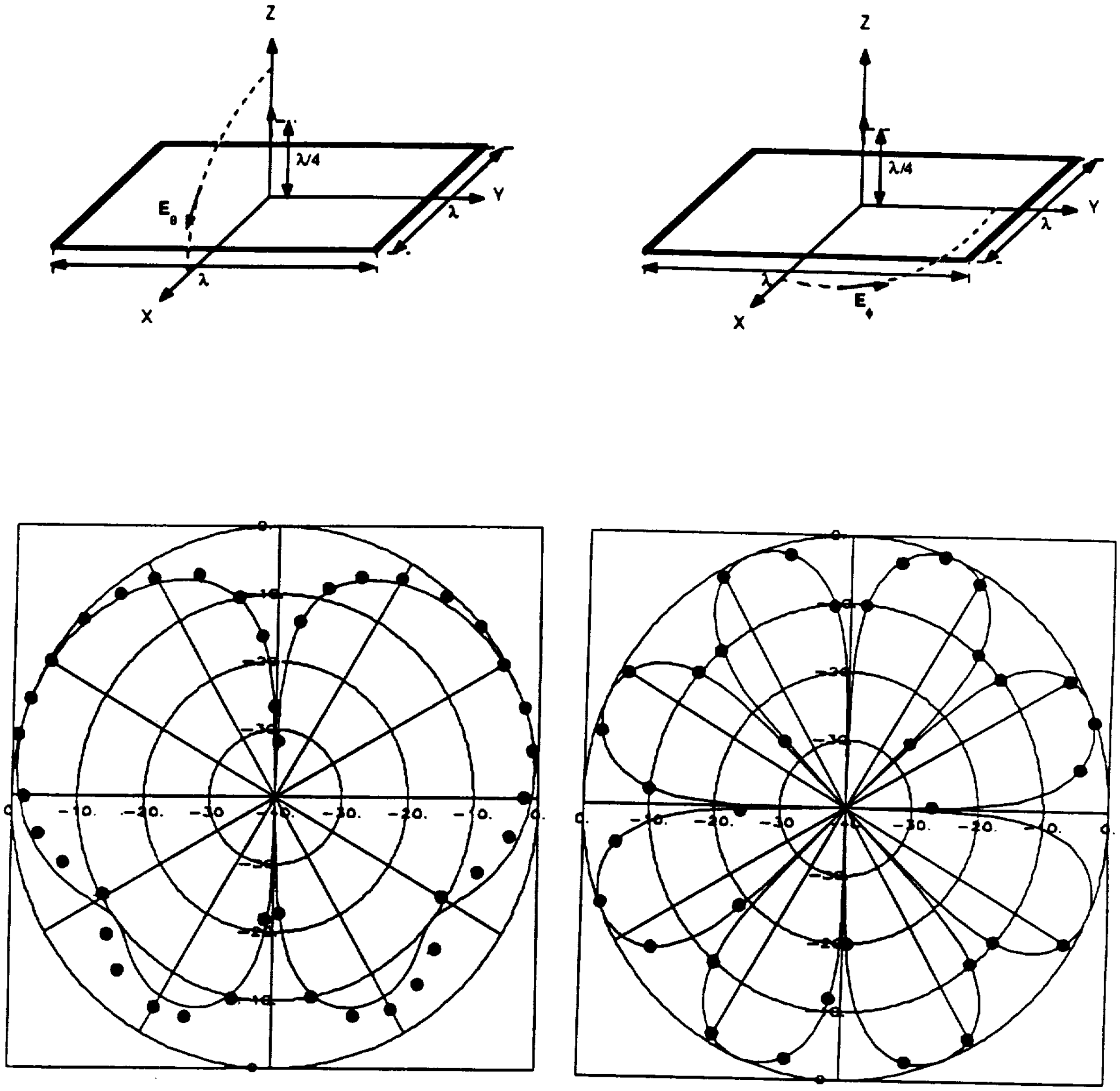

(a)

(b)

Figure 4.15: The principal plane radiation patterns of a Hertzian dipole vertically positioned at a distance $\lambda/4$ above a $1\lambda \times 1\lambda$ conducting plate computed by the MoM (—), and CGFT (• • •) using sinusoidal basis functions. (a) E_θ pattern. (b) E_ϕ pattern.

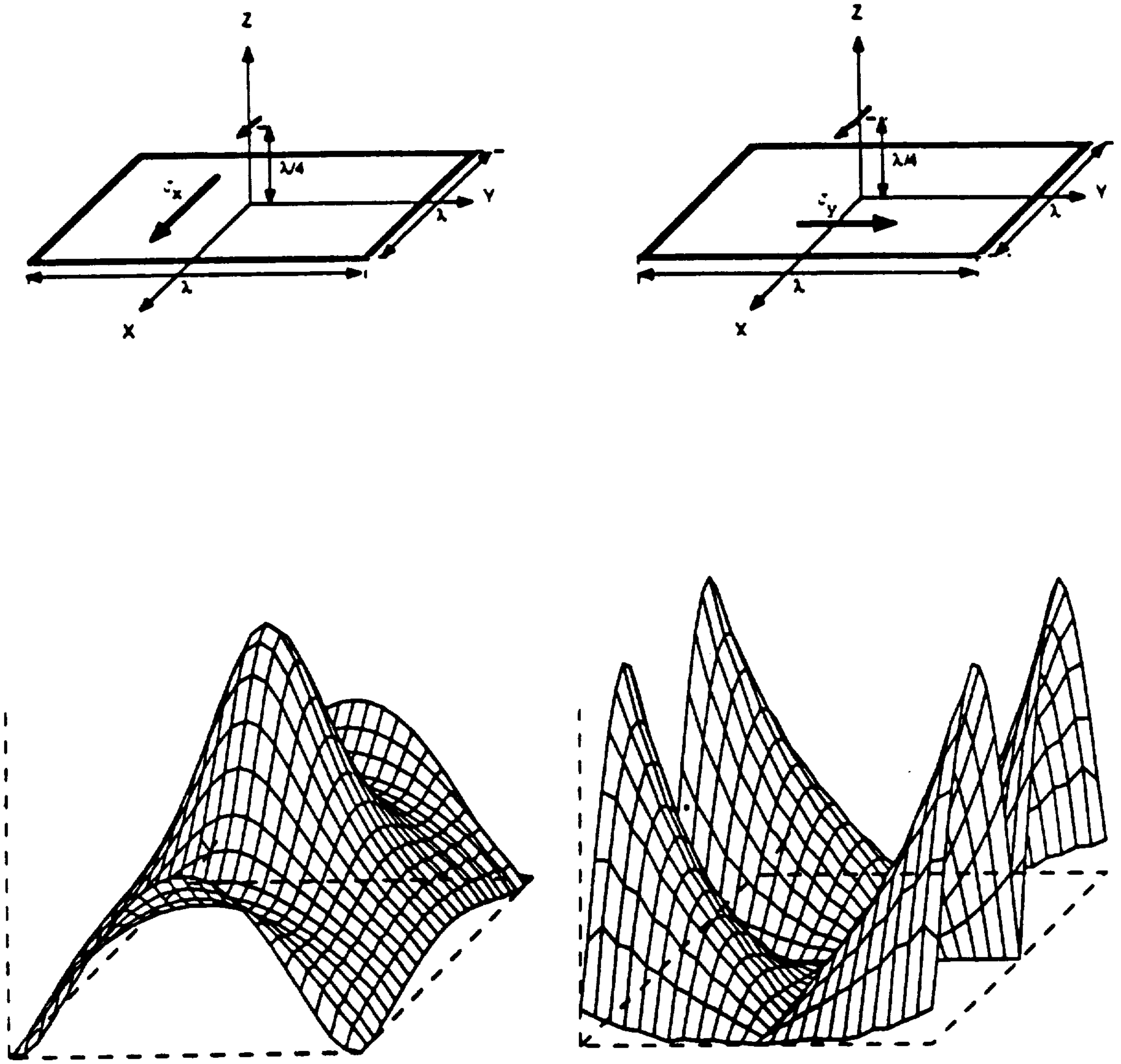

(a) (b)

Figure 4.16: The excited surface current density on a $1\lambda \times 1\lambda$ conducting plate irradiated by a horizontal Hertzian dipole positioned a distance $\lambda/4$ above the center of the plate; 25×25 unknowns and FFT pad of order $\varrho = 2$. (a) Co-polarized component. (b) Cross-polarized component.

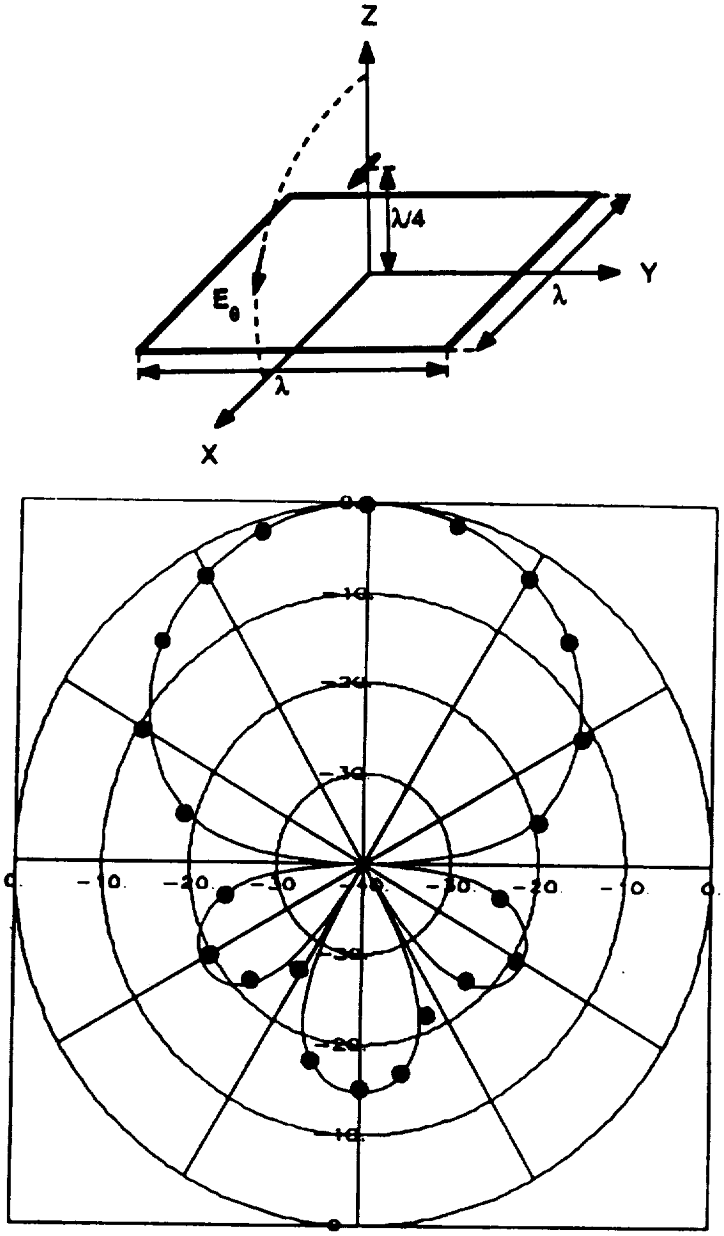

Figure 4.17: The principle plane radiation pattern (E_θ) of a Hertzian dipole horizontally positioned at a distance $\lambda/4$ above a $1\lambda \times 1\lambda$ conducting plate computed by the MoM (—), and CGFT (• • •) using sinusoidal basis functions.

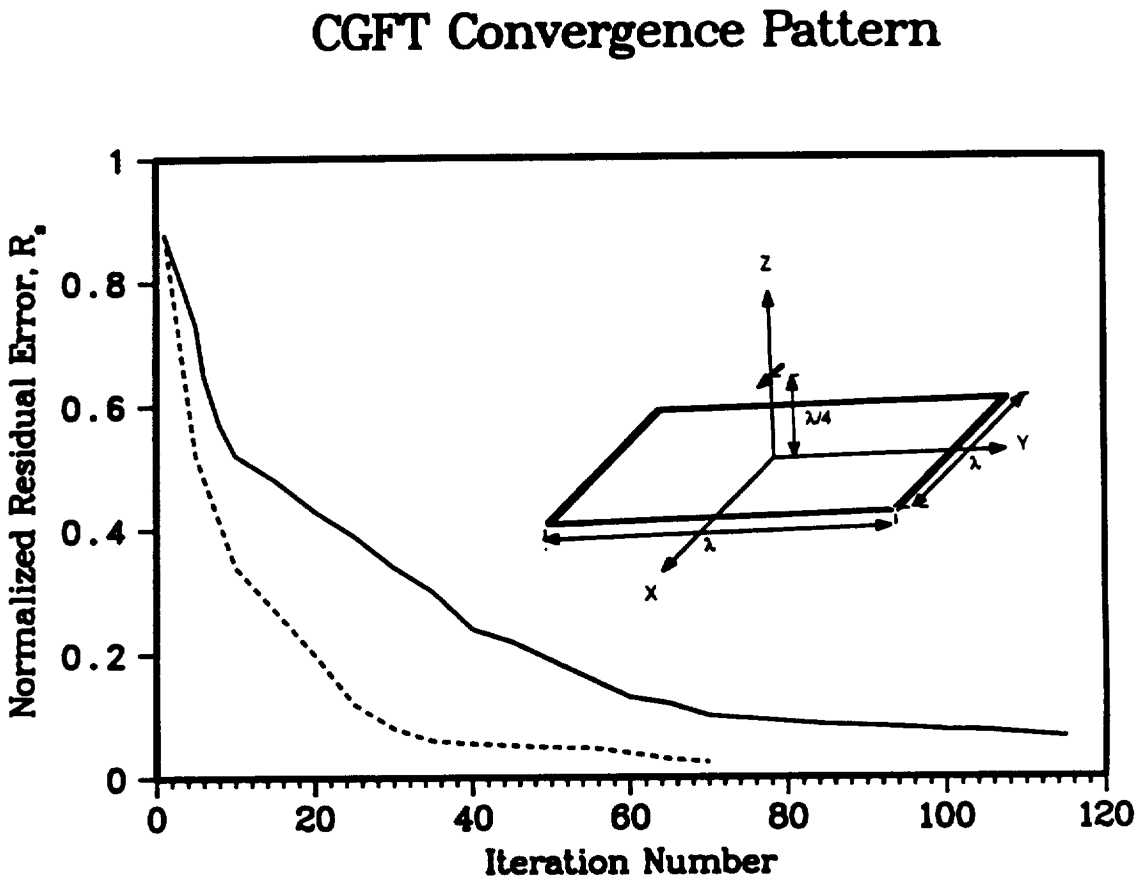

Figure 4.18: Improvement in the convergence rate of the CGFT solution for the problem of a hertzian dipole positioned above a conducting plate: Sinusoidal basis functions (···), conventional FFT (delta basis) (—); 25 × 25 unknowns and FFT pad of order $\varrho = 2$.

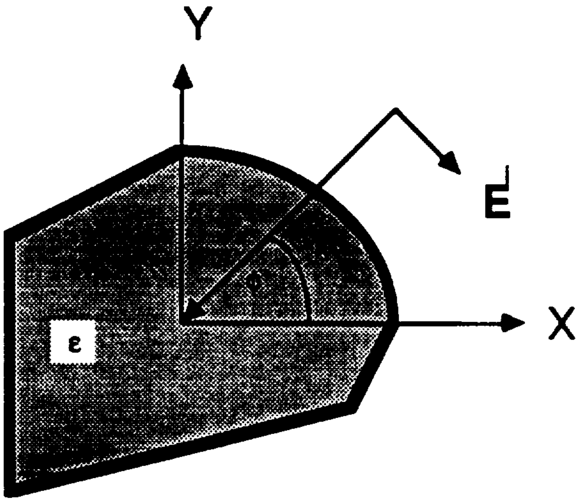

Figure 4.19: Geometry for a dielectric cylinder illuminated by a plane wave.

4.3 Scattering by Dielectric Cylinders

We now turn our attention to the problem of scattering by an inhomogeneous isotropic dielectric cylinder of relative permittivity ϵ_r, as shown in Figure 4.19. The cylinder axis coincides with the z-axis and is infinite in extent in this direction. It is illuminated by a plane wave given by (4.28) incident at an angle $\theta = \pi/2$

$$\mathbf{E}^{\mathrm{i}} = \mathbf{E}_o e^{jk_o(x\cos\phi_o + y\sin\phi_o)} \tag{4.48}$$

where

$$\mathbf{E}_o = E_o[\sin\alpha(-\hat{x}\sin\phi_o + \hat{y}\sin\phi_o) - \hat{z}\cos\alpha\cos\phi_o]$$

To solve for the scattered field, we Introduce the equivalent polarization current density (see (3.23))

$$\mathbf{J} = \frac{jk_o}{Z_o}(\epsilon_r - 1)\mathbf{E}^{\mathbf{T}}, \tag{4.49}$$

within the cylinder, where $\mathbf{E}^T$ is the total field given by

$$\mathbf{E}^T = \mathbf{E}^{\mathrm{i}} + \mathbf{E}^{\mathrm{s}} = Z_c\mathbf{J}, \tag{4.50}$$

in which

$$Z_c = \frac{Z_o}{jk_o(\epsilon_r - 1)} \tag{4.51}$$

The governing system of integral equations is now obtained by substituting for the scattered field in (4.50). For an arbitrary polarization of incidence we have

$$\mathbf{E}^{\mathbf{i}}(\boldsymbol{\rho}) = Z_c(\boldsymbol{\rho})\mathbf{J}(\boldsymbol{\rho}) + jk_oZ_o\int_{s'}\mathbf{J}(\boldsymbol{\rho}')\cdot\bar{\mathbf{\Gamma}}(\boldsymbol{\rho};\boldsymbol{\rho}')ds' \tag{4.52}$$

where Γ is now given by

$$\bar{\mathbf{\Gamma}} = \begin{pmatrix} (1+\frac{1}{k^2}\frac{\partial^2}{\partial x^2}) & \frac{1}{k^2}\frac{\partial^2}{\partial x\partial y} & 0 \\ \frac{1}{k^2}\frac{\partial^2}{\partial y\partial x} & (1+\frac{1}{k^2}\frac{\partial^2}{\partial y^2}) & 0 \\ 0 & 0 & 1 \end{pmatrix} G_c(\boldsymbol{\rho};\boldsymbol{\rho}') \tag{4.53}$$

and

$$G_c(\boldsymbol{\rho};\boldsymbol{\rho}') = \frac{1}{4j}H_o^{(2)}(k_o|\boldsymbol{\rho}-\boldsymbol{\rho}'|) \tag{4.54}$$

Following the same procedure discussed earlier in connection with the plate problem, we may write

$$\mathbf{J}(x,y) = \sum_{m=0}^{M-1}\sum_{n=0}^{N-1}\mathbf{J}_{mn}\cdot\bar{\mathbf{\Phi}}_{\mathbf{mn}}(x,y) \tag{4.55}$$

where

$$\bar{\mathbf{\Phi}}_{\mathbf{mn}}(x,y) = \bar{\mathbf{\Phi}}(x-x_m, y-y_n) \tag{4.56}$$

$$\bar{\mathbf{\Phi}}(x,y) = \hat{x}\hat{x}\phi_x(x,y) + \hat{y}\hat{y}\phi_y(x,y) + \hat{z}\hat{z}\phi_z(x,y) \tag{4.57}$$

and ϕ_ℓ denotes the expansion function in the ℓ-direction.

The two-dimensional continuous Fourier transform of G_c is given by (Appendix B)

$$\tilde{G}_c(k_x,k_y) = \frac{1}{k_x^2+k_y^2-k_o^2} \tag{4.58}$$

However, as noted earlier, the use of (4.58) in the CGFFT solution of (4.52) will result in aliasing errors. An additional difficulty will also arise because of the ring singularity of (4.58) occuring when $k_x^2 + k_y^2 = k_o^2$. The inherent approximation in the implementation of the inverse FFT that the transform be constant over each cell is obviously not valid for those cells coinciding with the ring singularity. This can cause substantial errors and often leads to the failure of the discrete system as an acceptable representation of the continuous one.

To correct both of the above sources of error, the procedure described earlier can be employed here as well. That is, the original continuous integrals are first discretized before proceeding with their evaluation via the discrete Fourier transform.

The new discrete system of equations is expressed as

$$\mathbf{E^i}_{ij} = \mathbf{Z}_{cij}\mathbf{J}_{ij} + \frac{k_o Z_o}{4} \sum_{mn} \bar{\mathbf{\Lambda}}_{ij} \cdot \mathbf{J}_{mn}, \tag{4.59}$$

where

$$\bar{\mathbf{\Lambda}} = \begin{pmatrix} \zeta^{xx} & \zeta^{xy} & 0 \\ \zeta^{yx} & \zeta^{yy} & 0 \\ 0 & 0 & \zeta^{zz} \end{pmatrix} \tag{4.60}$$

which should be compared with (4.15) and (4.16). Similarly, the non-trivial entries of Λ are now given by

$$\begin{aligned}
\zeta_{ij}^{xx} &= \left(1 + \frac{1}{k_o^2}\frac{\partial^2}{\partial y^2}\right) \int_{\sigma_{mn}} H_0^{(2)}(x,y;x',y')\phi_x(x'-x_m, y'-y_n)ds' \\
\zeta_{ij}^{xy} &= \frac{1}{k_o^2}\frac{\partial^2}{\partial x \partial y} \int_{\sigma_{mn}} H_0^{(2)}(x,y;x',y')\phi_y(x'-x_m, y'-y_n)ds' \\
\zeta_{ij}^{yx} &= \frac{1}{k_o^2}\frac{\partial^2}{\partial x \partial y} \int_{\sigma_{mn}} H_0^{(2)}(x,y;x',y')\phi_x(x'-x_m, y'-y_n)ds' \\
\zeta_{ij}^{yy} &= \left(1 + \frac{1}{k_o^2}\frac{\partial^2}{\partial x^2}\right) \int_{\sigma_{mn}} H_0^{(2)}(x,y;x',y')\phi_y(x'-x_m, y'-y_n)ds' \\
\zeta_{ij}^{zz} &= \int_{\sigma_{mn}} H_0^{(2)}G(x,y;x',y')\phi_z(x'-x_m, y'-y_n)ds'
\end{aligned} \tag{4.61}$$

which may be considered as the 'cylindrical counterparts' to (4.17) since σ_{mn} here denotes the incremental surface element corresponding to the mnth cylindrical cell on the target. Again, these expressions are evaluated at $(x, y) = (x_i, y_j)$. Applying the convolution theorem to (4.59) yields the final form of the system of equations

$$\mathbf{E}_{ij} = Z_{cij}\mathbf{J}_{ij} + \frac{k_o Z_o}{4}\,\mathrm{DFT}^{-1}\{\hat{\bar{\boldsymbol{\Lambda}}} \cdot \hat{\mathbf{J}}\} \tag{4.62}$$

where

$$\hat{\bar{\boldsymbol{\Lambda}}} = \frac{1}{k_o^2} \begin{pmatrix} k_o^2 - D_x^2 & -D_x D_y & 0 \\ -D_y D_x & k_o^2 - D_y^2 & 0 \\ 0 & 0 & 1 \end{pmatrix} \hat{\zeta} \tag{4.63}$$

and D_x and D_y are given by (4.21)-(4.22). In the above, $\hat{\zeta}$ is the discrete Fourier transform of the sequence

$$\zeta_{mn} = \int_{\sigma_{mn}} H_0^{(2)}(k_o\sqrt{x^2 + y^2})ds \tag{4.64}$$

This integral can be evaluated numerically except when $(m = n)$ which corresponds to the self-cell term. When $(m = n)$ we must resort to an analytical evaluation similar to (4.26) as [36]:

$$\zeta_{00} \simeq \frac{1}{2k}[\pi k r_0 H_1^{(2)}(k r_0) - 2j] \tag{4.65}$$

with r_0 as given in (4.27).

To illustrate the accuracy of the above formulation, the bistatic scattering from an infinitely long triangular cylinder is shown in Figure 4.20. The cylinder is perfectly conducting and as seen, our result agrees very well with a corresponding direct solution provided in [53].

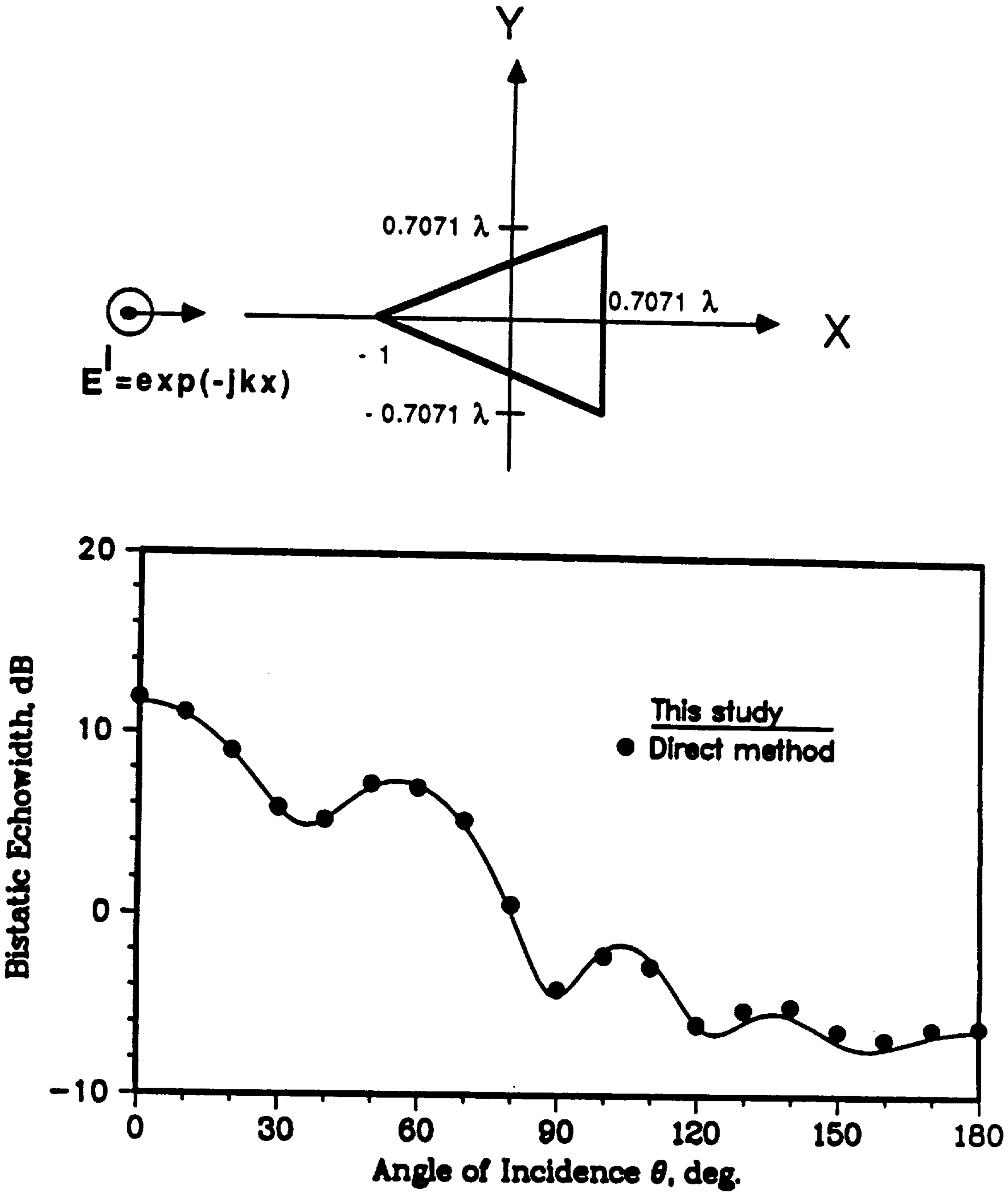

Figure 4.20: Scattering from a conducting triangular cylinder illuminated by an E-polarized plane wave. (a) Geometry. (b) Comparison of bistatic echo widths obtained from the CGDFT method (—) and the direct method (• • •) [53].

4.4 Summary

Two formulations for a conjugate gradient solution of the scattering by plates of arbitrary shapes were presented. One of the formulations (CGFT) employed the sampled (truncated) continuous transform of the Green's function for the evaluation of the convolution integrals. The other (CGDFT) employed finite duration discrete Fourier transforms for the evaluation of the same integrals. As with the strip problem studied in the previous chapter, the latter method was found to provide an accurate simulation of the plate scattering by eliminating aliasing errors (other than those due to under-sampling). It was also found to be substantially more efficient than the former method. Furthermore, it was noted that the convergence of the solution is substantially faster for plates of non-zero resistivity and this is attributed to the less singular behavior of the edge currents.

The CGDFT method was also applied to the problem of scattering by dielectric and conducting cylinders of arbitrary cross sections and a degree of accuracy and efficiency similar to the plate problem was observed.

CHAPTER V

GENERALIZED IMPEDANCE BOUNDARY CONDITIONS

5.1 Introduction

Generalized Impedance Boundary Conditions (GIBC) are higher order boundary conditions which involve derivatives of the fields beyond the first. They have been found to be more effective than the traditional first order (standard) conditions (SIBC) in modeling thick dielectric coatings and layers. The GIBCs offer several advantages in both asymptotic and numerical analysis of electromagnetic problems. For example, in the case of high frequency analysis, they allow an accurate replacement of a coating on a layer with a sheet boundary condition amenable to a Wiener-Hopf analysis [14, 54], or some function theoretic approach [55]. In numerical analysis, the profile of a coating can be replaced by a simple boundary condition on the surface of the coating. This eliminates the need for introducing unknown polarization currents within the volume of the coating or material layer, thus leading to a more efficient solution from the numerical standpoint.

A convenient form of these conditions is expressed in terms of the normal derivatives of the field components

$$\sum_{m=0}^{M} \frac{a_m}{(-jk_o)^m} \frac{\partial^m E_n}{\partial n^m} = 0$$

$$\sum_{m=0}^{M} \frac{a'_m}{(-jk_o)^m} \frac{\partial^m H_n}{\partial n^m} = 0 \tag{5.1}$$

where the subscript n denotes the normal component to the surface and a_m and a'_m are constants specific to the material and geometrical properties of the structure. These constants are chosen so that the application of the boundary conditions will reproduce the desired scattering behavior of the surface or coating layer under consideration. They can be derived by employing a suitable expansion of the coating's Fresnel reflection coefficient and by matching the constants of the expansion to those of the compatible conditions implied by the GIBC (5.1). Since for a given problem, the electric and magnetic fields may not be specified independently, the coefficients a_m and a'_m are related by the relation [13]

$$\left(\sum_{m=0,2,\cdots} a_m\right)\left(\sum_{m=0,2,\cdots} a'_m\right) = \left(\sum_{m=1,3,\cdots} a_m\right)\left(\sum_{m=1,3,\cdots} a'_m\right) \tag{5.2}$$

which is a form of duality condition. The integer M in (5.1) is the order of the conditions. For example, when $M = M' = 1$, we have a first order condition

$$E_n - \frac{1}{jk_o\eta}\frac{\partial E_n}{\partial n} = 0 \quad , \quad H_n - \frac{\eta}{jk_o}\frac{\partial H_n}{\partial n} = 0 \tag{5.3}$$

The above first order condition can be shown to be equivalent to the standard impedance boundary condition (SIBC), also known as the Leontovich boundary condition [56]-[58], provided $\eta = a_o/a_1 = a'_1/a'_o$ is identified as the normalized surface impedance of the sheet. The SIBC is often used for simulating material coating on conducting bodies and in this case the normalized surface impedance η is given by

$$\eta = \frac{a_0}{a_1} = j\frac{\aleph}{\epsilon_r}\tan(\aleph k_o t) \tag{5.4}$$

where t is the coating thickness and $\aleph = \sqrt{\epsilon_r \mu_r}$ is the index of refraction. The validity of this SIBC has been examined by several authors [57], [59]-[61] and in general it holds when

$$|\aleph| \gg 1 \tag{5.5}$$

and

$$|\Im\mathrm{m}\aleph| k_o t \gg 1 \tag{5.6}$$

The first condition ensures that within the medium, the field behaves essentially as a plane wave propagating in the direction of the inward normal to the coating. The second condition, on the other hand, imposes the requirement that the inward traveling field suffers enough attenuation so that no outward traveling waves exit at the interface due to reflection. Also, for inhomogeneous materials, the SIBC remains valid if the lateral variations of the impedance in the medium are slow, that is

$$\left|\frac{1}{k\eta}\nabla\eta\right| \ll 1 \tag{5.7}$$

where ∇ denotes gradient in coordinates transverse to the normal.

Inherently, the SIBC does not permit modeling of polarization currents which are normal to the layer and is thus most suited for near normal incidences. However, by increasing the order of the condition, it is possible to allow accurate simulations of fairly thick layers and unlike the SIBC, the accuracy of the higher order conditions improves as the incidence angle approaches grazing.

A third order GIBC derived recently [62] for the simulation of high contrast dielectric coatings is given by (5.1) with $M = 3$ and

$$a_0 = \left(\aleph - \frac{1}{2\aleph}\right)\left[\tan(\aleph k_o t) - \tan\left(\frac{k_o t}{2\aleph}\right)\right]$$

$$
\begin{aligned}
a_1 &= -j\epsilon_r\left[1+\tan(\aleph k_ot)\tan\left(\frac{k_ot}{2\aleph}\right)\right] \\
a_2 &= \frac{1}{2\aleph}\left\{\tan(\aleph k_ot)-\tan\left(\frac{k_ot}{2\aleph}\right)+k_ot\left(\aleph-\frac{1}{2\aleph}\right)\right. \\
&\qquad \left.\cdot\left[1+\tan(\aleph k_ot)\tan\left(\frac{k_ot}{2\aleph}\right)\right]\right\} \qquad (5.8) \\
a_3 &= \frac{jk_ot\epsilon_r}{2\aleph}\left[\tan(\aleph k_ot)-\tan\left(\frac{k_ot}{2\aleph}\right)\right]
\end{aligned}
$$

and

$$
\begin{aligned}
a_0' &= \left(\aleph-\frac{1}{2\aleph}\right)\left[1+\tan(\aleph k_ot)\tan\left(\frac{k_ot}{2\aleph}\right)\right] \\
a_1' &= j\mu_r\left[\tan(\aleph k_ot)-\tan\left(\frac{k_ot}{2\aleph}\right)\right] \\
a_2' &= \frac{1}{2\aleph}\left\{1+\tan(\aleph k_ot)\tan\left(\frac{k_ot}{2\aleph}\right)-k_ot\left(\aleph-\frac{1}{2\aleph}\right)\right. \\
&\qquad \left.\cdot\left[\tan(\aleph k_ot)-\tan\left(\frac{k_ot}{2\aleph}\right)\right]\right\} \qquad (5.9) \\
a_3' &= \frac{jk_ot\mu_r}{2\aleph}\left[1+\tan(\aleph k_ot)\tan\left(\frac{k_ot}{2\aleph}\right)\right]
\end{aligned}
$$

The GIBCs are usually applied at the top layer of the surface under study. However, in some applications it is desirable to apply the conditions at another plane of reference. This is convenient for a coating on a ground plane where one may be interested in invoking the image theory. In such cases the original coefficients a_m must be replaced by (Appendix C)

$$
A_m = \sum_{n=0}^{m}\frac{(-jk_ot)^n}{n!}a_{m-n} \quad , \qquad m = 0,\ldots,M \qquad (5.10)
$$

where t denotes the transfer distance.

5.2 Two-dimensional Impedance Inserts

In the two-dimensional case, the impedance insert is assumed to be infinite in length with no field variations along the z-direction ($\frac{\partial}{\partial z} = 0$). The insert is assumed to satisfy a generalized impedance boundary condition at its surface. This may serve as a model of a partially coated conducting plane or a material filled groove whose scattering behavior under plane wave illumination is of interest (Figure 5.1).

Introducing the equivalent magnetic current density over the insert we have

$$\mathbf{M} = \mathbf{E} \times \hat{n} \quad : \quad \begin{cases} M_z = E_x \\ M_x = -E_z \end{cases} \tag{5.11}$$

and by imposing the continuity of the tangential field components an integral equation for the current density can be obtained and solved numerically.

In the following, we will derive integral equations for the equivalent current density based on a third order generalized boundary condition ($M = 3$). The two principal polarizations are treated separately.

5.2.1 H-Polarization

The incident fields are assumed to be of the form

$$\mathbf{H}^i = \hat{z}\, e^{jk_o(x\cos\phi_o + y\sin\phi_o)} \tag{5.12}$$

$$\mathbf{E}^i = Z_o(\hat{x}\sin\phi_o - \hat{y}\cos\phi_o)\, e^{jk_o(x\cos\phi_o + y\sin\phi_o)} \tag{5.13}$$

and the first of the conditions (5.1) is relevant in this case. For a third order condition we write

$$\sum_{m=0}^{3} \frac{a_m}{(-jk_o)^m} \frac{\partial^m E_y}{\partial y^m} = 0$$

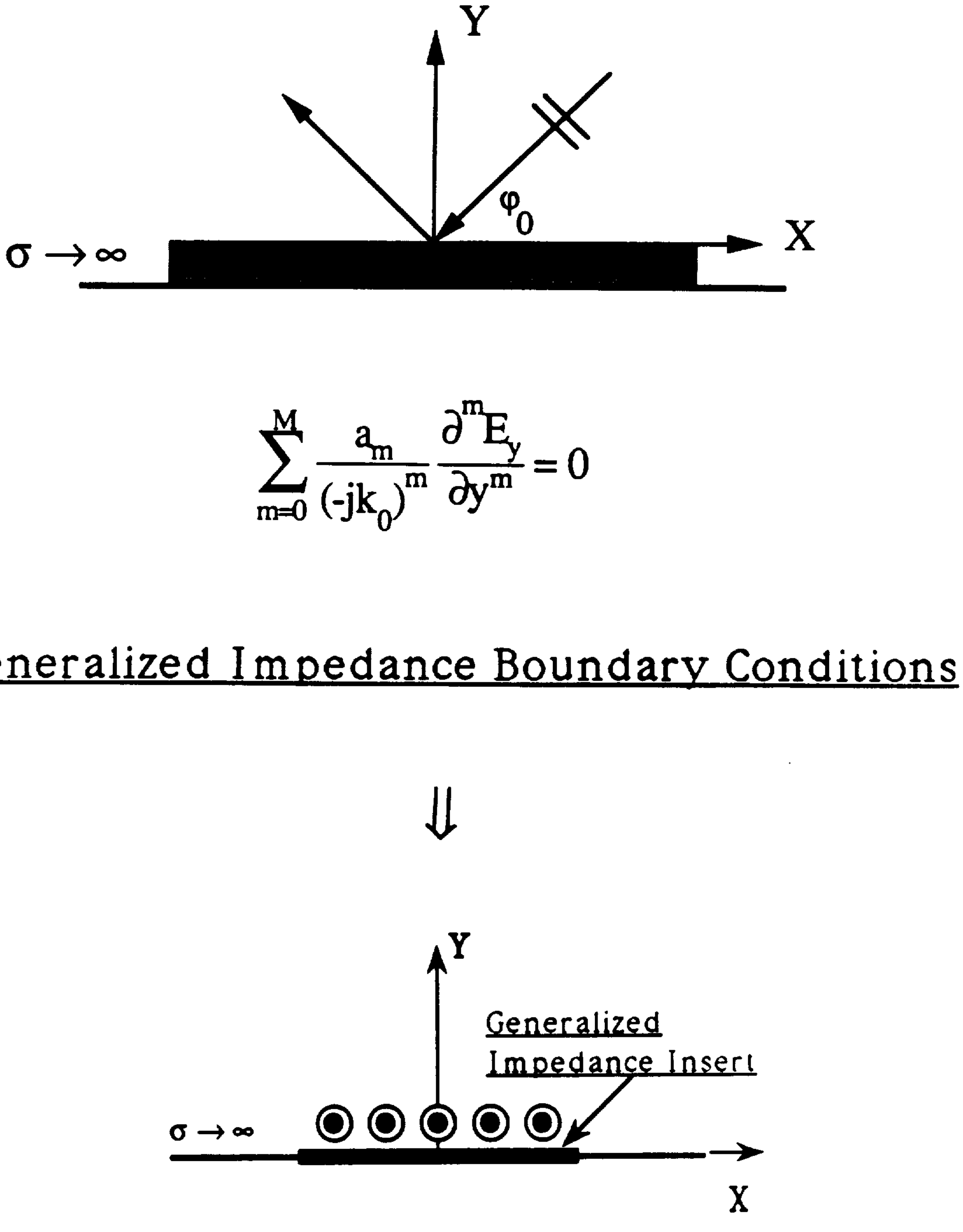

Figure 5.1: Simulation of a partially coated conducting ground plane by an impedance insert.

or equivalently,

$$\left(a_o - \frac{a_2}{k_o^2}\frac{\partial^2}{\partial y^2}\right)E_y + \left(-\frac{a_1}{jk_o} + \frac{a_3}{jk_o^3}\frac{\partial^2}{\partial y^2}\right)\frac{\partial}{\partial y}E_y = 0 \tag{5.14}$$

In order to derive an integral equation on the basis of (5.14), it is desirable to work with transverse derivatives. This allows for a convenient application of the Fourier transform to solve the resulting integral equation. To do so, we note from the divergence relation that

$$\nabla \cdot \mathbf{E} \;=\; 0\,, \qquad \frac{\partial E_y}{\partial y} = -\frac{\partial E_x}{\partial x} \tag{5.15}$$

and from the wave equation

$$\left(\nabla^2 + k_o^2\right)\mathbf{E} \;=\; 0\,, \qquad \frac{\partial^2 E_y}{\partial y^2} = -\left(k_o^2 + \frac{\partial^2}{\partial x^2}\right)E_y \tag{5.16}$$

Introducing these into (5.14) along with (5.11), we have

$$\left[1 + F_2\left(1 + \frac{1}{k_o^2}\frac{\partial^2}{\partial x^2}\right)\right]E_y + \frac{1}{jk_o}\left[F_1 + F_3\left(1 + \frac{1}{k_o^2}\frac{\partial^2}{\partial x^2}\right)\right]\frac{\partial}{\partial x}M_z = 0 \tag{5.17}$$

where

$$F_\ell = \frac{a_\ell}{a_o}\,, \qquad \ell = 1, 2, 3 \tag{5.18}$$

and E_y is the component of the total field normal to the coating. It can be expressed as the sum of the geometrical optics field in the absence of the sheet (short-circuited) and the scattered field in its presence

$$E_y = E_y^{GO} + E_y^s = E_y^i + E_y^r + E_y^s \tag{5.19}$$

Since the tangential electric field vanishes over the conducting ground plane, the reflected field is given by

$$E_y^r = E_y^i = -Z_o \cos\phi_o e^{jk_o x\cos\phi_o}, \qquad y = 0 \tag{5.20}$$

Also, the scattered field can be expressed as as

$$E_y^s = \frac{1}{4j}\int_{-w/2}^{w/2} 2M_z(x')\frac{\partial}{\partial x}H_o^{(2)}(k_o|x-x'|)dx' \tag{5.21}$$

where the factor of two has been introduced in accordance with the image theory. Substituting these into (5.17) yields

$$\begin{aligned} 2\left[1+F_2\left(1+\frac{1}{k_o^2}\frac{\partial^2}{\partial x^2}\right)\right]&\left\{\frac{1}{4j}\frac{\partial}{\partial x}\int_{-w/2}^{w/2} M_z(x')H_o^{(2)}(k_o|x-x'|)dx'\right. \\ &\left.- Z_o\cos\phi_o e^{jk_o x\cos\phi_o}\right\} + \frac{1}{jk_o}\left[F_1+F_3\left(1+\frac{1}{k_o^2}\frac{\partial^2}{\partial x^2}\right)\right]\frac{\partial}{\partial x}M_z(x) = 0 \end{aligned} \tag{5.22}$$

To eliminate the x derivative, we integrate both sides with respect to x and obtain

$$\begin{aligned} \left(1+F_2\sin^2\phi_o\right)Z_o e^{jk_o x\cos\phi_o} &= \frac{1}{2}\left[F_1+F_3\left(1+\frac{1}{k_o^2}\frac{\partial^2}{\partial x^2}\right)\right]M_z(x) \\ &+ \left[1+F_2\left(1+\frac{1}{k_o^2}\frac{\partial^2}{\partial x^2}\right)\right]\frac{k_o}{4}\int_{-w/2}^{w/2} M_z(x')H_o^{(2)}(k_o|x-x'|)dx' \end{aligned} \tag{5.23}$$

which is the desired integral equation in M_z.

5.2.2 E-Polarization

The incident fields in this case are of the form

$$\mathbf{E}^i = \hat{z}e^{jk_o(x\cos\phi_o+y\sin\phi_o)} \tag{5.24}$$

$$\mathbf{H}^i = -(\hat{x}\sin\phi_o - \hat{y}\sin\phi_o)Y_o e^{jk_o(x\cos\phi_o+y\sin\phi_o)} \tag{5.25}$$

and the appropriate boundary condition is given by the second relation in (5.1) with $M=3$

$$\left(a'_o - \frac{a'_2}{k_o^2}\frac{\partial^2}{\partial y^2}\right)H_y + \left(-\frac{a'_1}{jk_o} + \frac{a'_3}{jk_o^3}\frac{\partial^2}{\partial y^2}\right)\frac{\partial}{\partial y}H_y = 0 \tag{5.26}$$

Again, using the divergence relation and the wave equation and following steps similar to those taken for H-polarization, we obtain

$$\left[F_1' + F_3'\left(1 + \frac{1}{k_o^2}\frac{\partial^2}{\partial x^2}\right)\right] H_x + \left[1 + F_2'\left(1 + \frac{1}{k_o^2}\frac{\partial^2}{\partial x^2}\right)\right] Y_o M_x = 0 \tag{5.27}$$

in which the definition of F_ℓ' is analogous to that given for F_ℓ (see (5.18)) and

$$H_x = H_x^{GO} + H_x^s = H_x^i + H_x^r + H_x^s \tag{5.28}$$

Imposing the condition on the tangential electric field, we find that

$$H_x^r = H_x^i = -Y_o \sin\phi_o e^{jk_o x\cos\phi_o} \qquad ,y = 0 \tag{5.29}$$

and write the scattered magnetic field as

$$H_x^s = \frac{k_o Y_o}{4}\left(1 + \frac{1}{k^2}\frac{\partial^2}{\partial x^2}\right)\int 2M_x(x')H_o^{(2)}(k_o|x - x'|)dx' \cdot \tag{5.30}$$

Substituting these back into (5.27) yields the integral equation

$$\begin{aligned}\left(F_1' + F_3'\sin^2\phi_o\right)\sin\phi_o e^{jk_o x\cos\phi_o} &= \frac{1}{2}\left[1 + F_2'\left(1 + \frac{1}{k_o^2}\frac{\partial^2}{\partial x^2}\right)\right] M_x(x) \\ &+ \left[F_1' + F_3'\left(1 + \frac{1}{k_o^2}\frac{\partial^2}{\partial x^2}\right)\right]\frac{k_o}{4}\left(1 + \frac{1}{k_o^2}\frac{\partial^2}{\partial x^2}\right)\int_{-w/2}^{w/2} M_x(x')H_o^{(2)}(k_o|x - x'|)dx'\end{aligned} \tag{5.31}$$

to be solved for M_x.

5.2.3 Specialization to SIBC

As mentioned earlier in this chapter, the SIBC formulation has been traditionally applied to coated conducting bodies as well as dielectric filled metal-backed cavities. The above integral equations can be readily reduced to those corresponding to the SIBC formulation by setting $F_\ell = F_\ell' = 0$, $\ell = 2,3$ in accordance with conditions (5.1). Doing so yields

$$Z_o e^{jk_o x\cos\phi_o} = \frac{1}{2\eta}M_z(x) + \frac{k_o}{4}\int_{-w/2}^{w/2} M_z(x')H_o^{(2)}(k_o|x - x'|)dx' \tag{5.32}$$

for H-polarization and

$$\sin\phi_o e^{jk_o x\cos\phi_o} = \frac{1}{2\eta}M_x(x) + \frac{k_o}{4}\left(1 + \frac{1}{k_o^2}\frac{\partial^2}{\partial x^2}\right)\int_{-w/2}^{w/2} M_x(x')H_o^{(2)}(k_o|x-x'|)dx' \tag{5.33}$$

for E-polarization where $\frac{1}{\eta} = F_1 = 1/F_1' = a_1/a_o$ is identified as the normalized surface admittance of the insert.

5.2.4 CGFFT Formulation

The integral equations (5.23) and (5.31) are amenable to a solution via the CGFFT method. To put them into a suitable form, we first discretize the magnetic current density using the piecewise constant basis functions and follow an analysis similar to that presented in Section 3.3.4 in connection with the scattering from a strip. The integral equations are then put into the form

$$\begin{aligned}\left[1 + F_2(x)\sin^2\phi_o\right] Z_o e^{jk_o x\cos\phi_o} &= \\ \frac{1}{2}\left[F_1(x)M_z(x) + \frac{1}{k_o^2}F_3(x)\,\text{DFT}^{-1}\left\{(k_o^2 - D_x^2)\widehat{M}_z\right\}\right]& \\ + \text{DFT}^{-1}\left\{\widehat{M}_z\hat{\Upsilon}\right\} + \frac{1}{k_o^2}F_2(x)\,\text{DFT}^{-1}\left\{(k_o^2 - D_x^2)\widehat{M}_z\hat{\Upsilon}\right\}&\end{aligned} \tag{5.34}$$

and

$$\begin{aligned}\left[F_1'(x) + F_3'(x)\sin^2\phi_o\right]\sin\phi_o e^{jk_o x\cos\phi_o} &= \\ \frac{1}{2}\left[M_x(x) + \frac{1}{k_o^2}F_2'(x)\,\text{DFT}^{-1}\left\{(k_o^2 - D_x^2)\widehat{M}_x\right\}\right]& \\ +\frac{F_1'(x)}{k_o^2}\,\text{DFT}^{-1}\left\{(k_o^2 - D_x^2)\widehat{M}_x\hat{\Upsilon}\right\} + \frac{F_3'(x)}{k_o^4}\,\text{DFT}^{-1}\left\{(k_o^2 - D_x^2)^2\widehat{M}_x\hat{\Upsilon}\right\}&\end{aligned} \tag{5.35}$$

where the spatial dependences of the F and F' coefficients are expressed explicitly to allow for slow lateral variations in the electrical properties of the sheet and $\hat{\Upsilon}$ is the discrete transform of the train Υ_{on} defined in (3.85). It is noted that the spatial derivatives are carried out relatively easily in the transform domain as was the case in the strip problem. A CGFFT implementation of (5.34) and (5.35) is a straightforward task.

5.3 Three-Dimensional Impedance Inserts

In the previous section, we presented an implementation of a third order GIBC for scattering by a two-dimensional impedance insert simulating an infinite groove recessed in and/or a coating on a ground plane. Here we present a corresponding implementation for the three-dimensional case.

5.3.1 The Integral Equations

Consider the geometry shown in Fig. 2 illuminated by a harmonic plane wave

$$\mathbf{H}^i = \mathbf{H}_o e^{-jk_o(\hat{k}_i \cdot \mathbf{r})} \tag{5.36}$$

$$\mathbf{E}^i = Z_o \mathbf{H}^i \times \hat{k}_i \tag{5.37}$$

where $\hat{k}_i$ is given by (4.30)

$$\hat{k}_i = -\left[\sin\theta_o(\hat{x}\cos\phi_o + \hat{y}\sin\phi_o) + \hat{z}\cos\theta_o\right]$$

k_o is the free space wave number, and $Z_o = 1/Y_o$ is the free space intrinsic impedance. Also,

$$\begin{aligned} H_{ox} &= Y_o(\sin\alpha\cos\theta_o\cos\phi_o + \cos\alpha\sin\phi_o) \\ H_{oy} &= Y_o(\sin\alpha\cos\theta_o\sin\phi_o - \cos\alpha\cos\phi_o) \\ H_{oz} &= -Y_o\sin\alpha\sin\theta_o \end{aligned} \tag{5.38}$$

and

$$
\begin{aligned}
E_{ox} &= \cos\alpha\cos\theta_o\cos\phi_o - \sin\alpha\sin\phi_o \\
E_{oy} &= \cos\alpha\cos\theta_o\sin\phi_o + \sin\alpha\cos\phi_o \qquad (5.39) \\
E_{oz} &= -\cos\alpha\sin\theta_o
\end{aligned}
$$

in which α represents the polarization angle of the incident field (when $\alpha = 0$ then $H_z^i = 0$, corresponding to H-polarization, and when $\alpha = \pi/2$ then $E_z^i = 0$, corresponding to E-polarization incidence).

As before, the application of the conditions (5.1) over the surface of the impedance sheet requires the introduction of a magnetic current density vector $\mathbf{M}(x, y)$ as defined in (5.11) with both transverse components present. A surface integral equation for $\mathbf{M}$ can then be derived by following a procedure similar to that discussed for the two-dimensional analysis. Before doing so, however, it is again instructive to rewrite the boundary conditions in terms of the tangential derivation. This is expected to directly yield a symmetric set of equations with respect to M_x and M_y. From [13] we find that conditions (5.1) are equivalent to ($M = 2$)

$$
\begin{aligned}
E_x &= -PZ_oH_y + \frac{1}{jk_o}Q\frac{\partial E_z}{\partial x} + \frac{1}{jk_o}\frac{Q'}{P'}Z_o\frac{\partial H_z}{\partial y} \\
& \qquad\qquad\qquad\qquad\qquad\qquad\qquad\qquad (5.40) \\
E_y &= PZ_oH_x + \frac{1}{jk_o}Q\frac{\partial E_z}{\partial y} - \frac{1}{jk_o}\frac{Q'}{P'}Z_o\frac{\partial H_z}{\partial x}
\end{aligned}
$$

where

$$P = \frac{a_2 + a_o}{a_1} \qquad (5.41)$$

$$Q = \frac{a_2}{a_1} \qquad (5.42)$$

and analogous expressions hold for the primed quantities P' and Q'. To derive the integral equation, we invoke (5.11) (note the new coordinate system)

$$\mathbf{M} = \mathbf{E} \times \hat{n} \quad : \quad \begin{cases} M_x = E_y \\ M_y = -E_x \end{cases}$$

and rewrite the conditions (5.40) as

$$\begin{aligned} &\frac{1}{P} M_y - Z_o H_y^s + \frac{1}{jk_o} \frac{Q}{P} \frac{\partial E_z^s}{\partial x} + \frac{1}{jk_o} \frac{Q'}{PP'} Z_o \frac{\partial H_z^s}{\partial y} \\ &= Z_o H_y^{GO} - \frac{1}{jk_o} \frac{Q}{P} \frac{\partial E_z^{GO}}{\partial x} - \frac{1}{jk_o} \frac{Q'}{PP'} Z_o \frac{\partial H_z^{GO}}{\partial y} \\ &\frac{1}{P} M_x - Z_o H_x^s - \frac{1}{jk_o} \frac{Q}{P} \frac{\partial E_z^s}{\partial y} + \frac{1}{jk_o} \frac{Q'}{PP'} Z_o \frac{\partial H_z^s}{\partial x} \\ &= Z_o H_x^{GO} + \frac{1}{jk_o} \frac{Q}{P} \frac{\partial E_z^{GO}}{\partial y} - \frac{1}{jk_o} \frac{Q'}{PP'} Z_o \frac{\partial H_z^{GO}}{\partial x} \end{aligned} \tag{5.43}$$

where we have also made use of the definitions

$$\begin{aligned} \mathbf{E} &= \mathbf{E}^i + \mathbf{E}^r + \mathbf{E}^s = \mathbf{E}^{GO} + \mathbf{E}^s \\ \mathbf{H} &= \mathbf{H}^i + \mathbf{H}^r + \mathbf{H}^s = \mathbf{H}^{GO} + \mathbf{H}^s \end{aligned} \tag{5.44}$$

Again, the superscript *GO* specifies the geometrical optics fields in the absence of the sheet and the superscript *s* specifies the scattered field in its presence. By imposing the boundary conditions on the tangential components of the electric field over the perfect conductor, we find that

$$\begin{aligned} \mathbf{E}^r &= (-E_{ox}\hat{x} - E_{oy}\hat{y} + E_{oz}\hat{z}) e^{-jk_o(\hat{k}_r \cdot \mathbf{r})} \\ \mathbf{H}^r &= (H_{ox}\hat{x} + H_{oy}\hat{y} - H_{oz}\hat{z}) e^{-jk_o(\hat{k}_r \cdot \mathbf{r})} \end{aligned} \tag{5.45}$$

where

$$\hat{k}_r = -\left[\sin\theta_o(\hat{x}\cos\phi_o + \hat{y}\sin\phi_o) - \hat{z}\cos\theta_o\right] \tag{5.46}$$

is the unit propagation vector for the reflected fields. The scattered magnetic field may be expressed in terms of the equivalent magnetic current density as

$$\mathbf{H}^s = -jk_oY_o \iint_S \overline{\Gamma}(\mathbf{r};\mathbf{r}')\cdot[2\mathbf{M}(\mathbf{r}')]ds' \tag{5.47}$$

where S denotes integration over the surface of the sheet and

$$\overline{\Gamma} = \left(\overline{\mathbf{I}} + \frac{1}{k_o^2}\nabla\nabla\right)G_p(\mathbf{r};\mathbf{r}') \tag{5.48}$$

is the free space dyadic Green's function with the factor of two accounting for the presence of the ground plane. More explicitly,

$$H_x^s = -\frac{2jY_o}{k_o}\int_S\left[M_x(x',y')\left(k_o^2 + \frac{\partial^2}{\partial x^2}\right) + M_y(x',y')\frac{\partial^2}{\partial x\partial y}\right]G_o(\mathbf{r};\mathbf{r}')ds' \tag{5.49}$$

$$H_y^s = -\frac{2jY_o}{k_o}\int_S\left[M_x(x',y')\frac{\partial^2}{\partial x\partial y} + M_y(x',y')\left(k_o^2 + \frac{\partial^2}{\partial y^2}\right)\right]G_o(\mathbf{r};\mathbf{r}')ds' \tag{5.50}$$

and

$$H_z^s = -\frac{2jY_o}{k_o}\int_S\left[M_x(x',y')\frac{\partial^2}{\partial x\partial z} + M_y(x',y')\frac{\partial^2}{\partial y\partial z}\right]G_o(\mathbf{r};\mathbf{r}')ds' \tag{5.51}$$

Rewriting the last equation and making use of the identity (Appendix D)

$$\frac{\partial}{\partial z}G(\mathbf{r};\mathbf{r}') = -\frac{1}{2}\delta(\mathbf{r}-\mathbf{r}') \tag{5.52}$$

it follows (from distribution theory) that

$$H_z^s = \frac{jY_o}{k_o}\left[\frac{\partial}{\partial x}M_x(x,y) + \frac{\partial}{\partial y}M_y(x,y)\right] \tag{5.53}$$

To formulate an integral equation from (5.43), we also need to express the normal component of the scattered electric field E_z^s in terms of $\mathbf{M}$. We have

$$E_z^s = 2\int_S \left[M_x(x',y')\frac{\partial}{\partial y} - M_y(x',y')\frac{\partial}{\partial x}\right] G_o(\mathbf{r};\mathbf{r}')ds' \qquad (5.54)$$

Substituting now for the field quantities in (5.43) yields

$$\begin{aligned}
&\frac{1}{2P}M_x \\
&+ \frac{j}{k_o}\int_S \left[M_x(x',y')\left(k_o^2 + \frac{\partial^2}{\partial x^2}\right) + M_y(x',y')\frac{\partial^2}{\partial x\partial y}\right] G_o(\mathbf{r};\mathbf{r}')ds' \\
&- \frac{1}{jk_o}\frac{Q}{P}\int_S \left[M_x(x',y')\frac{\partial}{\partial y} - M_y(x',y')\frac{\partial}{\partial x}\right]\frac{\partial}{\partial y}G_o(\mathbf{r};\mathbf{r}')ds' \\
&+ \frac{1}{2k_o^2}\frac{Q'}{PP'}\frac{\partial}{\partial x}\left[\frac{\partial}{\partial x}M_x(x,y) + \frac{\partial}{\partial y}M_y(x,y)\right] \\
&= \left[Z_oH_{ox} + \frac{Q}{P}\sin\theta_o\sin\phi_o E_{oz}\right]\exp\{jk_o\left[\sin\theta_o\left(x\cos\phi_o + y\sin\phi_o\right)\right]\}
\end{aligned}$$

$$(5.55)$$

$$\begin{aligned}
&\frac{1}{2P}M_y(x,y) \\
&+ \frac{j}{k_o}\int_S \left[M_x(x',y')\frac{\partial^2}{\partial x\partial y} + M_y(x',y')\left(k_o^2 + \frac{\partial^2}{\partial y^2}\right)\right] G_o(\mathbf{r};\mathbf{r}')ds' \\
&+ \frac{1}{jk_o}\frac{Q}{P}\int_S \left[M_x(x',y')\frac{\partial}{\partial y} - M_y(x',y')\frac{\partial}{\partial x}\right]\frac{\partial}{\partial x}G_o(\mathbf{r};\mathbf{r}')ds' \\
&+ \frac{1}{2k_o^2}\frac{Q'}{PP'}\frac{\partial}{\partial y}\left[\frac{\partial}{\partial x}M_x(x,y) + \frac{\partial}{\partial y}M_y(x,y)\right]
\end{aligned}$$

$$= \left[Z_o H_{oy} - \frac{Q}{P}\sin\theta_o \cos\phi_o E_{oz}\right] \exp\{jk_o\left[\sin\theta_o\left(x\cos\phi_o + y\sin\phi_o\right)\right]\} \tag{5.56}$$

which is a coupled pair of integral equations to be solved for M_x and M_y.

5.3.2 Specialization to SIBC

The first order (standard) impedance boundary condition is obtained from (5.41)-(5.42) by letting $a_2 = a_2' \rightarrow 0$ eliminating the corresponding terms in (5.40)

$$\begin{aligned} E_x &= -PZ_oH_y \\ E_y &= PZ_oH_x \end{aligned} \tag{5.57}$$

where $P = a_o/a_1 = \eta_s$ may be regarded as the normalized surface impedance of the sheet. Expressing these conditions in vector form, we may write

$$\mathbf{E} - (\hat{n}\cdot\mathbf{E})\,\hat{n} = \eta_s Z_o \hat{n} \times \mathbf{H} \tag{5.58}$$

In view of (5.57), equations (5.55) and (5.56) reduce to the simpler pair of integral equations

$$\frac{1}{2\eta_s}M_x(x,y) + \frac{j}{k_o}\int_S \left[M_x(x,y)\left(k_o^2 + \frac{\partial^2}{\partial x^2}\right) + M_y(x',y')\frac{\partial^2}{\partial x \partial y}\right]G_o(\mathbf{r};\mathbf{r}')ds' = Z_oH_x^i \tag{5.59}$$

$$\frac{1}{2\eta_s}M_y(x,y) + \frac{j}{k_o}\int_S \left[M_x(x',y')\frac{\partial^2}{\partial x \partial y} + M_y(x',y')\left(k_o^2 + \frac{\partial^2}{\partial y^2}\right)\right]G_o(\mathbf{r};\mathbf{r}')ds' = Z_oH_y^i \tag{5.60}$$

As expected when $\eta_s \rightarrow \infty$, indicating an open gap in a conducting screen, these equations further reduce to the dual of those pertaining to a perfectly conducting plate already discussed in Chapter 4.

5.3.3 CGFFT Formulation

In order to put the integral equations (5.55) and (5.56) into a form suitable for a CGFFT, we expand $\mathbf{M}(x,y)$ in piecewise constant basis functions. In particular, we set

$$\mathbf{M}(x,y) = \sum_{p=0}^{N_x-1} \sum_{q=0}^{N_y-1} \mathbf{M}_{pq} P(x-x_p) P(y-y_q) \tag{5.61}$$

where $x_p = p\Delta x + \frac{\Delta x}{2}$, $y_q = q\Delta y + \frac{\Delta y}{2}$ and $\mathbf{M}_{pq} = \hat{x} M_{xpq} + \hat{y} M_{ypq}$ represent the unknown coefficients of the expansion function. Employing this expansion, we may rewrite the surface integrals as

$$\int_S \mathbf{M}(\mathbf{r}') \cdot \overline{\boldsymbol{\Gamma}}_o(\mathbf{r};\mathbf{r}') ds' = \sum_{p=0}^{N_x-1} \sum_{q=0}^{N_y-1} \mathbf{M}_{pq} \cdot \overline{\boldsymbol{\Xi}}_{ij} \tag{5.62}$$

where $\overline{\boldsymbol{\Xi}}_{ij}$ is given by (4.16). Applying the discrete Fourier transform, the above further reduces to

$$\int_S \mathbf{M}(\mathbf{r}') \cdot \overline{\boldsymbol{\Gamma}}_o(\mathbf{r};\mathbf{r}') ds' = \text{ DFT }^{-1}\{\hat{\overline{\boldsymbol{\Xi}}} \cdot \widehat{\mathbf{K}}\} \tag{5.63}$$

where $\hat{\overline{\boldsymbol{\Xi}}}$ denotes the discrete Fourier transform of $\overline{\boldsymbol{\Xi}}$ and is given by (3.109). Employing this result in (5.55) and (5.56), yields

$$
\begin{aligned}
& F_1(x,y) M_x(x,y) \\
+ \quad & \frac{2j}{k_o} \mathrm{DFT}^{-1}\left\{\left[\widehat{M}_x(k_0^2 - D_x^2) - \widehat{M}_y D_x D_y\right] \widehat{\xi}\right\} \\
+ \quad & \frac{2}{jk_o} F_2(x,y) \mathrm{DFT}^{-1}\left\{\left(\widehat{M}_x D_y^2 - \widehat{M}_y D_x D_y\right) \widehat{\xi}\right\} \\
- \quad & \frac{F_3}{k_o^2} \mathrm{DFT}^{-1}\left\{\widehat{M}_x D_x^2 + \widehat{M}_y D_x D_y\right\}
\end{aligned}
$$

$$= \quad 2\left[Z_o H_{ox} + F_2(x,y)\sin\theta_o \sin\phi_o E_{oz}\right]\exp\{jk_o\left[\sin\theta_o\left(x\cos\phi_o + y\sin\phi_o\right)\right]\} \tag{5.64}$$

and

$$\begin{aligned}
& F_1(x,y)M_y(x,y) \\
+ \quad & \frac{2j}{k_o}\mathrm{DFT}^{-1}\left\{\left[-\widehat{M}_x D_x D_y + \widehat{M}_y(k_0^2 - D_y^2)\right]\hat{\xi}\right\} \\
+ \quad & \frac{2}{jk_o}F_2(x,y)\mathrm{DFT}^{-1}\left\{\left(-\widehat{M}_x D_x D_y + \widehat{M}_y D_x^2\right)\hat{\xi}\right\} \\
- \quad & \frac{F_3}{k_o^2}\mathrm{DFT}^{-1}\left\{\widehat{M}_x D_x D_y + \widehat{M}_y D_y^2\right\} \\
= \quad & 2\left[Z_o H_{oy} - F_2(x,y)\sin\theta_o \cos\phi_o E_{oz}\right]\exp\{jk_o\left[\sin\theta_o\left(x\cos\phi_o + y\sin\phi_o\right)\right]\}
\end{aligned} \tag{5.65}$$

which are applicable for a solution via the CGDFT method. In the above,

$$F_1 = \frac{1}{P} \quad F_2 = \frac{Q}{P}$$

and the spatial dependence of the F coefficients are again shown to indicate the presence of a slow planar variation in the electrical properties of the sheet.

5.4 Summary

In this chapter, we introduced the generalized impedance boundary conditions and studied their incorporation in the general CGFFT formulation. The formulation was applied to the simulation of what could be referred to as generalized impedance inserts. In particular, a third order GIBC was applied to the simulation of two-dimensional impedance inserts while a second order condition was considered in the three-dimensional case. In both cases, the first order (SIBC) formulation was obtained by setting the appropriate higher order coefficients to zero.

The combined GIBC/CGFFT formulations discussed here can be used in the study of partially coated conducting planes as well as cavity-backed apertures recessed in a ground plane. These structures may be adequately represented by impedance inserts with appropriately chosen coefficients. This will be the subject of Part Two of the Thesis.

Part II

SCATTERING BY CAVITY STRUCTURES

CHAPTER VI

SCATTERING BY MATERIAL FILLED GROOVES

6.1 Introduction

The study of electromagnetic scattering from filled cavities recessed in ground planes is important in modeling the radar response to various man-made structures.

In this chapter, an exact full-wave formulation is first developed for the rectangular groove problem based on the Generalized Network Theory [63]. This theory has been applied to a number of aperture and slot problems in the past [64, 65]. In this method the external fields are expressed in terms of the scattering integral while the fields internal to the dielectric medium are given in terms of appropriate waveguide modes specific to the particular problem. An integral equation is then set up by employing the equivalence principle and enforcing continuity of the electromagnetic fields across the interface. This method, although rigorous, is computationally intensive and is limited in application to structures whose electrical size is relatively small. Moreover, due to the nature of the formulation, a solution is possible only for canonical geometries for which the orthogonal wave functions associated with the cavity can be found.

Next, the formulation is specialized to narrow grooves. Analytical expressions for the equivalent magnetic current distribution over the aperture of narrow grooves are derived based on a quasi-static approximation of the pertinent integral equations. The solutions exhibit the expected edge behavior at the terminations and are used to find closed form expressions for the echo width of the groove.

Finally, an approximate formulation based on the GIBCs is presented and shown to be amenable to the CGFFT method of solution having an order $\mathcal{O}(N)$ memory requirement. In contrast, the exact integral equation does not lend itself to such a solution and must be solved by a matrix inversion approach having an $\mathcal{O}(N^2)$ memory requirement. It is found, unfortunately, that the GIBC formulation yields satisfactory results only when the contributions of the groove's terminations are negligible. This is because the GIBCs were derived for a coating without terminations and must be supplemented by more accurate conditions in the vicinity of such material discontinuities. A hybrid procedure is, therefore, introduced that combines the exact and GIBC formulations. The proposed procedure utilizes the solution obtained from the GIBC/CGFFT in a region sufficiently away from the terminations and then finds the near-edge currents based on the exact formulation. Despite an increase in the complexity of the formulation, the memory requirement of the hybrid method remains essentially of the order $\mathcal{O}(N)$ and can be used when the material constituency of the filling does not allow the application of neither SIBC nor GIBCs of higher order.

6.2 Full-Wave Formulation

Consider the infinitely long groove of width w, and depth d illuminated by the plane wave

$$\mathbf{H}^i(\text{ or }\mathbf{E}^i) = \hat{z}e^{jk_o(x\cos\phi_o + y\sin\phi_o)} \tag{6.1}$$

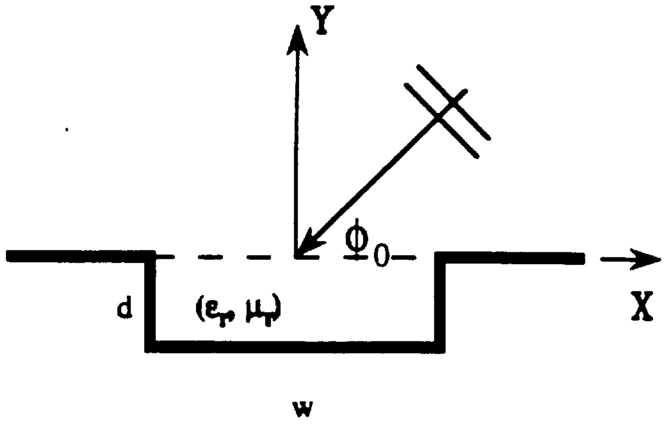

Figure 6.1: Geometry of a filled rectangular groove.

for H- (or E-) polarization, where $k_o = 2\pi/\lambda$ is the free space wave number and ϕ_o is the angle of incidence (Figure 6.1). The groove is assumed to be filled with a material of index of refraction $\aleph = \sqrt{\epsilon_r \mu_r}$. A standard approach to formulate the scattered field by the groove is to employ the equivalence principle [66]. Accordingly, the aperture is closed by a perfect conductor and the equivalent magnetic current (Figure 6.2)

$$\mathbf{M} = \mathbf{E} \times \hat{n} = \mathbf{E} \times \hat{y} \tag{6.2}$$

is introduced over the aperture at $y = 0^+$. The scattered fields outside the cavity are those radiated by the equivalent magnetic current and consistent with the continuity of the tangential electric field, the field inside the cavity is that radiated by $-\mathbf{M}$ placed at $y = 0^-$ across the aperture. To find the equivalent magnetic current we must also enforce the continuity of the tangential magnetic field across the aperture. We have

$$\hat{n} \times \left[\mathbf{H}^a(\mathbf{M}) + \mathbf{H}^{ia}\right] = \hat{n} \times \mathbf{H}^b(\mathbf{M}') \tag{6.3}$$

where $\mathbf{H}^{ia}$ is the total field on the ground plane in the absence of the groove (aperture short-circuited), $\mathbf{H}^a$ represents the tangential scattered field above the aperture and $\mathbf{H}^b$ is the total field below the aperture. To construct an integral equation in $\mathbf{M}$, $\mathbf{H}^a$ and $\mathbf{H}^b$ must be expressed in terms of the Green's function corresponding to each region. The external scattered field (attributed to $\mathbf{M}$) can be expressed as the surface integral

$$\mathbf{H}^a(\mathbf{r}) = -jk_oY_o\int_{-w/2}^{w/2} 2\mathbf{M}(x')\cdot\bar{\mathbf{\Gamma}}(\mathbf{x};\mathbf{x}')d\mathbf{x}' \tag{6.4}$$

where Y_o is the intrinsic admittance of the free space and $\bar{\mathbf{\Gamma}}$ is the two dimensional dyadic Green's function

$$\bar{\mathbf{\Gamma}}(x;x') = \frac{1}{4j}\left[(1+\frac{1}{k_o^2}\frac{\partial^2}{\partial x^2})\hat{x}\hat{x}+\hat{z}\hat{z}\right]H_o^{(2)}(k_o|x-x'|) \tag{6.5}$$

and a factor of two was introduced in (6.4) based on the image theory to account for the presence of the ground plane.

The internal fields (those attributed to $\mathbf{M}'$) can be written in terms of the $\mathrm{TM_Z}$and $\mathrm{TE_Z}$waveguide modes as

$$\begin{aligned}\mathbf{E}^b = \mathbf{E}^{TM}+\mathbf{E}^{TE} &= -jk_bZ_b(\hat{z}\Psi^{TM}) - \nabla\times(\hat{z}\Psi^{TE}) \quad (6.6)\\ \mathbf{H}^b = \mathbf{H}^{TM}+\mathbf{H}^{TE} &= \nabla\times(\hat{z}\Psi^{TM}) - jk_bY_b(\hat{z}\Psi^{TE}) \quad (6.7)\end{aligned}$$

where $k_b = \aleph k_o$ is the wave number inside the cavity and $Z_b = 1/Y_b$ is the intrinsic impedance of the filling material. The functions Ψ^{TM} and Ψ^{TE} are the wave potentials both satisfying the scalar wave equation

$$\left(\frac{\partial^2}{\partial x^2}+\frac{\partial^2}{\partial y^2}+k_b^2\right)\Psi = 0 \tag{6.8}$$

subject to the boundary conditions

$$\begin{aligned}E_x &= E_z = 0 \quad ; \quad y=-d \quad (6.9)\\ E_y &= E_z = 0 \quad ; \quad x=\pm w/2 \quad (6.10)\end{aligned}$$

on the cavity walls, and

$$\mathbf{M}' = \mathbf{E} \times \hat{n}' \qquad y = 0 \tag{6.11}$$

over the aperture.

Below, we consider the two principal polarizations separately.

6.2.1 H-polarization

For H-polarization (TE_Zcase) we have

$$H_z^{ia} = H_z^{\text{inc}} + H_z^{\text{refl}} = 2e^{jk_o x \cos\phi_o} \tag{6.12}$$

which is the geometrical optics field in the absence of the groove. The tangential component of the external scattered field is given by

$$H_z^a(M_z) = -\frac{k_o Y_o}{2} \int_{-w/2}^{w/2} M_z(x') H_o^{(2)}(k_o|x - x'|) dx' \tag{6.13}$$

while the internal fields are given by (6.6) and (6.7) and in this case we have

$$\begin{aligned} \mathbf{E}^b = \mathbf{E}^{TE} &= -\nabla \times (\hat{z}\Psi^{TE}) = -\hat{x}\frac{\partial}{\partial y}\Psi^{TE} + \hat{y}\frac{\partial}{\partial x}\Psi^{TE} && (6.14) \\ \mathbf{H}^b = \mathbf{H}^{TE} &= -jk_b Y_b(\hat{z}\Psi^{TE}) && (6.15) \end{aligned}$$

In order to find useful expressions for $\mathbf{E}^b$ and $\mathbf{H}^b$, we need to solve for the wave potential Ψ^{TE}. To this end, Ψ^{TE} can be expressed as an infinite sum of orthogonal modes

$$\Psi^{TE} = \sum_{p=0}^{\infty} A_p \psi_p^h \tag{6.16}$$

where ψ_p^h are the waveguide modes all satisfying the wave equation (6.8) and A_p are coefficients to be found. Substituting for Ψ^{TE} in (6.14), and using (6.9)–(6.10), the

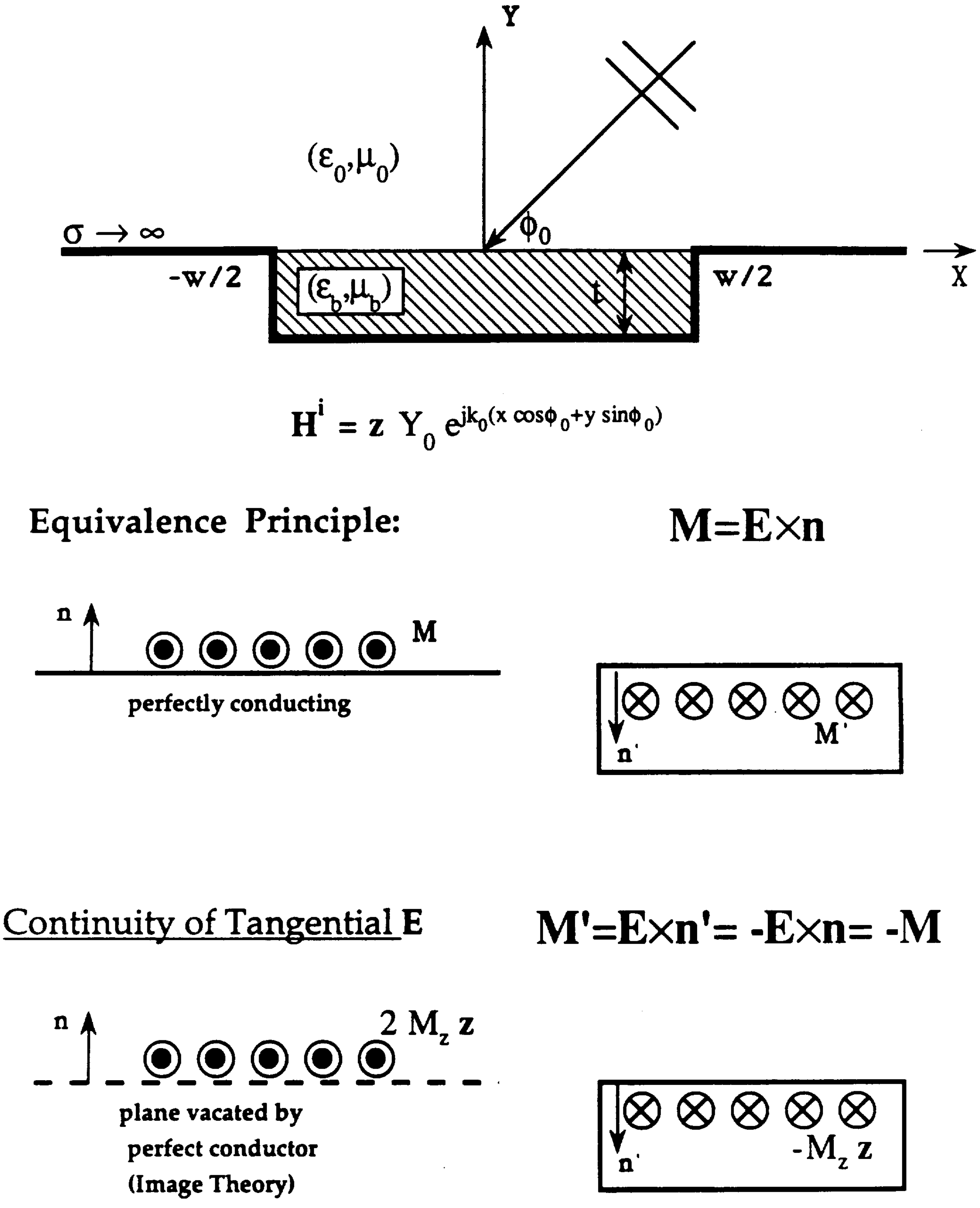

Figure 6.2: Application of the equivalence principle to aperture problems.

boundary conditions to be imposed on the cavity walls are

$$\frac{\partial}{\partial y}\psi_p^h = 0 \qquad y = -d \tag{6.17}$$

$$\frac{\partial}{\partial x}\psi_p^h = 0 \qquad x = \pm w/2 \tag{6.18}$$

and a set of eigenfunctions which satisfy these and the wave equation is

$$\psi_p^h = \cos[k_p(y+d)]\cos\left[\frac{p\pi}{w}(x - w/2)\right] \tag{6.19}$$

where k_p satisfies the separation parameter equation

$$k_p^2 = k_b^2 - \left(\frac{p\pi}{w}\right)^2 \tag{6.20}$$

We now seek to find the coefficients A_p. Upon enforcing the condition (6.11) on the aperture ($y = 0$), we find that

$$\sum_p k_p A_p \sin(k_p d)\cos\left[\frac{p\pi}{w}(x - w/2)\right] = -M_z' = M_z \tag{6.21}$$

Multiplying both sides by $\cos\left[\frac{q\pi}{w}(x - w/2)\right]$ and integrating over the aperture yields

$$\sum_p k_p A_p \sin(k_p d)\int_{-w/2}^{w/2}\cos\left[\frac{p\pi}{w}(x - w/2)\right]\cos\left[\frac{q\pi}{w}(x - w/2)\right]dx$$

$$= \int_{-w/2}^{w/2} M_z(x)\cos\left[\frac{q\pi}{w}(x - w/2)\right]dx \tag{6.22}$$

and by invoking the orthogonality relation

$$\int_{-w/2}^{w/2}\cos\left[\frac{p\pi}{w}(x - w/2)\right]\cos\left[\frac{q\pi}{w}(x - w/2)\right]dx = \begin{cases} \frac{w}{2}[1+\delta_{po}] & p = q \\ 0 & p \neq q \end{cases} \tag{6.23}$$

we find

$$A_p = \frac{2}{[1+\delta_{po}]w k_p \sin(k_p d)}\int_{-w/2}^{w/2} M_z(x)\cos\left[\frac{p\pi}{w}(x - w/2)\right]dx \tag{6.24}$$

where δ_{pq} is the Kronecker delta defined in (3.117). Thus, the function Ψ^{TE} in (6.16) is completely defined and the magnetic field in the internal region may now be expressed explicitly as

$$H_z(x,y) = -jk_bY_b\sum_{p=0}^{\infty}\frac{2}{[1+\delta_{po}]wk_p\sin(k_pd)}\cos[k_p(y+t)]\cos[\frac{p\pi}{w}(x-w/2)]$$

$$\cdot\int_{-w/2}^{w/2}M_z(x')\cos[\frac{p\pi}{w}(x'-w/2)]dx' \qquad (6.25)$$

which at $y=0$ gives the tangential field just below the aperture

$$H_z(x,0) = -jk_bY_b\sum_{p=0}^{\infty}\frac{2}{[1+\delta_{po}]wk_p\tan(k_pd)}\cos[\frac{p\pi}{w}(x-w/2)]$$

$$\cdot\int_{-w/2}^{w/2}M_z(x')\cos[\frac{p\pi}{w}(x'-w/2)]dx' \qquad (6.26)$$

This is equivalent to expressing the tangential internal fields as

$$H_z^b(-M_z) = -jk_bY_b\int_{-w/2}^{w/2}M_z(x')G^h(x;x')dx' \qquad (6.27)$$

where the Green's function is given by (see (6.26))

$$G^h(x,x') = \sum_{p=0}^{\infty}\frac{2}{\varepsilon_pwk_p\tan(k_pd)}\cos[\frac{p\pi}{w}(x-w/2)]\cos[\frac{p\pi}{w}(x'-w/2)] \qquad (6.28)$$

and

$$\varepsilon_p = 1+\delta_{po} \qquad (6.29)$$

Substituting (6.12), (6.13), and (6.27) into (6.3) we obtain

$$Z_oe^{jk_ox\cos\phi_o} = \frac{k_o}{4}\int_{-w/2}^{w/2}M_z(x')H_o^{(2)}(k_o|x-x'|)dx$$

$$+\sum_{p=0}^{\infty}\frac{\cos[\frac{p\pi}{w}(x-w/2)]}{\varepsilon_pw\eta_{hp}}\int_{-w/2}^{w/2}M_z(x')\cos[\frac{p\pi}{w}(x'-w/2)]dx' \qquad (6.30)$$

where η_{hp} are the normalized H-mode impedances of the cavity given by

$$\eta_{hp} = j\frac{k_p}{k_b} z_b \tan(k_p d) \tag{6.31}$$

and $z_b = \sqrt{\mu_r/\epsilon_r}$ is the normalized intrinsic impedance of the internal region. Equation (6.30) is an exact integral equation to be solved for $M_z(x)$.

6.2.2 E-polarization

For E-polarization (TMzcase), we have

$$H_x^{ia} = -2Y_o \sin\phi_o e^{jk_o x \cos\phi_o} \tag{6.32}$$

and the corresponding tangential scattered fields are given by

$$H_x^a(M_x) = \frac{k_o Y_o}{2}\left(1 + \frac{1}{k_o^2}\frac{\partial^2}{\partial x^2}\right)\int_{-w/2}^{w/2} M_x(x') H_o^{(2)}(k_o|x - x'|)dx' \tag{6.33}$$

and

$$H_x^b(-M_x) = -j\frac{Y_b}{k_b}\int_{-w/2}^{w/2} M_x(x') G^e(x; x')dx' \tag{6.34}$$

To find the cavity Green's function G^e we note that

$$\mathbf{E}^b = \mathbf{E}^{TM} = -jk_b Z_b(\hat{z}\Psi^{TM}) \tag{6.35}$$

$$\mathbf{H}^b = \mathbf{H}^{TM} = \nabla \times (\hat{z}\Psi^{TM}) = \hat{x}\frac{\partial}{\partial y}\Psi^{TM} - \hat{y}\frac{\partial}{\partial x}\Psi^{TM} \tag{6.36}$$

Following steps similar to those taken for the H-polarization case, the wave potential Ψ^{TM} is expressed as

$$\Psi^{TM} = \sum_{p=0}^{\infty} B_p \psi_p^e \tag{6.37}$$

and the boundary conditions to be satisfied on the walls are

$$\psi_p^e = 0 \qquad y = -d \tag{6.38}$$

$$\psi_p^e = 0 \qquad x = \pm w/2 \tag{6.39}$$

which are satisfied by chhosing ψ_p^h as

$$\psi_p^e = \sin[k_p(y+d)] \sin[\frac{p\pi}{w}(x - w/2)] \tag{6.40}$$

and k_p is defined in (6.20). Enforcing now the boundary condition (6.11) on the aperture, we have

$$\sum_p k_p B_p \sin(k_p d) \sin[\frac{p\pi}{w}(x - w/2)] = M_x \tag{6.41}$$

To find B_p, we multiply both sides by $\sin[\frac{q\pi}{w}(x - w/2)]$ and integrate over the extent of the aperture. As before, by employing the orthogonality relation

$$\int_{-w/2}^{w/2} \sin[\frac{p\pi}{w}(x - w/2)] \sin[\frac{q\pi}{w}(x - w/2)] dx = \begin{cases} \frac{w}{2}[1 - \delta_{po}] & p = q \\ 0 & p \neq q \end{cases} \tag{6.42}$$

we find

$$B_p = -\frac{2Y_b}{jk_b w \sin(k_p d)} \int_{-w/2}^{w/2} M_x(x) \sin[\frac{p\pi}{w}(x - w/2)] dx \tag{6.43}$$

The magnetic field in the internal region may now be expressed explicitly as

$$\begin{aligned} H_x(x,y) &= j\frac{Y_b}{k_b} \sum_{p=1}^{\infty} \frac{2k_p}{w \sin(k_p d)} \cos[k_p(y+t)] \sin[\frac{p\pi}{w}(x - w/2)] \\ &\quad \cdot \int_{-w/2}^{w/2} M_x(x') \sin[\frac{p\pi}{w}(x' - w/2)] dx' \end{aligned} \tag{6.44}$$

which upon setting $y = 0$ gives the tangential aperture field

$$\begin{aligned} H_x(x,0) &= j\frac{Y_b}{k_b} \sum_{p=1}^{\infty} \frac{2k_p}{w \tan(k_p d)} \sin[\frac{p\pi}{w}(x - w/2)] \\ &\quad \cdot \int_{-w/2}^{w/2} M_x(x') \sin[\frac{p\pi}{w}(x' - w/2)] dx' \end{aligned} \tag{6.45}$$

Comparing this with (6.34) we deduce that

$$G^e(x;x') = -\sum_{p=1}^{\infty} \frac{2k_p}{w \tan(k_p d)} \sin[\frac{p\pi}{w}(x - w/2)] \sin[\frac{p\pi}{w}(x' - w/2)] \tag{6.46}$$

Substituting (6.32)–(6.34) and (6.46) into (6.3) yields the integral equation

$$\sin\phi_o e^{jkx\cos\phi_o} = \frac{k_o}{4}\left(1+\frac{1}{k_o^2}\frac{\partial^2}{\partial x^2}\right)\int_{-w/2}^{w/2} M_x(x')H_o^{(2)}(k_o|x-x'|)dx'$$

$$+\sum_{p=1}^{\infty}\frac{\sin\left[\frac{p\pi}{w}(x-w/2)\right]}{w\eta_{ep}}\int_{-w/2}^{w/2} M_x(x')\sin\left[\frac{p\pi}{w}(x'-w/2)\right]dx' \qquad (6.47)$$

where

$$\eta_{ep} = j\frac{k_b}{k_p}z_b\tan(k_pd) \qquad (6.48)$$

are the normalized E-mode impedances of the cavity. Equation (6.47) is an exact integral equation to be solved for $M_x(x)$.

Clearly, (6.30) and (6.47) are both invalid when

$$\tan(k_pd) = 0 \qquad (6.49)$$

and this occurs only when the material filling the groove is lossless. To be specific, the modal solutions fail if there exist integers p and q such that[1]

$$(\frac{p}{w})^2 + (\frac{q}{d})^2 = (\frac{2\aleph}{\lambda})^2 \qquad p,q\in\mathcal{I} \qquad (6.50)$$

This difficulty in the evaluation of the internal Green's functions may be circumvented by assuming a small loss in the material. We also note that for the proper behavior of the field in the internal region, we must have

$$\Re\mathrm{e}\{k_p\} \geq 0 \qquad (6.51)$$

$$\Im\mathrm{m}\{k_p\} \leq 0 \qquad (6.52)$$

when using (6.20).

---

[1] The formulation for the H-polarization case also fails if $k_p = 0$ in addition to (6.49). This is equivalent to $p/w = q/d$ when $p,q\in\mathcal{I}$.

Upon a solution of the integral equations, the scattering echo widths of the groove may be calculated from (3.44) and (3.45) with Z_oK_z and K_x replaced by $2Y_oM_z$ and $2M_x$, respectively, and the polarization subscripts e and h interchanged in accordance with the image theory and Babinet's principle [19]. Thus,

$$\sigma_h \;=\; k_o\left|Y_o\int_{-w/2}^{w/2} M_z(x')e^{jk_ox'\cos\phi}dx'\right|^2 \tag{6.53}$$

$$\sigma_e \;=\; k_o\left|\sin\phi\int_{-w/2}^{w/2} M_x(x')e^{jk_ox'\cos\phi}dx'\right|^2 \tag{6.54}$$

6.2.3 Numerical Solution

The integral equations derived in the previous subsections may be solved numerically by the moment method and will serve as the reference for the validation of the results obtained from alternative formulations presented in the rest of this chapter.

Considering the H-polarization case, the integral equation (6.30) may be discretized by expanding $M_z(x)$ as

$$M_z(x) = \sum_{n=0}^{N-1} M_z(x_n)P(x-x_n), \qquad x_n = n\Delta + \frac{\Delta}{2} \tag{6.55}$$

where $P(x)$ denotes piecewise constant basis function. Substituting for the current expansion in (6.30) and applying point matching, the admittance elements are given by

$$Y_{mn} = \Upsilon_{mn} + \Pi_{mn} \tag{6.56}$$

where Υ_{mn} are elements attributed to the external tangential fields and are given by (3.85), while Π_{mn} are those attributed to the internal tangential fields and are given by

$$\Pi_{mn} = \Delta_x\sum_{p=0}^{\infty}\frac{1}{\varepsilon_p w k_p \eta_{hp}}\cos\left[\frac{p\pi}{w}(x_m - w/2)\right]\cos\left[\frac{p\pi}{w}(x_n - w/2)\right]\mathrm{sinc}\left(\frac{p\pi}{w}\frac{\Delta_x}{2}\right) \tag{6.57}$$

A similar discretization can be carried out for E-polarization.

Figure 6.3 shows a sample calculation of the backscattering echo width for an empty groove based on the above formulation. The groove is assumed to be 10λ long and the usual physical optics approximation (1.26) was invoked to relate the two-dimensional echo width given by (6.53) or (6.54) to the corresponding three-dimensional radar cross section. The results are in good agreement with a corresponding finite element method (FEM) solution [67].

6.3 Partially Loaded Grooves

We now consider the partially loaded groove shown in Figure 6.4. If the filling material is electrically dense, we may consider the equivalent problem of a homogeneously filled groove of depth d terminated with a floor consisting of an impedance sheet. In this case, the boundary conditions on the cavity walls and the aperture of the groove remain the same as (6.10) and (6.11), while the floor satisfies the impedance boundary condition (5.58)

$$\mathbf{E} - (\hat{y} \cdot \mathbf{E})\hat{y} = \eta_\ell Z_o \hat{y} \times \mathbf{H} \tag{6.58}$$

where η_ℓ is the normalized surface impedance of the floor. The above condition replaces (6.9), and in scalar form

$$E_x = \eta_\ell Z_o H_z \qquad y = -d \tag{6.59}$$

$$E_z = -\eta_\ell Z_o H_x \qquad y = -d \tag{6.60}$$

Following an analysis similar to that of the previous section, new integral equations can be derived for the solution of the equivalent magnetic current density over the aperture of the groove. In particular, employing the equivalence principle, the

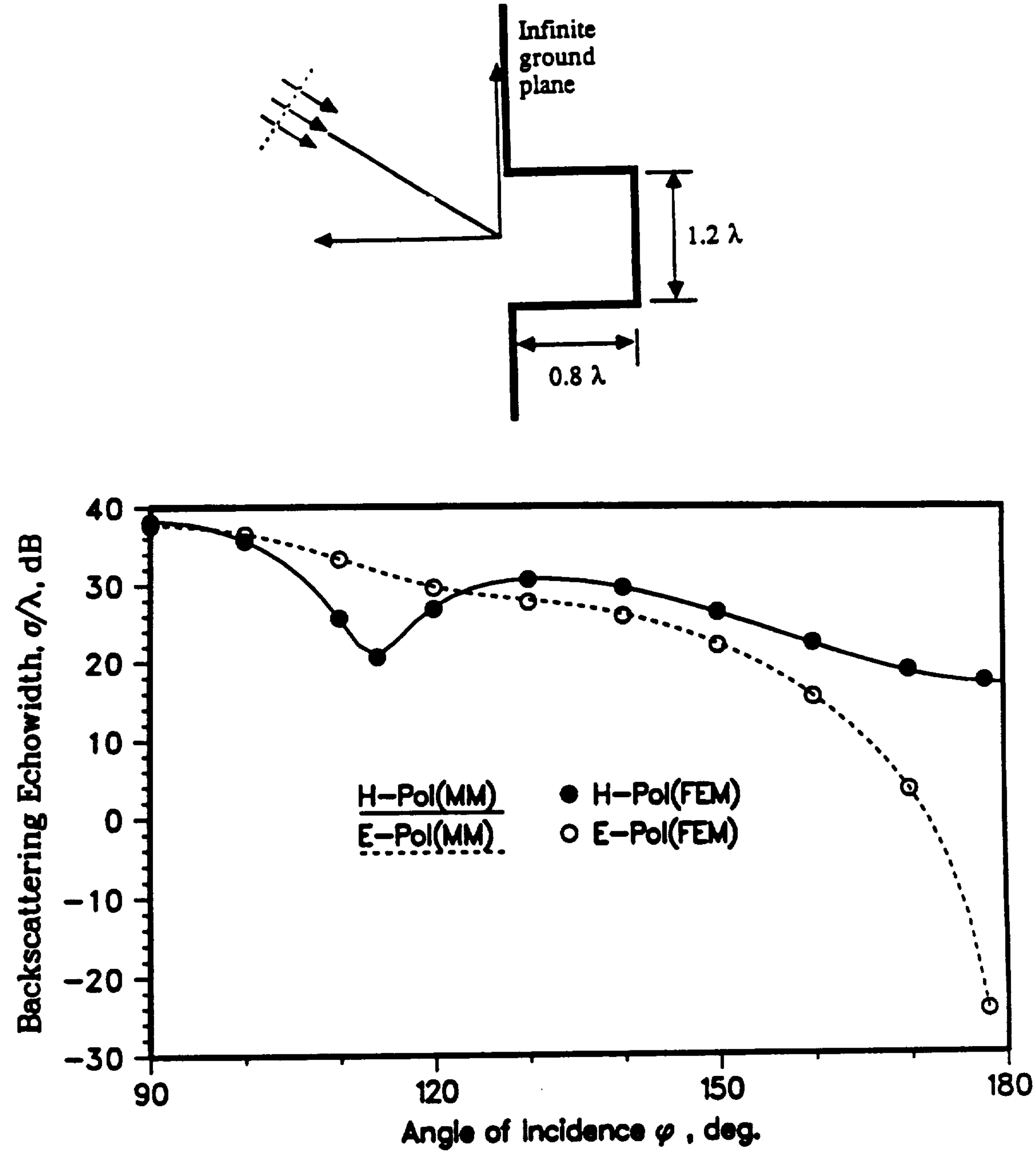

Figure 6.3: Comparison of the backscattering patterns of a long two-dimensional groove obtained from a finite element solution (FEM) [67] and the method of moments (this study). The groove is assumed to be 10λ long. (20 samples/ λ with 60 waveguide modes).

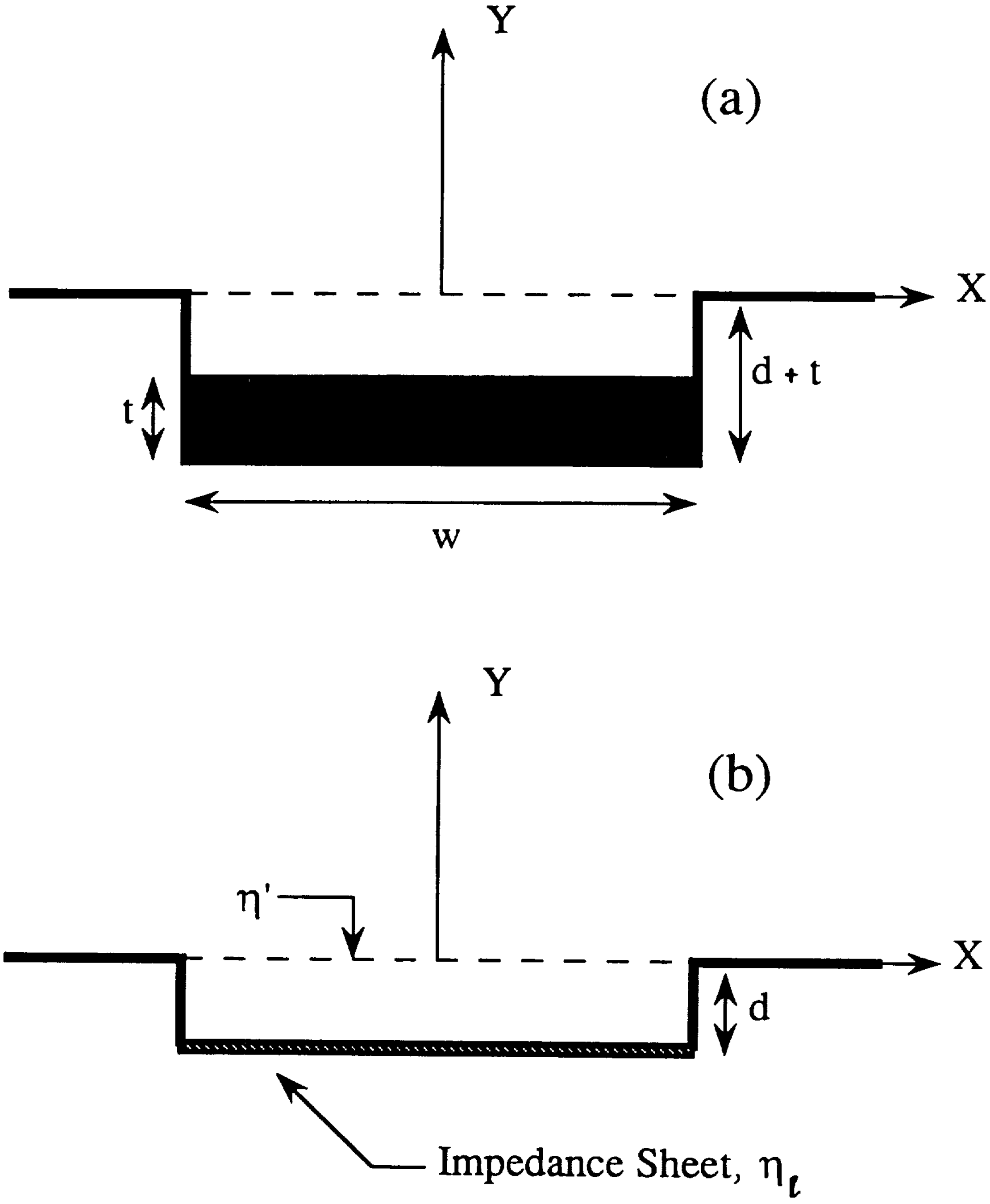

Figure 6.4: Scattering from a groove partially loaded with electrically dense material. (a) Geometry. (b) Equivalent problem using an impedance sheet.

tangential magnetic fields in the external and internal regions are expressed in terms of the pertinent Green's functions and used to enforce the continuity of the fields across the aperture. In this case, the expressions for the external fields remain unchanged and are given by (6.13) and (6.33) for H- and E-polarizations, respectively. As for the internal fields, the Green's functions G^h and G^e must be modified to accommodate the new boundary condition on the groove's floor.

Considering the H-polarization case, once again the wave potential Ψ^{TE} is expressed in terms of an infinite sum of orthogonal modes as in (6.16). The new boundary conditions to be satisfied by these modes are

$$\frac{\partial}{\partial y}\psi_p^h = \eta_\ell Z_o(jk_bY_b\psi_p^h) \qquad y=-d \tag{6.61}$$

$$\frac{\partial}{\partial x}\psi_p^h = 0 \qquad x=\pm w/2 \tag{6.62}$$

A set of eigenfunctions satisfying the second condition along with the wave equation is

$$\psi_p^h = \left[e^{jk_p(y+d)} - R_h e^{-jk_p(y+d)}\right]\cos\left[\frac{p\pi}{w}(x-w/2)\right] \tag{6.63}$$

where R_h is the reflection coefficient of the floor and k_p is defined in (6.20). Enforcing the second condition yields

$$jk_p(1+R_h) = \eta_\ell\sqrt{\frac{\epsilon_r}{\mu_r}}jk_b(1-R_h) \tag{6.64}$$

which upon solving for R_h gives

$$R_h = \frac{\eta_\ell - \dfrac{k_p}{k_b}z_b}{\eta_\ell + \dfrac{k_p}{k_b}z_b} \tag{6.65}$$

Upon imposing the equivalent current condition (6.11) on the aperture and solving for the new set of coefficients A_p, we find

$$A_p = \frac{2j}{\varepsilon_p w k_p(e^{jk_pd}+R_he^{-jk_pd})}\int_{-w/2}^{w/2} M_z(x)\cos\left[\frac{p\pi}{w}(x-w/2)\right]dx \tag{6.66}$$

and, therefore, the new Green's function is given by

$$G^h(x,x') = \sum_{p=0}^{\infty} \frac{2j}{\varepsilon_p w k_p} \left[\frac{e^{jk_pd} - R_h e^{-jk_pd}}{e^{jk_pd} + R_h e^{-jk_pd}} \right] \cos\,[\frac{p\pi}{w}(x - w/2)] \cos\,[\frac{p\pi}{w}(x' - w/2)] \tag{6.67}$$

where ε_p is given by (6.29). Employing the above results, the integral equation to be satisfied by the aperture current for the H-polarization case is

$$Z_o e^{jk_o x \cos\phi_o} = \frac{k_o}{4} \int_{-w/2}^{w/2} M_z(x') H_o^{(2)}(k_o|x - x'|)dx$$

$$+ \sum_{p=0}^{\infty} \frac{\cos\,[\frac{p\pi}{w}(x - w/2)]}{\varepsilon_p w \eta'_{hp}} \int_{-w/2}^{w/2} M_z(x') \cos\,[\frac{p\pi}{w}(x' - w/2)]dx' \tag{6.68}$$

where η'_{hp} is the normalized equivalent surface impedance of the groove looking into the aperture, given by

$$\eta'_{hp} = z_\ell \frac{\eta_\ell + j z_b \dfrac{k_p}{k_b} \tan k_p d}{j \eta_\ell \dfrac{k_b}{k_p} \tan k_p d + z_b} \tag{6.69}$$

For the E-polarization case, the boundary conditions to be enforced in the internal region are

$$\psi_p^e = \quad \eta_\ell Z_o(jk_b Y_b \tfrac{\partial}{\partial y} \psi_p^e) \qquad y = -d \tag{6.70}$$

$$\psi_p^e = \qquad 0 \qquad x = \pm w/2 \tag{6.71}$$

suggesting the following form for the eigenfunctions ψ_p^e

$$\psi_p^e = \left[e^{jk_p(y+d)} + R_e e^{-jk_p(y+d)} \right] \sin\,[\frac{p\pi}{w}(x - w/2)] \tag{6.72}$$

where R_e is the reflection coefficient of the floor given by

$$R_e = \frac{\eta_\ell - \dfrac{k_b}{k_p} z_b}{\eta_\ell + \dfrac{k_b}{k_p} z_b} \tag{6.73}$$

Solving for the mode amplitudes B_p, we find

$$B_p = \frac{-2Y_b}{jwk_b(e^{jk_pd} + R_e e^{-jk_pd})} \int_{-w/2}^{w/2} M_x(x) \sin\left[\frac{p\pi}{w}(x - w/2)\right] dx \tag{6.74}$$

and the new Green's function is given by

$$G^e(x, x') = \sum_{p=1}^{\infty} \frac{-2k_p}{w} \left[\frac{e^{jk_pd} - R_e e^{-jk_pd}}{e^{jk_pd} + R_e e^{-jk_pd}}\right] \sin\left[\frac{p\pi}{w}(x - w/2)\right] \sin\left[\frac{p\pi}{w}(x' - w/2)\right] \tag{6.75}$$

Employing the above results, the integral equation for the E-polarization case is obtained as

$$\sin\phi_o e^{jkx\cos\phi_o} = \frac{k_o}{4}\left(1 + \frac{1}{k_o^2}\frac{\partial^2}{\partial x^2}\right) \int_{-w/2}^{w/2} M_x(x') H_o^{(2)}(k_o|x - x'|) dx'$$

$$+ \sum_{p=1}^{\infty} \frac{\sin\left[\frac{p\pi}{w}(x - w/2)\right]}{w\eta'_{ep}} \int_{-w/2}^{w/2} M_x(x') \sin\left[\frac{p\pi}{w}(x' - w/2)\right] dx' \tag{6.76}$$

where η'_{hp} is the normalized surface impedance of the groove looking into the aperture, given by

$$\eta'_{ep} = z_b \frac{\eta_\ell + j z_b \frac{k_b}{k_p} \tan k_p d}{j\eta_\ell \frac{k_p}{k_b} \tan k_p d + z_b} \tag{6.77}$$

It is noted that (6.68) and (6.76) are identical to (6.30) and (6.47) with the only modification that the normalized mode impedances η_{hp} and η_{ep} are replaced by the normalized equivalent impedances η'_{hp} and η'_{ep} looking into the aperture. It is also noted that if the groove is terminated by a perfect conductor, $\eta_\ell = 0$ and

$$\eta'_{hp} = \eta_{hp} \quad , \quad \eta'_{ep} = \eta_{ep}$$

and the formulation reduces to that of the homogeneously filled rectangular groove.

6.4 Dominant-Mode (Quasi-Static) Formulation

For large apertures, a numerical approach is the only alternative to the solution of (6.30) and (6.47). However, in many cases the characterization of narrow width grooves is of practical interest. With this motivation the narrow groove has been modelled as an impedance insert in an effort to simplify the analysis [68]. Unfortunately, the resulting quasi-static integral equations were not amenable to an analytical solution but, nevertheless, it was possible to derive accurate empirical echo width formulae through the examination of numerical data. This was essentially done without a direct (analytical) evaluation of the current on the impedance insert.

In this section we consider the solution of the integral equations for a narrow rectangular groove without invoking the impedance approximation used in [68]. It is shown that by retaining the dominant mode supported by the rectangular groove, the resulting quasi-static integral equations are comparable to those associated with the perfectly conducting narrow strip considered in Section (3.3.2). They are therefore amenable to analytic solution yielding the exact field distribution or equivalent currents across the groove's aperture. The derived currents exhibit the an edge behavior similar to that associated with the currents of a perfectly conducting half plane or strip. On the other hand, the corresponding current behavior based on the (numerical) impedance simulation of the groove is quite different. However the resulting echo widths are comparable.

The derived analytical expressions for the equivalent aperture currents are of potential importance in constructing suitable models for long and narrow three-dimensional apertures. Also, unlike the echo width formulae given in [68], these derived here are valid for all groove depths and material fillings. In this sections, the exact integral equations derived for a two-dimensional rectangular groove will be simplified to the case of a narrow width groove and solved for the equivalent magnetic currents across the aperture. The accuracy of the currents is examined by a comparison with the numerical data. Simple echo width expressions are also given for the principal polarizations which are treated separately.

6.4.1 H-polarization

When $kw \ll 1$, the Green's function $G^h(x;x')$ can be substantially simplified by retaining the first term of the sum, corresponding to the lowest order mode in the cavity. The integral equation (6.30) then reduces to

$$Z_o e^{jkx\cos\phi_o} = \frac{1}{2w\eta_h}\int_{-w/2}^{w/2} M_z(x')dx' + \frac{k_o}{4}\int_{-w/2}^{w/2} M_z(x')H_o^{(2)}(k_o|x-x'|)dx' \tag{6.78}$$

where

$$\eta_h = j\sqrt{\frac{\mu_r}{\epsilon_r}}\tan(k_b d) \tag{6.79}$$

is the normalized impedance of the dominant mode which can be also identified as the normalized impedance at the surface of a grounded slab of thickness d. It is interesting to note that if the first integral in the right hand side of (6.78) is replaced by $wM_z(x)$, then (6.78) reduces to

$$Z_o e^{jkx\cos\phi_o} = \frac{M_z(x)}{2\eta_h} + \frac{k_o}{4}\int_{-w/2}^{w/2} M_z(x')H_o^{(2)}(k_o|x-x'|)dx' \tag{6.80}$$

which is the integral equation based on the impedance boundary condition

$$E_x(x) = \eta_h Z_o H_z(x) \tag{6.81}$$

applied over the extent of the aperture (see equation (5.32)). On the other hand, the integral equation (6.78) is based on the relation

$$\frac{1}{w}\int_{-w/2}^{w/2} E_x(x')dx' = \eta_h Z_o H_z(x) \tag{6.82}$$

This observation reveals the inherent local nature of the impedance boundary condition and its underlying assumption that the current is more likely to be slowly varying. Not surprisingly, (6.80) predicts a rather smooth behavior of the current distribution near the edges of the groove at $x = \pm w/2$. In contrast, a numerical solution of (6.78) gives the usual singular form of $M_z(x)$ at the same locations. Another interesting property of the "boundary condition" (6.82) is the independence of the left hand member from x. This property will be exploited later to arrive at a closed-form solution to the integral equation.

To further simplify (6.78) for $k_o w \ll 1$, we introduce the small argument expansion for the Hankel function as we did for the narrow strip,

$$H_o^{(2)}(z) \simeq 1 - j\frac{2}{\pi}\ln\left(\frac{\gamma z}{2}\right) + \mathcal{O}(z^2, z^2\ln z) \tag{6.83}$$

where $\ln\gamma$ is Euler's constant. Substituting this into (6.78) and retaining only terms to $\mathcal{O}(kw)$ we have

$$\int_{-w/2}^{w/2} M_z(x')\ln|x - x'|dx' = j\frac{2\pi}{k_o}Z_o$$
$$+\left[\frac{\pi}{jk_o w\eta_h} - \ln\left(\frac{k_o\gamma}{2}\right) - j\frac{\pi}{2}\right]\int_{-w/2}^{w/2} M_z(x')dx' \tag{6.84}$$

Further, by introducing the same change of variables as (3.51)

$$\xi = \frac{2x}{w} \;,\quad \xi' = \frac{2x'}{w} \tag{6.85}$$

(6.84) becomes

$$\int_{-1}^{1} M_z(\xi')\ln|\xi - \xi'|d\xi' = j\frac{4\pi}{k_o w}Z_o + \left[\frac{\pi}{jk_o w\eta_h} - \ln\left(\frac{k_o w\gamma}{4}\right) - \frac{j\pi}{2}\right]\int_{-1}^{1} M_x(\xi')d\xi' \tag{6.86}$$

The above singular integral equation can be inverted by noticing that the right hand side of (6.86) is independent of ξ, and upon invoking the identity (3.54)

$$\int_{-1}^{1}(1-x'^2)^{-1/2}\ln|x-x'|dx' = -\pi\ln 2 \qquad x\in[-1,1]$$

we find

$$M_z(\xi) = Z_o\chi_h(1-\xi^2)^{-1/2} = Z_o\frac{\chi_h}{\sqrt{1-\left(\frac{x}{w/2}\right)^2}} \tag{6.87}$$

where χ_h is a complex constant given by

$$\chi_h = \frac{4j}{k_o w\left[\ln\left(\frac{k_o w\gamma}{8}\right)+j\frac{\pi}{2}\left(1+\frac{2}{k_o w\eta_h}\right)\right]} \tag{6.88}$$

It is noted that the aperture magnetic current (6.87) has a functional form exactly similar to that of the electric current of a narrow strip (3.56). In fact, when $\eta_h\rightarrow\infty$ corresponding to an open slot, we find that

$$\lim_{\eta_h\rightarrow\infty}\chi_h = \frac{4j}{k_o w\left[\ln\left(\frac{k_o w\gamma}{8}\right)+j\frac{\pi}{2}\right]} \tag{6.89}$$

which is analogous to the E-polarization result obtained for the narrow strip (3.58). This result is, of course, expected based on Babinet's principle [19, 66].

6.4.2 E-polarization

A similar derivation can be carried out for E-polarization. By retaining the lowest order mode in the groove, (6.47) becomes

$$\sin\phi_o e^{jkx\cos\phi_o} = \frac{1}{w\eta_e}\cos(\frac{\pi x}{w})\int_{-w/2}^{w/2}M_x(x')\cos\frac{\pi x'}{w}dx'$$

$$+\frac{k_o}{4}\left(1+\frac{1}{k_0^2}\frac{\partial^2}{\partial x^2}\right)\int_{-w/2}^{w/2}M_x(x')H_o^{(2)}(k_o|x-x'|)dx' \tag{6.90}$$

where

$$\eta_e = j\frac{k_b}{k_1}\sqrt{\frac{\mu_r}{\epsilon_r}}\tan(k_1 d) \tag{6.91}$$

is the normalized wave impedance of the lowest order mode with

$$k_1^2 = k_b^2 - \left(\frac{\pi}{w}\right)^2 \tag{6.92}$$

Next, by introducing the small argument expansion of the Hankel function and the change of variables defined in (6.85) we obtain

$$\begin{aligned}\sin\phi_o &= \frac{1}{2\eta_e}\cos\left(\frac{\pi}{2}\xi\right)\int_{-1}^{1} M_x(\xi')\cos\left(\frac{\pi}{2}\xi'\right)d\xi' \\ &\quad -\frac{j}{\pi k_o w}\frac{d^2}{d\xi^2}\int_{-1}^{1} M_x(\xi')\ln|\xi-\xi'|d\xi' \end{aligned}\tag{6.93}$$

where we have retained only terms to $\mathcal{O}(kw)$. An approximate solution for M_x can now be obtained by satisfying (6.93) at $\xi = 0$. We have

$$\frac{d^2}{d\xi^2}\int_{-1}^{1} M_x(\xi')\ln|\xi-\xi'|d\xi' = j\pi k_o w\left[\sin\phi_o - \frac{1}{2\eta_e}\int_{-1}^{1} M_x(\xi')\cos(\frac{\pi}{2}\xi')d\xi'\right] \tag{6.94}$$

whose right hand side is independent of ξ. Thus, by invoking the identity (3.55)

$$\frac{d^2}{dx^2}\int_{-1}^{1}\sqrt{1-x'^2}\ln|x-x'|dx' = \pi \qquad x\in[-1,1]$$

the above integral equation is inverted and M_x may be expressed as

$$M_x(\xi) = \chi_e\sqrt{1-\xi^2} = \chi_e\sqrt{1-\left(\frac{x}{w/2}\right)^2} \tag{6.95}$$

where χ_e is given by

$$\chi_e = \frac{jk_o w\sin\phi_o}{1+\dfrac{jk_o w J_1(\pi/2)}{\eta_e}} \tag{6.96}$$

and J_1 denotes the first order Bessel function. In arriving at this result, we also made use of the identity [69]

$$\int_{-1}^{1} \sqrt{1-x^2}\cos(\mu x)dx = \frac{\pi}{2\mu}J_1(\mu) \tag{6.97}$$

It is noted that η_e is generally inductive for $kw \ll 1$, and thus the derived expression for χ_e is nonsingular within the expected validity range of (6.95). Again, as $\eta_e \rightarrow \infty$ corresponding to an open gap,

$$\lim_{\eta_e \rightarrow \infty} \chi_h = jk_o w \sin\phi_o \tag{6.98}$$

which is analogous to the H-polarization result obtained for the narrow strip (3.59).

The far zone scattered field at a point (ρ, ϕ) in cylindrical coordinates can be computed from (6.53)-(6.54). Upon approximating the exponential $e^{jk_o x' \cos\phi}$ with unity, we have

$$\sigma_h = k_o \left| Y_o \int_{-w/2}^{w/2} M_z(x')dx' \right|^2 = k_o \left| \frac{\pi w}{2} \chi_h \right|^2 \tag{6.99}$$

and

$$\sigma_e = k_o \left| \sin\phi \int_{-w/2}^{w/2} M_x(x')dx' \right|^2 = k_o \left| \frac{\pi w}{4} \chi_e \sin\phi \right|^2 \tag{6.100}$$

which in the backscattering direction, yield

$$\sigma_h = \frac{2\pi\lambda}{\left| \ln\left(\frac{k_o w \gamma}{8}\right) + j\frac{\pi}{2}\left(1 + \frac{2}{k_o w \eta_h}\right) \right|^2} \tag{6.101}$$

$$\sigma_e = \frac{\pi\lambda \left(\frac{k_o w}{2\sin\phi}\right)^4}{2\left| 1 + 0.5696\frac{jk_o w}{\eta_e} \right|^2} \tag{6.102}$$

Before a detailed examination of the the above quasi-static results, we remark that the same analysis presented above is applicable to a narrow groove whose floor

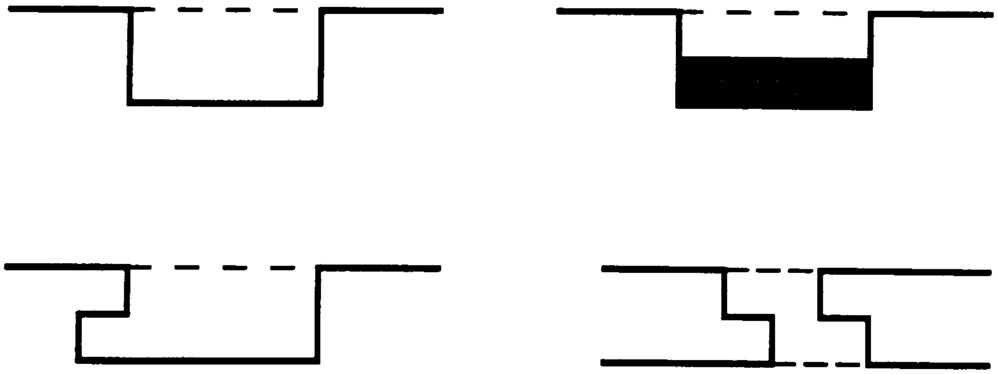

Figure 6.5: Geometries of some gaps and crack of practical interest.

satisfies an impedance boundary condition. In this case the mode impedances η_h and η_e are replaced by the corresponding normalized equivalent impedances η'_h and η'_e looking into the aperture. This allows an analysis of partially filled narrow grooves as well as narrow cracks of simple shapes (Figure 6.5). For such geometries, a quasi-static or empirical estimate of the impedance may be used [68].

The derived formulae for the gap echo width and aperture currents are based on low frequency approximations to the exact integrals. They are thus expected to be valid for small groove widths and it is, therefore, of interest to examine their accuracy limitations as the width of the groove increases. Also, of interest is a comparison of the analytical echo width formulae derived here with the corresponding empirical ones given in [68].

Figure 6.6 presents a comparison of the derived H-polarization current distribution (6.87) versus that obtained from a numerical solution of the full-wave integral equation (6.80). Similar comparisons are also given in Figure 6.7 for E-polarization. In both cases $\phi_o = \pi/2$ and for this incidence the expressions (6.87) and (6.95) are in good agreement with the exact data (although only amplitude comparisons are shown, good agreement was observed for the phase as well). This holds independent of ϕ_o for small w. As the groove width increases, however, the exact current is to an increasing extent a function of ϕ_o and as noted in [68] the angular dependence is noticeable for $w \geq 0.15\lambda$. Since the quasi-static H-polarization current (6.87) is independent of ϕ_o, it is then applicable up to this value of w. Nevertheless, we have found that for normal incidence, (6.87) is quite accurate up to $w \approx 0.25\lambda$ and its accuracy improves for filled grooves. For E-polarization, the derived quasi-static current solution is an explicit function of ϕ_o and, therefore, remains accurate for all angles of incidence up to $w \approx 0.25\lambda$.

Comparisons of the echo width formulae with numerical data are given in Figures 6.8 – 6.11 for the H-polarization and Figures 6.12 – 6.13 for the E-polarization case, respectively. These results correspond to the backscattering computations at normal incidence ($\phi = \phi_o = \pi/2$). It is observed that the quasi-static formulae remain accurate for all groove depths provided w is kept within its validity bounds. The empirical formulae given in [68] were generally found to agree with these results, except near the resonance regions for the H-polarization where the empirical formula fails. This is illustrated in Figure 6.11 for an empty groove whose resonant depth is $d = 0.234\lambda$ when $w = 0.1\lambda$. Also, in contrast to H-polarization, the E-polarization echo width does not display any resonant characteristics for small w since there is no traveling mode in the cavity. In fact, for $w < 0.2\lambda$, the E-polarization echo width of an empty groove is independent of depth for $d > 0.1\lambda$.

Finally, we remark that the above solutions are of potential utility in the analysis of long three-dimensional (finite) grooves. For example, Figure 6.14 shows the radar cross section from a 2.5λ long groove whose width and depth are $\lambda/4$. In this case, the quasi-static result was obtained from (1.26) based on the physical optics approximation. Good agreement with the full-wave three-dimensional moment method solution (Chapter 7) is observed.

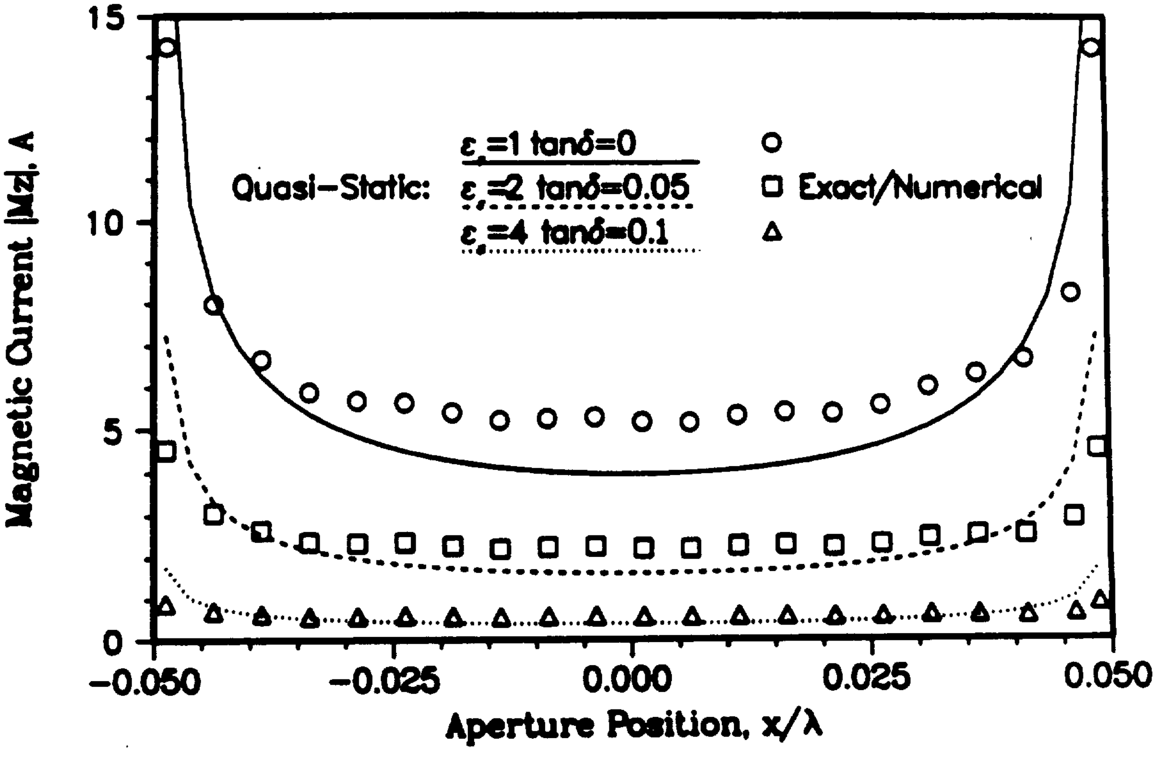

Figure 6.6: H-polarization equivalent surface magnetic currents for a groove of width $w = 0.1\lambda$ and depth $d = 0.2\lambda$; Comparison of analytical and numerical data.

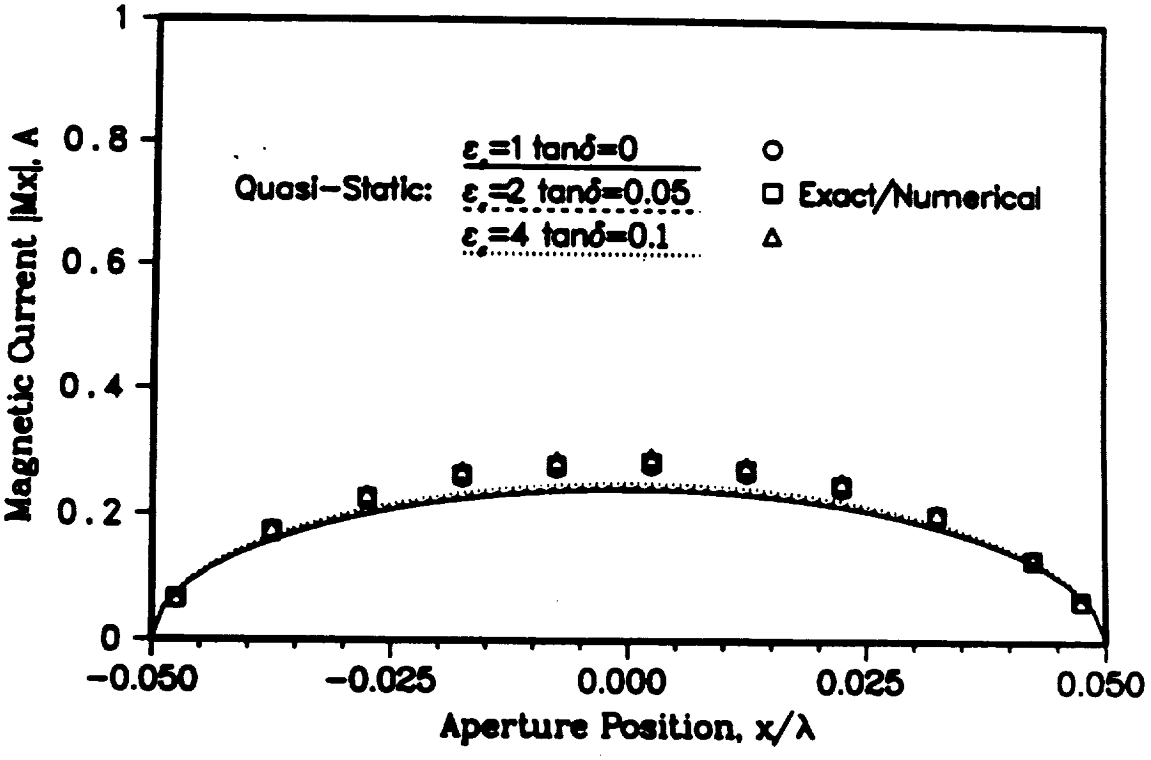

Figure 6.7: E-polarization equivalent surface magnetic currents for a groove of width $w = 0.1\lambda$ and depth $d = 0.2\lambda$; Comparison of analytical and numerical data.

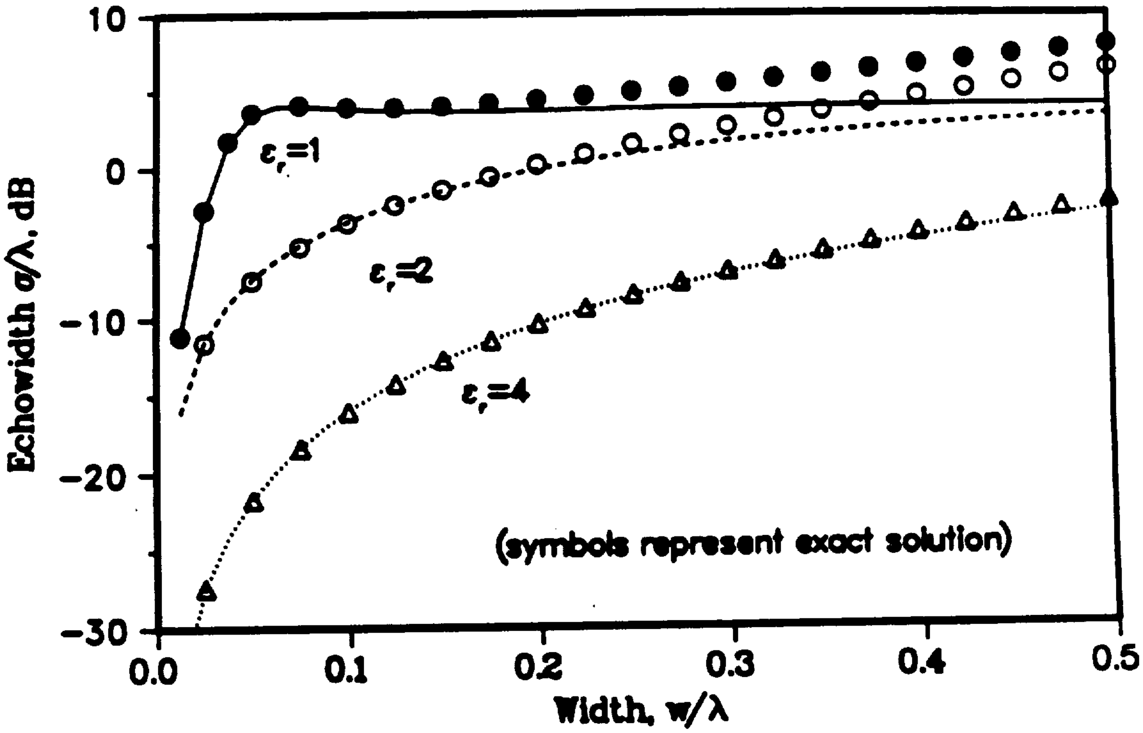

Figure 6.8: H-polarization normal incidence echo width for a groove of depth $d = 0.2\lambda$ as a function of width for three different material fillings.

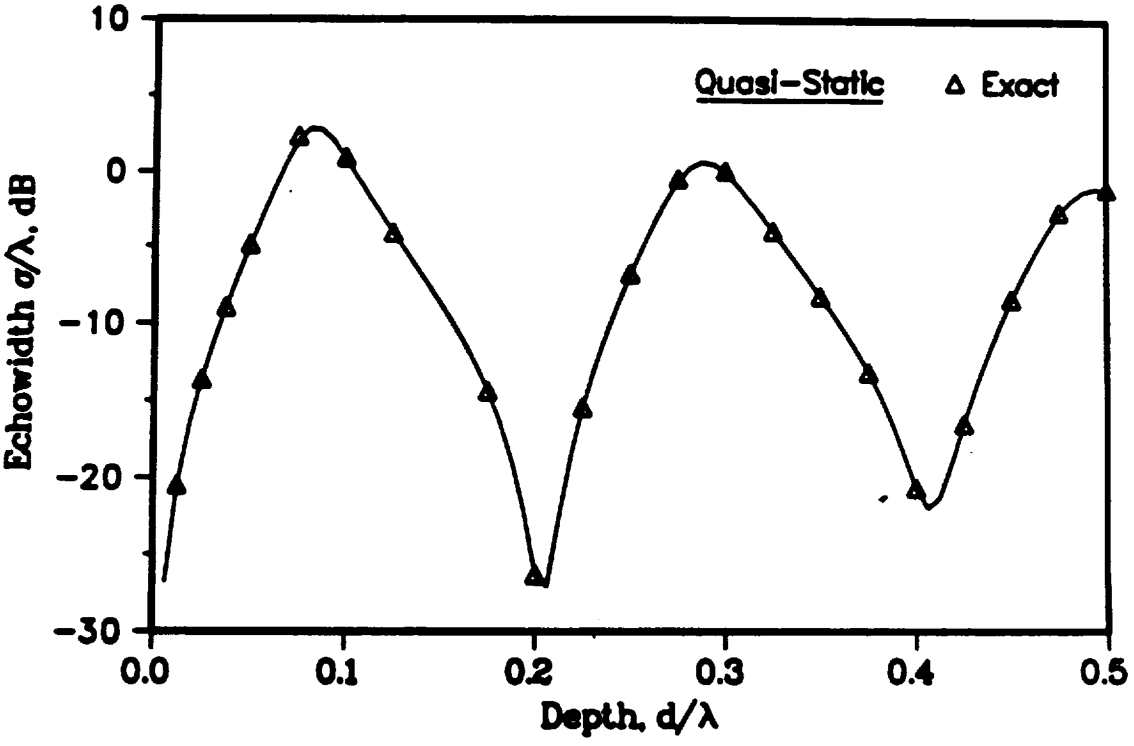

Figure 6.9: H-polarization normal incidence echo width for an empty groove as a function of depth for three different widths ($w = 0.05\lambda, 0.1\lambda$, and 0.2λ).

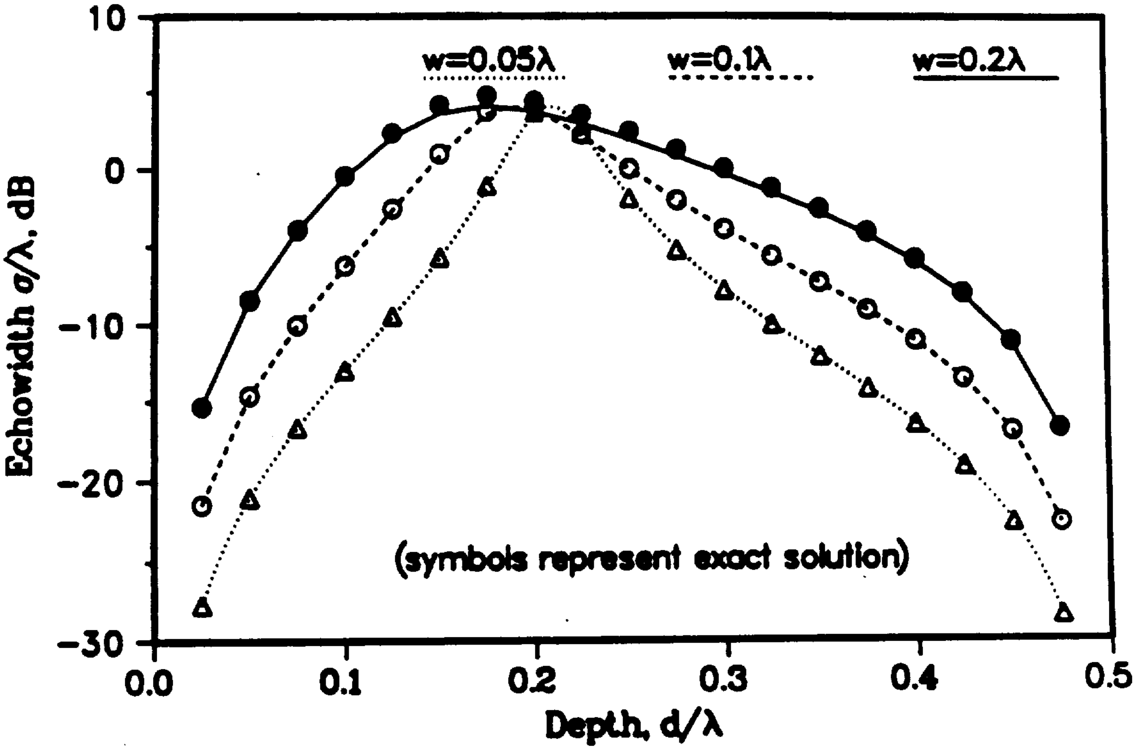

Figure 6.10: H-polarization normal incidence echo width as a function of depth for a groove of width $w = 0.15\lambda$ filled with a material having $\epsilon_r = 4 - j1$ and $\mu_r = 1.5 - j0.05$.

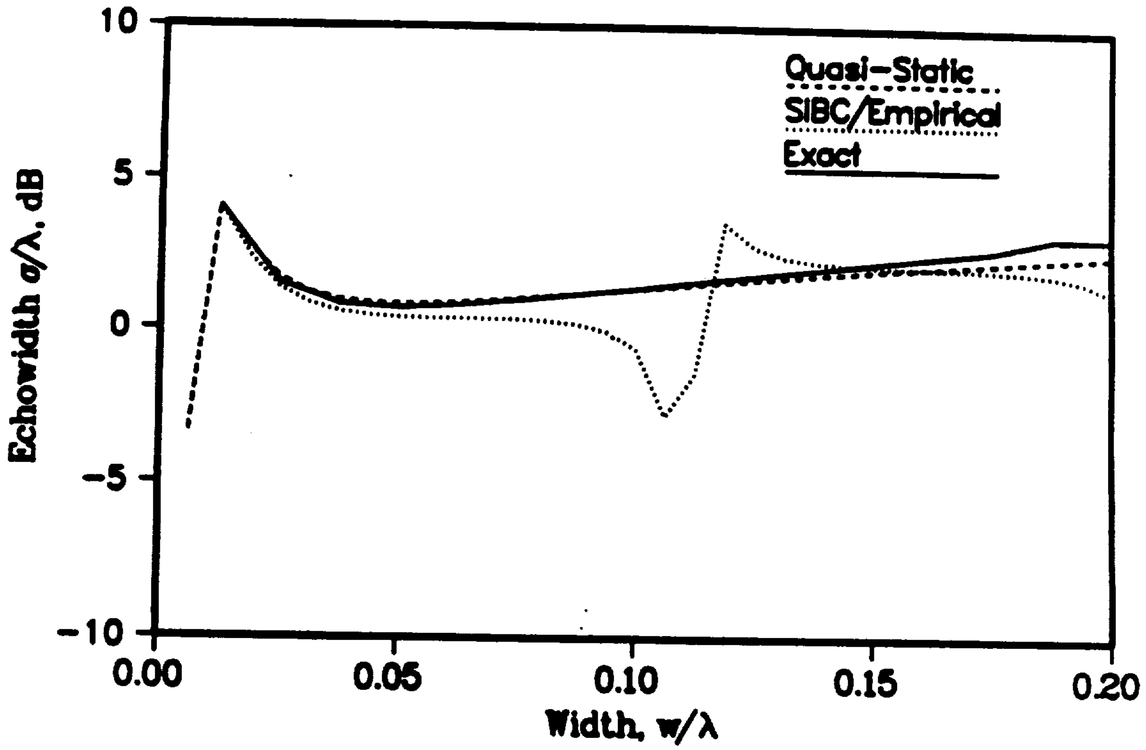

Figure 6.11: Comparison of the quasi-static and empirical solutions [68] with numerical data as a function of width for $d = 0.234\lambda$ (near resonance).

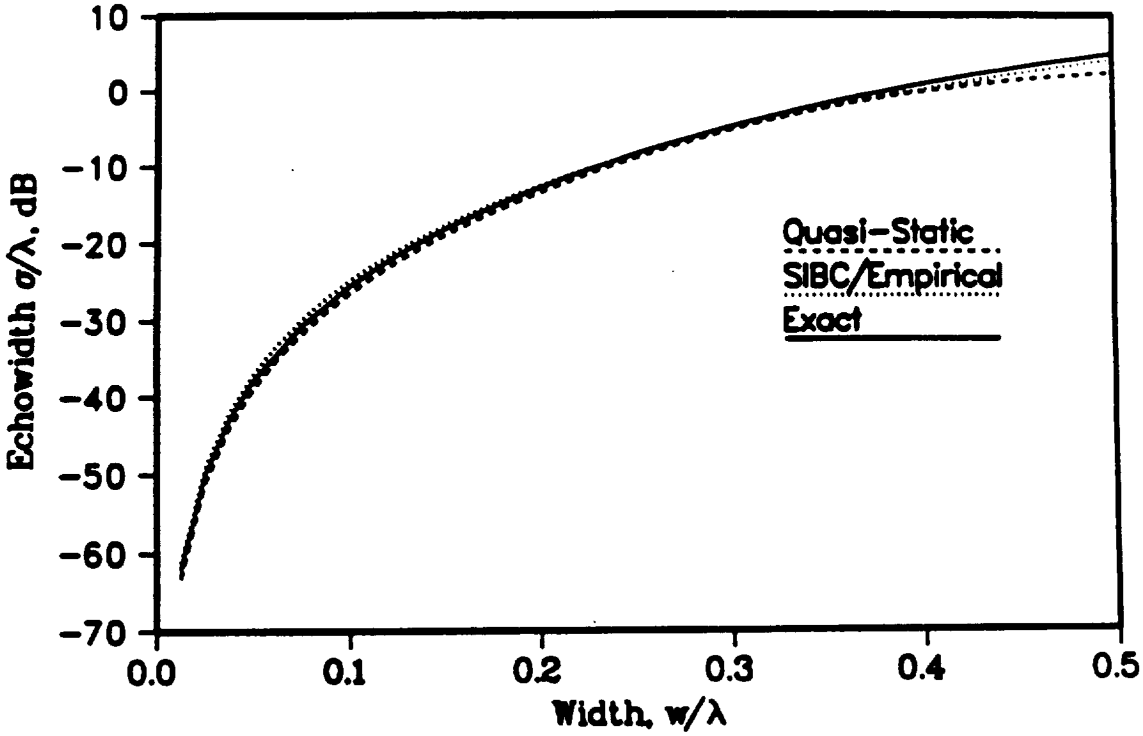

Figure 6.12: E-polarization normal incidence echo widths for an empty groove as a function of width ($d = 0.2\lambda$); Comparison of the quasi-static, empirical [68], and numerical solutions.

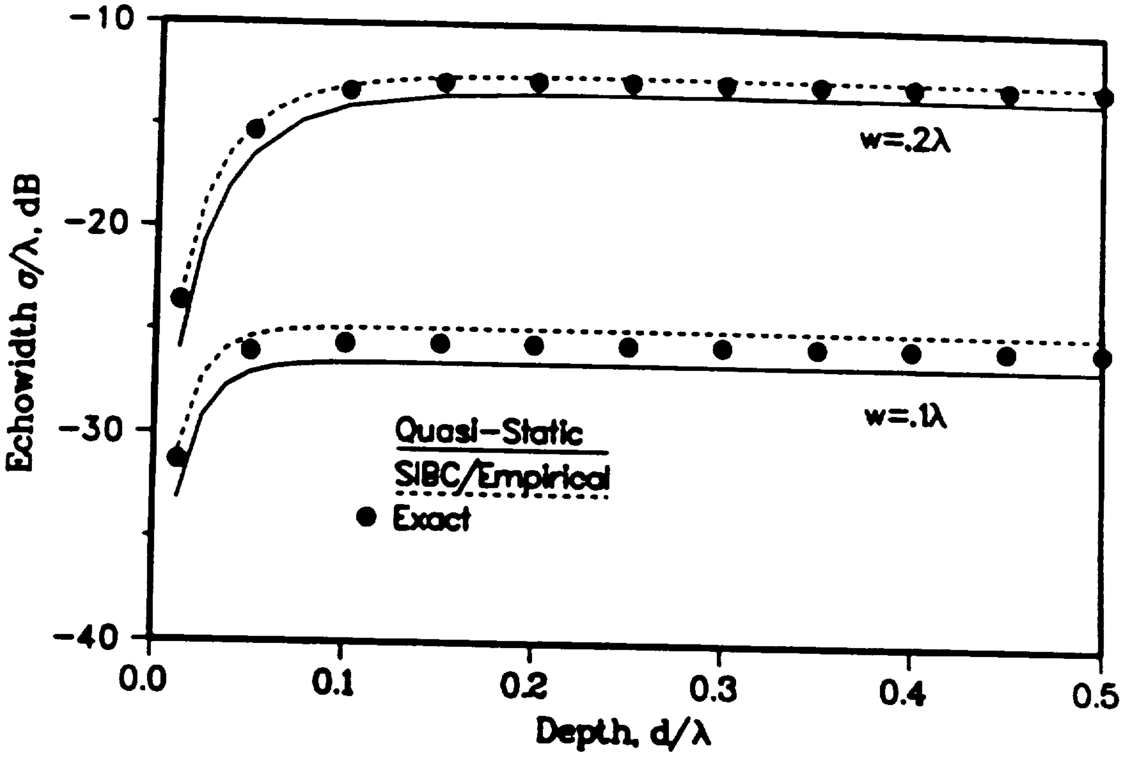

Figure 6.13: E-polarization normal incidence echo widths for an empty groove as a function of depth; Comparison of the quasi-static, empirical [68], and numerical solutions.

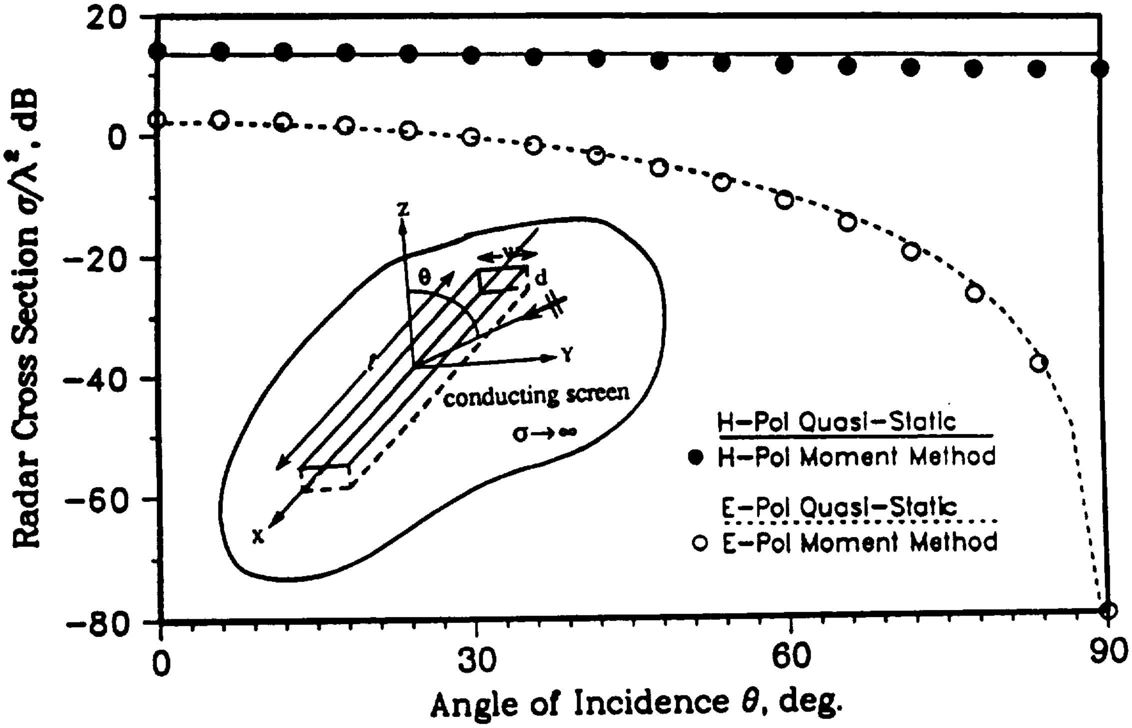

Figure 6.14: Backscattering cross section of a long empty cavity ($\ell = 2.5\lambda, w = 0.25\lambda, d = 0.25\lambda$); Comparison of the quasi-static (factored echo width) and full-wave three-dimensional Moment Method solution.

6.5 GIBC Formulation

In the previous sections, we presented a rigorous full-wave formulation for computing the scattering by a filled rectangular groove in a ground plane. This was further approximated to the case of a narrow groove based on a quasi-static analysis of the pertinent integral equations. In this section, we present another class of approximate formulations for the general analysis of grooves which make use of generalized impedance boundary conditions.

As mentioned in Chapter 5, the material filled groove may be simulated by a two-dimensional impedance insert. Indeed, we have already encountered the SIBC formulation for the groove in equation (6.80). In this section, we examine the accuracy of this boundary condition as well as those of higher orders.

Consider first the SIBC. In this case, the integral equations (5.32) and (5.33) are applicable and by setting $F_\ell = F'_\ell = 0$, $\ell = 2, 3$ in (5.34) and (5.35), we obtain

$$Z_o e^{jk_o x \cos\phi_o} = \frac{1}{2} F_1(x) M_z(x) + \text{DFT}^{-1}\left\{\widehat{M}_z \hat{\Upsilon}\right\} \tag{6.103}$$

and

$$\sin\phi_o e^{jk_o x \cos\phi_o} = \frac{1}{2F'_1(x)} M_x(x) + \frac{1}{k_o^2}\,\text{DFT}^{-1}\left\{(k_o^2 - D_x^2)\widehat{M}_x \hat{\Upsilon}\right\} \tag{6.104}$$

which are subsequently solved by the CGFFT method.

Figure 6.15 shows the amplitude and phase of the equivalent magnetic current density for a half-wavelength deep (in free space), two wavelengths wide rectangular groove filled with a lossy material of high index of refraction. In this case, the conditions (5.5)-(5.6) are satisfied

$$|\aleph| = 7.7 \qquad |\Im\text{m}\aleph| k_o d = 5.5$$

and the agreement with the full-wave solution is very good. In contrast, when the groove is filled with a relatively low contrast material, SIBC is no longer applicable as the validity conditions of SIBC are violated (Figure 6.16).

Consider the same groove, now simulated by an impedance sheet (insert) satisfying a third order boundary condition. In this case, the integral equations (5.23) and (5.31) are applicable and the CGFFT implementation is given by (5.34)–(5.35). From Figure 6.17, it is seen that the GIBC solution agrees reasonably well with the exact one except near the groove terminations.

Generally, the current distribution based on the proposed third-order GIBC is not of acceptable accuracy when within 0.25λ of the groove's terminations. However, because it is in good agreement with the exact current distribution elsewhere, one approach in retaining the memory advantage associated with the application of the GIBCs is to combine the exact and GIBC formulations. This is discussed in the next section.

6.6 Hybrid Exact–GIBC Formulation

Based on the above discussion, a procedure for combining the exact and GIBC formulations is to feed the currents predicted by the GIBC integral equation (5.23)–(5.31) away from the edges into the exact integral equation (6.30)–(6.47). The last can then be solved for the remaining currents in the vicinity of the groove terminations. This only requires the inversion of a small matrix and hence the memory demand is essentially unaffected.

To demonstrate this hybrid approach, let us consider the H-polarization and a similar formulation applies to the other polarization as well. Suppose that $M_z^G(x)$ denotes the current computed via the GIBC integral equation (5.23) and we choose

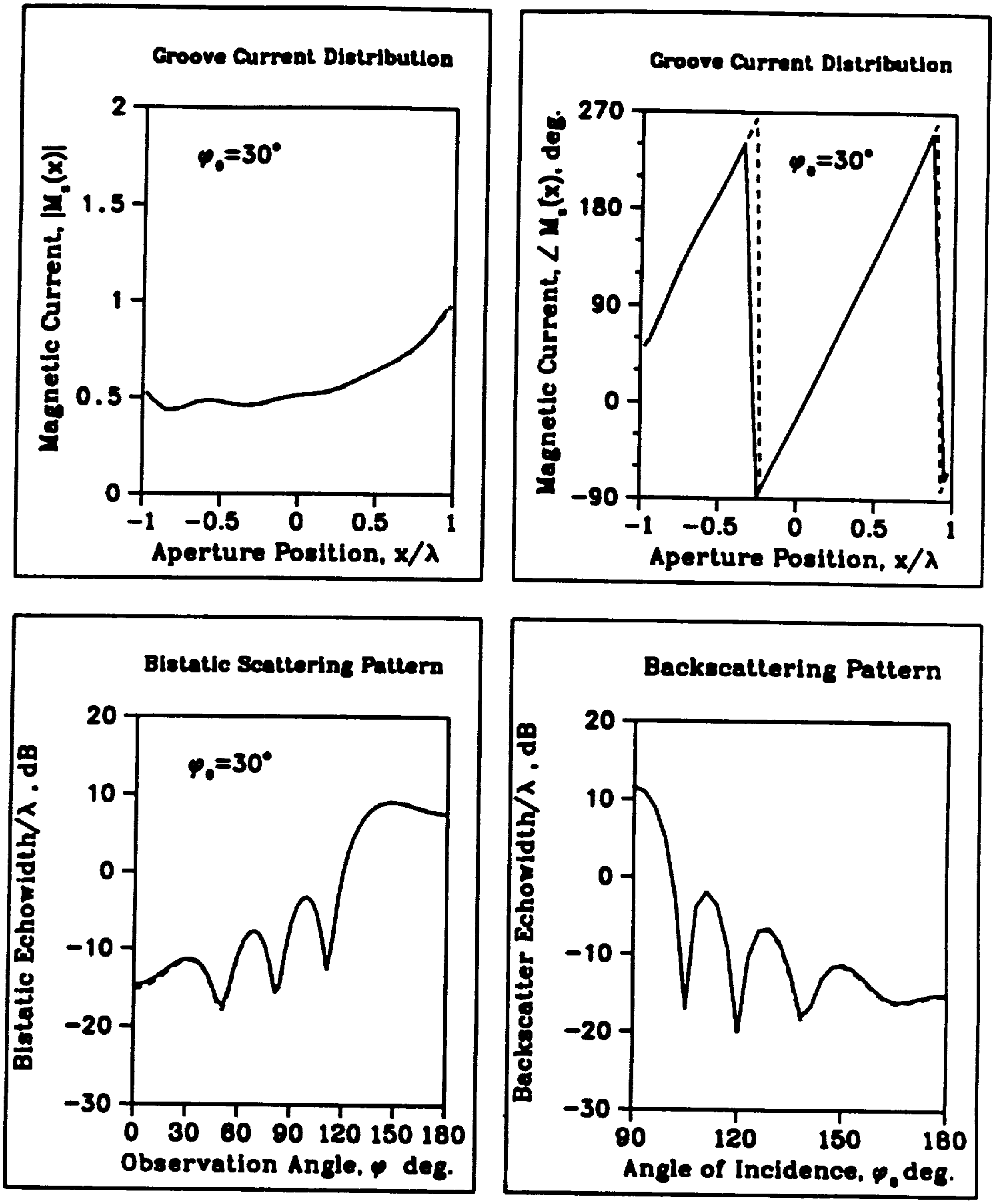

Figure 6.15: Simulation of a groove filled with a high-contrast material; $w = 2\lambda$, $d = 0.5\lambda$; $\epsilon_r = 12.5 - j2.5$, $\mu_r = 4.5 - j1.2$, and $\phi_o = 30°$. Comparison of the full-wave (—) and SIBC (- - -) results.

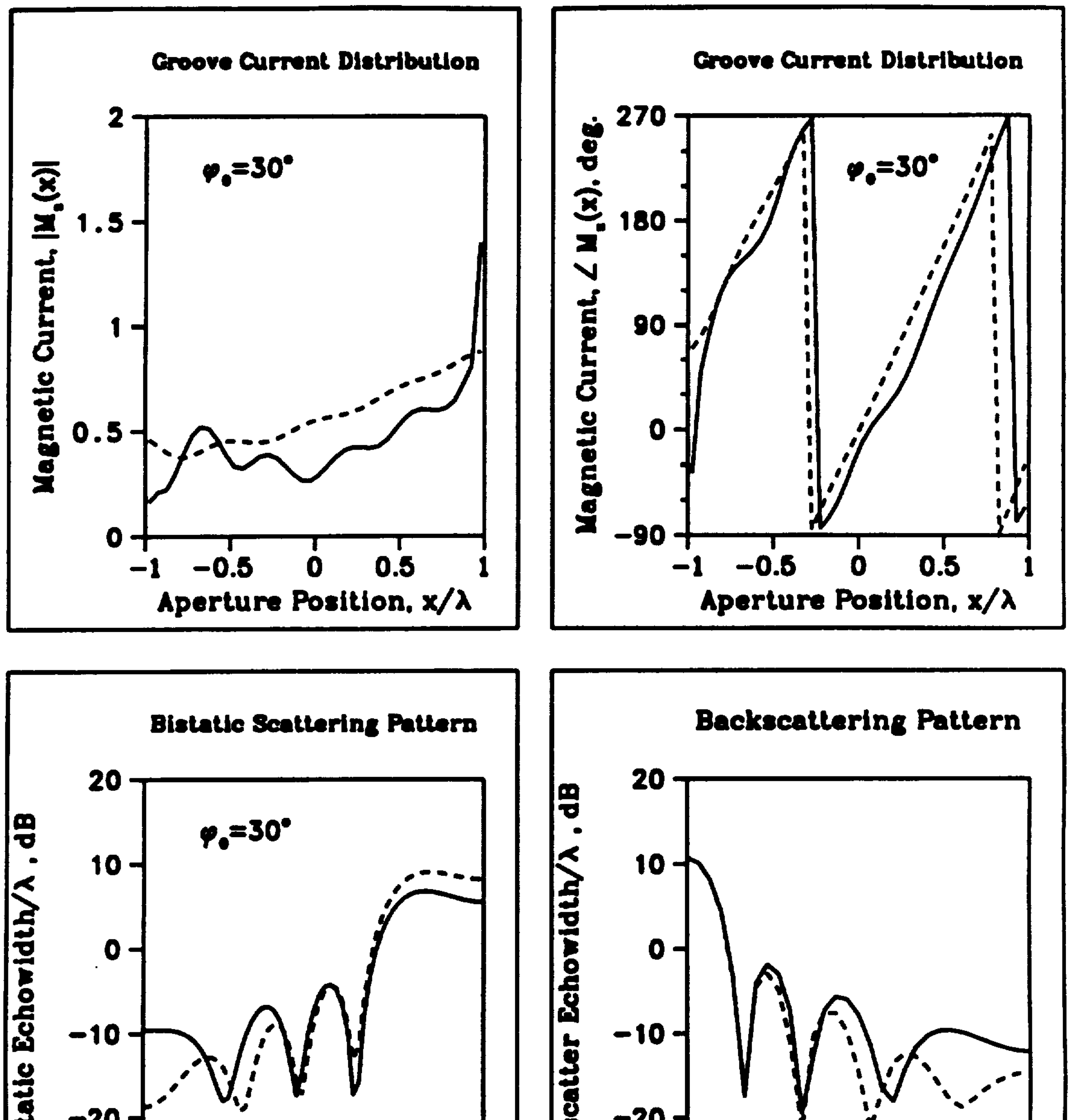

Figure 6.16: Simulation of a filled groove; $w = 2\lambda$, $d = 0.5\lambda$; $\epsilon_r = 12.5 - j2.5$, $\mu_r = 4.5 - j1.2$, and $\phi_o = 30°$. Comparison of the full-wave (—) and SIBC (- - -) results.

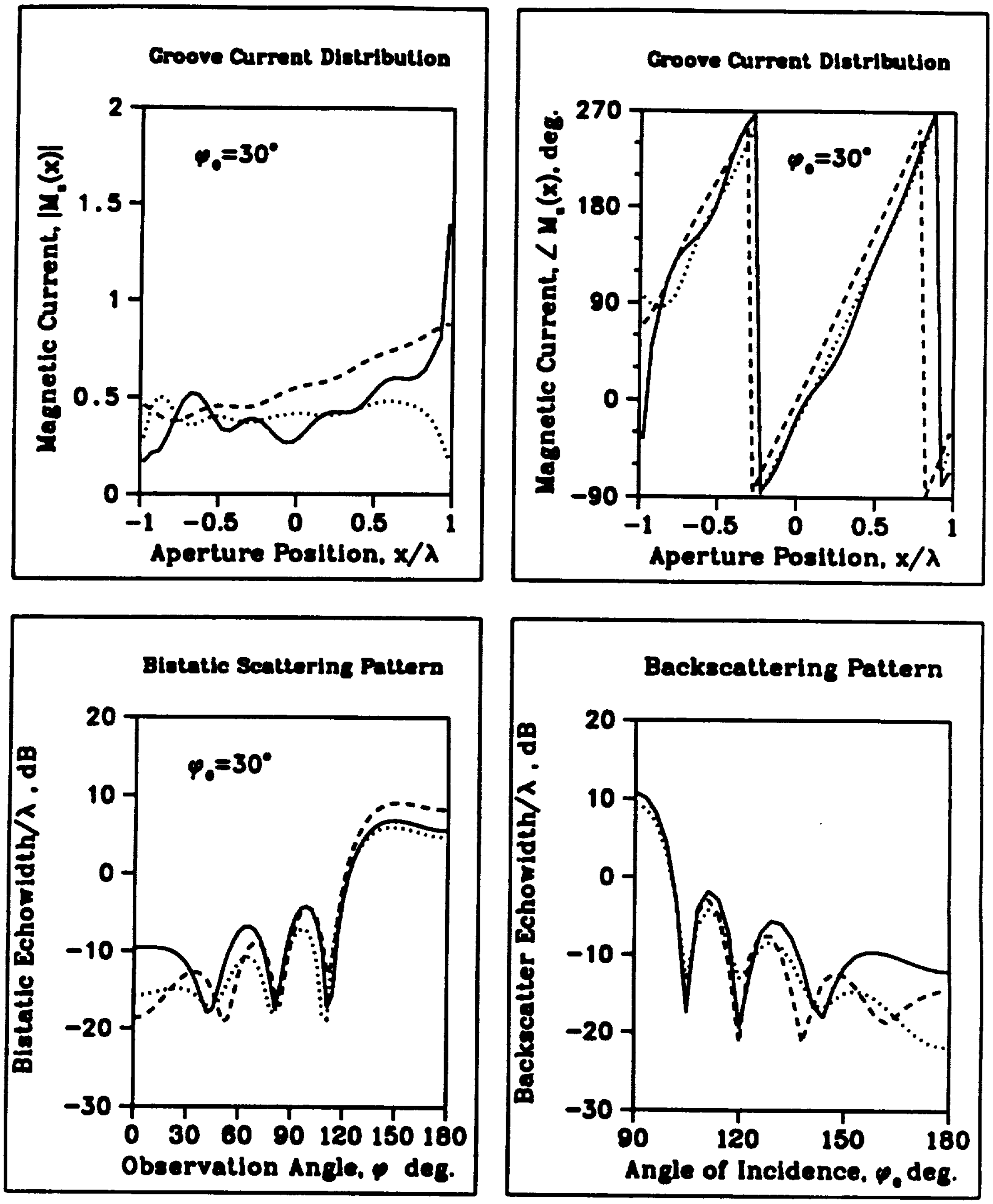

Figure 6.17: Comparison of the full-wave (—), SIBC (- - -), and the third order GIBC (···) solutions for a filled groove; $w = 2\lambda$, $d = 0.5\lambda$; $\epsilon_r = 2.5 - j0.2$, $\mu_r = 1.8 - j0.1$.

to approximate the true aperture current as

$$M_z(x) = \begin{cases} M_z^G(x) & |x| < \frac{w}{2} - x_\Delta \\ M_z^C(x) & |x| > \frac{w}{2} - x_\Delta \end{cases} \tag{6.105}$$

where M_z^C denotes the unknown currents near the edges of the groove. To compute M_z^C we substitute (6.105) into (6.30) and this yields

$$\begin{aligned} 2e^{jk_o x \cos\phi_o} + & \int_{-w/2+x_\Delta}^{w/2-x_\Delta} M_z^G(x') \left[jk_o Y_b G_b(x,x') - \frac{k_o Y_o}{2} H_o^{(2)}(k_o|x-x'|) \right] dx' \\ = & -\int_{-w/2}^{-w/2+x_\Delta} M_z^C(x') \left[jk_b Y_b G_b(x,x') - \frac{k_o Y_o}{2} H_o^{(2)}(k_o|x-x'|) \right] dx' \\ & -\int_{w/2-x_\Delta}^{w/2} M_z^C(x') \left[jk_b Y_b G_b(x,x') - \frac{k_o Y_o}{2} H_0^{(2)}(k_o|x-x'|) \right] dx' \end{aligned} \tag{6.106}$$

Assuming that $M_z^G(x)$ has already been computed via a CGFFT solution of (5.23), the entire left-hand side of (6.106) is known and thus, for $x_\Delta < 0.25$, a 4×4 or a 6×6 square admittance matrix is required for the solution of $M_z^C(x)$. In general, continuity of the current density must be imposed at the transition regions between $M_z^G(x)$ and $M_z^C(x)$, and this can be accomplished through a simple averaging.

Figure 6.18 shows the results obtained for the aperture current density of the groove considered before. Clearly, the proposed hybrid solution (HYBRID-3) provides the necessary correction near the terminations where the GIBC solution fails. Bistatic and backscattering patterns corresponding to the same groove are given in Figure 6.19. It is observed from these patterns that the SIBC solution is substantially in error for angles near grazing. The same holds for the GIBC since, as is well known, the contribution of the edge currents is a dominating factor in the computation of the echo width. Notably, the patterns predicted by the hybrid formulation are always in good agreement with the full-wave moment method solution.

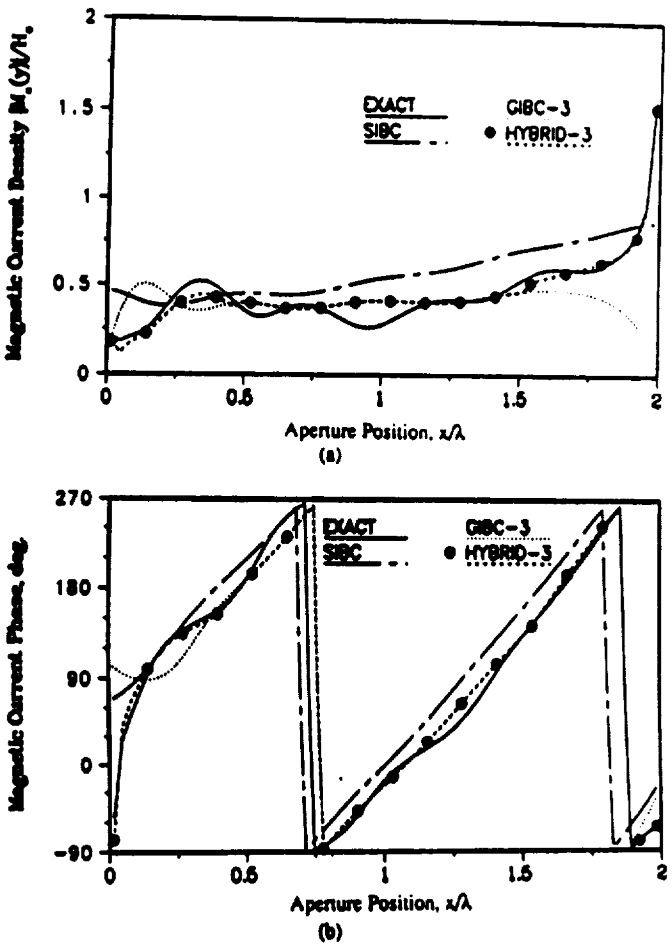

Figure 6.18: Comparison of the current density for a rectangular groove as obtained by the full-wave and approximate formulations; $w = 2\lambda$, $d = 0.5\lambda$; $\epsilon_r = 2.5 - j0.2$, $\mu_r = 1.8 - j0.1$, and $\phi_o = 30°$. (a) Amplitude. (b) Phase.

C-3

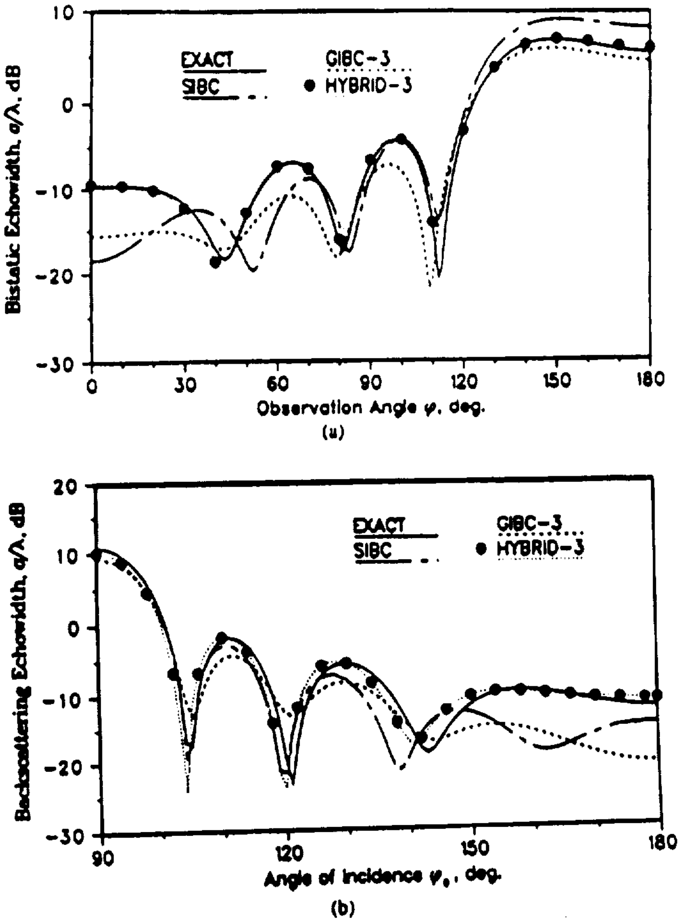

Figure 6.19: Comparison of TE scattering patterns for a rectangular groove as obtained by the full-wave and approximate formulations; $w = 2\lambda$, $d = 0.5\lambda$; $\epsilon_r = 2.5 - j0.2$, $\mu_r = 1.8 - j0.1$. (a) Bistatic $\phi_o = 30°$. (b) Backscatter.

6.7 Tapered Grooves

The GIBC formulation can be directly applied to the scattering from tapered grooves, provided the constant coefficients associated by the employed GIBC are allowed to vary. This, clearly, avoids a need to compute the Green's function or to use a more sophisticated technique such as the finite element method (FEM) [70]. The condition on the slow variation of the impedance for the SIBC is given by (5.7) in addition to (5.5) and (5.6). However, it is possible to simulate more rapid variations by using a higher order GIBC. Consider, for example, the non-rectangular groove shown in Figure 6.20. In this case, the SIBC is inadequate in modelling the groove while a direct application of the third order GIBC formulation is sufficient to yield accurate results.

6.8 Summary

The problem of scattering from two-dimensional rectangular grooves was studied using a full-wave analysis. The analysis is applicable to grooves terminated with perfect or imperfect surfaces. This formulation was specialized to the case of electrically narrow grooves by considering the dominant waveguide modes in the groove and employing the finite Hilbert transform theory based on a quasi-static approximation of the resulting integral equations. Analytical expressions were derived for the equivalent magnetic current distribution over the aperture of narrow grooves. The solutions were found to exhibit the familiar edge behavior observed in the case of narrow strips and slits. Using the derived current distributions, closed form expressions were given for the echo width of the narrow groove and these were compared with numerical data. Their accuracy was examined as a function of width, depth and material filling and were found to be in good agreement with the echo width

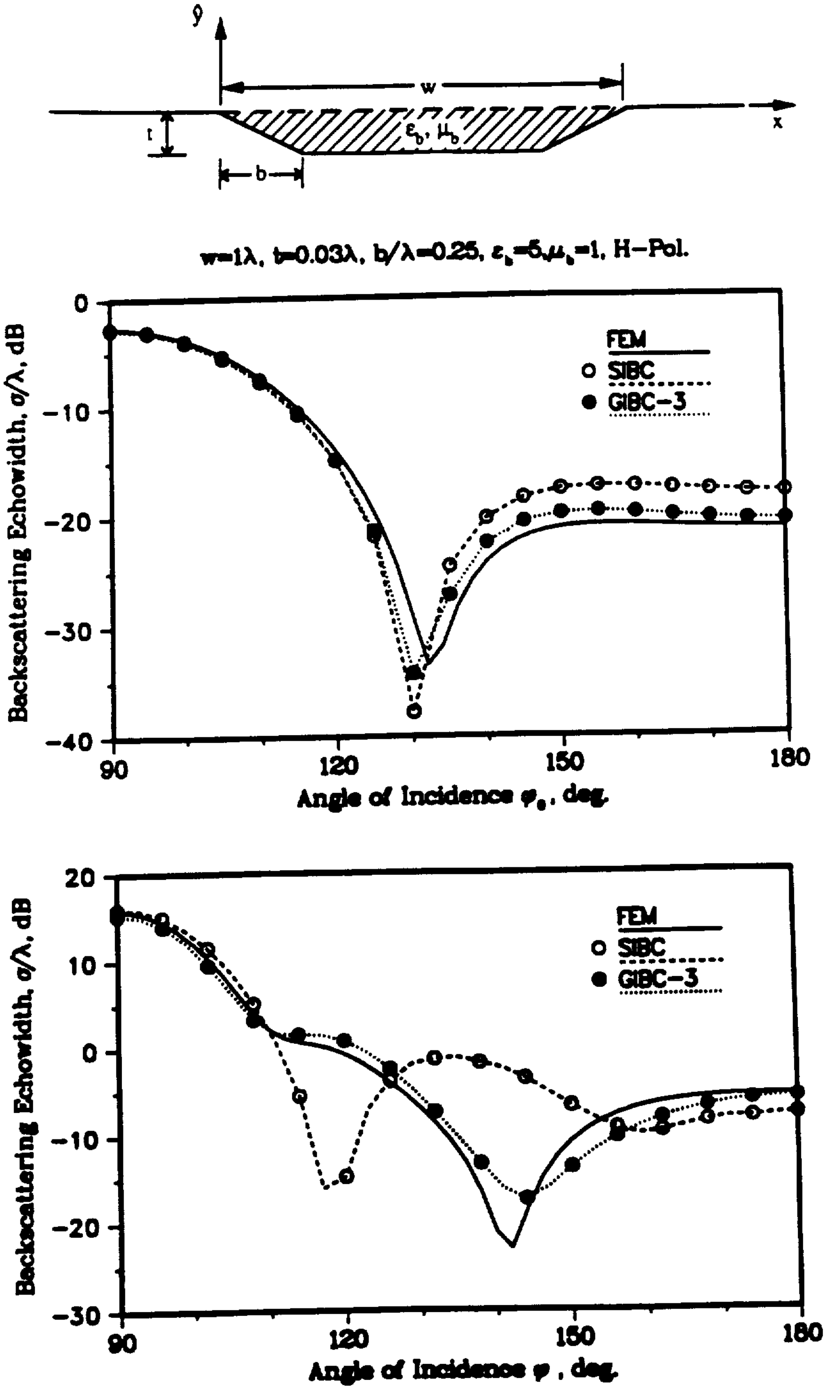

Figure 6.20: Comparison of TE backscattering results based on the SIBC, GIBC-3, and FEM [70] for a non-rectangular filled groove ($\epsilon_r = 5, \mu_r = 1$). (a) Geometry. (b) $w = 1\lambda, d = 0.03\lambda, b = 0.25\lambda$. (c) $w = 2\lambda, d = 0.1\lambda, b = 0.5\lambda$.

data based on full-wave solution for all angles of incidence, provided $w < 0.15\lambda$ for H-polarization and $w < 0.25\lambda$ for E-polarization regardless of the groove's depth. The closed form solutions obtained here were found to be of potential use in the study of the long and narrow grooves and could significantly simplify their analyses.

Furthermore, the scattering behavior of the groove was simulated by the impedance boundary conditions. Both first order (SIBC) and third order GIBC formulations were studied. The formulations based on these boundary conditions were found easier to implement than the full-wave formulation. Also, unlike the exact integral equations, they were amenable to a CGFFT implementation. For high-contrast material fillings, the SIBC was found adequate in modeling the groove. An analytical comparison of the integral equation based on a SIBC simulation with that from a full-wave formulation, revealed a well-known limitation of the SIBC formulation. That is, the SIBC integral equation generates an average of the actual current distribution. By resorting, though, to a third order GIBC the correct current behavior was reasonably predicted away from any abrupt terminations of the groove. The predicted current based on the GIBC simulation was in general incorrect near the edges and to correct this defficiency, a hybrid approach was proposed. Specifically, the currents computed via the GIBC formulation away from the rectangular groove terminations were employed in the exact integral equation to generate a small matrix for the currents in the vicinity of the terminations. This was referred to as the hybrid exact-GIBC formulation and was found to yield a reasonably good prediction of the scattering by filled rectangular grooves.

Finally, when the groove terminations are not abrupt, the hybrid formulation is not required and a direct application of the GIBC formulation may be sufficient.

CHAPTER VII

SCATTERING BY OPEN RECTANGULAR CAVITIES RECESSED IN GROUND PLANES

7.1 Introduction

The characterization of apertures in a ground plane is of considerable importance in radar cross section (RCS) and electromagnetic pulse (EMP) studies. Indeed, a large body of work exists for the analysis of two-dimensional slits in a thick ground plane [71]-[76] or cavity-backed apertures [77]-[79]. Extensions of these procedures to three dimensional characterizations are possible, but so far this has only been done for high frequency techniques. Numerical solutions for three dimensional apertures have been limited to scattering and transmission by openings in a thin ground plane [50],[80]-[82] primarily due to the excessive computational demands and complexity of the solution. The only exception to this is the use of the mode-matching technique for the analysis of rectangular [67] and spherical [83] cavity-backed apertures. Although in principle exact, the mode-matching approach leads to an infinite system of equations in addition to being cumbersome. A need, therefore, exists to develop numerical solutions for cavity backed apertures. Such solutions can provide a characterization of this structure and could serve as a reference for validating new solution algorithms.

In this chapter we consider the scattering by a rectangular cavity-backed aperture. The solution technique employed in the analysis is the full-wave moment method approach considered in the two-dimensional applications of Chapter 6. A fundamental aspect of this method is to employ the aperture fields as the equivalent sources of the fields interior and exterior to the cavity. The complete integral representation of the fields within the cavity makes use of the modal Green's function whereas that external to the cavity makes use of the free space dyadic Green's function. An integral equation for the aperture fields is then constructed by enforcing tangential field continuity across the aperture. Except for being tedious, the entire solution process is straightforward and in an effort to maintain the level of complexity to a minimum, a pulse-basis moment method solution of the integral equation is first discussed. The more useful roof-top basis is also presented. As can be expected, the roof-top basis formulation leads to a more efficient numerical solution at the expense of additional complexity. In either case, the admittance elements associated with the external fields are identical to the impedance elements for a perfectly conducting plate. However, the major difference in computational efficiency among the two formulations lies in the evaluation of the admittance elements associated with the internal fields. These are given in terms of a double sum series whose convergence is substantially improved when higher order basis functions are employed.

In the following sections we first develop the complete field representations in the interior and exterior regions of the cavity. The integral equation is then formulated by requiring continuity of the tangential magnetic field across the aperture and discretized using pulse and roof-top basis functions. The evaluation of the admittance elements is discussed in some detail since these are of crucial importance in the overall accuracy and efficiency of the solution. An important aspect of this chapter is

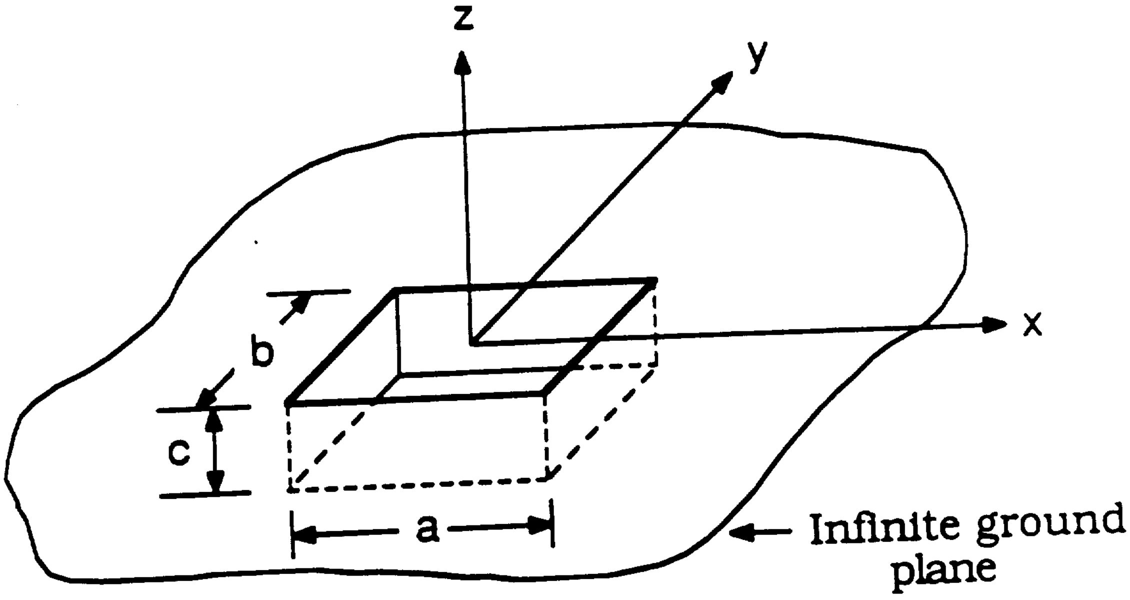

Figure 7.1: Geometry of an open cavity recessed in a ground plane.

the presentation of a number of scattering patterns some of which are validated with data obtained via an alternative solution method.

7.2 Full-Wave Formulation

Consider the aperture shown in Figure 7.1 illuminated by a harmonic plane wave given by (5.36) and (5.37). This represents a two-media problem with the aperture dividing the space into two regions, one external to the cavity ($z > 0$) and another internal to it ($-c < z < 0$). To formulate the fields scattered by the cavity, an analysis similar to the two-dimensional case is carried out based on the equivalence principle. Accordingly, the aperture is closed by a perfect conductor and the equivalent magnetic current

$$\mathbf{M} = \mathbf{E} \times \hat{n} = \mathbf{E} \times \hat{z} = \hat{x}E_y - \hat{y}E_x \tag{7.1}$$

is placed on the aperture at $z = 0^+$. The radiation of this current represents the scattered field in the external region and by demanding continuity of the tangential electric field, it follows that equivalent sources for the internal fields are the magnetic currents

$$\mathbf{M}' = \mathbf{E} \times \hat{n}' = \mathbf{E} \times -\hat{z} = -\mathbf{M} \tag{7.2}$$

placed across and just below the aperture at $z = 0^-$. It remains to also enforce continuity of the tangential magnetic field across the aperture and this will provide the required condition for determining the magnetic currents. By denoting the fields in the external region as $(\mathbf{E}^a, \mathbf{H}^a)$ and those in the internal region as $(\mathbf{E}^b, \mathbf{H}^b)$, we have

$$\hat{z} \times [\mathbf{H}^a(\mathbf{M}) + \mathbf{H}^{ia}] = \hat{z} \times \mathbf{H}^b(\mathbf{M}'), \qquad z = 0 \tag{7.3}$$

where $\mathbf{H}^{ia}$ represents the incident magnetic field in the absence of the aperture. Upon substitution for $\mathbf{H}^a$ and $\mathbf{H}^b$, (7.3) then yields an integral equation for the equivalent magnetic currents.

The external scattered field can be expressed as the surface integral

$$\mathbf{H}^a(\mathbf{r}) = -jk_oY_o \int_S 2\mathbf{M}(r') \cdot \bar{\mathbf{\Gamma}}(\mathbf{r};\mathbf{r}')\mathbf{ds}' \tag{7.4}$$

where S denotes the surface of the aperture, $\bar{\mathbf{\Gamma}}$ is the free space dyadic Green's function

$$\bar{\mathbf{\Gamma}}(\mathbf{r};\mathbf{r}') = \left(\bar{\mathbf{I}} + \frac{1}{k_o^2}\nabla\nabla\right) G_p(\mathbf{r};\mathbf{r}')$$

Also, a factor of two was introduced in (7.4) to account for the ground plane's presence. By expanding the $\bar{\mathbf{\Gamma}}$ in cartesian coordinates, (7.4) can be written more explicitly as given by

$$H_x^a = -\frac{2jY_o}{k_o} \int_S \left[M_x(x',y')\left(k_o^2 + \frac{\partial^2}{\partial x^2}\right) + M_y(x',y')\frac{\partial^2}{\partial x \partial y}\right] G_o(\mathbf{r};\mathbf{r}')ds' \tag{7.5}$$

$$H_y^a = -\frac{2jY_o}{k_o} \int_S \left[M_x(x',y')\frac{\partial^2}{\partial x \partial y} + M_y(x',y')\left(k_o^2 + \frac{\partial^2}{\partial y^2}\right)\right] G_o(\mathbf{r};\mathbf{r}')ds' \tag{7.6}$$

The internal fields can be written in terms of the TM$_Z$and TE$_Z$waveguide modes. We have

$$\mathbf{E}^b = \mathbf{E}^{TM} + \mathbf{E}^{TE} = -jk_b Z_b \left[1 + \frac{1}{k_b^2}\nabla\nabla\cdot\right](\hat{z}\Psi^{TM}) - \nabla \times (\hat{z}\Psi^{TE}) \tag{7.7}$$

$$\mathbf{H}^b = \mathbf{H}^{TM} + \mathbf{H}^{TE} = \nabla \times (\hat{z}\Psi^{TM}) - jk_b Y_b \left[1 + \frac{1}{k_b^2}\nabla\nabla\cdot\right](\hat{z}\Psi^{TE}) \tag{7.8}$$

where as before, $k_b = \aleph k_o$ is the wave number in the internal region and $Z_b = 1/Y_b$ is the intrinsic impedance of that region. The functions Ψ^{TM} and Ψ^{TE} are the wave potentials both satisfying the wave equation

$$\left(\frac{\partial^2}{\partial x^2} + \frac{\partial^2}{\partial y^2} + \frac{\partial^2}{\partial z^2} + k_b^2\right)\Psi = 0 \tag{7.9}$$

subject to the boundary conditions

$$E_x = E_y = 0, \quad z = -c \tag{7.10}$$

$$E_x = E_z = 0, \quad y = 0 \quad \text{and} \quad y = b \tag{7.11}$$

$$E_y = E_z = 0, \quad x = 0 \quad \text{and} \quad x = a \tag{7.12}$$

on the cavity walls. Referring to Figure 7.1, we have

$$\Psi^{TM} = \sum_{m=1}^{\infty}\sum_{n=1}^{\infty} A_{mn} \sin\left(\frac{m\pi}{a}x\right) \sin\left(\frac{n\pi}{b}y\right) \cos\left[k_z(z+c)\right] \tag{7.13}$$

and

$$\Psi^{TE} = \sum_{m=0}^{\infty}\sum_{n=0}^{\infty} B_{mn} \cos\left(\frac{m\pi}{a}x\right) \cos\left(\frac{n\pi}{b}y\right) \sin\left[k_z(z+c)\right] \quad \text{excluding } m = n = 0 \tag{7.14}$$

where A_{mn} and B_{mn} are constants to be determined and k_z satisfies the separation parameter equation

$$\left(\frac{m\pi}{a}\right)^2 + \left(\frac{n\pi}{b}\right)^2 + k_z^2 = k_b^2 \tag{7.15}$$

Observing the restriction on the mode propagation constant $\gamma = jk_z$ for the proper field behavior, we demand that

$$\Re e\{k_z\} \geq 0 \tag{7.16}$$

$$\Im m\{k_z\} \leq 0 \tag{7.17}$$

implying that

$$k_z = k_{mn} = \begin{cases} -j\sqrt{\left(\frac{m\pi}{a}\right)^2 + \left(\frac{n\pi}{b}\right)^2 - k_b^2} & , \quad k_b < \sqrt{\left(\frac{m\pi}{a}\right)^2 + \left(\frac{n\pi}{b}\right)^2} \\ \\ \sqrt{k_b^2 - \left(\frac{m\pi}{a}\right)^2 - \left(\frac{n\pi}{b}\right)^2} & , \quad k_b > \sqrt{\left(\frac{m\pi}{a}\right)^2 + \left(\frac{n\pi}{b}\right)^2} \end{cases}$$

when k_b is real. Substituting (7.13)-(7.14) into (7.7) we obtain

$$\begin{aligned} E_x^b &= \sum_{m,n} \left[jZ_b \left(\frac{m\pi}{a}\right) \frac{k_{mn}}{k_b} A_{mn} + \left(\frac{n\pi}{b}\right) B_{mn} \right] \\ &\cdot \cos\left(\frac{m\pi}{a}x\right) \sin\left(\frac{n\pi}{b}y\right) \sin\left[k_{mn}(z+c)\right] \end{aligned} \tag{7.18}$$

$$\begin{aligned} E_y^b &= \sum_{m,n} \left[jZ_b \left(\frac{n\pi}{b}\right) \frac{k_{mn}}{k_b} A_{mn} - \left(\frac{m\pi}{a}\right) B_{mn} \right] \\ &\cdot \sin\left(\frac{m\pi}{a}x\right) \cos\left(\frac{n\pi}{b}y\right) \sin\left[k_{mn}(z+c)\right] \end{aligned} \tag{7.19}$$

and

$$\begin{aligned} H_x^b &= \sum_{m,n} \left[\left(\frac{n\pi}{b}\right) A_{mn} + jY_b \left(\frac{m\pi}{a}\right) \frac{k_{mn}}{k_b} B_{mn} \right] \\ &\cdot \sin\left(\frac{m\pi}{a}x\right) \cos\left(\frac{n\pi}{b}y\right) \cos\left[k_{mn}(z+c)\right] \end{aligned} \tag{7.20}$$

$$\begin{aligned} H_y^b &= \sum_{m,n} \left[-\left(\frac{m\pi}{a}\right) A_{mn} + jY_b \left(\frac{n\pi}{b}\right) \frac{k_{mn}}{k_b} B_{mn} \right] \\ &\cdot \cos\left(\frac{m\pi}{a}x\right) \sin\left(\frac{n\pi}{b}y\right) \cos\left[k_{mn}(z+c)\right] \end{aligned} \tag{7.21}$$

The mode coefficients A_{mn} and B_{mn} can be expressed in terms of the equivalent current **M** by enforcing the boundary conditions (7.1) and (7.2)

$$E_x = M_y' = -M_y, \qquad z = 0 \tag{7.22}$$

$$E_y = -M_x' = M_x, \qquad z = 0 \tag{7.23}$$

and by invoking mode orthogonality we find

$$\begin{aligned} A_{mn} &= -\frac{2jk_bY_b}{k_{mn}ab\sin(k_{mn}c)}\left\{\left(\frac{m\pi}{a}\right)^2+\left(\frac{n\pi}{b}\right)^2\right\}^{-1} \\ &\quad\cdot\left[\varepsilon_n\left(\frac{n\pi}{b}\right)I_x^{mn}-\varepsilon_m\left(\frac{m\pi}{a}\right)I_y^{mn}\right] \end{aligned} \tag{7.24}$$

$$\begin{aligned} B_{mn} &= -\frac{2}{ab\sin(k_{mn}c)}\left\{\left(\frac{m\pi}{a}\right)^2+\left(\frac{n\pi}{b}\right)^2\right\}^{-1} \\ &\quad\cdot\left[\varepsilon_n\left(\frac{m\pi}{a}\right)I_x^{mn}+\varepsilon_m\left(\frac{n\pi}{b}\right)I_y^{mn}\right] \end{aligned} \tag{7.25}$$

where

$$I_x^{mn} = \int_S M_x(x',y')\sin\left(\frac{m\pi}{a}x'\right)\cos\left(\frac{n\pi}{b}y'\right)ds' \tag{7.26}$$

$$I_y^{mn} = \int_S M_y(x',y')\cos\left(\frac{m\pi}{a}x'\right)\sin\left(\frac{n\pi}{b}y'\right)ds' \tag{7.27}$$

and

$$\varepsilon_m = \begin{cases} 1 & m = 0 \\ 2 & m \geq 1 \end{cases} \tag{7.28}$$

The above expressions for the internal cavity fields are invalid when

$$k_{mn}\tan(k_{mn}c) = 0 \tag{7.29}$$

which may occur if the cavity is filled with lossless material. Hence, the modal solution fails if there exist integers m, n, and p such that

$$\left(\frac{m}{a}\right)^2+\left(\frac{n}{b}\right)^2+\left(\frac{p}{c}\right)^2=\left(\frac{2\aleph}{\lambda}\right)^2 \tag{7.30}$$

where ℵ is the index of refraction of the material filling the cavity. As mentioned before in connection with the two-dimensional grooves, this situation may be handled simply by introducing a small loss in the material.

The desired system of integral equations is now obtained based on the continuity of the aperture magnetic fields (7.3), upon substitution for the pertinent field quantities.

7.2.1 Reduction to the Two-Dimensional Case

Before we consider the numerical solution of the above integral equations, we consider the special case of the long cavity. We show that the above formulation reduces to that of the two-dimensional case studied in Chapter 5 when the cavity is taken to be infinite along one aperture dimension. Although this analysis is quite general in its application, we limit our attention to the H-polarization case here. In particular, as $b \to \infty$, we may neglect the contribution of the transverse x-component of the equivalent magnetic current density in favor of the dominant longitudinal y-component. Also, the problem is invariant in the y-direction and we set $\frac{\partial}{\partial y} = 0$. Hence, from (7.6) and (7.21) we obtain

$$\lim_{b\to\infty} H_y^a = -2jk_oY_o \int_{-w/2}^{w/2}\int_{-\infty}^{\infty} M_y(x',y')G_p(x,y;x',y')dx'dy' \tag{7.31}$$

and

$$\lim_{b\to\infty} H_y^b = -2jk_bY_b \left[\frac{1}{ab}\sum_{m=0}^{\infty}\sum_{n=0}^{\infty}\frac{\varepsilon_m k_b^2}{k_{mn}\tan(k_{mn}d)} I_y^{mn}\right] \tag{7.32}$$

Using the identity

$$\int_{-\infty}^{\infty} G_p(k_o\sqrt{x^2+y^2})dy = \frac{1}{4j}H_o^{(2)}(k_o|x|) \tag{7.33}$$

equation (7.31) can be rewritten as

$$\lim_{b\to\infty} H_y^a = -\frac{k_o Y_o}{2}\int_{-w/2}^{w/2} M_y(x') H_o^{(2)}(k_o|x-x'|)dx' \tag{7.34}$$

which is compatible with the two-dimensional scattering integral (6.13). Furthermore, substituting for I_y^{mn} and setting $k_{mn} = k_m \simeq \sqrt{k_b^2 - (\frac{m\pi}{a})^2}$ in (7.32) yields

$$\lim_{b\to\infty} H_y^b = \frac{-jk_b Y_b}{a}\sum_{m=0}^{\infty}\frac{\varepsilon_m}{k_m\tan(k_m d)} S_y \cos(\frac{m\pi}{a}x)\int_0^a M_y(x')\cos(\frac{m\pi}{a}x')dx' \tag{7.35}$$

where

$$S_y = \frac{2}{b}\sum_{n=0}^{\infty}\sin(\frac{n\pi}{b}y)\int_{-\infty}^{\infty}\sin(\frac{n\pi}{b}y')dy' \tag{7.36}$$

and S_y should equal unity for (7.35) to reduce to the two-dimensional result (6.30). This can be verified by invoking the distribution theory. Specifically, by interchanging the order of summation and integration, and noting that [84]

$$\sum_{n=1}^{\infty}\sin(n\pi y)\sin(n\pi y') = \delta(y-y') \tag{7.37}$$

we find that

$$S_y = \int_{-\infty}^{\infty}\left[\sum_{n=0}^{\infty}\frac{\sin(\frac{n\pi}{b}y)\sin(\frac{n\pi}{b}y')}{\frac{b}{2}}\right]dy' = \int_{-\infty}^{\infty}\delta(y-y')dy' = 1 \tag{7.38}$$

7.2.2 Numerical Solution via Galerkin's Method

In accordance with the method of moments, the integral equation to be solved for $\mathbf{M}$ is (see (7.3))

$$\int_S \left[\mathbf{H}_t^a(x,y) - \mathbf{H}_t^b(x,y)\right]\cdot\mathbf{W}(x,y)ds = -\int_S \mathbf{H}_t^{ia}(x,y)\cdot\mathbf{W}(x,y)ds \quad , \quad z=0 \tag{7.39}$$

where $\mathbf{H}_t^a = \hat{z}\times\mathbf{H}^a$, $\mathbf{H}_t^b = \hat{z}\times\mathbf{H}^b$, and $\mathbf{H}_t^{ia} = \hat{z}\times\mathbf{H}^{ia}$ with $\mathbf{H}^a$ and $\mathbf{H}^b$ as given by (7.5)-(7.6) and (7.20)-(7.21), respectively and $\mathbf{W}(x,y)$ is a weighting function. To discretize (7.39), $\mathbf{M}$ is expanded in terms of subdomain basis functions

$$\mathbf{M}(x,y) = \sum_{p,q} \mathbf{M}_{pq} \cdot [\hat{x}\hat{x}\xi_x(x - x_p; y - y_q) + \hat{y}\hat{y}\xi_y(x - x_p; y - y_q)] \tag{7.40}$$

where ξ_x and ξ_y are separable functions of x and y representing the expansion functions in the x and y directions, respectively. Further, $\mathbf{M}_{pq} = \hat{x}M_{xpq} + \hat{y}M_{ypq}$ are the unknown coefficients of the basis functions. In accordance with Galerkin's method we will choose the weighting functions to be the same as the expansion functions, i.e.

$$\mathbf{W}(x,y) = \begin{cases} \hat{x}\xi_x(x - x_i; y - y_j) \\ \\ \hat{y}\xi_y(x - x_i; y - y_j) \end{cases} \tag{7.41}$$

for testing at the point (x_i, y_j).

Solution with Piecewise Constant Basis Functions

Choosing piecewise constant basis functions, (7.40) becomes

$$\mathbf{M}(x,y) = \sum_{p=1}^{N_x} \sum_{q=1}^{N_y} \mathbf{M}_{pq} P(x - x_p) P(y - y_q) \tag{7.42}$$

where $x_p = p\Delta x - \frac{\Delta x}{2}, y_q = q\Delta y - \frac{\Delta y}{2}$, and

$$P(x) = \begin{cases} 1 & |x| < \frac{\Delta x}{2} \\ 0 & \text{otherwise} \end{cases}$$

$$P(y) = \begin{cases} 1 & |y| < \frac{\Delta y}{2} \\ 0 & \text{otherwise} \end{cases} \tag{7.43}$$

Substituting (7.42) into (7.39) yields the system

$$\begin{bmatrix} Y_{xx}^a - Y_{xx}^b & Y_{xy}^a - Y_{xy}^b \\ \\ Y_{yx}^a - Y_{yx}^b & Y_{yy}^a - Y_{yy}^b \end{bmatrix} \begin{bmatrix} M_x \\ \\ M_y \end{bmatrix} = - \begin{bmatrix} I_x^{\text{inc}} \\ \\ I_y^{\text{inc}} \end{bmatrix} \tag{7.44}$$

where the admittance elements with the superscript a are associated with the external fields whereas those with the superscript b are associated with the internal fields. The external admittance elements Y^a_{xx}, Y^a_{yx} and Y^a_{yy} are given in terms of the integral

$$\begin{aligned} g_{ijpq} &= g(x_i, y_j; x_p, y_q) = \int_{S_{ij}} \int_{S_{pq}} G_o(\mathbf{r}, \mathbf{r}')ds'ds \\ &= \int_{(i-1)\Delta x}^{i\Delta x} \int_{(j-1)\Delta y}^{j\Delta y} \int_{(p-1)\Delta x}^{p\Delta x} \int_{(q-1)\Delta y}^{q\Delta y} G_o(\mathbf{r}, \mathbf{r}')dy'dx'dydx \end{aligned} \tag{7.45}$$

and its second derivatives. This requires analytical evaluation when $|i-p| \leq 1$ and $|j-q| \leq 1$ and to do this, we rewrite g_{ijpq} as ($R = |\mathbf{r} - \mathbf{r}'|$)

$$g_{ijpq} = \frac{1}{4\pi} \int_{S_{ij}} \int_{S_{pq}} \left[\frac{e^{-jk_oR}}{R} - \frac{1}{R} \right] ds'ds + \frac{1}{4\pi} \int_{S_{ij}} \int_{S_{pq}} \frac{1}{R} ds'ds$$

The first integral has a nonsingular integrand for all i, j, p and q and can, therefore, be evaluated numerically using, for example, Gaussian integration. The second integral has a singular integrand when $i = p$ and $j = q$ but can be evaluated analytically to yield

$$\begin{aligned} \int_{S_{ij}} \int_{S_{pq}} \frac{ds'ds}{R} = \Bigg[&\frac{(x-x')(y-y')}{2} \{(x-x') \ln[(y-y') + R] \\ &+ (y-y') \ln[(x-x') + R]\} - \frac{(x-x')(y-y')[(x-x') + (y-y')]}{4} \\ &- \frac{R^3}{6} \Bigg] \Bigg|_{x'=(p-1)\Delta x}^{p\Delta x} \Bigg|_{y'=(q-1)\Delta y}^{q\Delta y} \Bigg|_{x=(i-1)\Delta x}^{i\Delta x} \Bigg|_{y=(j-1)\Delta y}^{j\Delta y} \end{aligned} \tag{7.46}$$

Unfortunately, the derivatives of g_{ijpq} do not exist in analytical form. A possible alternative is to evaluate them discretely using the computed values of g_{ijpq}, and a convenient way to do this is to employ the discrete Fourier transform. Proceeding in this manner, we first define the sample train

$$\chi_{ij} = \sum_{p=1}^{N_x} \sum_{q=1}^{N_y} g_{ijpq} \delta(x - x_p) \delta(y - y_q) \tag{7.47}$$

whose two-dimensional DFT will be denoted by $\hat{\chi}_{ij}$. Using a central difference scheme for the derivatives, the DFT of the sample train

$$\chi_{ij}^{xx} = \sum_{p=1}^{N_x}\sum_{q=1}^{N_y}\left[\int_{S_{ij}}\int_{S_{pq}}\frac{\partial^2}{\partial x^2}\frac{e^{-jk_oR}}{4\pi R}ds'ds\right]\cdot\delta(x-x_p)\delta(y-y_q) \tag{7.48}$$

with x_i and y_j kept constant, can be approximated as

$$\hat{\chi}_{ij}^{xx} = -D_x^2\hat{\chi}_{ij} \tag{7.49}$$

The admittance matrix elements can then be expressed as

$$(Y_{xx}^a)_{ij} = -\frac{2jY_o}{k_o}\,\text{DFT}^{-1}\left\{\left[k_o^2 - D_x^2\right]\hat{\chi}_{ij}\right\} \tag{7.50}$$

$$\left(Y_{xy}^a\right)_{ij} = -\frac{2jY_o}{k_o}\,\text{DFT}^{-1}\left\{-D_xD_y\hat{\chi}_{ij}\right\} \tag{7.51}$$

$$\left(Y_{yx}^a\right)_{ij} = -\frac{2jY_o}{k_o}\,\text{DFT}^{-1}\left\{-D_yD_x\hat{\chi}_{ij}\right\} \tag{7.52}$$

$$\left(Y_{yy}^a\right)_{ij} = -\frac{2jY_o}{k_o}\,\text{DFT}^{-1}\left\{\left[k_o^2 - D_y^2\right]\hat{\chi}_{ij}\right\} \tag{7.53}$$

where DFT^{-1} denotes the inverse discrete Fourier transform. These give the admittance elements for the matrix row associated with the testing point (x_i, y_j). The other row elements can be obtained by a simple rearrangement of this row upon invoking the symmetry properties of the matrix.

To evaluate the admittance matrix elements associated with the cavity region we refer to (7.20)-(7.21). Substituting the expansion (7.42) into (7.24)-(7.25) and then into (7.39) yields

$$\begin{aligned}\left(Y_{xx}^b\right)_{ijpq} &= C\sum_m\sum_n \eta_{mn}\epsilon_n\left[k_b^2 - \left(\frac{m\pi}{a}\right)^2\right] \\ &\quad\cdot\ \sin\left(\frac{m\pi}{a}x_p\right)\sin\left(\frac{m\pi}{a}x_i\right)\cos\left(\frac{n\pi}{b}y_q\right)\cos\left(\frac{n\pi}{b}y_j\right)\end{aligned} \tag{7.54}$$

$$\begin{aligned}\left(Y_{xy}^{b}\right)_{ijpq} &= -C\sum_{m}\sum_{n}\eta_{mn}\varepsilon_{m}\left(\frac{m\pi}{a}\right)\left(\frac{n\pi}{b}\right) \\ &\quad\cdot \cos\left(\frac{m\pi}{a}x_{p}\right)\sin\left(\frac{m\pi}{a}x_{i}\right)\sin\left(\frac{n\pi}{b}y_{q}\right)\cos\left(\frac{n\pi}{b}y_{j}\right)\end{aligned} \tag{7.55}$$

$$\begin{aligned}\left(Y_{yx}^{b}\right)_{ijpq} &= -C\sum_{m}\sum_{n}\eta_{mn}\varepsilon_{n}\left(\frac{m\pi}{a}\right)\left(\frac{n\pi}{b}\right) \\ &\quad\cdot \sin\left(\frac{m\pi}{a}x_{p}\right)\cos\left(\frac{m\pi}{a}x_{i}\right)\cos\left(\frac{n\pi}{b}y_{q}\right)\sin\left(\frac{n\pi}{b}y_{j}\right)\end{aligned} \tag{7.56}$$

and

$$\begin{aligned}\left(Y_{yy}^{b}\right)_{ijpq} &= C\sum_{m}\sum_{n}\eta_{mn}\varepsilon_{m}\left[k_{b}^{2}-\left(\frac{n\pi}{b}\right)^{2}\right] \\ &\quad\cdot \cos\left(\frac{m\pi}{a}x_{p}\right)\cos\left(\frac{m\pi}{a}x_{i}\right)\sin\left(\frac{n\pi}{b}y_{q}\right)\sin\left(\frac{n\pi}{b}y_{j}\right)\end{aligned} \tag{7.57}$$

In these

$$\eta_{mn}=\frac{\operatorname{sinc}^{2}\left(\frac{m\pi}{2a}\Delta x\right)\operatorname{sinc}^{2}\left(\frac{n\pi}{2b}\Delta y\right)}{k_{mn}\tan\left(k_{mn}c\right)} \tag{7.58}$$

$$C=-\frac{2jY_{o}}{k_{o}\mu_{b}}\frac{(\Delta x\Delta y)^{2}}{ab} \tag{7.59}$$

and ε_m have been defined in (7.28).

It remains to compute the excitation elements $(I_x^i)_{ij}$ and $\left(I_y^i\right)_{ij}$ given by

$$\left(I_{x}^{\mathrm{inc}}\right)_{ij}=2\int_{(i-1)\Delta x}^{i\Delta x}\int_{(j-1)\Delta y}^{j\Delta y}H_{x}^{i}(x,y,z=0)dydx \tag{7.60}$$

$$\left(I_{y}^{\mathrm{inc}}\right)_{ij}=2\int_{(i-1)\Delta x}^{i\Delta x}\int_{(j-1)\Delta y}^{j\Delta y}H_{x}^{i}(x,y,z=0)dydx. \tag{7.61}$$

Integrating, we obtain

$$\begin{aligned}\left(I_{x}^{\mathrm{inc}}\right)_{ij} &= 2H_{ox}e^{jk_{o}\sin\theta_{o}(x_{i}\cos\phi_{o}+y_{j}\sin\phi_{o})}\Delta x\Delta y \\ &\quad\cdot \operatorname{sinc}\left(\frac{k_{o}\Delta x\sin\theta_{o}\cos\phi_{o}}{2}\right)\operatorname{sinc}\left(\frac{k_{o}\Delta y\sin\theta_{o}\sin\phi_{o}}{2}\right)\end{aligned} \tag{7.62}$$

and

$$\begin{aligned} \left(I_y^{\text{inc}}\right)_{ij} &= 2H_{oy} e^{jk_o \sin\theta_o (x_i \cos\phi_o + y_j \sin\phi_o)} \Delta x \Delta y \\ &\quad \cdot \operatorname{sinc}\left(\frac{k_o \Delta x \sin\theta_o \cos\phi_o}{2}\right) \operatorname{sinc}\left(\frac{k_o \Delta x \sin\theta_o \sin\phi_o}{2}\right) \end{aligned} \tag{7.63}$$

where H_{ox} and H_{oy} are given in (5.38).

This completes the derivation of all elements appearing in the system (7.44) whose solution yields the current densities M_x and M_y. Unfortunately, the computation of the matrix elements $Y^b_{xx}, Y^b_{xy}, Y^b_{yy}$ and Y^b_{yx} requires the evaluation of double infinite summations which are slowly converging. The asymptotic behaviors of the summation terms for Y^b_{xx} and Y^b_{xy} are of the form $\frac{1}{n^2\sqrt{n^2+m^2}}$ and $\frac{1}{mn\sqrt{n^2+m^2}}$, respectively, implying that for fixed n, Y^b_{xy} and Y^b_{yx} have slow convergence whereas Y^b_{xx} and Y^b_{yy} are strictly non-convergent. As will be seen later, however, for long and narrow cavities, a finite number of summation terms are sufficient to obtain acceptable results. Nevertheless, substantial amount of computer time is required for evaluating the mode sums given in (7.54)–(7.57) making the solution impractical unless the convergence of the sums is improved. One way to achieve this is by using roof-top basis functions considered next.

Solution with Piecewise Linear Basis Functions

The equivalent magnetic current components are now expanded as

$$\begin{aligned} M_x(x,y) &= \sum_{p=1}^{P-1} \sum_{q=1}^{Q} M_{xpq} T_p(x) P_q(y) \\ M_y(x,y) &= \sum_{p=1}^{P} \sum_{q=1}^{Q-1} M_{ypq} P_p(x) T_q(y) \end{aligned} \tag{7.64}$$

where

$$T_s(\xi) = \begin{cases} \dfrac{\xi - (s-1)\Delta\xi}{\Delta\xi} & (s-1)\Delta\xi \le \xi \le s\Delta\xi \\[2ex] \dfrac{(s+1)\Delta\xi - \xi}{\Delta\xi} & s\Delta\xi \le \xi \le (s+1)\Delta\xi \\[2ex] 0 & |\xi - s\Delta\xi| \ge \Delta\xi \end{cases} \tag{7.65}$$

for

$$s = 1, 2, \ldots, S-1 \tag{7.66}$$

and $P(\zeta)$ is the piecewise constant basis function considered before.

When these are used in (7.39) with the weighting functions the same as the expansion functions, we obtain a system similar to (7.44). The external admittance elements are now given by

$$\begin{aligned} (Y^a_{xx})_{ijpq} &= \frac{-2jY_o}{k_o} \int_{(j-1)\Delta y}^{j\Delta y} \int_{(q-1)\Delta y}^{q\Delta y} \int_{(i-1)\Delta x}^{(i+1)\Delta x} T_i(x) \int_{(p-1)\Delta x}^{(p+1)\Delta x} T_p(x') \\ &\quad \cdot \left(k_o^2 + \frac{\partial^2}{\partial x^2}\right) G_o(\mathbf{r};\mathbf{r}')dx'dxdy'dy \end{aligned} \tag{7.67}$$

$$\begin{aligned} \left(Y^a_{xy}\right)_{ijpq} &= \frac{-2jY_o}{k_o} \int_{(j-1)\Delta y}^{j\Delta y} \int_{(q-1)\Delta y}^{(q+1)\Delta y} T_q(y') \int_{(i-1)\Delta x}^{(i+1)\Delta x} T_i(x) \int_{(p-1)\Delta x}^{p\Delta x} \\ &\quad \cdot \frac{\partial^2}{\partial x \partial y} G_o(\mathbf{r};\mathbf{r}')dx'dxdy'dy \end{aligned} \tag{7.68}$$

$$\begin{aligned} \left(Y^a_{yx}\right)_{ijpq} &= \frac{-2jY_o}{k_o} \int_{(j-1)\Delta y}^{(j+1)\Delta y} T_j(y) \int_{(q-1)\Delta y}^{q\Delta y} \int_{(i-1)\Delta x}^{i\Delta x} \int_{(p-1)\Delta x}^{(p+1)\Delta x} T_p(x') \\ &\quad \cdot \frac{\partial^2}{\partial x \partial y} G_o(\mathbf{r};\mathbf{r}')dx'dxdy'dy \end{aligned} \tag{7.69}$$

$$\left(Y^a_{yy}\right)_{ijpq} = \frac{-2jY_o}{k_o}\int_{(j-1)\Delta y}^{(j+1)\Delta y} T_j(y)\int_{(q-1)\Delta y}^{(q+1)\Delta y} T_q(y')\int_{(i-1)\Delta x}^{i\Delta x}\int_{(p-1)\Delta x}^{p\Delta x} \cdot \left(k_o^2+\frac{\partial^2}{\partial y^2}\right) G_o(\mathbf{r};\mathbf{r}')dx'dxdy'dy \tag{7.70}$$

The calculation of these elements may be simplified by applying integration by parts and sampling the 'field' integrands at two points [50]. Taking for example the first integral, we have after integrating by parts

$$(Y^a_{xx})_{ijpq} = \frac{-2jY_o}{k_o}\int_y\int_{y'}\left\{k_o^2\int_x T_i(x)\int_{x'} T_p(x')G_o dx'dx - \int_x T_i'(x)\int_{x'} T_p'(x')G_o dx'dx\right\}dy'dy \tag{7.71}$$

where T_s' denotes the derivative of T_s. Performing midpoint integration for the unprimed integrals by sampling at the two points $\left[\left(i\pm\frac{1}{2}\right)\Delta x, \left(j-\frac{1}{2}\right)\Delta y\right]$ and repeating the process for the other elements yields

$$\begin{aligned}Y^a_{xx\,ijpq} = -jY_ok_o\Delta x\Delta y\Big\{&(\xi+\frac{3}{2})I(\xi+1,\zeta)+I(\xi,\zeta)-(\xi-\frac{3}{2})I(\xi-1,\zeta)\\ &+\frac{1}{\Delta x}\left[I_x(\xi-1,\zeta)-I_x(\xi+1,\zeta)\right]\\ &+\frac{2}{(k_o\Delta x)^2}\left[I(\xi+1,\zeta)-2I(\xi,\zeta)+I(\xi-1,\zeta)\right]\Big\}\end{aligned} \tag{7.72}$$

$$Y^a_{xy\,ijpq} = \frac{-2jY_o}{k_o}\left[-I(\xi,\zeta)+I(\xi+1,\zeta)+I(\xi,\zeta-1)-I(\xi+1,\zeta-1)\right] \tag{7.73}$$

$$Y^a_{yx\,ijpq} = \frac{-2jY_o}{k_o}\left[-I(\xi,\zeta)+I(\xi,\zeta+1)+I(\xi-1,\zeta)-I(\xi-1,\zeta+1)\right] \tag{7.74}$$

and

$$Y^a_{yy\,ijpq} = -jY_ok_o\Delta x\Delta y\Big\{(\zeta+\frac{3}{2})I(\xi,\zeta+1)+I(\xi,\zeta)-(\zeta-\frac{3}{2})I(\xi,\zeta-1)$$

$$+ \quad \frac{1}{\Delta y}\left[I_y(\xi,\zeta-1) - I_y(\xi,\zeta+1)\right] \tag{7.75}$$

$$+ \quad \frac{2}{(k_o\Delta y)^2}\left[I(\xi,\zeta+1) - 2I(\xi,\zeta) + I(\xi,\zeta-1)\right]\Big\}$$

where $\xi = i - p$, $\zeta = j - q$ and

$$I(\xi,\zeta) = \int_{(\zeta-\frac{1}{2})\Delta y}^{(\zeta+\frac{1}{2})\Delta y} \int_{(\xi-\frac{1}{2})\Delta x}^{(\xi+\frac{1}{2})\Delta x} \frac{e^{-jk_o\sqrt{x^2+y^2}}}{4\pi\sqrt{x^2+y^2}}dxdy \tag{7.76}$$

$$I_x(\xi,\zeta) = \int_{(\zeta-\frac{1}{2})\Delta y}^{(\zeta+\frac{1}{2})\Delta y} \int_{(\xi-\frac{1}{2})\Delta x}^{(\xi+\frac{1}{2})\Delta x} x\frac{e^{-jk_o\sqrt{x^2+y^2}}}{4\pi\sqrt{x^2+y^2}}dxdy \tag{7.77}$$

$$I_y(\xi,\zeta) = \int_{(\zeta-\frac{1}{2})\Delta y}^{(\zeta+\frac{1}{2})\Delta y} \int_{(\xi-\frac{1}{2})\Delta x}^{(\xi+\frac{1}{2})\Delta x} y\frac{e^{-jk_o\sqrt{x^2+y^2}}}{4\pi\sqrt{x^2+y^2}}dxdy \tag{7.78}$$

The above integrals can be evaluated using a four term Taylor series expansion and are given in [50].

The evaluation of the internal elements of the admittance matrix is straightforward and yields the following expressions

$$\left(Y^b_{xx}\right)_{ijpq} = C\sum_m\sum_n \eta_{mn}\varepsilon_n \mathrm{sinc}^2\left(\frac{m\pi}{a}\frac{\Delta x}{2}\right)\left[k_b^2 - \left(\frac{m\pi}{a}\right)^2\right]$$

$$\cdot \quad \sin\left(\frac{m\pi}{a}p\Delta x\right)\sin\left(\frac{m\pi}{a}i\Delta x\right) \tag{7.79}$$

$$\cdot \quad \cos\left[\frac{n\pi}{b}(q-1/2)\Delta y\right]\cos\left[\frac{n\pi}{b}(j-1/2)\Delta y\right]$$

$$\left(Y^b_{xy}\right)_{ijpq} = -C\sum_m\sum_n \eta_{mn}\varepsilon_m \mathrm{sinc}\left(\frac{m\pi}{a}\frac{\Delta x}{2}\right)\mathrm{sinc}\left(\frac{n\pi}{b}\frac{\Delta y}{2}\right)\left(\frac{m\pi}{a}\right)\left(\frac{n\pi}{b}\right)$$

$$\cdot \quad \cos\left[\frac{m\pi}{a}(p-1/2)\Delta x\right]\sin\left(\frac{m\pi}{a}i\Delta x\right) \tag{7.80}$$

$$\cdot \quad \sin\left(\frac{n\pi}{b}q\Delta y\right)\cos\left[\frac{n\pi}{b}(j-1/2)\Delta y\right]$$

$$\begin{aligned}\left(Y^b_{yx}\right)_{ijpq} &= -C\sum_m\sum_n \eta_{mn}\varepsilon_n \text{sinc}\left(\frac{n\pi}{b}\frac{\Delta y}{2}\right)\text{sinc}\left(\frac{m\pi}{a}\frac{\Delta x}{2}\right)\left(\frac{m\pi}{a}\right)\left(\frac{n\pi}{b}\right)\\ &\cdot\ \sin\left(\frac{m\pi}{a}p\Delta x\right)\cos\left[\frac{m\pi}{a}(i-1/2)\Delta x\right] \qquad (7.81)\\ &\cdot\ \cos\left[\frac{n\pi}{b}(q-1/2)\Delta y\right]\sin\left(\frac{n\pi}{b}j\Delta y\right)\end{aligned}$$

and

$$\begin{aligned}\left(Y^b_{yy}\right)_{ijpq} &= C\sum_m\sum_n \eta_{mn}\varepsilon_m \text{sinc}^2\left(\frac{n\pi}{b}\frac{\Delta y}{2}\right)\left[k_b^2-\left(\frac{n\pi}{b}\right)^2\right]\\ &\cdot\ \cos\left[\frac{m\pi}{a}(p-1/2)\Delta x\right]\cos\left[\frac{m\pi}{a}(i-1/2)\Delta x\right] \qquad (7.82)\\ &\cdot\ \sin\left(\frac{n\pi}{b}q\Delta y\right)\sin\left(\frac{n\pi}{b}j\Delta y\right)\cdot\end{aligned}$$

where η_{mn} and C are given in (7.58) and (7.59). The corresponding excitation elements are computed as

$$\begin{aligned}(I_x^{\text{inc}})_{ij} &= 2H_{ox}e^{jk_o\sin\theta_o(i\Delta x\cos\phi_o+(j-1/2)\Delta y\sin\phi_o)}\Delta x\Delta y\\ &\cdot\text{sinc}^2\left(\frac{k_o\Delta x\sin\theta_o\cos\phi_o}{2}\right)\text{sinc}\left(\frac{k_o\Delta y\sin\theta_o\sin\phi_o}{2}\right)\end{aligned} \qquad (7.83)$$

$$\begin{aligned}(I_y^{\text{inc}})_{ij} &= 2H_{oy}e^{jk_o\sin\theta_o((i-1/2)\Delta x\cos\phi_o+j\Delta y\sin\phi_o)}\Delta x\Delta y\\ &\cdot\text{sinc}\left(\frac{k_o\Delta x\sin\theta_o\cos\phi_o}{2}\right)\text{sinc}^2\left(\frac{k_o\Delta y\sin\theta_o\sin\phi_o}{2}\right)\end{aligned} \qquad (7.84)$$

We observe that the asymptotic behavior of the summation terms in (7.79)–(7.82) is now of the form

$$\frac{1}{(mn)^2\sqrt{n^2+m^2}}$$

and the double sums are therefore expected to converge rapidly. The required number of modes for convergence within an acceptable tolerance will, of course, depend on the geometry and electrical properties of the cavity.

7.2.3 Results and Validation

The implementation task of the presented numerical solution is a tedious one as is usually the case with most three-dimensional numerical solutions. The validation of the code also proved challenging because of the scarcity of reference data and the long execution times. The calculation of mode sums constitutes the major part of the computer processing time. As noted earlier, for a piecewise constant basis implementation the mode sums are slowly converging and Figures 7.2 a and 7.2 b give the convergence of the like-polarized and cross-polarized admittance elements, respectively, for these basis functions. The double sums were computed using the scheme discussed in [85] and the shown curves correspond to the element located at the center of a square $1\lambda \times 1\lambda$ aperture. We observe that the mode sums for the cross-polarization admittance elements converge rather rapidly. As expected, Y_{yy} of the self-cell has not converged even after adding 1000 modes in each direction in the piecewise constant basis solution whereas only 50 modes (in each direction) are sufficient to reach convergence when using roof-top basis functions as demonstrated in Figures 7.2 c and 7.2 d. In general, though, for narrow and long cavities only a few modes need be kept along the narrow dimension and this leads to a much more rapid convergence since the double sums are essentially reduced to single sums. In fact, for very narrow cavities, one may only keep the lowest order mode [86, 87]. This was explored to some extent in Chapter 6. It should be noted, though, that for long and narrow apertures the pulse basis formulation is preferable to the roof-top one described here unless the external self-cell admittance elements are more accurately evaluated (i.e., midpoint integration should be replaced with a more accurate integration scheme.)

To validate the presented moment method full-wave formulations and associated computer codes we relied on comparisons with data obtained from a corresponding finite element-boundary integral (FEM) solution [88]. This was developed in parallel with the moment method/modal solution in an effort to avoid cavity shape restrictions and the long processing time required for filling the MoM matrix. In the Figures to follow, the RCS pattern is presented for the principal plane cuts of the cavity-backed aperture. Figure 7.3 presents the two like- and cross-polarization backscatter RCS patterns for a 1.73λ deep cavity with $a = 0.7\lambda$ and $b = 0.1\lambda$. These are conical cuts and were generated with the code based on the piecewise constant basis formulation. They are clearly in good agreement with the FEM data and have also been found to agree with the only other [67] available calculations that appeared recently in the literature.

Backscatter curves for a filled cavity are given in Figure 7.4. These were generated with the code based on the roof-top basis formulation and correspond to a $0.4\lambda \times 0.4\lambda$ cavity backed aperture, 0.25λ deep and filled with homogeneous material having $\epsilon_r = 2 - j0.5$ and $\mu_r = 1.2 - j0.1$. The principal plane like-polarized RCS patterns are again in good agreement with FEM data. Additional curves for a long and narrow $2.5\lambda \times 0.25\lambda$ cavity are given in Figures 7.5 and 7.6. They are based on the piecewise constant basis formulation and correspond to a 0.25λ deep cavity, empty or filled with material having $\epsilon_r = 7 - j1.5$ and $\mu_r = 1.8 - j0.1$. Figure 7.5 presents the

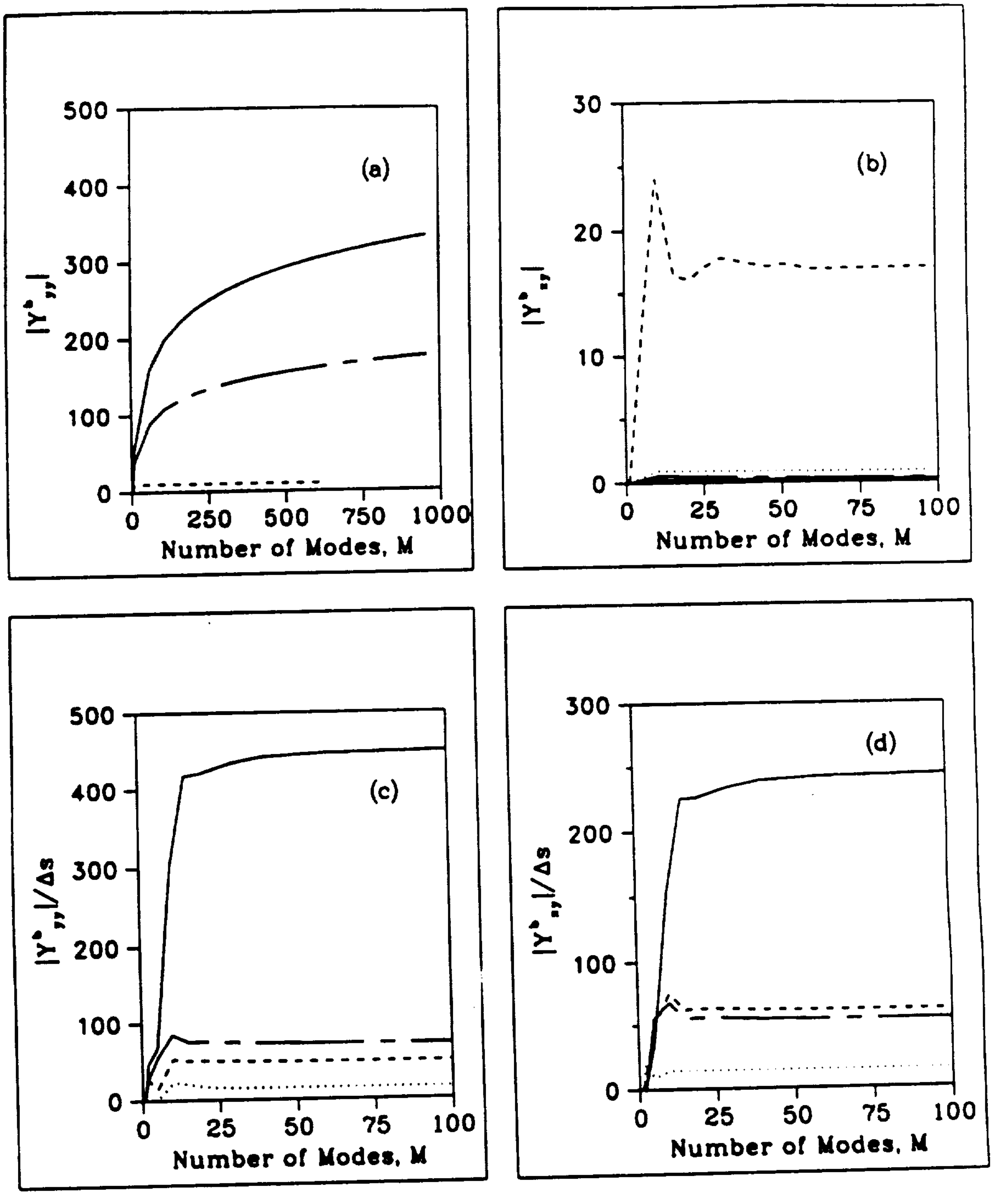

Figure 7.2: Comparison of the mode convergence for a $1\lambda \times 1\lambda \times 0.25\lambda$ cavity using the piecewise constant (a and b) and roof-top (c and d) basis functions. $(i, j; p, q) = (5, 5; 5, 5)$ solid line; $(5, 5; 5, 4)$ chain-dashed; $(5, 5; 4, 4)$ dashed; $(5, 5; 1, 1)$ dotted line. M is the number of modes in each direction.

like-polarized backscatter RCS patterns for the empty cavity in both principal planes whereas Figure 7.6 includes the corresponding patterns for the filled cavity. As seen, the RCS patterns in the principal plane normal to the long side agree with the scaled two-dimensional RCS data (using the conversion (1.26)), whereas the principal plane patterns normal to the short side agree with the FEM data. Finally, the scattering characteristics of a square cavity ($1\lambda \times 1\lambda \times 0.5\lambda$) filled with a high contrast material ($\epsilon_r = 12 - j2.5, \mu_r = 4.5 - j1.2$) is shown in Figure 7.7. It is noted that for this particular case, a sampling interval of $\lambda/15$ and a total of only 50 modes in each directions were sufficient for the MoM solution to reach the converged solution. This is, of course, due to the fact that higher order modes are suppressed because of the high losses in the material filling the cavity.

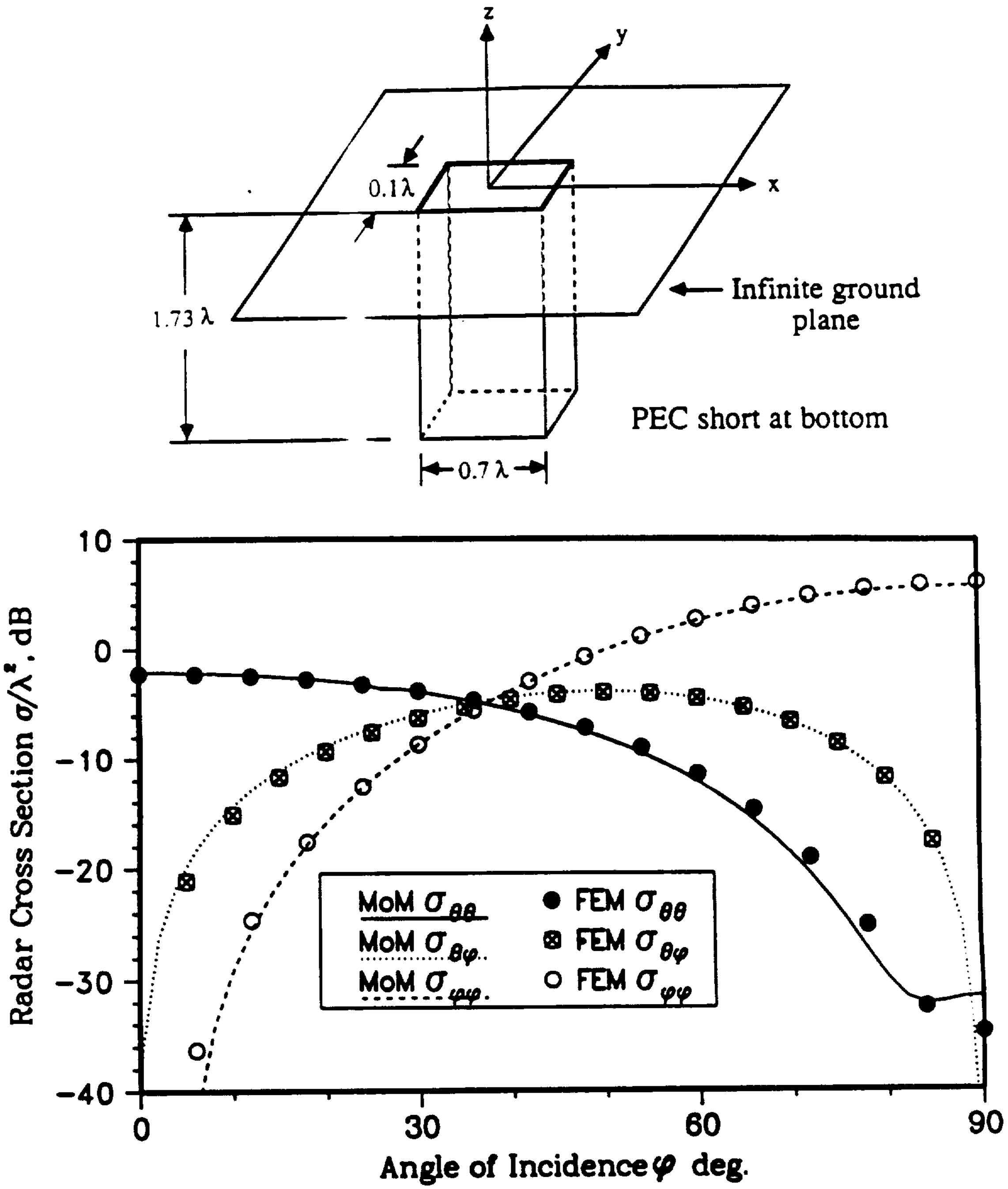

Figure 7.3: Comparison of conical ($\theta = 40°$) backscatter RCS patterns for a $0.7\lambda \times 0.1\lambda \times 1.73\lambda$ empty cavity obtained from the moment method solution using piecewise constant basis functions and the finite element method (FEM) [67].

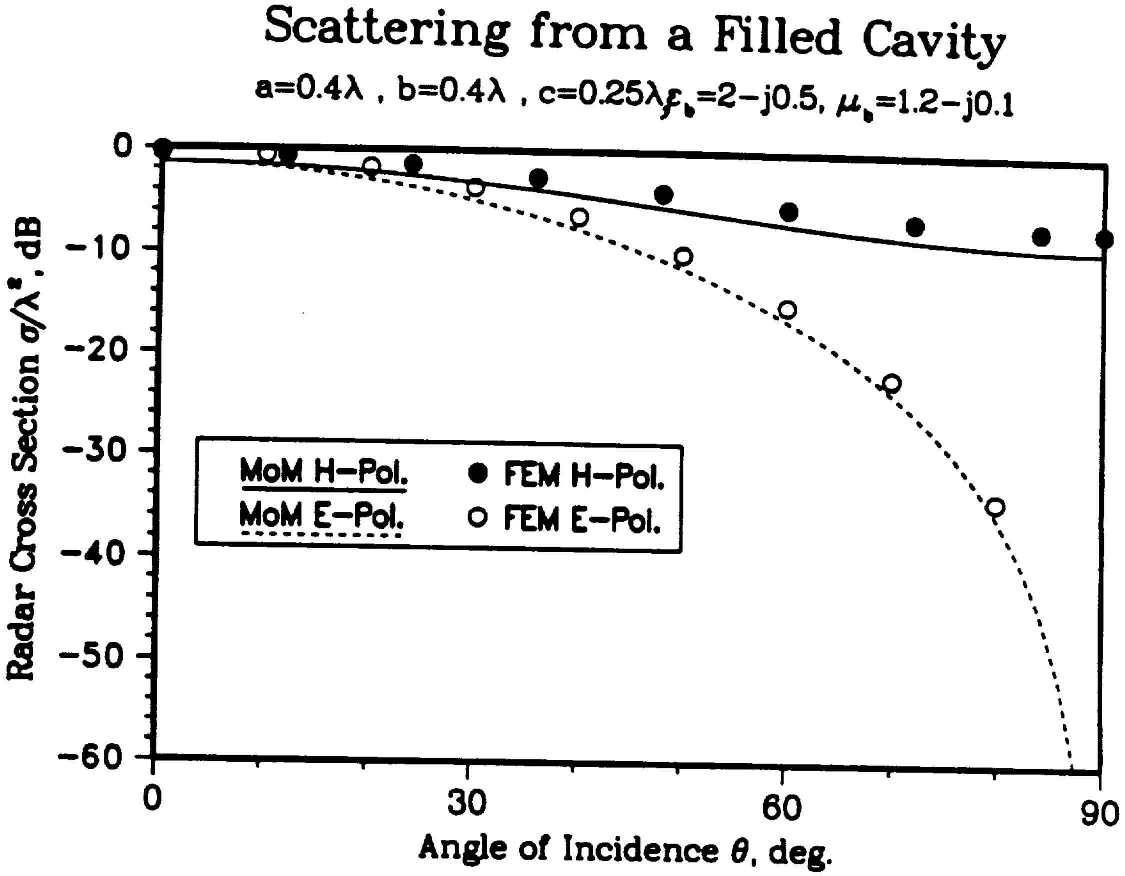

Figure 7.4: Backscatter RCS elevation patterns for a $0.4\lambda \times 0.4\lambda \times 0.25\lambda$ cavity filled with a homogeneous material ($\epsilon_r = 2-j0.5, \mu_r = 1.2-j0.1$); Comparison of the MoM solution using piecewise linear (roof-top) basis functions with the FEM [67].

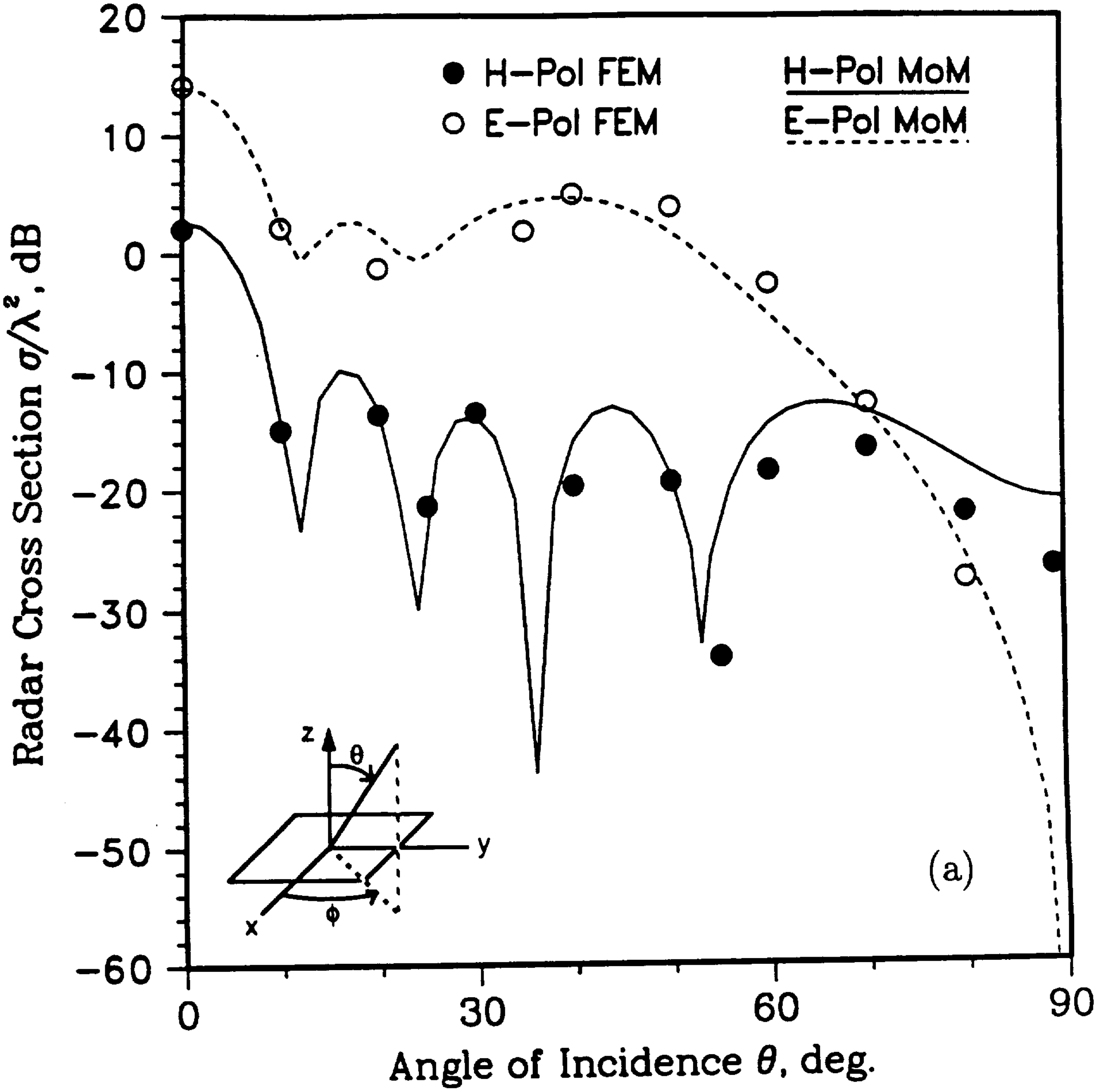

Figure 7.5: Backscatter RCS elevation patterns for a 2.5λ × 2.5λ × 0.25λ empty cavity using piecewise constant basis functions. (a) $\phi = \phi_o = 0$ (symbols denote FEM results [88]). (b) $\phi = \phi_o = \pi/2$ (symbols denote the scaled two-dimensional RCS data).

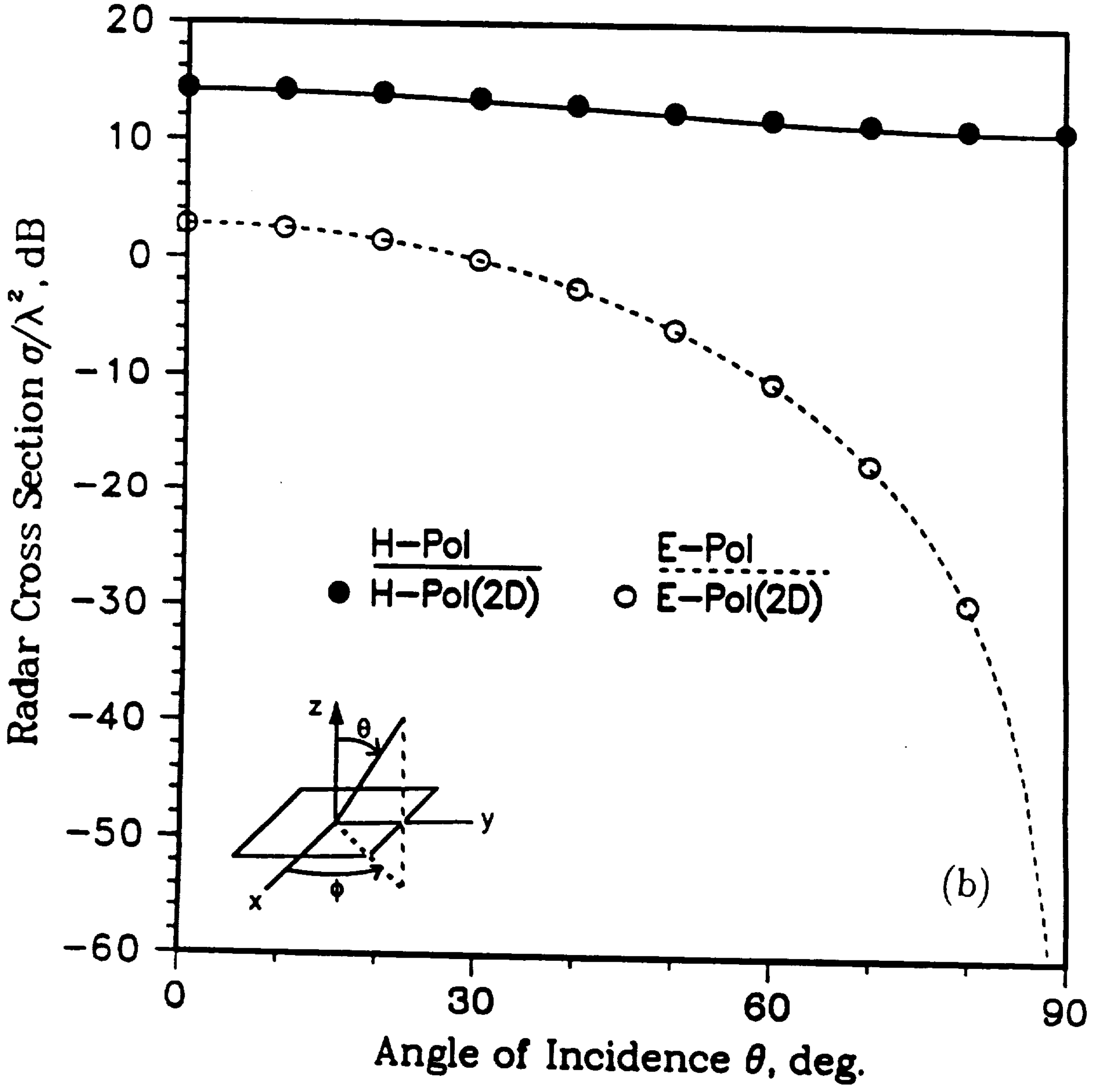
20
10
0
−10
−20
−30
−40
−50
−60
Radar Cross Section σ/λ², dB
0
30
60
90
Angle of Incidence θ, deg.
H−Pol
● H−Pol(2D)
E−Pol
○ E−Pol(2D)
z
θ
y
x
ϕ
(b)

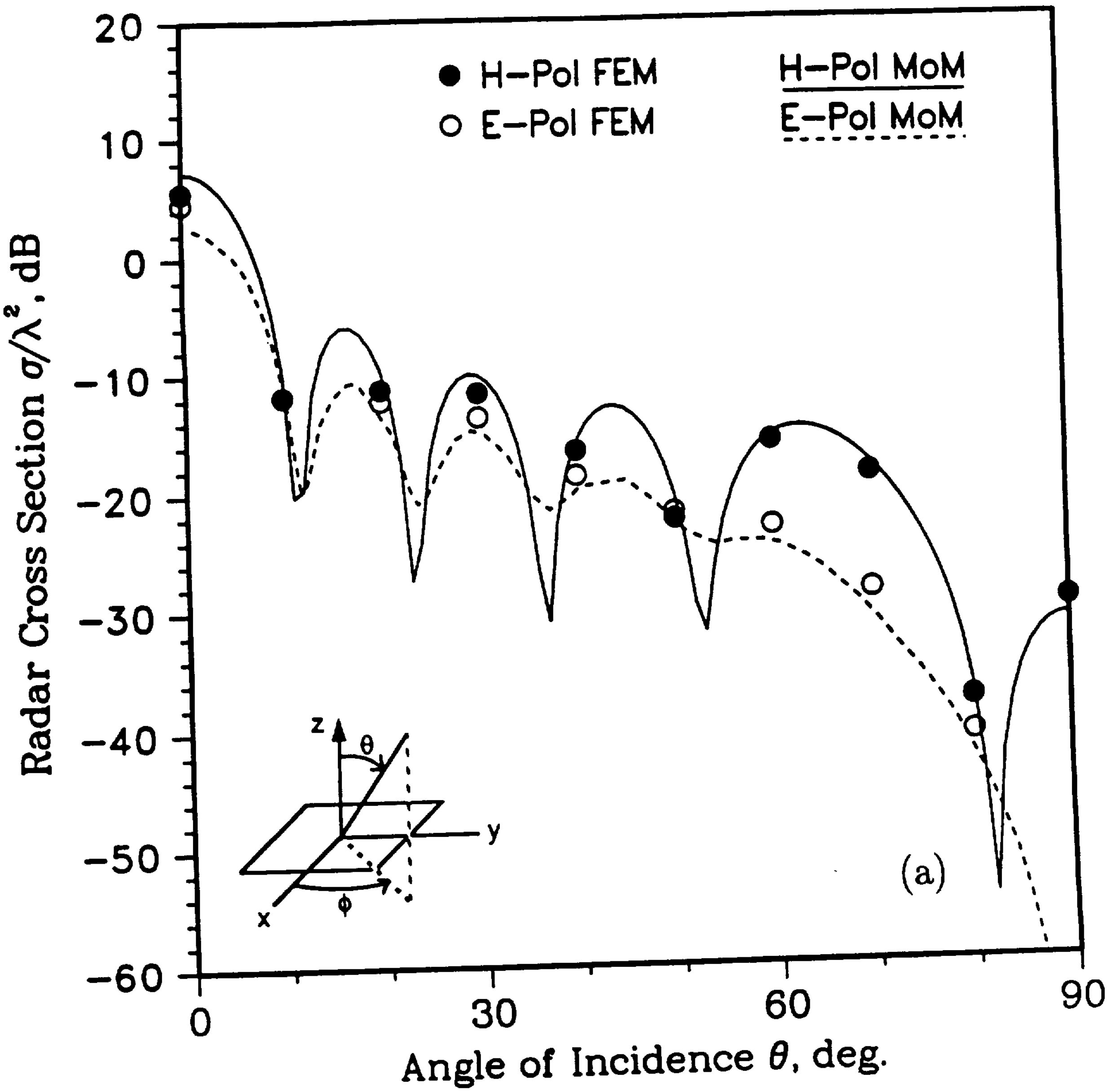

Figure 7.6: Backscatter RCS elevation patterns for a 2.5λ × 2.5λ × 0.25λ filled cavity ($\epsilon_r = 7 - j1.5, \mu_r = 1.8 - j0.1$) using piecewise constant basis functions. (a) $\phi = \phi_o = 0$ (symbols denote FEM results [88]). (b) $\phi = \phi_o = \pi/2$ (symbols denote the scaled two-dimensional RCS data).

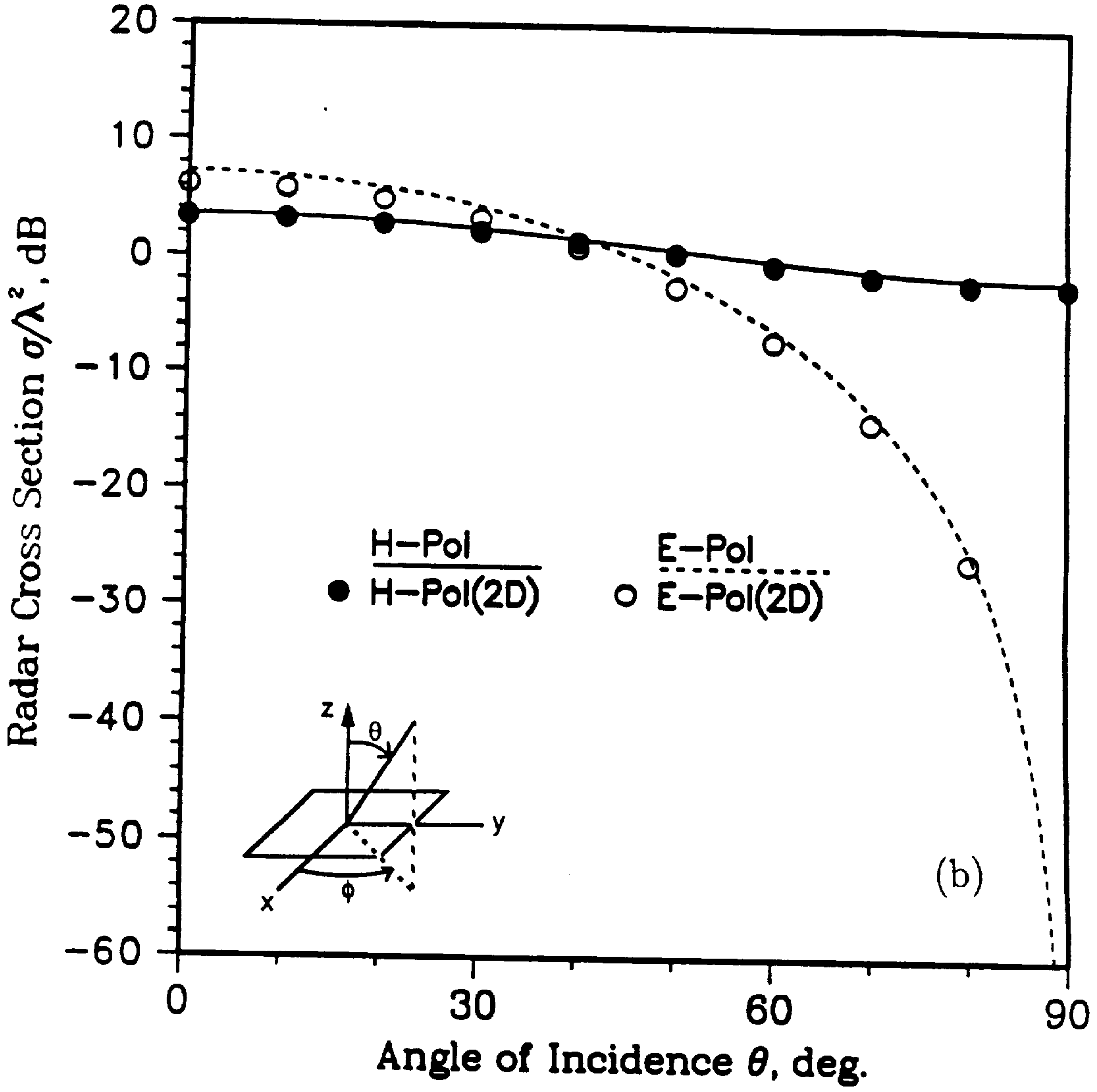

20
10
0
−10
−20
−30
−40
−50
−60
Radar Cross Section σ/λ², dB
0
30
60
90
Angle of Incidence θ, deg.
H−Pol
H−Pol(2D)
E−Pol
E−Pol(2D)
z
θ
y
x
φ
(b)

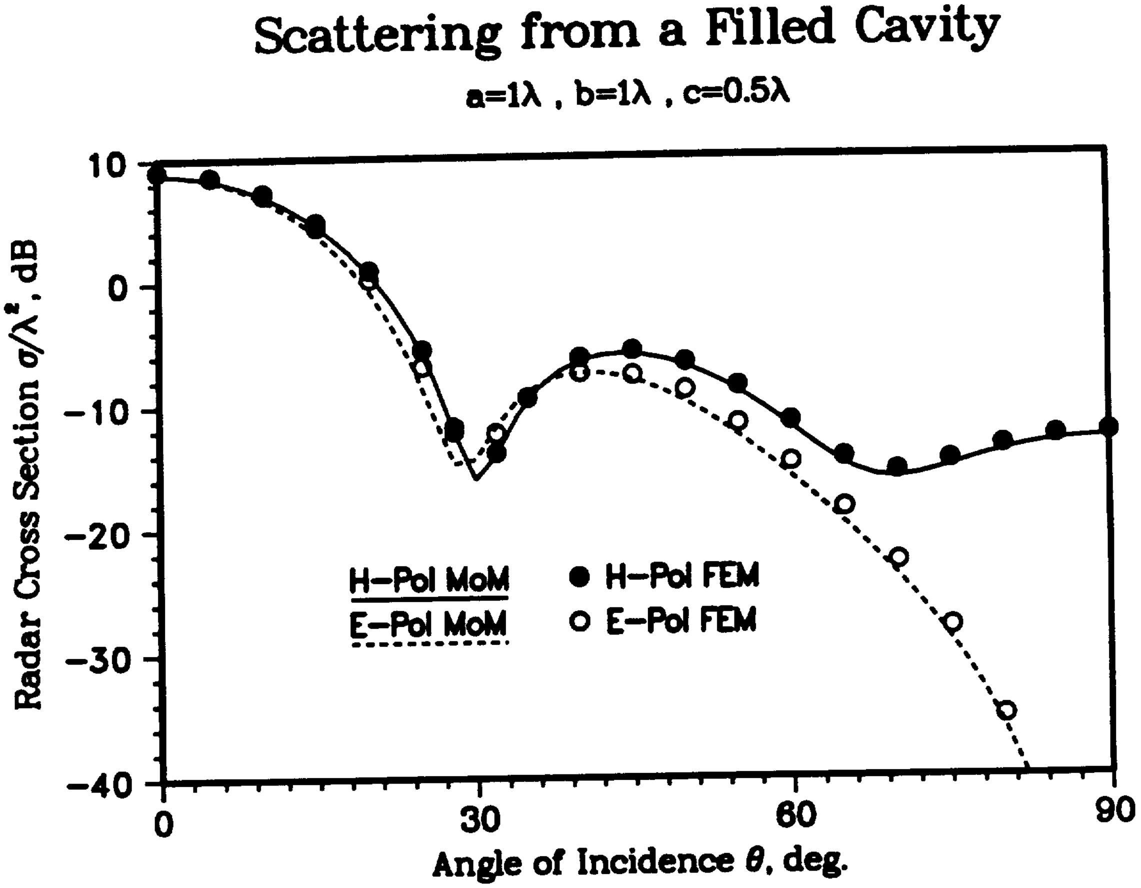

Figure 7.7: Backscatter RCS elevation patterns for a $1\lambda \times 1\lambda \times 0.5\lambda$ cavity filled with a high contrast material ($\epsilon_r = 12 - j2.5, \mu_r = 4.5 - j1.2$); Comparison of the MoM solution using piecewise constant basis functions with the FEM [88].

7.3 GIBC Formulation

The full-wave formulation presented in the previous sections is applicable only for the cavities of rectangular shapes and may not be employed for the analysis of nonrectangular geometries. Furthermore, this formulation is not very efficient when considering aperture areas larger than $1\lambda^2$. Therefore, in this section, as in the two-dimensional case, we present an approximate formulation based on a simulation of the cavity backed apertures by an impedance insert satisfying impedance boundary conditions. The analysis of three-dimensional impedance inserts was given in Chapter 5.

Considering first the SIBC, the relevant integral equations are (5.59) and (5.60). Again, by setting $F_2 = 0$ in (5.64) and (5.65), we have

$$\begin{aligned} F_1(x,y)M_x(x,y) &+ \frac{2j}{k_o}\mathrm{DFT}^{-1}\left\{\left[\widehat{M}_x(k_o^2 - D_x^2) - \widehat{M}_y D_x D_y\right]\hat{\xi}\right\} \\ &= 2Z_oH_{ox}\exp\{jk_o\left[\sin\theta_o\left(x\cos\phi_o + y\sin\phi_o\right)\right]\} \end{aligned} \tag{7.85}$$

and

$$\begin{aligned} F_1(x,y)M_y(x,y) &+ \frac{2j}{k_o}\mathrm{DFT}^{-1}\left\{\left[-\widehat{M}_x D_x D_y + \widehat{M}_y(k_o^2 - D_y^2)\right]\hat{\xi}\right\} \\ &= 2Z_oH_{oy}\exp\{jk_o\left[\sin\theta_o\left(x\cos\phi_o + y\sin\phi_o\right)\right]\} \end{aligned} \tag{7.86}$$

which may be solved by the CGFFT method.

Figure 7.8 shows a comparison of the full-wave and SIBC solutions for scattering from the filled $1\lambda^2$ square cavity considered earlier. Since the filling material is of high contrast ($\epsilon_r = 12 - j2.5, \mu_r = 4.5 - j1.2$), good agreement is observed between the two solutions. When the losses in the cavity are not sufficiently high, the SIBC is not applicable and a higher order GIBC is required. Figure 7.9 shows the results for a long cavity $2.5\lambda \times 2.5\lambda \times 0.25\lambda$ filled by a material of lower loss ($\epsilon_r = 7 - j1.5$ and $\mu_r = 1.8 - j0.1$). The second order GIBC based on equations (5.64) and (5.65) is seen to yield an improved result for the longitudinal cut considered in this case. For H-polarization incidence, the magnetic currents do not vanish at $x = \pm 1.25\lambda$ and thus, as noted for two-dimensional cavities, the GIBC simulation would not be of acceptable accuracy in predicting the currents in the immediate vicinity of the cavity edges. This is a limitation in the numerical and analytical application of the GIBC, and stems from their non-uniqueness [89]. As noted in [90], additional conditions must be imposed at the cavity terminations to supplement the GIBC. Although the notion of these supplemental conditions is understood, their numerical implementation is cumbersome and inefficient in the context of the CGFFT solution. Thus, additional research is required before the GIBC can be employed for simulating coatings and filled cavities with abrupt terminations. On the other hand, if the cavity depth on the coating thickness is tapered to zero–as is often the case in practice–the presented formulation is then directly applicable. Unfortunately, no reference data are available for tapered three-dimensional coatings and cavities which will permit validation of the GIBC formulation.

7.4 Summary

A full-wave moment method formulation was presented for computing the scattering by an aperture formed by a rectangular cavity in a ground plane. In constructing the integral equations, the equivalence principle was employed to introduce equiva-

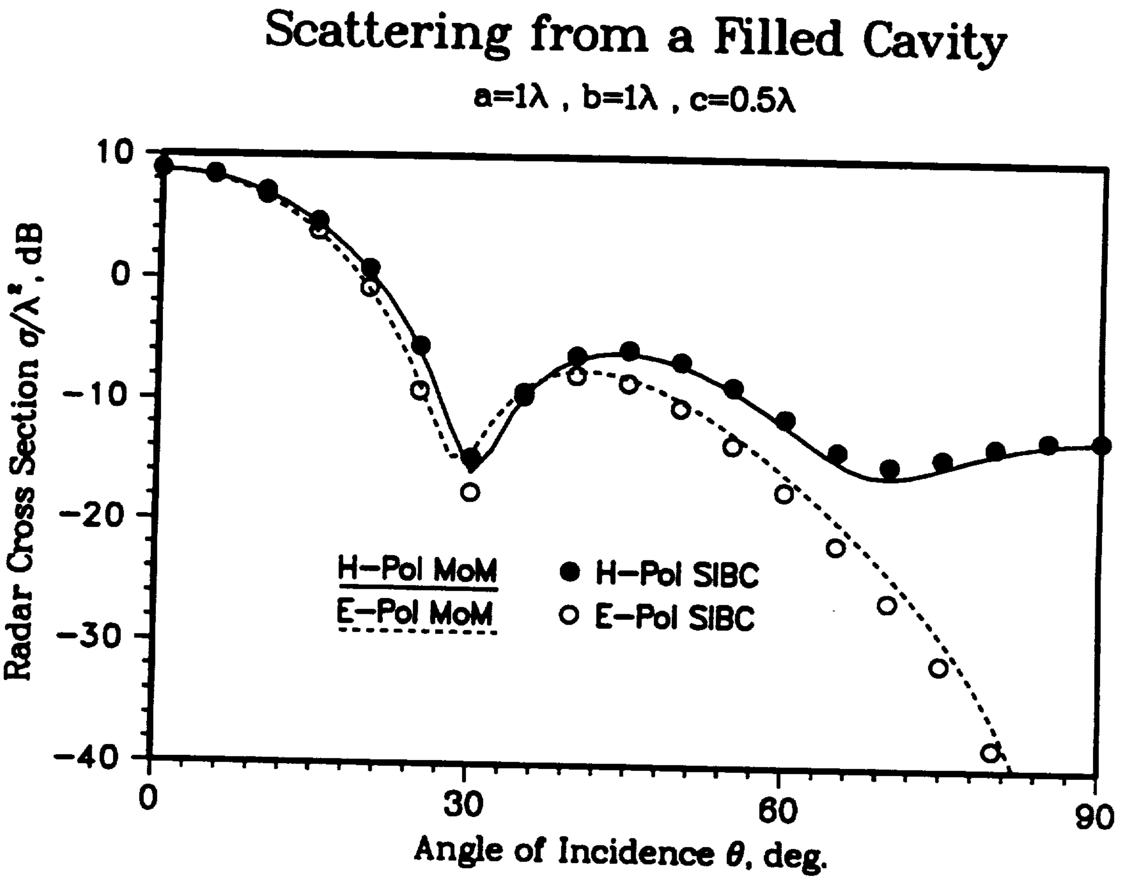

Figure 7.8: Backscatter RCS elevation patterns for a $1\lambda \times 1\lambda \times 0.5\lambda$ cavity filled with a high contrast material ($\epsilon_r = 12 - j2.5, \mu_r = 4.5 - j1.2$); Comparison of the full-wave (MoM) with the SIBC (CGFFT) solutions.

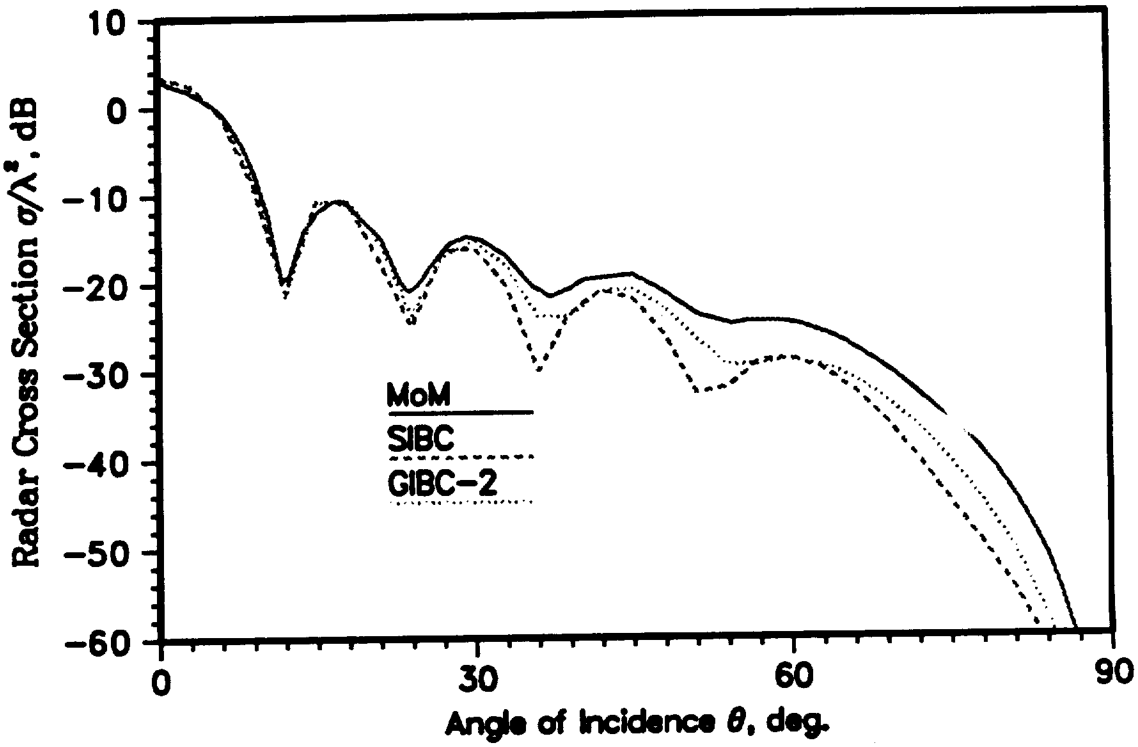

Figure 7.9: Comparison of the E-polarization scattering patterns for the long $2.5\lambda \times 2.5\lambda \times 0.25\lambda$ filled cavity ($\epsilon_r = 7 - j1.5, \mu_r = 1.8 - j0.1$) as obtained by the full-wave and approximate formulations (longitudinal $\phi = 0°$ cut).

lent magnetic currents across the cavity aperture. The fields interior and exterior to the cavity were then expressed as the radiation of the equivalent magnetic currents in conjunction with the modal and free space Green's function, respectively. Coupled integral equations for the two components of the magnetic currents were then obtained by enforcing continuity of the tangential fields across the cavity. These were discretized using Galerkin's technique in conjunction with piecewise constant and roof-top basis expansion functions. The resulting matrix system was solved by LU decomposition.

The most challenging aspect of the implementation was the computation of the slowly converging mode sums required for the evaluation of the interior admittance elements. This is particularly so for the piecewise constant basis implementation unless the cavity is narrow in one direction. The roof-top basis implementation provided a much more rapid convergence at the expense of complexity in the evaluation of the external admittance elements. Nevertheless, as is usually the case with three-dimensional moment method solutions, the presented solution demands excessive CPU time when the aperture size is beyond one square wavelength. It is, therefore, more applicable for smaller cavities and particularly those which are narrow in one direction.

Next, an alternative approach based on the GIBC was presented. In this case, the structure is essentially modelled as an impedance insert and since this formulation is amenable to a CGFFT solution, larger cavity-backed apertures can be handled. For the analysis of cavities filled with electrically dense materials, very good results were obtained when employing the SIBC. A second order GIBC was also considered which is believed to yield acceptable results for lower contrast material fillings.

An important contribution of this Chapter was the presentation of RCS patterns for various empty and filled rectangular cavities and to our knowledge these are the first validated patterns to appear in the literature for this basic cavity shape.

Part III

VECTOR-CONCURRENT APPLICATIONS

CHAPTER VIII

OPTIMIZATION OF THE CGFFT ALGORITHM

8.1 Introduction

Computational electromagnetics relies heavily on vector-oriented algorithms to simulate complex problems. With the computer technology approaching the limits of semiconductor speeds, the exploitation of parallel processing has emerged in order to meet the processing demands of computationally intensive applications in electromagnetics. Most modern computing facilities now offer vector and parallel processing capabilities. A vector facility exploits the independence of operations, particularly those associated with the elements in an array or vector. In such machines, instructions are vectorized and distributed across different vector processors for concurrent execution as opposed to the traditional approach where the computers are limited to sequential processing of data on a single scalar processing unit.

The CGFFT lends itself to efficient execution in vectorized fashion. Most operations involve array manipulations which are vectorizable. Also, several of the steps in the iteration algorithm can be treated independently and can thus be performed on different processors. Most importantly, since the FFT is a highly vectorizable algorithm, it plays a major role in the speed of the solution algorithm and overall efficiency of the optimized code. In this chapter, a vector-concurrent form of the CGFFT method suitable for implementation on parallel multiprocessor systems is applied to the problem of scattering from electrically large planar structures. To demonstrate the speed advantage which can be realized when executing the CGFFT solution on a vector-concurrent facility, a few tests were performed on the supercomputers and mini-supercomputers.

8.2 Optimization

Before an assessment of the vectorizability of the CGFFT algorithm, a brief review of some general concepts in vector and parallel processing will be presented. This discussion is followed by an overview of the optimized CGFFT algorithm used in this study.

8.2.1 Vectorization

The crux of parallel computing is the process of vectorization and distribution of code among multiple processors. Typically, a vector instruction is capable of operating on 32 to 128 elements of data at once, depending on the machine used, resulting in two to four times gain in speed over the corresponding sequential scalar instruction. Vectorization requires some degree of independence in the access of data by the code. A dependence occurs when two statements—or iterations of the same statement—refer to the same storage location. Some data dependences *inhibit* vectorization; they are called *recurrences*. By changing the structure of the code, it may be possible to eliminate a recurrence and vectorize the modified code.

A typical example of vectorization occurs when performing element by element addition or product of two independent arrays/vectors. In a scalar machine, each element product or addition will be done sequentially, whereas in a vector facility vector registers are employed to perform several of the element operations concurrently. That is, when a DO loop is encountered, the loop iterations are not executed sequentially but in parallel, provided there are no data dependences among the loop iterations. When a parallel (concurrent) facility is also available, independent operations or sections of the program may be executed on different processors. In this manner, several matrix operations involving independent vectors/arrays may be performed in parallel.

In order to measure the improvement in the speed of a vectorized code, several parameters are defined. The ***program speedup*** is defined as the increase in the speed of execution when a code is run in vector mode relative to that in the scalar mode. Therefore, referring to Figure 8.1, if a code runs for T_s seconds in scalar mode and for T_v seconds in vector mode (i.e. after optimization), the corresponding program speedup is given by

$$\text{program speedup} = T_s/T_v \tag{8.1}$$

Also, the ***vector content*** of a program is that percent of the scalar code which vectorizes. Thus, if for a given code, the scalar portion which may not be vectorized runs in t_s seconds, and that which is vectorizable runs in t_v seconds in scalar mode and in t_{vf} seconds in vector mode[1], we have

$$\text{vector content} = t_v/T_s \times 100 \tag{8.2}$$

and

$$\text{vector speedup} = t_v/t_{vf} \tag{8.3}$$

---

[1] t_{vf} would be the time the code actually spends in the vector facilities.

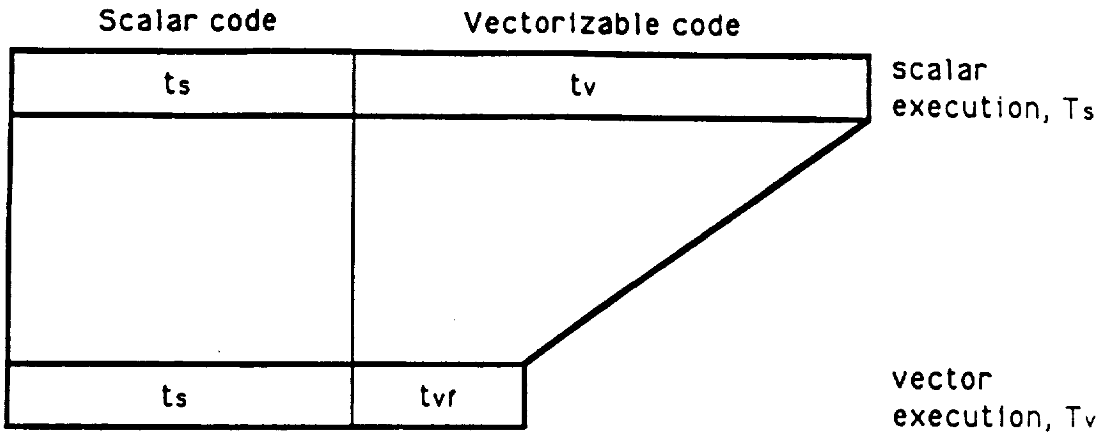

Figure 8.1: Scalar and vector execution times in a typical vectorized code.

Typically, programs with more than about 70% vector content run 1.5 to 2 times faster in vector mode. However, as will be shown later, higher vector contents are achievable for the case of CGFFT algorithm.

8.2.2 Concurrency

Although it is increasingly expensive to make a single processor faster, fairly fast processors are inexpensive. Therefore using several relatively inexpensive processors in parallel is often more efficient than using a single fast processor. A multiple processor system can devote several processors to the execution of different parts of a single program simultaneously. The compiler inserts protective synchronization code into the optimized loops so that the multiple processors work together without interfering with each other. Synchronization is needed to prevent conflicts in the use of memory shared by parallel tasks and is considered the major cost of parallel processing. Optimization is suppressed whenever the possibility of a data dependence exists. Also, from Amdahl's law the increase in the speed of execution in concurrent mode as the number of processors is increased, approaches an upper limit set by the presence of the sequential constructs in the algorithm.

In general, the concepts of data dependence in parallel processing are the same as those in vector processing; the consequences of certain dependences, however, are different.

A parameter of interest when processing in concurrent mode is the *efficiency* of execution. Efficiency is a measure of parallelism in the algorithm. An efficient parallel tasking system makes possible a nearly linear speedup in performance as processors are added, if the algorithm is parallel. Thus, if $T^{(n)}$ denotes the time required to run on n processors, we may define

$$\text{concurrency speedup} = \frac{T^{(1)}}{T^{(n)}} \tag{8.4}$$

and

$$\text{efficiency\%} = \frac{T^{(n)}}{nT^{(1)}} \times 100 \tag{8.5}$$

8.3 Optimized CGFFT Algorithm

Here, the vectorizable nature of the CGFFT algorithm is exploited by identifying the major processes involved in a given iteration. From (2.1), it can be seen that each iteration in (2.3) requires two convolution operations, two norm calculations and three scalar products. A considerable amount of computation time is spent in the calculation of the convolutions carried out in $\mathcal{A}[\mathbf{P}_n]$ and $\mathcal{A}^a[\mathbf{R}_n]$. Each convolution includes a pair of forward and inverse Fourier transform operations on the relevant components of the current density vector along with a Hadamard (element by element) multiplication of the current and the dyadic Green's function in the spectral domain. Since for a given current component there is no data recurrence at a particular point in an iteration, these operations may be vectorized to increase the speed of calculations. The same observation is true for the computation of the norms and the dot products used to update the current **J**, the residual vector **R**, and the search vector **P**. More importantly, since the FFT is a highly vectorizable algorithm, it plays a major role in the speed and efficiency of the optimized code.

The processing was carried out on two vector machines available at the time of this study, namely, the Alliant FX/8 multiprocessor and the IBM 3090/600E supercomputer. Some general guidelines for code optimization are given in Appendix E and have been followed in optimizing the CGFFT algorithm in the present study. It should be noted that the data reported here on the actual performance of the algorithm on a given mode of execution will be of little value, as current and future advancements in computer technology renders them obsolete; however, it is the relative performance improvement which is of interest when the algorithm is executed in the optimized mode as compared with the sequential mode.

To assess the efficiency of the optimized code, the rectangular plate problem discussed in Chapter 4 was examined in some detail. Tables 8.1 and 8.2 show the performance of the optimized CGFFT algorithm executed on the Alliant and IBM vector facilities for computing the currents on a $2\lambda \times 2\lambda$ conducting plate. The plate was assumed to be illuminated at normal incidence by an E-polarization plane wave and 63×63 unknowns and 128×128 FFT pad (order 1) were employed. The percent vectorizable code of 97% indicates a highly optimized algorithm resulting in a program speedup of more than four times. It is clear from the tables that the vectorized FFT is mainly responsible and contributes to the speedup in the execution time. The performance point of the IBM supercomputer for this particular case is given in Figure 8.2 indicating the remarkably high efficiency of the optimized algorithm.

In the case of the Alliant, the overall speedup was more than 600 percent per iteration. The speedup in execution time is even more impressive when all four processors of the Alliant are utilized. As seen from Table (8.4), a speedup of 3.5 was achieved when using four concurrent processors at an efficiency of 88%. This implies a speedup of more than 20 times per iteration when combined with the data in Table (8.2). Again, the improvements in the performance of the algorithm is attributed to the vectorized FFT which is the most significant factor in the solution process. This is illustrated in Figure 8.3 where the distribution of the CPU time among the computationally intensive routines in the scalar and vector modes are shown.

In order to further evaluate the efficiency of the method when the size of the problem grows, the cases of $5\lambda \times 5\lambda$ and $10\lambda \times 10\lambda$ plates were also considered with the corresponding results reported in Tables 8.4 and 8.5. The sampling density in these cases were 625 unknowns/λ^2 with a FFT pad of order one. Interestingly, similar speedups are observed for larger plates indicating that the aforementioned results are independent of the cache memory. Figures 8.4 and 8.5 show the components of the surface current densities excited on the conducting plates and calculated by the CGFFT method in the vector-concurrent mode. It should be noted that the calculation of the surface currents associated with the conducting plate in Figure 8.5 required 125,000 unknowns. This large number of unknowns presents a challenge for direct matrix inversion approaches because of their large storage requirement. In contrast, the CGFFT solution could be performed on a relatively small computer.

Finally, the backscattering behavior of an equilateral triangular conducting plate of side length 5λ at near grazing (conical cut at $\theta_o = \theta = 80°$) is shown in Figure 8.6. Due to the symmetry of the problem, the full-range data was replicated from that calculated in the range $0 \leq \phi < 60°$.

8.4 Summary

It was shown that the conjugate gradient FFT algorithm is suitable for vector-concurrent optimization and may be efficiently implemented on multi-processor computers. The FFT plays a crucial role in the speedup and the efficiency of such an application. As the size of the problem becomes larger, there is a corresponding degradation in the performance of the optimized code due to the complexity of the memory cache references. This complexity, however, has not proven restrictive in the examples considered because the CGFFT method does not suffer from the same memory requirements as the direct methods do. Thus, relatively large problems can be handled without considerable loss of efficiency and speed.

Although this study was concerned with automatic parallelization, which is limited to optimization of individual loops, parallelism at a larger granularity can be specified by the programmer to achieve a superior performance for more complex problems. An example of such an application is the problem of scattering by a dielectric plate of finite thickness where the normal component of the current density is totally independent of the planar components and can be solved for by a dedicated processor in parallel with them.

CGFFT Code	Execution Mode		
Performance	Scalar (scalar FFT)	Vector (scalar FFT)	Vector (vector FFT)
ELAPSED CPU, sec	148	129	34
VECTOR CPU, sec	-	9	30
VECTORIZABLE CODE, sec	-	28	144
VECTOR CONTENT	-	18.9%	97.3%
VECTOR SPEEDUP	-	3.1	4.8
PROGRAM SPEEDUP	-	1.15	4.35

Table 8.1: Performance of the scalar and vectorized code on the IBM 3090.

CGFFT Code	Execution Mode		
Performance	Scalar (scalar FFT)	Vector (scalar FFT)	Vector (vector FFT)
INITIALIZATION, sec	2.39	0.72	0.80
CGFFT LOOP, sec	4307.0	1255.2	342.8
TOTAL CPU TIME, sec	4309.3	1255.9	343.6
ITERATIONS	111	111	59
PER ITERATION, sec	38.80	11.31	5.8
MEGAFLOPS	0.0527	0.1807	0.3512
PROGRAM SPEEDUP	-	3.43	12.54
SPEEDUP/ITERATION	-	3.43	6.69

Table 8.2: Performance of the scalar and vectorized code on the Alliant FX/8.

Optimized CGFFT	NO. of processors			
Performance	1	2	3	4
INITIALIZATION, sec	1.60	0.86	0.61	0.50
CGFFT LOOP, sec	407.4	211.0	146.7	115.6
TOTAL CPU TIME, sec	409.0	211.8	147.3	116.1
ITERATIONS	59	59	59	59
PER ITERATION, sec	6.91	3.58	2.49	1.96
MEGAFLOPS	0.2951	0.5697	0.8192	1.0340
SPEEDUP	-	1.93	2.78	3.52
EFFICIENCY	-	96.5%	92.7%	88.0%

Table 8.3: Vector-Concurrent performance for a $2\lambda \times 2\lambda$ plate.

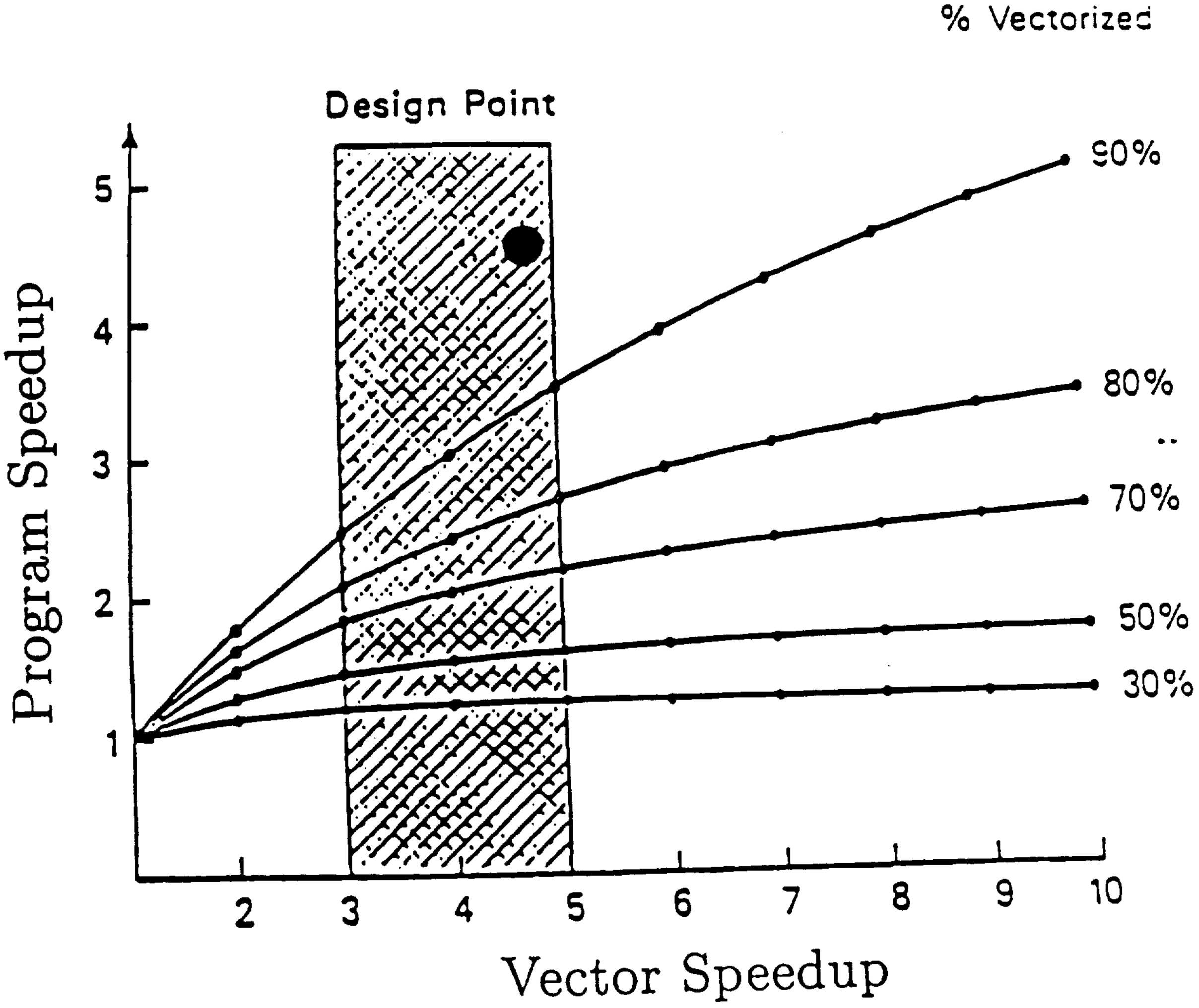

Figure 8.2: Performance of the optimized CGFFT algorithm on the IBM 3090.

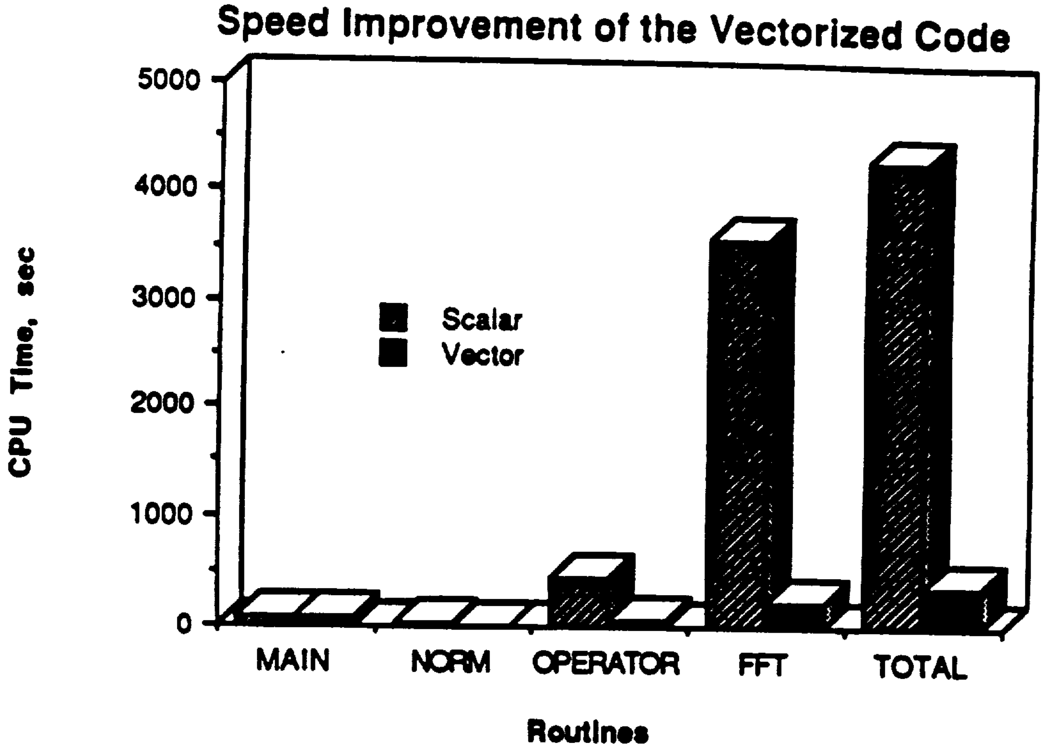

Figure 8.3: Distribution of the CPU time among the computationally intensive routines.

Optimized CGFFT	NO. of processors			
Performance	1	2	3	4
INITIALIZATION, sec	6.35	3.26	2.32	1.90
CGFFT LOOP, sec	1096.6	568.9	398.4	319.0
TOTAL CPU TIME, sec	1103.0	572.2	400.7	320.9
ITERATIONS	46	46	46	46
PER ITERATION, sec	23.98	12.44	8.71	6.98
MEGAFLOPS	0.3848	0.7417	1.0590	1.3226
SPEEDUP	-	1.93	2.75	3.43
EFFICIENCY	-	96.5%	91.7%	85.8%

Table 8.4: Vector-Concurrent performance for a $5\lambda \times 5\lambda$ plate.

Optimized	NO. of processors			
Performance	1	2	3	4
INITIALIZATION, sec	24.55	13.60	9.10	7.23
CGFFT LOOP, sec	3673.3	1973.0	1349.8	1080.5
TOTAL CPU TIME, sec	3697.8	1986.6	1358.9	1087.7
ITERATIONS	38	38	38	38
PER ITERATION, sec	97.31	52.28	35.76	28.62
MEGAFLOPS	0.4223	0.7861	1.1492	1.4357
SPEEDUP	-	1.86	2.72	3.40
EFFICIENCY	-	93.0%	90.7%	85.0%

Table 8.5: Vector-Concurrent performance for a $10\lambda \times 10\lambda$ plate.

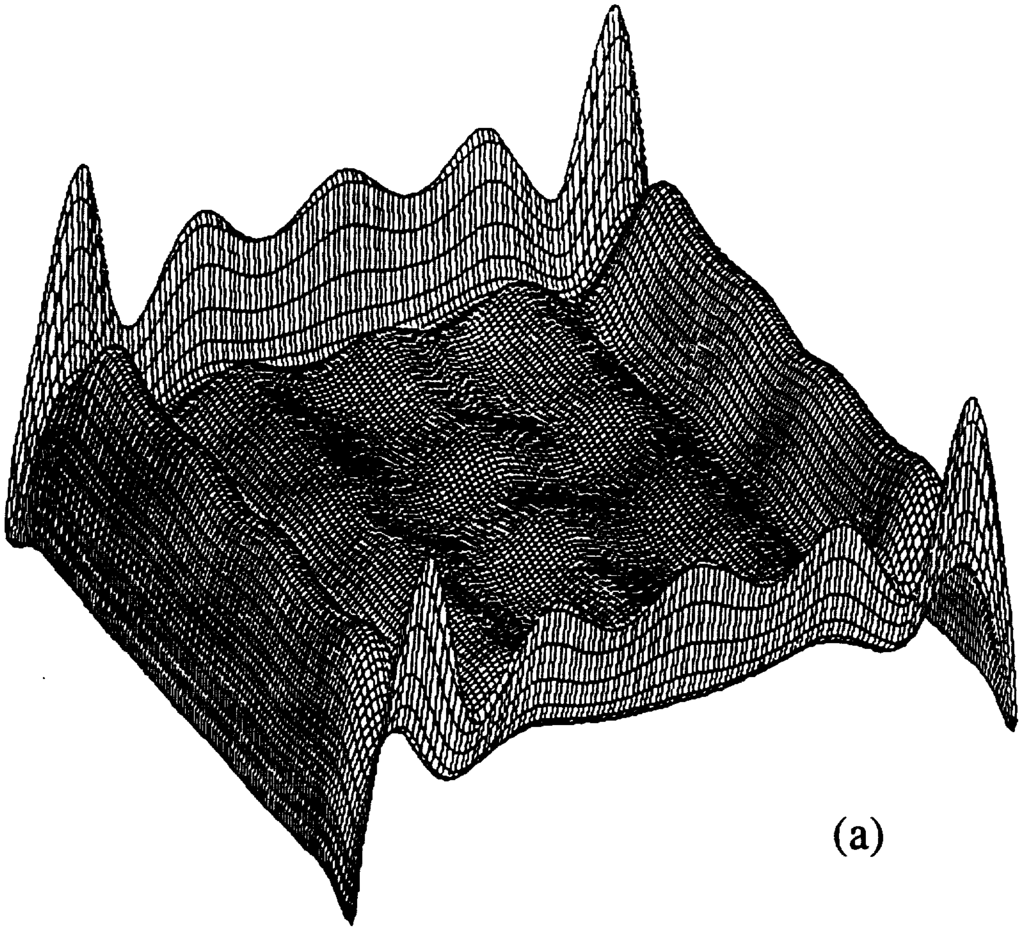

Figure 8.4: E-polarization plane wave scattering from a $5\lambda \times 5\lambda$ conducting plate at normal incidence (125×125 unknowns and FFT pad of order $\varrho = 1$). (a) Co-polarized component of the current density. (b) Cross-polarized component of the current density.

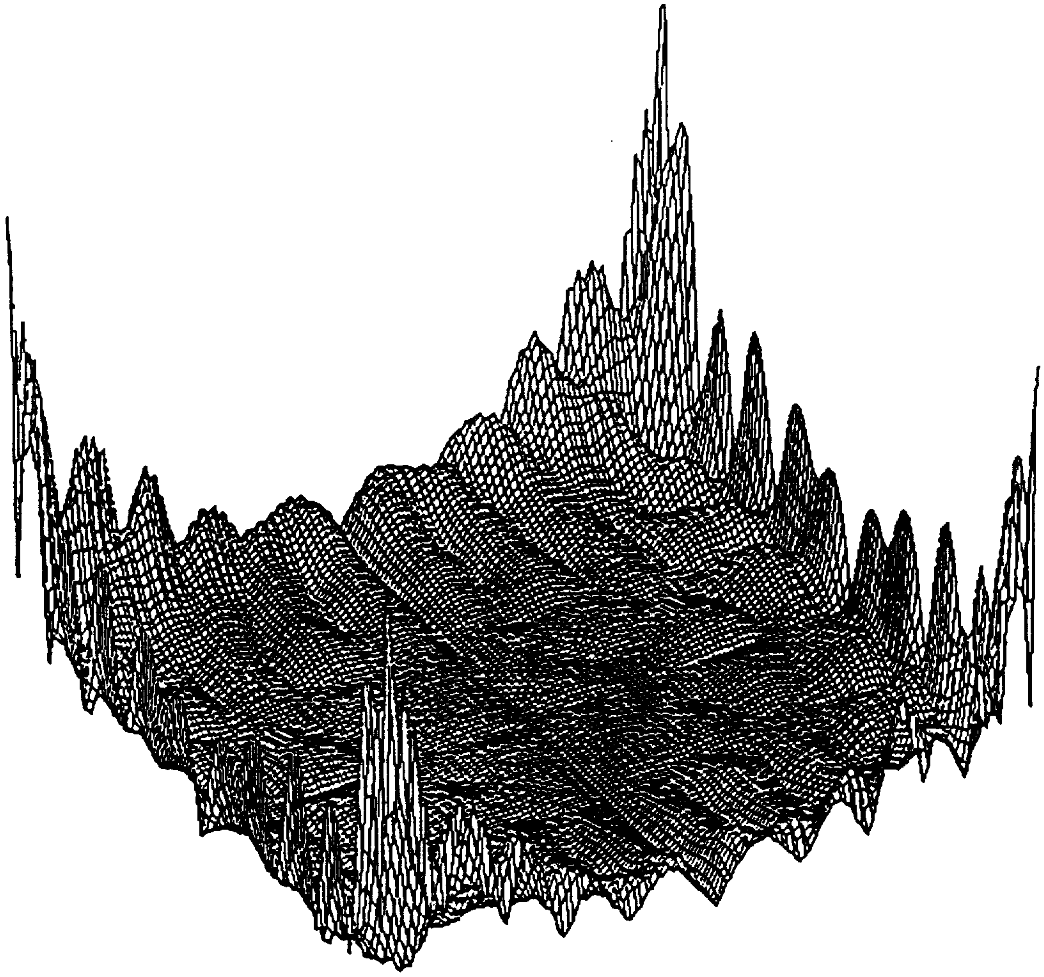

(b)

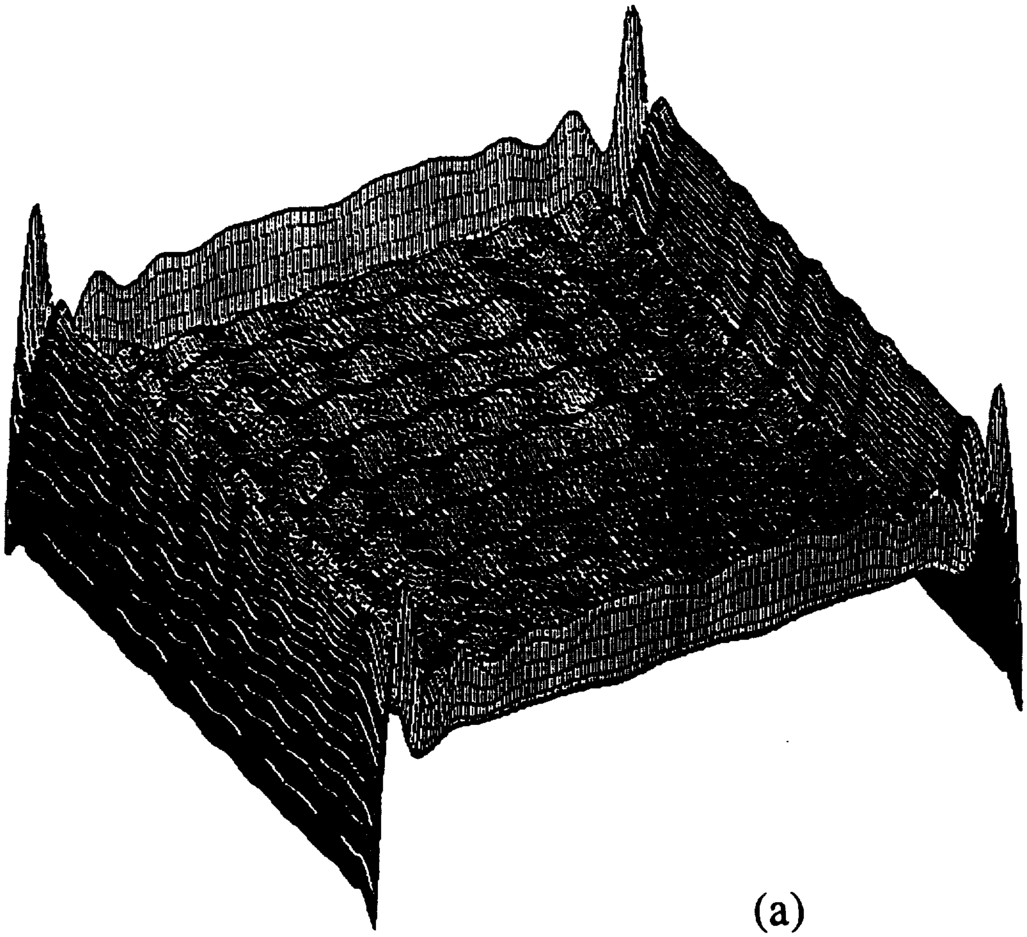

Figure 8.5: E-polarization plane wave scattering from a $10\lambda \times 10\lambda$ conducting plate at normal incidence (250×250 unknowns and FFT pad of order $\varrho = 1$). (a) Co-polarized component of the current density. (b) Cross-polarized component of the current density.

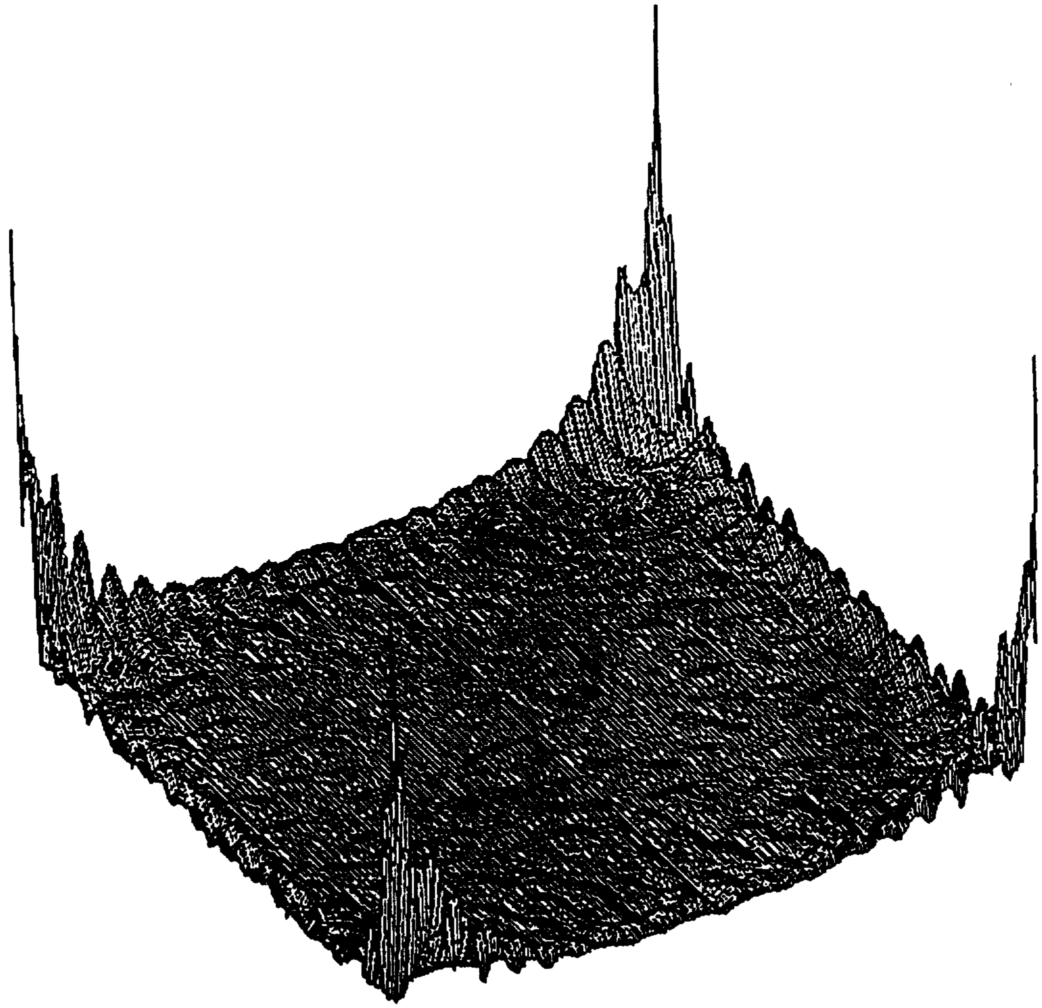

(b)

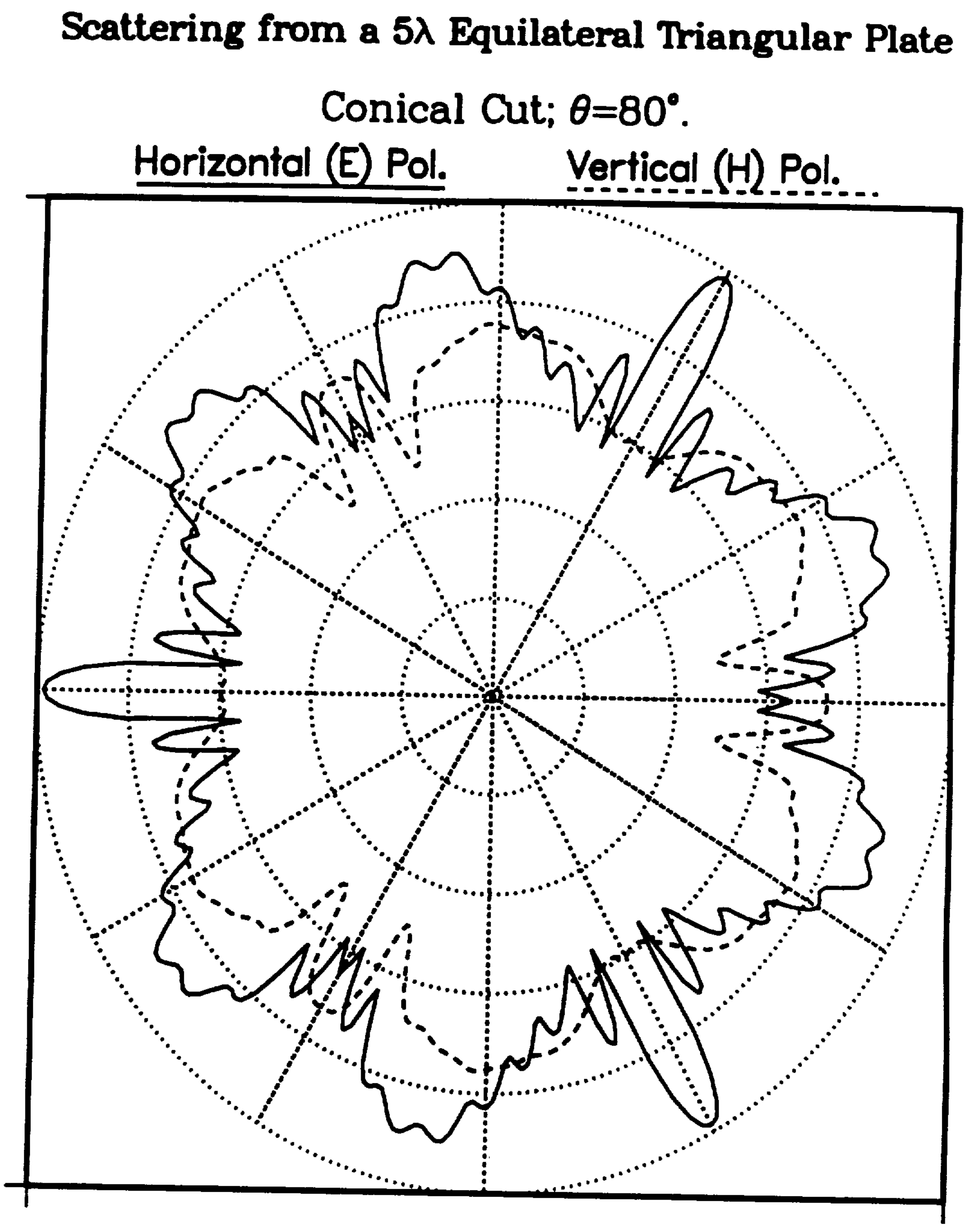

Figure 8.6: Conical backscattering cross section of an equilateral triangular conducting plate of side 5λ at $\theta = 80°$; 625 unknowns/λ^2; Maximum number of iterations: 250; Average tolerance: 0.015 (E-Pol.) and 0.025 (H-Pol.).

CHAPTER IX

Conclusions

The theoretical and computational aspects related to the application of the conjugate gradient FFT method in computational electromagnetics have been examined.

The first Part of the thesis was devoted to the problems of electromagnetic radiation and scattering from linear, cylindrical, and planar structures. Both perfectly conducting and imperfect bodies were treated. A number of highly efficient and accurate numerical codes have been developed for the solution of these problems. These programs cover a broad range of operations in terms of frequency, material composition, and structural geometry and may be used for both analysis and design purposes.

The provisions of incorporating various expansion functions into the CGFFT method was discussed in Chapter 2. It was found that by employing subdomain basis functions, the convergence rate of the CGFFT method can be improved drastically. In particular, a quantitative measure of convergence improvement was established for a class of such basis functions. Illustrative examples of CGFFT applications to two- and three-dimensional problems were presented in Chapters 3 and 4, respectively. Two different but related approaches in computing the integrodifferential convolutions were presented. The first approach (CGFT) was based on employing the sampled continuous transform of the Green's function, while the other (CGDFT) employed finite duration discrete Fourier transforms. The latter method was found to provide a more efficient (and more accurate) simulation, particularly for E-polarization cases.

Other variations in formulating the CGFFT method have appeared in the literature recently. These approaches differ primarily in the chosen (or implied) basis functions for the unknown current density, and the method of computing the integrodifferential operator in the spectral domain. Some examples of these variations have already been discussed in this thesis. In addition to these approaches, some authors have proposed other methods of formulating the integral equations. In particular, it has been shown that by introducing the surface charge density in the integral formulation and expanding the vector potential instead of the current density, smoother and more stable solutions may be achieved [91].

Incorporation of the impedance boundary conditions into CGFFT was considered in Chapter 5. Advantages include the elimination of a need to sample within the volume, further reducing the memory demand and also avoiding the difficulties associated with the calculation of the Green's function. Application of the generalized impedance boundary conditions in modelling the two- and three-dimensional impedance inserts was shown to be compatible with the basic CGFFT formulation, thus allowing an efficient simulation of coated structures and filled cavity-backed apertures.

The problems of scattering from two- and three-dimensional rectangular grooves and cavities were studied in Part Two of the thesis. After presenting a general full-wave analysis, approximate solutions based on the impedance boundary conditions were considered. GIBCs of up to order 3 were employed. The formulations based on these boundary conditions were amenable to a CGFFT solution and were found easier to implement than the full-wave formulation. The predicted currents based on the GIBC simulations are in general incorrect near the edges. However, for high-contrast material fillings, the SIBC was found adequate in modeling the groove. Further research is needed to study the applicability of the higher order conditions to terminated cavity and coated structures, and to establish the ranges of validity for such applications. For the two-dimensional case, a hybrid exact-GIBC approach was proposed which provided a good prediction of the scattering behavior of rectangular grooves without compromising the advantages offered by CGFFT. In contrast, when the impedance variations of the insert are sufficiently slow, a direct application of the impedance boundary condition is sufficient.

A vector-concurrent implementation of the CGFFT method was presented in Part Three. It was shown that the CGFFT algorithm is highly vectorizable and may be efficiently implemented on supercomputers and multiprocessor machines. Vectorization and parallelization of the underlying algorithms will be of great importance in reducing the computation time and improving the efficiency of the CGFFT solution method.

Beyond the basic applications considered in this study, the extension to three-dimensional structures with and without anisotropy is straightforward by employing the three-dimensional FFT. Also, the CGFFT method is directly applicable in solving systems relating to scattering, transmission and radiation by periodic structures and arrays. In that case, the resulting system is discrete and no need arises for corrective measures due to discretization.

New emerging methodologies which combine the CGFFT with other numerical techniques are of potential importance in future research. In addition to the hybrid exact-GIBC solution discussed in Chapter 6, the Finite Element and CGFFT methods can be combined to reduce the dimensionality of the required FFT and consequently improve the efficiency of the solution process [92].

The numerical results presented in this thesis will serve two purposes. First, they can be used as reference for future developments in this area. Second, future work may use the various programs developed in this study to investigate the behavior of different scatterers in an attempt to develop simple mathematical and physical models. Since the main advantage of the CGFFT method in comparison with matrix inversion techniques is its reduced memory demand, it is particularly useful in large scale electromagnetic simulations.

APPENDICES

APPENDIX A

THE METHOD OF MOMENTS

Traditionally, equation (1.1) is solved directly by the Method of Moments(MoM) [20, 93]. The method of moments is a projective method in which a functional equation in an infinite dimensional function space is approximated by a matrix equation in a finite dimensional subspace.

Consider the linear operator equation

$$A[f] = g \tag{A.1}$$

where A is the linear operator, g is a known function, and f is an unknown function to be determined. In the method of moments the unknown function f is represented approximately by a linear combination of a finite set of functions f_n in the domain of A

$$f \simeq \sum_{n=1}^{N} c_n f_n \qquad f_n \in \mathcal{D}_A \tag{A.2}$$

where c_n are scalars to be determined. The functions f_n are known as basis or expansion functions. Substituting (A.2) into (A.1) gives

$$\sum_{n=1}^{N} c_n A[f_n] \simeq g \tag{A.3}$$

where the linearity of the operator has been employed. Defining the residual error R

$$R = g - \sum_{n=1}^{N} c_n A[f_n] \tag{A.4}$$

the coefficients c_n are computed so that the residual error is orthogonalized, with respect to an inner product, to a sequence of weighting functions w_n defined in the range of A

$$< w_m, R >= 0 \qquad m = 1, \cdots, N \qquad w_m \in \mathcal{R}_A \tag{A.5}$$

The above inner products are called the weighted residuals. This represents a system of linear equations

$$\sum_{n=1}^{N} c_n < w_m, A[f_n] >=< w_m, g > \qquad m = 1, \cdots, N \tag{A.6}$$

which can also be put in the matrix form

$$[A_{mn}][c_n] = [g_m] \tag{A.7}$$

where $[A_{mn}]$ is the matrix of elements

$$A_{mn} =< w_m, A[f_n] > \tag{A.8}$$

and $[g_m]$ is the column vector

$$g_m =< w_m, g > \tag{A.9}$$

If $[A_{mn}]$ is nonsingular, its inverse exists, and $[c_n]$ is given by

$$[c_n] = [A_{mn}]^{-1}[g_m] \tag{A.10}$$

The solution f is then obtained from (A.2)

$$f = [f_n]^t[A_{mn}]^{-1}[g_m] \tag{A.11}$$

where $[f_n]^t$ is the row vector of basis functions.

Two classical approaches have found utility in choosing the weighting functions w_n. These are referred to as the Galerkin's method and the point matching method.

A.1 Galerkin's Method

Galerkin's method may be considered as the specialization of moment method to the case of self-adjoint operators. The adjoint operator A^a is defined with respect to the inner product as

$$< w, A[f] >=< A^a[w], f > \qquad f \in \mathcal{D}_A \qquad w \in \mathcal{D}_A^a \tag{A.12}$$

and if the domains of A and A^a are the same, we can choose $w_n = f_n$. For self-adjoint operators ($A = A^a$), this choice of weighting functions makes $[A_{mn}]$ a symmetric matrix which may be desirable from a numerical standpoint.

A.2 Point Matching

If the weighting functions are formally chosen to be Dirac delta functions, equation (A.3) is satisfied at discrete points in the region of interest. This is the simplest specialization of the moment method. The major advantage of this method is that the integrations represented by the inner products (A.8) and (A.9) now become trivial since they are evaluated at discrete points.

APPENDIX B

THE FREE SPACE GREEN'S FUNCTION AND ITS TRANSFORM

Consider the complex vector wave equation (Helmholtz equation) satisfied by the electric field in a homogeneous isotropic medium

$$\nabla \times \nabla \times \mathbf{E} - k^2\mathbf{E} = -j\omega\mu\mathbf{J} \tag{B.1}$$

The field may be expressed in terms of the Hertz vector potential of electric type

$$\mathbf{\Pi}(\mathbf{r}) = -\frac{jZ}{k}\iiint_V \mathbf{J}(\mathbf{r}')G(\mathbf{r};\mathbf{r}')dv' \tag{B.2}$$

where G is the scalar free space Green's function satisfying the scalar wave equation

$$\nabla^2 G(\mathbf{r}) + k^2 G(\mathbf{r}) = -\delta(\mathbf{r}) \tag{B.3}$$

The Green's function can be regarded as the response due to a point source and it is of interest to find the Green's function and its Fourier transform corresponding to a line source (two dimensional case) and a point source (three dimensional case).

B.1 Line Source

For a two dimensional problem ($\frac{\partial G}{\partial z} = 0$), the Helmholtz equation reads

$$(\frac{\partial^2}{\partial x^2} + \frac{\partial^2}{\partial y^2} + k^2)G(x,y) = -\delta(x)\delta(y) \tag{B.4}$$

Due to the axial symmetry of the problem, the wave equation can be written in cylindrical coordinates as

$$(\frac{\partial^2}{\partial\rho^2} + \frac{1}{\rho}\frac{\partial}{\partial\rho} + k^2)G(\rho) = -\delta(\rho) \tag{B.5}$$

where $\delta(\rho) = \delta(x)\delta(y)$. Outside the source region, the right hand side is zero and (B.5) is the Bessel equation of the zeroth order. Therefore, in view of the time convention $e^{j\omega t}$, a solution of (B.5) representing an outgoing wave that satisfies the radiation condition is the Hankel function of the second kind [~~96~~]
94

$$G(\rho) = \frac{1}{4j}H_o^{(2)}(k\rho) \tag{B.6}$$

The asymptotic expansion of the Hankel function is given by [44]

$$H_o^{(2)}(k\rho) \sim \sqrt{\frac{2j}{\pi k\rho}}e^{-jk\rho}, \qquad k\rho \to \infty \tag{B.7}$$

and G shows the proper behavior in the far field.

In order to find the Fourier transform $\tilde{G}$, we write

$$G(x,y) = \frac{1}{(2\pi)^2}\int_{-\infty}^{\infty}\int_{-\infty}^{\infty}\tilde{G}(k_x,k_y)e^{j(k_xx+k_yy)}dk_xdk_y \tag{B.8}$$

$$\delta(x,y) = \frac{1}{(2\pi)^2}\int_{-\infty}^{\infty}\int_{-\infty}^{\infty}e^{j(k_xx+k_yy)}dk_xdk_y \tag{B.9}$$

and substitute these in (B.4) to obtain for all x and y we have

$$\frac{1}{(2\pi)^2}\int_{-\infty}^{\infty}\int_{-\infty}^{\infty}(-k_x^2 - k_y^2 + k^2)\tilde{G}(k_x,k_y)e^{j(k_xx+k_yy)}dk_xdk_y = -\frac{1}{(2\pi)^2}\int_{-\infty}^{\infty}\int_{-\infty}^{\infty}e^{j(k_xx+k_yy)}dk_xdk_y, \qquad \forall x,y \tag{B.10}$$

Consequently, we may formally write

$$\tilde{G}(k_x,k_y) = -\frac{1}{k^2 - k_x^2 - k_y^2} \tag{B.11}$$

and equivalently,

$$G(x,y) = -\frac{1}{(2\pi)^2}\int_{-\infty}^{\infty}\int_{-\infty}^{\infty}\frac{1}{k^2-k_x^2-k_y^2}e^{j(k_xx+k_yy)}dk_xdk_y \tag{B.12}$$

However, this integral is undefined for real values of k, because the poles

$$k_y = \pm\sqrt{k^2-k_x^2} \tag{B.13}$$

are located in the path of integration on the real k_y-axis (Figure B.1). This difficulty can be alleviated by introducing a small loss in the medium so that $k = k' - jk''$, and the poles are given by

$$k_y = \mp(k'_\rho - jk''_\rho) \tag{B.14}$$

The singularities are now located off the real axis and the inverse transform (B.12) is defined. Furthermore, in accordance with the radiation condition, we demand the following functional form for the transform

$$\tilde{G}^+(k_x,y) = \phi^+(k_x)e^{jk_y^+y}, \qquad y>0 \tag{B.15}$$

$$\tilde{G}^-(k_x,y) = \phi^-(k_x)e^{jk_y^-y}, \qquad y<0 \tag{B.16}$$

where $k_y^\pm$ are such that

$$\begin{cases}\Re e\{k_y^+\}<0\\ \Im m\{k_y^+\}>0\end{cases} \quad\text{and}\quad \begin{cases}\Re e\{k_y^-\}>0\\ \Im m\{k_y^-\}<0\end{cases} \tag{B.17}$$

The k_y integral may now be carried out by contour integration in the upper and lower half planes corresponding to $y > 0$ and $y < 0$, respectively. Using Jordan's Lemma and Cauchy's theorem, we obtain

$$G(x,y) = -\frac{1}{4\pi j}\int_{-\infty}^{\infty}\frac{e^{jk_y^+y}}{k_y^+}e^{jk_xx}dk_x, \qquad y>0 \tag{B.18}$$

$$G(x,y) = -\frac{1}{4\pi j}\int_{-\infty}^{\infty}\frac{e^{jk_y^-y}}{k_y^-}e^{jk_xx}dk_x, \qquad y<0 \tag{B.19}$$

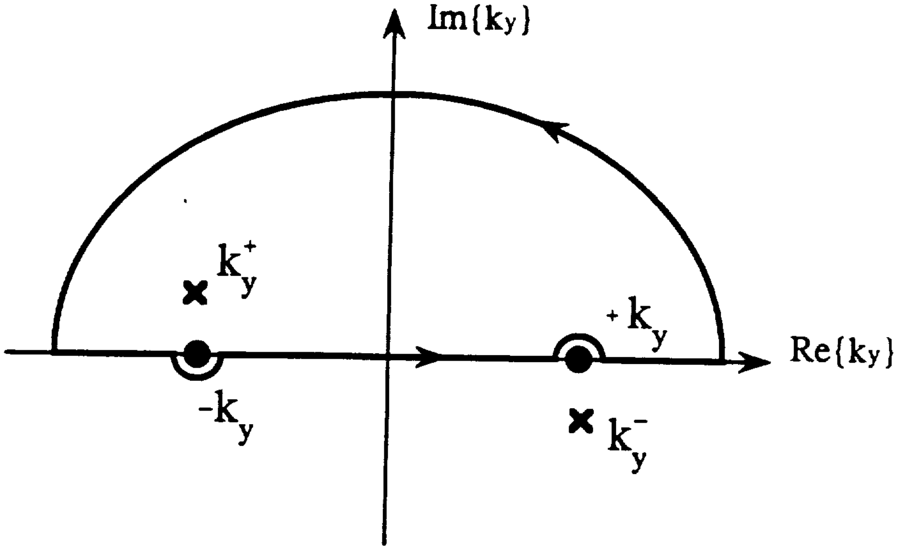

Figure B.1: Path of integration for the Fourier transform integral.

where $k_y^{\pm}$ are given by (B.13):

$$k_y^{\pm} = \mp\sqrt{k^2 - k_x^2} \tag{B.20}$$

Therefore, by uniqueness of the solution to partial differential equations satisfying the required boundary conditions, the final result holding for all values of y is given by

$$\frac{1}{4j} H_o^{(2)}(k\rho) = \frac{1}{4\pi j} \int_{-\infty}^{\infty} \frac{e^{-jk_y|y|}}{\text{sgn}\,(y) k_y} e^{jk_x x} dk_x, \qquad \forall y \tag{B.21}$$

where sgn is the signum function and k_y satisfies the second of conditions (B.17).

The above equation was derived for a lossy medium (k complex) but it remains valid for the lossless case (k real) provided the path of integration is stipulated to avoid the singularities [94]. In this case k_y should satisfy

$$k_y = \begin{cases} \sqrt{k^2 - k_x^2} & k > k_x \\ -j\sqrt{k_x^2 - k^2} & k < k_x \end{cases} \tag{B.22}$$

In the limit as $|y| \to 0$, we have

$$\frac{1}{4j}H_o^{(2)}(k|x|) \overset{\mathcal{F}}{\Longleftrightarrow} \frac{1}{2jk_y} \qquad \begin{cases} \Re\mathrm{e}\{k_y\} > 0 \\ \Im\mathrm{m}\{k_y\} < 0 \end{cases} \tag{B.23}$$

and when k is real, the Fourier transform pair is given by

$$\tilde{G}(k|x|) \overset{\mathcal{F}}{\Longleftrightarrow} \begin{cases} \dfrac{1}{2j\sqrt{k^2 - k_x^2}} & k > k_x \\ \dfrac{1}{2\sqrt{k_x^2 - k^2}} & k < k_x \end{cases} \tag{B.24}$$

B.2 Point Source

In the three dimensional case, the Helmholtz equation takes the form

$$(\frac{\partial^2}{\partial x^2} + \frac{\partial^2}{\partial y^2} + \frac{\partial^2}{\partial y^2} + k^2)G(x,y,z) = -\delta(x)\delta(y)\delta(z) \tag{B.25}$$

Solving this equation in the spherical coordinates, gives

$$G(r) = \frac{e^{-jkr}}{4\pi r} \tag{B.26}$$

Following an analysis similar to the two dimensional case, the inverse Fourier transform integral is introduced as

$$G(x,y,z) = \frac{1}{(2\pi)^3}\int_{-\infty}^{\infty}\int_{-\infty}^{\infty}\int_{-\infty}^{\infty} \tilde{G}(k_x,k_y,k_z)e^{j(k_x x + k_y y + k_z z)}dk_x dk_y dk_z \tag{B.27}$$

$$\delta(x,y,z) = \frac{1}{(2\pi)^3}\int_{-\infty}^{\infty}\int_{-\infty}^{\infty}\int_{-\infty}^{\infty} e^{j(k_x x + k_y y + k_z z)}dk_x dk_y dk_z \tag{B.28}$$

which upon substitution in (B.25) yields the formal expression for G

$$G(x,y,z) = -\frac{1}{(2\pi)^3}\int_{-\infty}^{\infty}\int_{-\infty}^{\infty}\int_{-\infty}^{\infty} \frac{1}{k^2 - k_x^2 - k_y^2 - k_z^2} e^{j(k_x x + k_y y + k_z z)}dk_x dk_y dk_z \tag{B.29}$$

The presence of the poles

$$k_z = \mp\sqrt{k^2 - k_x^2 - k_y^2} \tag{B.30}$$

in the path of integration on the real k_z-axis renders the above integral undefined. Again, introducing a small loss in the medium and following the procedure outlined in the previous section, the k_z integration may be carried out in the complex plane. Thus, contour integration in the upper and lower half planes corresponding to $z > 0$ and $z < 0$, respectively yields

$$G(x,y,z) = \frac{j}{8\pi^2}\int_{-\infty}^{\infty}\int_{-\infty}^{\infty}\frac{e^{jk_z^+ z}}{k_z^+}e^{j(k_x x + k_y y)}dk_x dk_y, \qquad z > 0 \tag{B.31}$$

$$G(x,y,z) = \frac{j}{8\pi^2}\int_{-\infty}^{\infty}\int_{-\infty}^{\infty}\frac{e^{jk_z^- z}}{k_z^-}e^{j(k_x x + k_y y)}dk_x dk_y, \qquad z < 0 \tag{B.32}$$

where k_z^{pm} are given by

$$k_z^{\pm} = \mp\sqrt{k^2 - k_x^2 - k_y^2} \tag{B.33}$$

and they satisfy conditions similar to (B.17). Combining the two equations, we obtain for all z

$$\frac{e^{-jkr}}{4\pi r} = \frac{1}{2j}\frac{1}{(2\pi)^2}\int_{-\infty}^{\infty}\int_{-\infty}^{\infty}\frac{e^{-jk_z|z|}}{\text{sgn}\,(z)k_z}e^{j(k_x x + k_y y)}dk_x dk_y, \qquad \forall z \tag{B.34}$$

where

$$\begin{cases} \Re\text{e}\{k_z\} > 0 \\ \Im\text{m}\{k_z\} < 0 \end{cases} \tag{B.35}$$

When k_z is real (lossless case), the path of integration is deformed to exclude the real poles and (B.34) remains valid provided

$$k_z = \begin{cases} \sqrt{k^2 - k_x^2 - k_y^2} & k^2 > k_x^2 + k_y^2 \\ -j\sqrt{k_x^2 + k_y^2 - k^2} & k^2 < k_x^2 + k_y^2 \end{cases} \tag{B.36}$$

In the limit as $|z| \to 0$, we have

$$\frac{e^{-jk\sqrt{x^2+y^2}}}{4\pi\sqrt{x^2+y^2}} \overset{\mathcal{F}}{\Longleftrightarrow} \frac{1}{2jk_z} \tag{B.37}$$

and when k is real the Fourier transform pair is given by

$$\tilde{G}(x,y) \overset{\mathcal{F}}{\Longleftrightarrow} \begin{cases} \dfrac{1}{2j\sqrt{k^2-k_x^2-k_y^2}} & k^2 > k_x^2+k_y^2 \\ \dfrac{1}{2\sqrt{k_x^2+k_y^2-k^2}} & k^2 < k_x^2+k_y^2 \end{cases} \tag{B.38}$$

APPENDIX C

MATHEMATICAL PROOFS

C.1 Proof of the Transformation (5.10)

Consider the generalized impedance boundary condition (5.1) applied to the normal field component U at the top surface ($y = t$) of the layer under study

$$\sum_{m=0}^{M} \frac{a_m}{(-jk_o)^m} \left.\frac{\partial^m U}{\partial y^m}\right|_{y=t} = 0 \tag{C.1}$$

where a_m and a'_m are the GIBC constants specific to the material properties of the layer. It is desired to replace this condition by an analogous one, applicable at the reference plane ($y = 0$) as

$$\sum_{m=0}^{M} \frac{A_m}{(-jk_o)^m} \left.\frac{\partial^m U}{\partial y^m}\right|_{y=0} = 0 \tag{C.2}$$

This may be the case when one is interested in applying the image theory for a coating of thickness t on a ground plane.

In order to find the relation between the two sets of coefficients A_m and a_m, we expand U at $y = t$ and its normal derivatives there in terms of the corresponding quantities at $y = 0$. Hence, by invoking Maclaurin series expansion of U, we have

$$\begin{aligned} U(t) &= \sum_{n=0}^{\infty} \left(\frac{t^n}{n!}\frac{\partial^n}{\partial y^n}\right) U(0) \\ &= \sum_{n=0}^{M} \left(\frac{t^n}{n!}\frac{\partial^n}{\partial y^n}\right) U(0) + \mathcal{O}(t^{M+1}, \partial^{M+1}) \end{aligned} \tag{C.3}$$

where we have retained only derivatives of at most M-th order as the original condition does not include higher order derivatives. Similarly, we have for the first normal derivative

$$\frac{\partial U(t)}{\partial y}=\sum_{n=1}^{M}\left(\frac{t^{n-1}}{(n-1)!}\frac{\partial^n}{\partial y^n}\right)U(0)+\mathcal{O}(t^M,\partial^{M+1}) \tag{C.4}$$

and generalizing this to higher orders

$$\frac{\partial^p U(t)}{\partial y^p}=\sum_{n=p}^{M}\left(\frac{t^{n-p}}{(n-p)!}\frac{\partial^n}{\partial y^n}\right)U(0)+\mathcal{O}(t^{M+1-p},\partial^{M+1}) \tag{C.5}$$

Substituting the above expansion back into (C.1), we obtain

$$\sum_{m=0}^{M}\frac{a_m}{(-jk_o)^m}\sum_{n=m}^{M}\left(\frac{t^{n-m}}{(n-m)!}\frac{\partial^n}{\partial y^n}\right)U(0)=0 \tag{C.6}$$

which after a simple re-arrangement of terms reduces to

$$\sum_{m=0}^{M}\frac{1}{(-jk_o)^m}\sum_{n=0}^{m}\frac{(-jk_ot)^n}{n!}a_{m-n}\frac{\partial^m U(0)}{\partial y^m}=0 \tag{C.7}$$

The above result is in the desired form (C.2) and by inspection, we find

$$A_m=\sum_{n=0}^{m}\frac{(-jk_ot)^n}{n!}\,a_{m-n} \quad , \qquad m=0,\ldots,M \tag{C.8}$$

C.2 Proof of the Identity (5.52)

We would like to show that

$$\lim_{z\to 0}\frac{\partial G(x,y,z;x',y',z')}{\partial z}\Big|_{z'=0}$$

is a Dirac Delta function. Consider the identity (Appendix B)

$$\frac{e^{jk_oR}}{4\pi R}=\frac{j}{2}\frac{1}{(2\pi)^2}\int_{-\infty}^{\infty}\int_{-\infty}^{\infty}\frac{1}{k_z}e^{jk_xx}e^{jk_yy}e^{jk_zz}dk_xdk_y \tag{C.9}$$

$$R=\sqrt{x^2+y^2+z^2} \tag{C.10}$$

implying the Fourier transform relation

$$\frac{e^{jk_oR}}{4\pi R} \Longleftrightarrow \frac{j}{2}\frac{e^{jk_zz}}{k_z} \tag{C.11}$$

where

$$k_z = \begin{cases} j\sqrt{k_x^2 + k_y^2 - k_o^2} & , \quad k_o < \sqrt{k_x^2 + k_y^2} \\ \\ \sqrt{k_o^2 - k_x^2 - k_y^2} & , \quad k_o > \sqrt{k_x^2 + k_y^2} \end{cases} \tag{C.12}$$

in accordance with the radiation condition. Differentiating with respect to z, we have

$$\frac{\partial}{\partial z}\tilde{G}(k_x, k_y) \quad = \quad -\frac{1}{2}e^{jk_zz} \tag{C.13}$$

whose limit as the sheet is approached is

$$\lim_{z\to 0} -\frac{1}{2}e^{jk_zz} = -\frac{1}{2} \tag{C.14}$$

Upon inverse transformation of the last equation, the desired result is obtained as

$$\lim_{z\to 0}\frac{\partial G(x, y, z)}{\partial z} = -\frac{1}{2}\delta(x, y) \tag{C.15}$$

APPENDIX D

OPTIMIZATION TECHNIQUES

Once a well written code is compiled, most vector and parallel constructs are recognized by the compiler and automatically optimized for efficient execution. This is achieved through loop level concurrency and vectorization of the sequential code. A typical compiler's optimization strategy may be summarized as follows:

For *each innermost loop* :

- If **vectorizable** then
    - If *next outer loop* is **parallelizable** then
        - ⋆ Concurrent-Outer Vector-Inner
    - Else
        - ⋆ Vector-Concurrent
    - Endif
- Elseif **parallelizable** then
    - ⋆ Scalar-Concurrent
- Else
    - ⋆ Not Optimized
- Endif

The fastest vector-concurrent mode of execution is achieved when all the available processors are utilized to attack a single task concurrently with vector operations performed on strides of data on each processor. The resulting high-performance, low-level parallelism can significantly boost the performance of computationally intensive operations such as Fourier transformations.

In this study the scalar and optimized FFT routines available on the IBM 3090's ESSL library and the Alliant's Fortran math library were used in both scalar and vector modes. These FFT routines are written in conjunction with assembler language and generate instructions appropriate for the architecture of the processors–they manage data to make efficient uses of the memory hierarchy.

In addition to automatic optimization, however, most vector compilers provide directives for additional control. Compiler directives are user supplied control structures to override decisions made by the compiler and to give additional information to it. Upon compilation, the directives are interpreted by the processor and converted to library calls to be executed in a more efficient manner. In particular, the associative transformation directive recognizes operations like dot products and norm computations as reduction functions and optimizes these otherwise non-vectorizable loops.

Some general guidelines for code optimization in various architectural levels are given in Table D.1.

ARCHITECTURAL TECHNIQUES	PROGRAMMER ACTIONS†
SCALAR PIPELINING	Use compiler switches (global optimization).
VECTOR PROCESSING	1. Restructure loops and use compiler directives. 2. Maximize vector lengths by renesting, merging, unrolling loops; largest iterates to be inside. 3. Eliminate conditionals in loops & distribute them. 4. "Supervector" loops to fill vector registers. 5. Move I/O statements out of the loops. 6. Turn off vectorization for short loops,or some vectorized loops with conditionals, dependences.
CONCURRENCY	1. Eliminate/relocate dependences, scalar carry-arounds. 2. Restructure for Concurrent-Outer Vector-Inner. 3. Create concurrently-callable subroutines. 4. Renest/merge loops for more concurrent iterations.
CACHE/MEMORY ACCESS	1. Possible problems with strides. 2. Leftmost array dimension should be the largest. 4. Outer loop corresponds to the leftmost array index. 3. Process compact vectors, columns instead of rows. 4. Localize memory references.

†*Extracted from IBM 3090 and Alliant FX/8 programming manuals*

Table D.1: Optimization techniques.

BIBLIOGRAPHY

BIBLIOGRAPHY

[1] M. R. Hestenes and E. Steifel, "Method of Conjugate Gradients for solving linear systems," *J. Res. Nat. Bur. Standard.*, vol. 49, no. 6, pp. 409–436, Dec. 1952.

[2] M. R. Hestenes, *Conjugate Direction Methods in Optimization*, New York:Springer-Verlag, 1980.

[3] J. W. Cooley and J. W. Tukey, "An algorithm for the machine calculation of complex Fourier series," *Mathematics of Computation*, vol. 19, no. 90, pp.279–301, 1965.

[4] T. K. Sarkar, E. Arvas and S. M. Rao, "Application of FFT and the Conjugate Gradient method for the solution of electromagnetic radiation from electrically large and small conducting bodies," *IEEE Trans. Antennas Propagat.*, vol. AP-34, no. 5, pp. 635–640, May 1986.

[5] N. N. Bojarski, "k-Space formulation of the electromagnetic scattering problem" *Tech. Report* AFAL-TR-71-75, Mar. 1971.

[6] W. L. Ko and R. Mittra, "A new approach based on a combination of integral equation and asymptotic techniques for solving electromagnetic scattering problems" *IEEE Trans. Antennas Propagat.*, vol. AP-25, pp. 187–197, Mar. 1977.

[7] D. Borup and O. P. Gandi, "Fast Fourier Transform method for calculation of SAR distributed in finely discretized inhomogeneous models of biological bodies," *IEEE Trans. Microwave Theory Tech.*, vol. MTT–32, no. 4, Apr. 1984.

[8] A. F. Peterson and R. Mittra, "Iterative-based computational methods for electromagnetic scattering from individual or periodic structures," *IEEE J. Oceanic Engin.*, vol. OE-12, no. 2, pp. 458–465, Apr. 1987.

[9] D. R. Wilton and S. Govind, "Incorporation of Edge Conditions in Moment Method Solutions," *IEEE Trans. Antennas Propagat.*, vol. AP-25, pp. 845-850, Nov. 1977.

[10] A. W. Glisson and D. R. Wilton, "Simple and efficient numerical methods for problems of electromagnetic radiation and scattering from surfaces," *IEEE Trans. Antennas Propagat.*, vol. AP-28, no. 5, pp. 593–603, Sept. 1980.

[11] R. Anders, "Criteria for the choice of optimal basis functions," in *Proc. IEE Int. Conf. Antennas and Propagation, Part I- Antennas*, London, 1978, pp. 170–173.

[12] S. N. Karp, and L. Karel, Jr., "Generalized impedance boundary conditions with application to surface wave structures," *Electromagnetic Wave Theory*, 479–483, Permagon: New York, 1965.

[13] T. B. A. Senior and J. L. Volakis, "Derivation and application of a class of generalized boundary conditions," *IEEE Trans. Antennas and Propagat.*, vol. AP-37, no. 12, pp. 1566–1572, Dec. 1989.

[14] J. L. Volakis and T. B. A. Senior, "Diffraction by a thin dielectric half-plane," *IEEE Trans. Antennas and Propagat.*, vol. AP-35, no. 12, pp. 1483–1487, Dec. 1987.

[15] K. W. Whites and R. Mittra, "A systematic study of the impedance boundary condition", IEEE AP-S International Symposium, Digest pp. 870–873, Dallas, TX, 1990.

[16] P. C. Clemmow, An Introduction to Electromagnetic Theory, Cambridge University Press, New York, 1973.

[17] C. A. Balanis, *Advanced Engineering Electromagnetics*, John Wiley, New York, 1989.

[18] C.-T. Tai, *Dyadic Green's Functions in Electromagnetic Theory*, Intext Educational Publishers, San Francisco, 1971.

[19] J. A. Kong, *Electromagnetic Wave Theory*, John Wiley, New York, 1986.

[20] R. F. Harrington, *Field Computation by Moment Methods*, Malabay, Florida: R. E. Krieger Publishing Co., 1968.

[21] T. K. Sarkar, "The application of the conjugate gradient method for the solution of operator equations arising in electromagnetic scattering from wire antennas," *Radio Sci.*, vol. 19, no. 5, pp. 1156-1172, Sept.-Oct. 1984.

[22] E. O. Brigham, *The Fast Fourier Transform and its Applications*, Englewood Cliffs, New Jersey: Prentice Hall, 1988.

[23] S. A. Bokhari and N. Balakrishnan, "A method to extend the spectral iteration technique," *IEEE Trans. Antennas Propagat.*, vol. AP-34, no. 1, pp. 51–57, Jan. 1986.

[24] T. J. Peters and J. L. Volakis, "On the formulation and implementation of a conjugate gradient FFT method," *J. Electromag. Waves and Appl.*, vol. 3, no. 8, pp. 675–696, 1989.

[25] K. Barkeshli and J. L. Volakis, "Improving the convergence rate of the CGFFT method using subdomain basis functions," *IEEE Trans. Antennas and Propagat.*, vol. AP-37, no. 7, pp. 893–900, July 1989.

[26] C. Y. Shen, K. J. Glover, M. I. Sancer and A. D. Varvatsis, "The Discrete Fourier Transform method of solving differential-integral equations in scattering theory," *IEEE Trans. Antennas and Propagat.*, vol. AP-37, no. 8, pp. 1032–1040, Aug. 1989.

[27] S. A. Schelkunoff, "Theory of antennas of arbitrary size and shape", *Proc. IRE*, vol. 29, pp. 493–521, 1941.

[28] R. W. P. King, "The linear antenna—Eighty years of progress," *IEEE Proceedings.*, vol. 55, no. 1, pp. 2–16, Jan. 1967.

[29] R. F. Harrington and J. R. Mautz, "Straight wires with arbitrary excitation and loading," *IEEE Trans. Antennas Propagat.*, vol. AP-15, pp. 502–515, July 1967.

[30] J. H. Richmond, "Radiation and scattering by thin wire structures in a homogeneous conducting medium," *IEEE Trans. Antennas and Propagat.*, vol. AP-22, no. 2, p. 365, Mar. 1974.

[31] M. D. Khashkind and L. A. Vainshteyn, "Diffraction of plane waves by a slit and a tape," *Radio Engin. Electron.*, vol. 9, pp. 1492–1502, 1964.

[32] T. B. A. Senior, "Scattering by resistive strips," *Radio Science*, vol. 14, no. 5, pp. 911–924, Sept.-Oct. 1979.

[33] T. B. A. Senior, "Backscattering from resistive strips," *IEEE Trans. Antennas and Propagat.*, vol. AP-27, no. 6, pp. 808–813, Nov. 1979.

[34] T. B. A. Senior and V. V. Liepa, "Backscattering from tapered resistive strips," *IEEE Trans. Antennas and Propagat.*, vol. AP-32, no. 7, pp. 747–751, July 1984.

[35] R. Haupt and V. V. Liepa, "Synthesis of tapered resistive strips," *IEEE Trans. Antennas and Propagat.*, vol. AP-35, no. 11, pp. 1217–1225, Nov. 1987.

[36] J. H. Richmond, "Scattering by a dielectric cylinder of arbitrary cross section shape," *IEEE Trans. Antennas and Propagat.*, vol. AP-13, pp.334–341, May. 1965.

[37] J. H. Richmond, "TE-wave scattering by a dielectric cylinder of arbitrary cross-section shape," *IEEE Trans. Antennas and Propagat.*, vol. AP-14, July 1966.

[38] R. S. Elliot, *Antenna Theory and Design*, Prentice-Hall, Englewood Cliffs, N.J., 1981.

[39] H. C. Pocklington, "Electrical oscillations in wire", Proc. Cambridge Philos. Soc., vol. 9, pp. 324-332, 1897.

[40] L. L. Tsai, "A numerical solution for the near and far fields of annular ring of magnetic current," *IEEE Trans. Antennas Propagat.*, vol. AP-20, no. 5, pp. 569-576, Sept. 1972.

[41] W. L. Stutzman and G. A. Thiele, *Antenna Theory and Design*, John Wiley, New York, Ch. 7, 1981.

[42] T. B. A. Senior and J. L. Volakis, "Sheet simulation of a thin dielectric layer," *Radio Science*, vol 22, pp. 1261–1272, 1987.

[43] C. M. Butler and D. R. Wilton, "General Analysis of Narrow Strips and Slots," *IEEE Trans. Antennas Propagat.*, vol. AP-28, no. 1, pp. 42–48, Jan. 1980.

[44] M. Abramowitz and I. E. Stegun, *Handbook of Mathematical Functions*, Dover, New York, 1970.

[45] Ll. G. Chambers, *Integral Equations; A Short Course*, London, England: International Textbook Co., 1976.

[46] J. Meixner, "The behavior of electromagnetic fields at edges,"*IEEE Trans. Antennas Propagat.*, vol. AP-20, no. 4, pp. 442–446, July 1972.

[47] S. K. Cho, C.-M. Chu and C.-T. Tai, "Proximity effect of semi-infinite parallel plate transmission line in the presence of a perfectly conducting ground," *University of Michigan Radiation Laboratory Tech. Report.* 494-2-T, Sensor and Simulation Notes, Aug. 1971.

[48] T. J. Peters and J. L. Volakis, "The applications of a conjugate gradient FFT method to scattering from thin planar material plates," *IEEE Trans. Antenna Propagat.*, vol. AP-36, no.4, pp. 518–526, Apr. 1988.

[49] Y. Rahmat-Samii and R. Mittra, "Electromagnetic coupling through small apertures in a conducting screen," *IEEE Trans. Antenna Propagat.*, vol. AP-25, no. 2, pp. 180–187, Mar. 1977.

[50] J. R. Mautz and R. F. Harrington, "Electromagnetic transmission through a rectangular aperture in a perfectly conducting plane," Scientific Report No. 10, prepared under contract F19628-73-C-0047 with the A.F. Cambridge Labs, Hanscom AFB, Feb. 1976.

[51] J. S. Hey and T. B. A. Senior, "Electromagnetic scattering by thin conducting plates at glancing incidence," *Proceedings of the Physical Society*, vol. 72, p. 981, 1958.

[52] L. N. Medgyesi-Mitschang and J. M. Putnam, "Scattering from irregular-edged planar and curved surfaces," *IEEE Trans. Antenna Propagat.*, vol. AP-38, no. 1, pp. 137–141, Jan. 1990.

[53] A. F. Peterson and S. P. Castillo, "A frequency-domain differential equation formulation for electromagnetic scattering from inhomogeneous cylinders," *IEEE Trans. Antennas Propagat.* vol. AP-37, no. 5, pp. 601–607, May 1989.

[54] J. L. Volakis, "High frequency scattering by a thin material half plane and strip," *Radio Science*, vol. 23, pp. 450–462, May-June 1988.

[55] J. L. Volakis and T. B. A. Senior, "Applications of a class of generalized boundary conditions to scattering by a metal-backed dielectric half-plane," *Proc. IEEE*, vol. 77, pp. 796–805, May 1989.

[56] M. A. Leontovich, "On the approximate boundary conditions for electromagnetic field on surface of well-conducting bodies", from Investigation of Propagation of Radio Waves, edited by B. A. Vrendnsky, Academy of Sciences, USSR, 1948.

[57] T. B. A. Senior, "Impedance boundary conditions for imperfectly conducting surfaces", *Appl. Sci. Res.*, sec. B, vol. 8, pp. 418–436, 1960.

[58] T. B. A. Senior, "Approximate boundary conditions", *IEEE Trans. Antennas and Propagat.*, vol. AP-29, no. 5, pp. 826–829, Sept. 1981.

[59] S-W Lee and W. Gee, "How good is the impedance boundary condition", *IEEE Trans. Antennas and Propagat.*, vol. AP-35, no. 11, pp. 1313–1315, Nov. 1987.

[60] D. S. Wang, "Limits and validity of the impedance boundary condition on penetrable surfaces", *IEEE Trans. Antennas and Propagat.*, vol. AP-35, no. 4, pp. 453–457, Apr. 1987.

[61] N. G. Alexopoulos and G. A. Tadler, "Accuracy of the Leontovich boundary condition for continuous and discontinuous surfaces impedances", *J. Appl. Phys.*, vol. 46, no. 8, pp. 3326–3332, 1975.

[62] J. L. Volakis, T. B. A. Senior and J. M. Jin, "Derivation and application of a class of generalized boundary conditions – II," *University of Michigan Radiation Laboratory Tech. Report.* 025921-T-1, prepared under NASA grant NAG-2-541, Feb. 1989.

[63] R.F. Harrington and J.R. Mautz, "A generalized network formulation for aperture problems," *IEEE Trans. Antennas Propagat.*, vol. AP-24, pp. 870-873, Nov. 1976.

[64] D. T. Auckland and R. F. Harrington, "Electromagnetic transmission through a filled slit in a conducting plate of finite thickness, TE case," *IEEE Trans. Antenna Propagat.*, vol. AP-26, no. 7, pp. 499-505, Jul. 1978.

[65] S. N. Sinha, D. K. Mehra and R. P. Agarwal, "Radiation from a waveguide-backed aperture in an infinite ground plane in the presence of a thin conducting plate," *IEEE Trans. Antennas Propagat.*, vol. AP-34, no. 4, pp. 539-545, Apr. 1986.

[66] R. F. Harrington, *Time Harmonic Electromagnetic Fields*, McGraw Hill, New York, 1969.

[67] S. W. Lee and H. Ling, *Data book for cavity RCS*, University of Illinois Electromagnetic Laboratory Technical Report SWL89-1, Jan. 1989.

[68] T. B. A. Senior and J. L. Volakis "Scattering by gaps and cracks," *IEEE Trans. Antennas Propagat.*, vol. AP-37, no. 6, pp. 744–750, June 1989.

[69] I. S. Gradshteyn and I. M. Ryzhik, *Table of Integrals, Series, and Products*, Academic Press, New York, 1980.

[70] J.-M. Jin and J. L. Volakis, "TM scattering by an inhomogeneous filled aperture in a thick conducting plane," *IEE Proceeding–H*, vol. 137, pp. 153–159, June 1990.

[71] N. Morita, "Diffraction of electromagnetic waves by a two-dimensional aperture with arbitrary cross-sectional shape," *Electron. Commun. Japan*, vol. 54-B, no. 5, pp. 58-61, 1971.

[72] S. C. Kashyap, M. A. K. Hamid, "Diffraction characteristics of a slit in a thick conducting screen," *IEEE Trans. Antenna Propagat.,* vol. AP-19, pp. 499-507, July 1971.

[73] K. Hongo and G. Ishii, "Diffraction of an electromagnetic plane wave by a thick slit," *IEEE Trans. Antennas Propagat.*, vol. AP-26, pp. 494-499, May 1978.

[74] H. Henke, H. Fruchting and R. Winz, "Diffraction by flanged parallel-plate waveguide and a slit in a thick screen," *Radio Sci.*, vol. 14, pp. 11-18, Jan.-Feb. 1979.

[75] D.T. Auckland and R.F. Harrington, "A nonmodal formulation for electromagnetic transmission through a filled slot of arbitrary cross section in a thick conducting screen," *IEEE Trans. Microwave Theory Tech.*, vol. MTT-28, no. 6, pp. 548-555, June 1980.

[76] J.-M. Jin and J. L. Volakis, "TE Scattering by an inhomogeneously filled aperture in a thick ground plane," *IEEE Trans. Antennas Propagat.*, vol. AP-38, no. 8, pp. 1280-1286, Aug. 1990.

[77] R. Kautz, P. H. Pathak and L. Peters, Jr, "EM scattering by slits and grooves in thick perfectly conducting planar surfaces," Technical Report 714349-6, The Ohio State University ElectroScience Laboratory, Department of Electrical Engineering, 1984.

[78] S. K. Jeng, "Aperture Admittance Matrix by Finite Element Method for Scattering by a Cavity-Backed Aperture," 1988 IEEE AP-S International Symposium, Digest pp. 1134–1137, Syracuse, NY, June 1988.

[79] T. B. A. Senior, K. Sarabandi and J. R. Natzke, "Scattering by a Narrow Gap," *IEEE Trans. Antennas Propagat.*, vol. AP-38, no. 7, pp. 1102–1110, Jul. 1990.

[80] C. M. Butler, Y. Rahmat-Samii and R. Mittra, "Electromagnetic penetration through apertures in conducting surfaces," *IEEE Trans. Antennas Propagat.*, vol. AP-26, no. 1, pp. 82-93, Jan. 1978.

[81] C.L. I and R. F. Harrington, "Electromagnetic transmission through an aperture of arbitrary shape in a conducting screen," Syracuse University Tech. Report TR-82-5, April 1982.

[82] C. M. Butler, "A formulation of the finite-length narrow slot or strip equation," *IEEE Trans. Antennas Propagat.*, vol. AP-30, pp. 1254–1257, Nov. 1982.

[83] R.W. Ziolkowski and W.A. Johnson, "Electromagnetic Scattering of an arbitrary plane wave from a spherical shell with a circular aperture," *J. Math Phys.*, vol. 28, no. 6, pp. 1263-1314, 1988.

[84] J. P. Keener, *Principles of Applied Mathematics: Transformation and Approximation*, Addison–Wesley, p. 289, 1988.

[85] D. B. Seidel, D. G. Dudley and C. M. Butler, "Aperture excitation of a wire in a rectangular cavity," Interaction Notes, Note 345, June 1977.

[86] A. J. Bahr, "Using electromagnetic scattering to estimate the depth of a rectangular slot," *IEEE Trans. Antennas Propagat.*, vol. AP-27, no. 6, pp. 738–746, Nov. 1979.

[87] C.-H. Liang and D. K. Cheng, "Electromagnetic fields coupled into a cavity with a slot-aperture under resonant conditions," *IEEE Trans. Antennas Propagat.*, vol. AP-30, no. 4, pp. 664–672, July 1982.

[88] J.-M. Jin and J. L. Volakis, "A finite element-boundary integral formulation for scattering by three-dimensional cavity-backed apertures," *IEEE Trans. Antennas Propagat.* vol. AP-39, no. 1, pp. 97–104, Jan. 1991.

[89] T. B. A. Senior and J. L. Volakis, "Generalized impedance boundary conditions in scattering," to appear in *Proc. IEEE*, 1991.

[90] M. A. Ricoy, "Electromagnetic Scattering from Two-Dimensional Thick Material Junctions," Ph.D. Dissertation, The University of Michigan, Ann Arbor, MI, 1990.

[91] A. P. Zwamborn and P. M. van den Berg, "A weak form of the conjugate gradient FFT method for plate problems," *IEEE Trans. Antennas Propagat.* vol. AP-39, no. 2, pp. 224–228, Feb. 1991.

[92] J. D. Collins, J. L. Volakis and J. M. Jin, "A combined finite element–boundary integral formulation for solution of two–dimensional scattering problems via CGFFT," *IEEE Trans. Antennas Propagat.*, vol. AP-38, no. 11, pp. 1852–1858, Nov. 1990.

[93] R. F. Harrington, "Method of moments in electromagnetics," J. Electromagnet. Waves Applicat., vol. 1, no. 3, pp. 181-200, 1987.

[94] W. C. Chew, *Waves and Fields in Inhomogeneous Media*, Van Nostrand Reinhold, New York, 1990.